



City Research Online

City, University of London Institutional Repository

Citation: Jhugroo, Eric (2007). Pattern formation in squares and rectangles. (Unpublished Doctoral thesis, City University)

This is the published version of the paper.

This version of the publication may differ from the final published version.

Permanent repository link: <https://openaccess.city.ac.uk/id/eprint/18271/>

Link to published version:

Copyright: City Research Online aims to make research outputs of City, University of London available to a wider audience. Copyright and Moral Rights remain with the author(s) and/or copyright holders. URLs from City Research Online may be freely distributed and linked to.

Reuse: Copies of full items can be used for personal research or study, educational, or not-for-profit purposes without prior permission or charge. Provided that the authors, title and full bibliographic details are credited, a hyperlink and/or URL is given for the original metadata page and the content is not changed in any way.

PATTERN FORMATION IN SQUARES
AND RECTANGLES

by
Eric Jhugroo

Thesis submitted for the degree of Doctor of
Philosophy

Centre for Mathematical Science
City University
London

April 2007

Contents

1	Introduction	7
1.1	Background	7
1.2	Plan of Study	10
2	Pattern Formation in Squares	12
2.1	Introduction	12
2.2	Formulation of the problem	14
2.3	Analysis of the periodic problem	15
2.3.1	Linear solution	15
2.3.2	Weakly nonlinear solution	16
2.4	Linear solution of the rigid problem	20
2.4.1	Numerical scheme	21
2.4.2	Accuracy	26
2.4.3	Results	27
2.4.4	Comparison with the periodic problem	30
2.5	Weakly nonlinear analysis of the quasi-periodic problem	31
2.6	Nonlinear solution of the time dependent rigid problem	40
2.6.1	Numerical scheme	40
2.6.2	Accuracy and validation	42
2.6.3	Results	43
2.7	Nonlinear solution of the steady-state rigid problem	47
2.7.1	Numerical scheme	47
2.7.2	Accuracy	51
2.7.3	Results	51
2.8	Discussion	56

3	Pattern Formation in Large Squares	126
3.1	Introduction	126
3.2	Formulation of the problem	127
3.3	Core expansion	129
3.4	Corner regions	131
3.5	Fourier transform theory	132
3.6	Linear Solution	135
	3.6.1 Solution method	135
	3.6.2 Results	137
	3.6.3 Comparison with numerical results	137
3.7	Nonlinear solution	139
	3.7.1 Solution method	140
	3.7.2 Results	141
3.8	Wall regions	141
3.9	Discussion	145
4	Convection Patterns in Rectangles	157
4.1	Introduction	157
4.2	Formulation of the problem	158
4.3	Results for aspect ratio 0.75	158
	4.3.1 Linear solution	158
	4.3.2 Nonlinear time-dependent solutions	161
	4.3.3 Nonlinear steady-state solutions	162
4.4	Results for aspect ratio 0.5	166
4.5	Discussion	167
5	Pattern Formation in Large Rectangles	235
5.1	Introduction	235
5.2	Formulation of the problem	235
5.3	Theory	236
5.4	Linear solution	240
	5.4.1 Solution method	240
	5.4.2 Results	241
	5.4.3 Comparison with numerical results	242

5.5	Nonlinear solution	243
5.5.1	Solution Method	243
5.5.2	Results	244
5.6	Discussion	246
6	Summary and conclusions	260

Acknowledgements

I would like to express my thanks to Professor Peter Daniels for his guidance and support throughout this research and the preparation of this thesis. I would also like to thank my wife Jay and my sister Emilie for all their help and encouragement. Finally, I would like to thank everyone in the School of Engineering and Mathematical Sciences who has helped me during my period at City University.

Declaration

I grant powers of discretion to the University Librarian to allow this thesis to be copied in whole or in part without further reference to me. This permission covers only single copies made for study purpose, subject to normal conditions of acknowledgement.

Abstract

This thesis considers pattern formation governed by the two dimensional Swift-Hohenberg equation in square and rectangular domains.

For the square, the dependence of the solution on the size of the square relative to the characteristic wavelength of the pattern is investigated for periodic, non-periodic (rigid) and quasi-periodic boundary conditions. Linear and weakly nonlinear analysis is used together with numerical computation to identify the bifurcation structure of steady-state solutions and to track their nonlinear development as a function of the control parameter. Nonlinear solutions arising from secondary bifurcations and fold bifurcations are also found. Time-dependent computations are also carried out in order to investigate stability, and to find certain nonlinear steady states.

The structure of solutions in the limit where the size of the square is much larger than the characteristic wavelength of the pattern is investigated using asymptotic methods.

For the rectangle, the dependence of the solution on the size of the rectangle relative to the characteristic wavelength of the pattern is investigated for non-periodic (rigid) boundary conditions. Most results are obtained for two aspect ratios, 0.75 and 0.5. Linear analysis is used together with numerical computations to identify the bifurcation structure of steady-state solutions and to track their nonlinear development. Nonlinear solutions arising from secondary bifurcations and fold bifurcations are also found, again making use of time-dependent calculations where necessary.

Finally, the structure of solutions in the limit where the size of the rectangle is much larger than the characteristic wavelength of the pattern is investigated using asymptotic methods.

The results are discussed in relation to patterns observed in physical systems such as Rayleigh-Bénard convection.

Chapter 1

Introduction

1.1 Background

Pattern formation through transition from a homogeneous or structureless state to a more complex state is a common occurrence in nature with well known examples occurring in fluid dynamics, chemical reactions and biological systems (see for example Cross and Hohenberg 1993). In laboratory experiments designed to understand such transitions, for example in Rayleigh-Bénard convection and Taylor-Couette flow (see the book by Koschmieder 1993), the container walls have a significant impact on the patterns that are observed not only in small aspect ratio systems but also in large scale systems where the dimensions of the geometry are much greater than the characteristic length scale of the instability.

In the Rayleigh-Bénard system, early theoretical work designed to take account of the lateral walls of the container includes that by Davis (1967) and Catton (1970) who used a ‘finite roll’ Galerkin approximation to the linearized Boussinesq equations to predict that in rectangular planform containers convection begins in the form of rolls parallel to the shorter sides. This is consistent with experimental observations in moderately sized planforms (Stork and Muller 1972, Buhler, Kirchartz and Oertel 1979, Kirchartz and Oertel 1988) and with the long channel limit considered by Davies-Jones (1970) although in larger planforms patterns appear to rarely consist of straight parallel rolls (Gollub and McCarriar and Steinman 1982). Other

experiments showing the range of patterns observed in Rayleigh-Bénard convection include those in square planform containers by Košmieder (1966), those in circular planform containers by Koschmieder (1974) and Croquette, Mory and Schosseler (1983), those on externally excited systems by Chen and Whitehead (1968) and Croquette and Schosseler (1982) and those on pattern dynamics by Croquette (1989).

For square containers, finite roll Galerkin approximations to the linearized system predict an orthogonal combination of "crossed rolls" at onset (Edwards 1988) whereas experiments in large planforms often reveal diagonal structures (Koschmieder 1966). A possible reason for this discrepancy as pointed out by Edwards (1988) is that Galerkin representations based on finite roll approximations parallel and perpendicular to the sides of the container are unlikely to be able to predict diagonal roll structures unless a large number of modes is used and this is generally not possible for large three dimensional domains (Arter and Newell 1988). This is a major drawback to the use of Galerkin methods because the preferred modes at onset generally do involve diagonal structures.

A better approach may be to use finite-difference or finite-element methods where no assumptions of the underlying structure of the eigenfunctions are involved. Even so one of the difficulties still encountered in such studies is the large computing power needed to solve even the linearized system for three dimensional domains large enough to contain more than just a few rolls. This led Greenside and Coughran (1984) to undertake a numerical study of the simpler Swift-Hohenberg system, a two dimensional relaxational model (Swift and Hohenberg 1977) designed to contain many of the ingredients of the Boussinesq system. This has the non dimensional form

$$\frac{\partial u}{\partial t} = \varepsilon u - (1 + \nabla^2)^2 u - u^3, \quad (1.1)$$

where $\nabla^2 = \frac{\partial^2}{\partial x^2} + \frac{\partial^2}{\partial y^2}$, x and y are non-dimensional Cartesian coordinates, ε is a control parameter and $u(x, y, t)$ is a characteristic property of the system such as the vertical velocity component at mid-height in a horizontal fluid layer. The control parameter ε is equivalent to the excess of the Rayleigh number above its critical value for an infinite layer, where non-trivial solutions of (1.1) first appear at $\varepsilon = 0$ with characteristic wavelength

2π . Greenside and Coughran (1984) carried out a time evolution study of (1.1) identifying many interesting patterns in both squares and rectangular domains and because of the relatively simple form of the equation it was possible to compute patterns over a wide range of domain sizes. Other work on the Swift-Hohenberg equation includes that for a rectangular geometry by Greenside, Coughran and Schryer (1982) and for a circular geometry by Morris, Bodenschatz, Cannell and Ahlers (1993).

A major development in the theoretical understanding of Rayleigh-Bénard convection was the development by Newell and Whitehead (1969) and Segel (1969) of multiple scale representations of the solution in large domains. This work showed how multiple-scale methods could be used to represent the solution as a set of convection rolls modulated by an envelope or amplitude function. This allowed a weakly-nonlinear theory to be formulated describing these solutions just beyond the onset of convection. The introduction of lateral walls in such systems was studied by Brown and Stewartson (1977, 1978) for rectangular and circular domains respectively. The effect of lateral boundaries in simpler two-dimensional containers was considered by Daniels (1977a, 1978) and later papers (Daniels 1981, 1984) studied the stability and evolution of the roll pattern. The main effect of the lateral boundary is to determine the boundary conditions for the amplitude functions, as also discussed by Cross (1982). This type of representation was used by Daniels and Weinstein (1992) to discuss the cross roll structure of the Swift-Hohenberg equation near a single lateral boundary and by Daniels and Weinstein (1996) to discuss orthogonal roll patterns for the Swift-Hohenberg equation in rectangular planforms. The structure of grain boundaries in the latter system was discussed by Daniels and Lee (1999). Other investigations of large planform systems include those by Cross and Newell (1984) and Newell, Passot and Souli (1990). More recently Daniels (2000) has used the amplitude formulation to describe the weakly-nonlinear structure of the Swift-Hohenberg system near onset in an arbitrary two dimensional planform. This work proposes that at onset the roll pattern forms along the largest available span of the domain. This is of relevance to the present work which is concerned with finding solutions of the Swift-Hohenberg equation in square or rectangular domains, where the longest spans are the diagonals.

1.2 Plan of Study

The main aim of the present work is to find solutions of the two dimensional Swift-Hohenberg equation in square and rectangular domains. In Chapter 2, the problem is formulated for a square domain $0 \leq x \leq L$, $0 \leq y \leq L$. Thus there are two non-dimensional parameters, the control parameter ε and the parameter L which determines the size of the domain relative to the characteristic wavelength which for an infinite layer is 2π . Unlike the study of Greenside and Coughran (1984) the main aim here is to undertake a bifurcation analysis allowing the underlying structure and symmetries of the system to be identified for a range of values of L and ε . The boundary conditions are taken to be

$$u = \frac{\partial^2 u}{\partial q^2} - \delta \frac{\partial u}{\partial q} = 0 \quad \text{on } x = 0, L \quad \text{and} \quad y = 0, L, \quad (1.2)$$

where q is the inward normal to the boundary and δ is a constant parameter. With $\delta = 0$ the conditions are referred to as periodic because they are then consistent with periodic solutions of (1.1) in an infinite domain. If δ is non-zero such solutions are excluded and the conditions are then non-periodic; in particular if δ is infinite u and its first derivative vanish on the boundary, equivalent to realistic rigid lateral boundaries in the Rayleigh-Bénard system. Most solutions determined here are for the rigid problem but the periodic problem ($\delta = 0$) and quasi-periodic problem (δ small) are studied in Sections 2.3 and 2.5 respectively using weakly-nonlinear theory to provide some useful analytical insight. In Section 2.4 a thirteen point finite-difference scheme is used to obtain the eigenvalues ε and eigenfunctions u of the steady linearized version of (1.1) for the rigid problem. Results are obtained for a wide range of values of L showing how the symmetry and structure of the preferred pattern changes as a function of L . Nonlinear solutions of the rigid problem are first found in Section 2.6 using an explicit time dependent finite-difference scheme to compute the solutions forward in time to reach steady-state. This reveals a wide range of steady-state solution patterns. In order to track these solutions and those found in the linear analysis of Section 2.4 into the nonlinear regime in Section 2.7 the finite difference scheme of Section 2.4 is extended and combined with a Newton iteration to track the nonlinear development of

these steady-state solutions for increasing ε . Secondary bifurcations and nonlinear fold bifurcations are also identified. The results are compared with experimental findings for the Rayleigh-Bénard system in Section 2.8.

In Chapter 3 an asymptotic theory is developed for the square domain in the limit as $L \rightarrow \infty$ and the results are compared with those of Chapter 2. The asymptotic theory is based on the analysis of Daniels (2000) but modified to allow for the corners of the square. This leads to significant differences in the scalings involved for the control parameter and length scales. The main core expansion is considered in Section 3.3 and uses a multiple scale representation of the roll pattern. The core solution must match with solutions in the corners of the square which are considered in Section 3.4. The leading order core solution is constructed using Fourier transform theory in Section 3.5 and linear and weakly nonlinear solutions are determined in Sections 3.6 and 3.7 respectively. Section 3.8 discusses further wall regions that are needed near the boundary of the square to adjust the solution to the rigid boundary conditions. The results are discussed in Section 3.9.

In Chapter 4 the results of Chapter 2 are extended to the case of the rectangular domain although here only the rigid problem is considered. The rectangle occupies the domain $0 \leq x \leq L$, $0 \leq y \leq M$ and most results are for two particular aspect ratios, $M/L = 0.75$ and $M/L = 0.5$. These are described in Sections 4.3 and 4.4 respectively. The results are discussed in Section 4.5.

Chapter 5 considers the limit of large rectangular domains where $L \rightarrow \infty$ and $M \rightarrow \infty$. The asymptotic theory of Chapter 3 is modified in Section 5.3 to allow for the rectangular geometry and linear and nonlinear solutions are obtained in Sections 5.4 and 5.5 respectively. The results are discussed and compared with the numerical results of Chapter 4 in Section 5.5.

Chapter 6 contains a summary of the main results and conclusions along with a discussion of possible future avenues of research.

Chapter 2

Pattern Formation in Squares

2.1 Introduction

This study investigates convection patterns in a square by finding solutions of the two-dimensional Swift-Hohenberg equation subject to various boundary conditions. The aim is to gain insight into the nature of patterns at the onset of convection and also in the supercritical nonlinear regime. The Swift-Hohenberg equation (Swift and Hohenberg 1977) is one of several phenomenological models (see, for example, Cross and Hohenberg 1993) which provide a simplification of the three-dimensional Rayleigh-Bénard system but have many features in common with the latter.

There have been a number of key studies of pattern formation in finite domains, although none of those have studied the square domain in great depth. Davis (1967) studied the linear theory for Rayleigh-Bénard convection in a rectangular box heated from below and used a Galerkin method based on ‘finite roll’ solutions to predict that convection would set in as rolls parallel to the shorter sides. Some of Davis’s findings were confirmed experimentally by Stork and Muller (1972) although their observations of patterns in moderately-sized rectangular boxes, including square boxes, also produced various cellular patterns not predicted by Davis’s linear theory. The occurrence of crossed rolls, a superposition of rolls parallel to both sides, was studied using linear theory by Edwards (1988) who showed that such patterns are preferred to unidirectional rolls in square or near-square boxes. In

the square, such solutions allow the four-fold rotational symmetry of the system to be preserved, and this helped to explain some of the other patterns observed by Stork and Muller (1972).

These theoretical and experimental studies of the three-dimensional Rayleigh-Bénard system were limited to boxes accommodating up to about six rolls. One of the advantages of studying the Swift-Hohenberg equation is that much larger domains can be investigated numerically, as in the study by Greenside and Coughran (1984). They used a time-dependent scheme to study nonlinear pattern evolution for the two-dimensional Swift-Hohenberg equation in rectangular domains, including the square, accommodating up to about thirty rolls. This identified a wide range of possible stable states of the system and although a bifurcation analysis was not carried out the relative stability of various nonlinear states was studied using a Lyapunov functional. A numerical study of a more complex two-dimensional system in rectangular domains has been carried out by Manneville (1983).

Theoretical studies of orthogonal roll patterns governed by the Swift-Hohenberg equation in large rectangular domains (that is, where many rolls can be accommodated) have been carried out by Daniels and Weinstein (1996) and Daniels and Lee (1999) using weakly nonlinear theory based on multiple-scale and matched asymptotic expansion techniques. These studies are limited to solutions composed of roll components parallel and perpendicular to the sides of the rectangle and do not include the limiting case of a square domain. Similar methods have been used to study patterns governed by the Swift-Hohenberg equation in large closed two-dimensional domains of arbitrary shape by Daniels (2000).

The main aim of the present study is to carry out a bifurcation analysis of the Swift-Hohenberg equation in a square. Section 2.2 sets out the equation and the various boundary conditions to be considered. In Section 2.3, analytical insight is gained by first studying the weakly nonlinear problem with periodic lateral boundaries. This is extended to the more realistic case of rigid lateral boundary conditions in Section 2.4, where a numerical scheme is developed based on finite differences. Qualitative differences between the periodic and rigid cases are considered in Section 2.5 by using weakly nonlinear theory to study a quasi-periodic system where the periodic conditions

are modified to incorporate a small rigid component. The next two sections consider the nonlinear system with rigid boundary conditions. Solutions are found using a time-dependent scheme in Section 2.6, and a bifurcation analysis of nonlinear steady-state solutions is carried out in Section 2.7 by tracking solutions using Newton iteration. Results are obtained for a wide range of sizes of the square. The results are discussed in Section 2.8.

2.2 Formulation of the problem

The Swift-Hohenberg equation is

$$\frac{\partial u}{\partial t} = \varepsilon u - (1 + \nabla^2)^2 u - u^3, \quad (2.1)$$

where t is the non-dimensional time, $\nabla^2 = \frac{\partial^2}{\partial x^2} + \frac{\partial^2}{\partial y^2}$ where x and y are non-dimensional Cartesian coordinates, ε is a control parameter and $u(x, y, t)$ is a scalar field.

The geometry that we are considering is a square $0 \leq x \leq L$, $0 \leq y \leq L$ with the equivalent of rigid lateral boundaries so that on the boundary u and its derivative normal to the boundary vanish:

$$u = \frac{\partial u}{\partial q} = 0 \quad \text{on} \quad x = 0, L \quad \text{and} \quad y = 0, L. \quad (2.2)$$

Note that here q is used to denote the inward normal direction.

In order to gain analytical insight we shall also consider the case of periodic boundary conditions where u and its second derivative normal to the boundary are equal to zero at the boundary:

$$u = \frac{\partial^2 u}{\partial q^2} = 0 \quad \text{on} \quad x = 0, L \quad \text{and} \quad y = 0, L. \quad (2.3)$$

In Section 2.5 we shall consider a combination of the rigid and periodic conditions:

$$u = \frac{\partial^2 u}{\partial q^2} - \delta \frac{\partial u}{\partial q} = 0 \quad \text{on} \quad x = 0, L \quad \text{and} \quad y = 0, L, \quad (2.4)$$

which we shall refer to as the quasi-periodic system. Here δ is a general parameter which is zero in the periodic problem and infinity in the rigid case.

2.3 Analysis of the periodic problem

In this section we shall consider the Swift-Hohenberg equation with the periodic boundary conditions (2.3). We first describe the analytical solution of the linear problem and obtain the eigenvalues ε at which steady-state linearized solutions exist. We then find the form of weakly nonlinear steady-state solutions near these bifurcation points and examine their stability.

2.3.1 Linear solution

Solutions of the linearized Swift-Hohenberg equation

$$\frac{\partial u}{\partial t} = \varepsilon u - (1 + \nabla^2)^2 u, \quad (2.5)$$

subject to the boundary conditions (2.3) can be expressed in the form

$$u = e^{\sigma t} \sin \frac{m\pi x}{L} \sin \frac{n\pi y}{L}, \quad (2.6)$$

where m and n are positive integers. Substitution into (2.5) shows that the growth rate σ is given by

$$\sigma = \varepsilon - \left(1 - \frac{(m^2 + n^2)\pi^2}{L^2}\right)^2, \quad (2.7)$$

and that steady-state linearized solutions exist for

$$\varepsilon = \varepsilon_{mn} \equiv \left(1 - \frac{(m^2 + n^2)\pi^2}{L^2}\right)^2. \quad (2.8)$$

Since $\sigma = \varepsilon - \varepsilon_{mn}$, our analysis shows that the trivial solution $u = 0$ becomes unstable to the mode (m, n) defined by

$$u = u_{mn} \equiv \sin \frac{m\pi x}{L} \sin \frac{n\pi y}{L}, \quad (2.9)$$

when $\varepsilon > \varepsilon_{mn}$. Figure 2.1 shows the eigenvalues ε_{mn} plotted as a function of L .

At low values of L the (1,1) mode is preferred (i.e. occurs at lowest ε) but at higher L the preferred mode depends on which steady-state eigenmode (2.9) best fits the size of the square. Table 2.1 shows the sequence of bifurcations predicted in the case $L = 5$.

m	n	ε_{mn}
1	1	0.044281478
1	2	0.948521881
2	2	4.658144105
1	3	8.689771045
2	3	17.07502964
1	4	32.61930171
3	3	37.28464245
2	4	47.55045122
3	4	78.66988223

Table 2.1: Bifurcation sequence for the case $L = 5$

Note also that modes (m, n) for which $m \neq n$ correspond to the existence of repeated eigenvalues $\varepsilon = \varepsilon_{mn} = \varepsilon_{nm}$ and thus the possibility of solutions formed from linear combinations of u_{mn} and its orthogonal rotation u_{nm} . A weakly nonlinear analysis is used (below) to identify the actual solutions of the nonlinear system in such cases.

2.3.2 Weakly nonlinear solution

We now investigate solutions of the nonlinear Swift-Hohenberg system (2.1), (2.3) near the bifurcation points (2.8) of the steady state solution. We assume an expansion for u in the form

$$u = \bar{\varepsilon}^{\frac{1}{2}} u_0 + \bar{\varepsilon} u_1 + \bar{\varepsilon}^{\frac{3}{2}} u_2 + \dots, \quad (2.10)$$

where

$$\bar{\varepsilon} = \varepsilon - \varepsilon_{mn}, \quad (2.11)$$

and $u_i = u_i(x, y, \tau)$. Here τ is a slow time scale defined by $\tau = \bar{\varepsilon} t$ and is included to allow the stability of weakly nonlinear steady-state solutions to be examined. Substitution of (2.10) into (2.1) and (2.3) gives at order $\bar{\varepsilon}^{\frac{1}{2}}$,

$$\varepsilon_{mn} u_0 - (1 + \nabla^2)^2 u_0 = 0; \quad u_0 = \frac{\partial^2 u_0}{\partial q^2} = 0 \quad \text{at} \quad x = 0, L; \quad y = 0, L. \quad (2.12)$$

This is the linearized steady-state system and so the solution is

$$u_0 = a(\tau)u_{mn} + b(\tau)u_{nm}, \quad (2.13)$$

where u_{mn} is the linear eigenfunction defined by (2.9) and a and b are arbitrary functions of τ . Here we allow for the possibility that $m \neq n$, so that both u_{mn} and u_{nm} are possible eigenstates; in the case where $m = n$ we may simply take $b = 0$. We do not consider cases where $\epsilon_{,mn}$ has the same value for different (m, n) combinations, such as (1,7) and (5,5).

At order $\bar{\epsilon}$, u_1 is found to satisfy the same linearized system as u_0 :

$$\epsilon_{mn}u_1 - (1 + \nabla^2)^2u_1 = 0; \quad u_1 = \frac{\partial^2 u_1}{\partial q^2} = 0 = 0 \quad \text{at} \quad x = 0, L; \quad y = 0, L \quad (2.14)$$

and so the solution can be taken to be $u_1 = 0$ without loss of generality.

At order $\bar{\epsilon}^{\frac{3}{2}}$, u_2 is found to satisfy the system

$$\epsilon_{mn}u_2 - (1 + \nabla^2)^2u_2 = \frac{\partial u_0}{\partial \tau} - u_0 + u_0^3; \quad u_2 = \frac{\partial^2 u_2}{\partial q^2} = 0 \quad \text{at} \quad x = 0, L; \quad y = 0, L. \quad (2.15)$$

A consistent solution for u_2 requires that the secular terms proportional to u_{mn} and u_{nm} on the right-hand side vanish. These can be found by substituting (2.13) into the right-hand side and expanding the nonlinear term into products of the form $\sin \frac{r\pi x}{L} \sin \frac{s\pi y}{L}$ where r and s are integers. After some algebra, it then follows that, from terms proportional to u_{mn} , we require

$$0 = \frac{da}{d\tau} - a + \frac{9}{16}a^3 + \frac{3}{4}ab^2, \quad (2.16)$$

and, from the terms proportional to u_{nm} , we require

$$0 = \frac{db}{d\tau} - b + \frac{9}{16}b^3 + \frac{3}{4}ba^2. \quad (2.17)$$

First consider the case of a non-repeated eigenvalue ($m = n$) where we take $b = 0$ and a satisfies

$$\frac{da}{d\tau} = a - \frac{9}{16}a^3. \quad (2.18)$$

For $\bar{\epsilon} > 0$ we see that there are three steady state solutions $a = a_s$ given by $a_s = 0$ and $a_s = \pm \frac{4}{3}$. The local stability of these can be examined by setting $a = a_s + \bar{A}e^{\bar{\sigma}\tau}$ in (2.18) with \bar{A} small. For $a_s = 0$ we obtain $\bar{\sigma} = 1$ confirming

that the trivial solution is unstable for $\bar{\varepsilon} > 0$, whilst for $a_s = \pm \frac{4}{3}$ we obtain $\bar{\sigma} = -2$, showing that the two nonlinear solutions

$$u \sim \pm \frac{4}{3}(\varepsilon - \varepsilon_{mn})^{\frac{1}{2}} \sin \frac{m\pi x}{L} \sin \frac{n\pi y}{L}, \quad (2.19)$$

are stable. The patterns associated with (2.19) for $(m, n) = (1, 1)$, $(2, 2)$ and $(3, 3)$ are shown in Figure 2.2.

Now consider the case of a repeated eigenvalue ($m \neq n$). In this case there are nine steady-state solutions $a = a_s, b = b_s$ of (2.16) and (2.17) consisting of the trivial solution $a_s = b_s = 0$ together with:

$$a_s = \pm \frac{4}{3}, \quad b_s = 0, \quad (2.20)$$

$$a_s = 0, \quad b_s = \pm \frac{4}{3}, \quad (2.21)$$

$$a_s = \pm \frac{4}{\sqrt{21}}, \quad b_s = \pm \frac{4}{\sqrt{21}}, \quad (2.22)$$

$$a_s = \pm \frac{4}{\sqrt{21}}, \quad b_s = \mp \frac{4}{\sqrt{21}}. \quad (2.23)$$

These correspond to supercritical onset solutions for u of the form

$$u \sim \pm \frac{4}{3}(\varepsilon - \varepsilon_{mn})^{\frac{1}{2}} \sin \frac{m\pi x}{L} \sin \frac{n\pi y}{L}, \quad (2.24)$$

$$u \sim \pm \frac{4}{3}(\varepsilon - \varepsilon_{mn})^{\frac{1}{2}} \sin \frac{n\pi x}{L} \sin \frac{m\pi y}{L}, \quad (2.25)$$

$$u \sim \pm \frac{4}{\sqrt{21}}(\varepsilon - \varepsilon_{mn})^{\frac{1}{2}} \left(\sin \frac{m\pi x}{L} \sin \frac{n\pi y}{L} + \sin \frac{n\pi x}{L} \sin \frac{m\pi y}{L} \right), \quad (2.26)$$

$$u \sim \pm \frac{4}{\sqrt{21}}(\varepsilon - \varepsilon_{mn})^{\frac{1}{2}} \left(\sin \frac{m\pi x}{L} \sin \frac{n\pi y}{L} - \sin \frac{n\pi x}{L} \sin \frac{m\pi y}{L} \right). \quad (2.27)$$

We can test the local stability of the solutions (2.20)-(2.23) by setting $a = a_s + \bar{A}e^{\bar{\sigma}\tau}$, $b = b_s + \bar{B}e^{\bar{\sigma}\tau}$ and linearizing in \bar{A} and \bar{B} in (2.16) and (2.17) to obtain

$$(\bar{\sigma} - 1 + \frac{27}{16}a_s^2 + \frac{3}{4}b_s^2)\bar{A} + \frac{3}{2}a_sb_s\bar{B} = 0, \quad (2.28)$$

$$(\bar{\sigma} - 1 + \frac{27}{16}b_s^2 + \frac{3}{4}a_s^2)\bar{B} + \frac{3}{2}a_sb_s\bar{A} = 0. \quad (2.29)$$

This yields growth rates $\bar{\sigma} = -2$ and $\bar{\sigma} = -\frac{1}{3}$ for each of the solutions (2.20) and (2.21) which are therefore stable, and growth rates $\bar{\sigma} = -2$ and $\bar{\sigma} = \frac{2}{7}$ for each of the solutions (2.22) and (2.23), which are therefore unstable. If

$$\hat{u} = \frac{1}{L} \left(\int_0^L \int_0^L u^2 dx dy \right)^{\frac{1}{2}} \quad (2.30)$$

is used as a measure of the amplitude of each solution then for (2.24) and (2.25),

$$\hat{u} \sim \frac{1}{2} \varepsilon^{\frac{1}{2}} (a_s^2 + b_s^2)^{\frac{1}{2}} = \frac{2}{3} (\varepsilon - \varepsilon_{mn})^{\frac{1}{2}} \quad (2.31)$$

whereas for (2.26) and (2.27)

$$\hat{u} \sim \frac{1}{2} \varepsilon^{\frac{1}{2}} (a_s^2 + b_s^2)^{\frac{1}{2}} = \sqrt{\frac{8}{21}} (\varepsilon - \varepsilon_{mn})^{\frac{1}{2}} \quad (2.32)$$

so that the solutions (2.24) and (2.25) of larger amplitude \hat{u} are the stable ones.

Finally we consider the nature of the weakly nonlinear patterns associated with the solutions (2.24)-(2.27). We ignore the possibility of changing the sign of u as this will not affect the patterns observed. We shall refer to the four solutions with the plus signs in (2.24)-(2.27) as u_1, u_2, u_3, u_4 respectively. There are four cases to consider, as follows:

(i) m even, n odd

In this case u_1 has OE symmetry, i.e it is odd in x about $x = \frac{1}{2}L$ and is even in y about $y = \frac{1}{2}L$. Since u_2 is obtained from u_1 by interchanging x and y it is just an orthogonal rotation of u_1 and has EO symmetry. Solution u_3 is unchanged by the transformation $x \rightarrow y, y \rightarrow x$ and is therefore symmetric about the diagonal $y = x$. Its sign is reversed by the transformation $L - x \rightarrow y, y \rightarrow L - x$ and it is therefore antisymmetric about the other diagonal, $y = L - x$. Solution u_4 is antisymmetric about $y = x$ and symmetric about $y = L - x$ and is just an orthogonal rotation of u_3 . Figure 2.3 shows an example with $m = 2$ and $n = 1$, where u_1 and u_2 are '2-cell parallel' modes (i.e consist of 2 cells parallel to one pair of boundaries) and u_3 and u_4 are '2 cell diagonal' modes. A further example with $m = 4$ and $n = 1$ is shown in Figure 2.4.

(ii) m odd, n even

Interchanging m and n in (2.24)-(2.27) is equivalent to swapping u_1 and u_2 , has no effect on u_3 and reverses the sign of u_4 , so the same patterns occur as in (i) except that now u_1 has EO symmetry and u_2 has OE symmetry.

(iii) m odd, n odd

In this case u_1 and u_2 both have EE symmetry. Again u_2 is just an orthogonal rotation of u_1 . Since u_1 and u_2 both have EE symmetry, any linear combination of them also has EE symmetry. Thus both u_3 and u_4 have EE symmetry. In addition, u_3 is symmetric about both diagonals $y = x$, $y = L - x$ and u_4 is antisymmetric about both diagonals. Figure 2.5 and Figure 2.6 show examples with $m = 3$, $n = 1$ and $m = 5$, $n = 1$.

Note that u_3 and u_4 are those combinations of u_1 and u_2 which, ignoring the sign of the solution for u_4 , possess 4-fold rotational and reflectional symmetry.

(iv) m even, n even

In this case u_1 and u_2 both have OO symmetry. Again u_2 is just an orthogonal rotation of u_1 . Since u_1 and u_2 both have OO symmetry, any linear combination of them also has OO symmetry. Thus u_3 and u_4 both have OO symmetry. In addition, as in (iii), u_3 is symmetric about both diagonals and u_4 is antisymmetric about both diagonals. Figure 2.7 shows an example with $m = 4$ and $n = 2$. Again u_3 and u_4 are those combinations of u_1 and u_2 which, ignoring the signs of the solutions, possess 4-fold rotational and reflectional symmetry.

2.4 Linear solution of the rigid problem

The linearized steady-state Swift-Hohenberg equation

$$\varepsilon u = (1 + \nabla^2)^2 u, \quad (2.33)$$

is now considered with rigid boundary conditions

$$u = \frac{\partial u}{\partial q} = 0 \quad \text{on} \quad x = 0, L \quad \text{and} \quad y = 0, L. \quad (2.34)$$

The system (2.33) is homogenous and constitutes an eigenvalue problem for ε with eigenfunction $u(x, y)$. The lowest eigenvalue ε defines the onset of

convection and the corresponding function $u(x, y)$ determines the pattern of convection at onset. Higher eigenvalues ε and eigenfunctions u determine the onset and nature of higher modes of convection at a given value of L . In Section 2.4.1 below a numerical scheme is developed to allow the eigenvalues ε and corresponding eigenfunctions $u(x, y)$ to be determined.

2.4.1 Numerical scheme

We can solve (2.33) with (2.34) numerically by a finite difference approach. Equation (2.33) is discretised on to a uniform grid

$$x = ih \quad \text{for } i = 0, \dots, M + 1, \quad (2.35)$$

$$y = jk \quad \text{for } j = 0, \dots, N + 1, \quad (2.36)$$

where h and k are the spatial step lengths in x and y respectively and $(M + 1)h = (N + 1)k = L$. We let $u_{i,j}$ be the numerical approximation to u at grid point (i, j) so that (2.33) becomes

$$\varepsilon u_{i,j} = \{(1 + \nabla^2)^2 u\}_{i,j}. \quad (2.37)$$

The spatial derivatives on the right-hand side of (2.37) are approximated using a second-order accurate 13-point central difference representation as follows. We first expand the right-hand side to get

$$\{u + 2u_{xx} + 2u_{yy} + 2u_{xxyy} + u_{xxxx} + u_{yyyy}\}_{i,j}. \quad (2.38)$$

To find approximations to each derivative listed in (2.38) we can use Taylor expansions as follows. For a function $f(x)$ of one variable, we have

$$f(x \pm h) = f(x) \pm hf'(x) + \frac{h^2}{2}f''(x) \pm \frac{h^3}{6}f'''(x) + \frac{h^4}{24}f''''(x) + \dots \quad (2.39)$$

$$f(x \pm 2h) = f(x) \pm 2hf'(x) + 2h^2f''(x) \pm \frac{4h^3}{3}f'''(x) + \frac{2h^4}{3}f''''(x) + \dots \quad (2.40)$$

Adding the two expressions in (2.39) and also the two expressions in (2.40) and solving simultaneously for f'' and f'''' , gives

$$f''(x) = -\frac{1}{12h^2}[f(x+2h) - 16f(x+h) + 30f(x) - 16f(x-h) + f(x-2h)] + O(h^4). \quad (2.41)$$

$$f''''(x) = \frac{1}{h^4}[f(x+2h) - 4f(x+h) + 6f(x) - 4f(x-h) + f(x-2h)] + O(h^2). \quad (2.42)$$

It also follows directly from adding the two expressions in (2.39) that

$$f''(x) = \frac{1}{h^2}[f(x+h) - 2f(x) + f(x-h)] + O(h^2). \quad (2.43)$$

Formulae (2.43) and (2.42) provide the following second-order accurate approximations to four of the five derivatives of $u(x, y)$ in (2.38):

$$\{u_{xx}\}_{i,j} = \frac{1}{h^2}(u_{i+1,j} - 2u_{i,j} + u_{i-1,j}) + O(h^2), \quad (2.44)$$

$$\{u_{yy}\}_{i,j} = \frac{1}{k^2}(u_{i,j+1} - 2u_{i,j} + u_{i,j-1}) + O(k^2), \quad (2.45)$$

$$\{u_{xxxx}\}_{i,j} = \frac{1}{h^4}[u_{i+2,j} - 4u_{i+1,j} + 6u_{i,j} - 4u_{i-1,j} + u_{i-2,j}] + O(h^2), \quad (2.46)$$

and similarly

$$\{u_{yyyy}\}_{i,j} = \frac{1}{k^4}[u_{i,j+2} - 4u_{i,j+1} + 6u_{i,j} - 4u_{i,j-1} + u_{i,j-2}] + O(k^2). \quad (2.47)$$

Note that for the second derivatives we use (2.43) rather than the more accurate fourth order approximation (2.41) to maintain a consistent level of approximation. It remains to find a second-order accurate numerical approximation to the mixed derivative u_{xxyy} . To do this, we first use the Taylor expansions of $u(x \pm h, y \pm k)$ and $u(x \pm h, y \mp k)$ to give

$$\begin{aligned} u(x+h, y+k) + u(x-h, y-k) + u(x+h, y-k) + u(x-h, y+k) = \\ 4u(x, y) + 2(h^2 u_{xx} + k^2 u_{yy})(x, y) + \left(\frac{h^4}{6} u_{xxxx} + h^2 k^2 u_{xxyy} + \frac{k^4}{6} u_{yyyy}\right)(x, y) \\ + O(h^6, h^4 k^2, h^2 k^4, k^6) \end{aligned} \quad (2.48)$$

An approximation to u_{xxyy} can now be obtained by using (2.41) and (2.42) to replace all of the other derivatives in (2.48), maintaining the error at the order of the sixth power of the step length. From this we obtain

$$\begin{aligned} \{u_{xxyy}\}_{i,j} = \frac{1}{h^2 k^2} [4u_{i,j} - 2(u_{i+1,j} + u_{i-1,j} + u_{i,j+1} + u_{i,j-1}) \\ + u_{i+1,j+1} + u_{i-1,j-1} + u_{i+1,j-1} + u_{i-1,j+1}] + O(h^2, k^2, \frac{h^4}{k^2}, \frac{k^4}{h^2}). \end{aligned} \quad (2.49)$$

This gives the discretized form of equation (2.37) as

$$D_{i,j} = \varepsilon u_{i,j}, \quad i = 1, \dots, M, \quad j = 1, \dots, N, \quad (2.50)$$

where

$$\begin{aligned} D_{i,j} = & u_{i,j} + \frac{2}{h^2}(u_{i+1,j} - 2u_{i,j} + u_{i-1,j}) + \frac{2}{k^2}(u_{i,j+1} - 2u_{i,j} + u_{i,j-1}) \\ & + \frac{1}{h^4}[u_{i+2,j} - 4u_{i+1,j} + 6u_{i,j} - 4u_{i-1,j} + u_{i-2,j}] \\ & + \frac{1}{k^4}[u_{i,j+2} - 4u_{i,j+1} + 6u_{i,j} - 4u_{i,j-1} + u_{i,j-2}] \\ & + \frac{2}{h^2k^2}[4u_{i,j} - 2(u_{i+1,j} + u_{i-1,j} + u_{i,j+1} + u_{i,j-1}) \\ & + u_{i+1,j+1} + u_{i-1,j-1} + u_{i+1,j-1} + u_{i-1,j+1}]. \end{aligned} \quad (2.51)$$

The equations (2.50) apply at all internal points of the grid; this requires evaluation of $u_{i,j}$ at fictitious points outside the grid where $i = -1$, $i = M+2$, $j = -1$ and $j = N+2$. This is done by using the boundary conditions $\frac{\partial u}{\partial q} = 0$ on $x = 0, L$ and $y = 0, L$ which in discretised form become

$$u_{-1,j} = u_{1,j}, \quad u_{M+2,j} = u_{M,j}, \quad u_{i,-1} = u_{i,1}, \quad u_{i,N+2} = u_{i,N}. \quad (2.52)$$

The values of $u_{i,j}$ in (2.50) on the boundary are replaced using the condition $u = 0$ on $x = 0, L$ and $y = 0, L$ which gives

$$u_{0,j} = u_{M+1,j} = u_{i,0} = u_{i,N+1} = 0. \quad (2.53)$$

Since $D_{i,j}$ is a linear function of the $u_{i,j}$'s, equation (2.50) can now be expressed in the matrix form

$$A\underline{u} = \varepsilon\underline{u}, \quad (2.54)$$

where \underline{u} is the column vector containing the values of $u_{i,j}$ at all internal grid

points:

$$u = \begin{pmatrix} u_{1,1} \\ u_{2,1} \\ \vdots \\ u_{M,1} \\ u_{1,2} \\ \vdots \\ u_{M,2} \\ \vdots \\ \vdots \\ u_{1,N} \\ \vdots \\ u_{M,N} \end{pmatrix} \quad (2.55)$$

and the $NM \times NM$ matrix A is given by

$$A = \begin{pmatrix} \bar{D} & B & C & 0 & 0 & \dots & \dots & 0 & 0 & 0 \\ B & D & B & C & 0 & 0 & \dots & \dots & 0 & 0 \\ C & B & D & B & C & 0 & 0 & \dots & \dots & 0 \\ \ddots & 0 \\ \ddots & 0 & 0 \\ \ddots & C & 0 & 0 \\ \ddots & \ddots & \ddots & \ddots & \ddots & \ddots & D & B & C & 0 \\ 0 & \ddots & \ddots & \ddots & \ddots & C & B & D & B & C \\ 0 & 0 & \ddots & \ddots & \ddots & 0 & C & B & D & B \\ 0 & 0 & 0 & \dots & \dots & 0 & 0 & C & B & \bar{D} \end{pmatrix} \quad (2.56)$$

$$C = \begin{pmatrix} a_5 & 0 & \dots & \dots & \dots & \dots & 0 & 0 & 0 & 0 \\ \ddots & a_5 & \ddots & \ddots & \ddots & \ddots & \ddots & 0 & 0 & 0 \\ \ddots & \ddots & a_5 & \ddots & \ddots & \ddots & \ddots & \ddots & 0 & 0 \\ \ddots & \ddots & \ddots & a_5 & \ddots & \ddots & \ddots & \ddots & \ddots & 0 \\ \ddots & \ddots & \ddots & \ddots & a_5 & \ddots & \ddots & \ddots & \ddots & \ddots \\ \ddots & \ddots & \ddots & \ddots & \ddots & a_5 & \ddots & \ddots & \ddots & \ddots \\ 0 & \ddots & \ddots & \ddots & \ddots & \ddots & a_5 & \ddots & \ddots & \ddots \\ 0 & 0 & \ddots & \ddots & \ddots & \ddots & \ddots & a_5 & \ddots & \ddots \\ 0 & 0 & 0 & \ddots & \ddots & \ddots & \ddots & \ddots & a_5 & 0 \\ 0 & 0 & 0 & 0 & \dots & \dots & \dots & \dots & 0 & a_5 \end{pmatrix} \quad (2.60)$$

are $M \times M$ matrices and

$$a_1 = 1 - \frac{4}{h^2} - \frac{4}{k^2} + \frac{6}{h^4} + \frac{6}{k^4} + \frac{8}{h^2k^2}, \quad (2.61)$$

$$a_2 = \frac{2}{h^2} - \frac{4}{h^4} - \frac{4}{h^2k^2}, \quad (2.62)$$

$$a_3 = \frac{2}{k^2} - \frac{4}{k^4} - \frac{4}{h^2k^2}, \quad (2.63)$$

$$a_4 = \frac{1}{h^4}, \quad (2.64)$$

$$a_5 = \frac{1}{k^4}, \quad (2.65)$$

$$a_6 = \frac{2}{h^2k^2}. \quad (2.66)$$

Note that A is a symmetric matrix. The matrix equation (2.54) was solved using Mathematica, which computes all of the eigenvalues and eigenvectors by the QR method in which A is first balanced and then transformed into upper Hessenberg form.

2.4.2 Accuracy

Initial calculations were made for fixed L with different step sizes $h(=k)$. Table 2.2 shows a comparison of the leading eigenvalues for the case $L=5$ for different grids. The eigenvectors associated with each eigenvalue for these

Mode	$h = k = 0.5$	$h = k = 0.25$	$h = k = 0.15625$	$h = k = 0.125$
1	1.020972753	1.076166636	1.090222056	1.091083918
2	4.107593799	4.751277379	4.900802877	4.933877698
3	10.08752594	11.82658277	12.24762645	12.346600
4	14.31531158	18.21773996	19.17849635	19.407716
5	14.71007557	18.61901068	19.57322833	19.800523
6	24.58668899	30.58976291	32.11738626	32.487922
7	35.78291717	50.66682575	54.58722708	55.546068
8	45.28573134	57.39985710	60.62084000	61.416953
9	50.52054596	69.01803175	74.04047113	75.284872
10	51.24628780	69.96693461	74.97978581	76.216988

Table 2.2: Leading eigenvalues ε for the case $L = 5$ on various grids

grids are also in reasonable agreement. For higher values of L and higher modes the variation of u across the square occurs more rapidly and so it can be expected that larger grids will be required to adequately resolve the solution.

2.4.3 Results

Results were obtained for values of L in the range 4 to 25 and Figures 2.8 and 2.9 show the eigenvalues ε plotted as a function of L . These are based mostly on computations of the eigenvalues at intervals of $\frac{1}{4}$ in L . The lowest eight modes are shown. The curves in Figure 2.8 are labelled according to their symmetry properties and their order at low values of L , where the patterns bear some resemblance with those of the periodic problem. Each branch corresponds to an eigensolution u with one of the symmetries described in relation to the periodic problem (EE, OO or OE/EO). Unlike the periodic problem, however, only the solutions with OE/EO symmetry, which also give rise to diagonal modes, are found to correspond to repeated eigenvalues - further discussion of this point is given in Section 2.5 below. As L increases, the various branches interweave as a particular mode 'best fits' the size of the square. However, unlike the periodic problem (Figure 2.1) where an

ever-increasing number of modes assume the position of leading eigenmode as L increases, here the most dangerous mode is confined to one of the three branches EE1, OE1 and OO1. The various branches appear to divide into distinct groups - branches EE1, OE1 and OO1 constitute the first group and members of the second group include branches EE2, OO2 and OE2 (see Figure 2.8). This behaviour is reminiscent of two-dimensional Rayleigh-Bénard solutions in finite cavities with rigid lateral walls, where pairs of solutions with odd and even symmetry combine into distinct groups (Drazin 1975, Daniels 1977b).

The leading group of modes consists of solutions with EE symmetry, OO symmetry and a repeated eigenvalue with OE/EO symmetry. The repeated eigenvalue is associated with two distinct patterns so that this group actually encompasses four patterns covering the various possible symmetry arrangements. We now discuss in more detail the patterns corresponding to each of the branches EE1, OE1 and OO1, and how they change as functions of L - unlike the periodic problem, the pattern is not conserved along each branch as L changes.

Branch EE1 has EE symmetry and at low values of L consists of a single-cell or 'one cell' solution. Contours of the eigenfunction u associated with this branch at various values of L are shown in Figures 2.10 and 2.11. It is the dominant mode for $L < 8$, for $10.1 < L < 12.7$ and then again when L reaches 18.9; at large L it continues to interweave with branches OE1 and OO1. The pattern changes in an interesting manner as L increases. In the region $8.2 < L < 10.1$ (where it is not the dominant mode) it develops four new cells in the corners, sitting at both ends of the diagonals. A further set of four cells is added when $12.7 < L < 18.9$ and it appears that this process continues as L increases. A computation for $L = 30$ (as seen in Figure 2.11) shows that the solution is developing into two sets of cells placed along the diagonals of the square.

Branch OE1 contains solutions with OE/EO symmetry. Because this branch corresponds to a repeated eigenvalue, the eigenvector determined by the numerical scheme is non-unique. However, from our analysis of the periodic problem, we expect the possible nonlinear solutions to have four symmetrical arrangements corresponding to the solutions u_1 , u_2 , u_3 and u_4

defined in Section 3.2. If we assume that u_1 has EO symmetry then if an eigenfunction produced by the numerical scheme is denoted by $\bar{u}(x, y)$ then we can construct u_1 as

$$u_1(x, y) = \bar{u}(x, y) + \bar{u}(L - x, y). \quad (2.67)$$

Then solution u_2 , which has OE symmetry, is determined as

$$u_2(x, y) = u_1(y, x) \quad (2.68)$$

and is just the orthogonal rotation of u_1 . The diagonal mode u_3 can now be determined as

$$u_3(x, y) = u_1(x, y) + u_2(x, y) \quad (2.69)$$

and is symmetric about the diagonal $y = x$ and antisymmetric about the diagonal $y = L - x$. Finally, u_4 is determined as

$$u_4(x, y) = u_1(x, y) - u_2(x, y) \quad (2.70)$$

and is antisymmetric about the diagonal $y = x$ and symmetric about the diagonal $y = L - x$. Contours of the OE solution u_1 and the diagonal mode u_3 at various values of L along branch OE1 are shown in Figures 2.12 and 2.13. At low values of L the solution u_1 is a 2-cell parallel mode and u_3 is a 2-cell diagonal mode, resembling the corresponding solutions of the periodic problem (Figure 2.3). The branch OE1 modes are dominant when $8.2 < L < 10.1$, $12.7 < L < 14.4$ and then again when $16.8 < L < 18.9$. As L increases, the diagonal mode u_3 gains additional cells and the simplest way of interpreting u_1 is as a superposition of this solution and its orthogonal rotation ($u_1(x, y) = \frac{1}{2}(u_3(x, y) + u_4(x, y))$). Thus at large L the solution u_1 is effectively a combination of cells placed along each diagonal - any resemblance to a parallel mode no longer exists. At $L = 30$, the solution u_1 is visually similar to that of branch EE1 at $L = 30$; the main difference is that whereas branch EE1 has EE symmetry and therefore contains an odd number of cells along each diagonal, the OE symmetry of u_1 implies that it must contain an even number of cells along each diagonal.

Branch OO1 has OO symmetry and contours of u at various values of L are shown in Figures 2.14 and 2.15. At low values of L the pattern consists

of a '4-cell' solution similar to the (2,2) mode of the periodic problem. This branch becomes the dominant mode for $14.4 < L < 16.8$. Four new cells appear in the corners when $L \approx 14$ and at $L = 30$ the solution consists of a combination of 12 cells placed along each diagonal. In this case the OO symmetry of the solution implies that there are an even number of cells along each diagonal, like the solution u_1 of branch OE1, but the solution here differs in that there is a saddle-point zero of u at the centre of the square, and the cells in the opposite corners are of common sign.

Figures 2.16, 2.17 and 2.18 show contours of u at various values of L on the branches EE2, EE3 and OE2. There is again an indication that diagonal patterns emerge at large values of L , but with dual cells along the diagonals rather than single cells.

2.4.4 Comparison with the periodic problem

The lack of repeated eigenvalues in the rigid case associated with EE or OO modes is a significant difference from the periodic problem, although many of the 4-fold symmetric patterns found in the rigid case bear a close resemblance to those which occur in the periodic case, especially for low and moderate values of L . Tests of the numerical code for the rigid problem described in Section 4.1 were carried out with different grid sizes to ascertain whether the lack of repeated EE and OO eigenvalues could be due to the approximations inherent in the numerical scheme. However, these tests showed no evidence of the convergence of such eigenvalues to common values with increasing grid size.

As a further check, the code was modified to solve the periodic problem numerically, to ascertain whether it correctly predicted repeated EE and OO eigenvalues in that case. The modifications are straightforward because implementation of the boundary condition $\frac{\partial^2 u}{\partial q^2} = 0$ in place of $\frac{\partial u}{\partial q} = 0$ just changes the sign of the four relations (2.52). This in turn is equivalent to changing the sign of the terms a_4 and a_5 which appear in the main diagonals of the matrices \bar{D} and D given in (2.57) and (2.58). Table 2.3 shows numerical results for the leading eigenvalues of the periodic problem at $L = 5$ obtained using step lengths $h = k = 0.15625$. A comparison with the analytical

m	n	ϵ_{mn}	numerical eigenvalue ϵ
1	1	0.044281478	0.0465318900453688
1	2	0.948521881	0.940022406381974
			0.940022406434657
2	2	4.658144105	4.61643751306343
1	3	8.689771045	8.53950540848336
			8.53950543374084
2	3	17.07502964	16.8243396048629
			16.8243396048807
1	4	32.61930171	31.7016479888962
			31.7016479889166
3	3	37.28464245	36.6636113944453
2	4	47.55045122	46.3760140550676
			46.3760142292442
3	4	78.66988223	76.7961119894832
			76.7961119894886

Table 2.3: Eigenvalues for the periodic problem with $L = 5$ obtained numerically and analytically.

formula (2.8) indicates reasonable agreement given that the numerical scheme is second-order accurate. Moreover, the scheme correctly identifies whether eigenvalues are repeated to an extremely high level of accuracy.

2.5 Weakly nonlinear analysis of the quasi-periodic problem

In Section 2.3 an analysis of the periodic problem showed that there are repeated eigenvalues

$$\epsilon = \epsilon_{mn} \equiv \left(1 - \frac{(m^2 + n^2)\pi^2}{L^2}\right)^2, \quad (2.71)$$

corresponding to the fact that for $m \neq n$

$$u = u_{mn} \equiv \sin \frac{m\pi x}{L} \sin \frac{n\pi y}{L}, \quad (2.72)$$

and $u = u_{nm}$ are both eigensolutions of the linearized system. If m is odd and n is even (or vice versa) these correspond to two weakly nonlinear solutions with EO (or OE) symmetry which also combine to produce two solutions with diagonal symmetry. If m and n are both odd (or both even) they correspond to two weakly nonlinear solutions with EE (or OO) symmetry which also combine to produce two solutions with 4-fold EE (or OO) symmetry. In the rigid problem, however, repeated eigenvalues are confined to the modes equivalent to (2.72) with EO (or OE) symmetry, and solutions with EE (or OO) symmetry bifurcate at different values of ε . Thus, for example, branch OE1 of the rigid problem (Figures 2.12 and 2.13) is a repeated eigenvalue whereas branches EE1, EE2, EE3 and OO1 are distinct. In order to gain insight into this qualitative difference between the periodic problem and the rigid problem, it is proposed in this section to study weakly nonlinear solutions of the quasi-periodic system

$$\frac{\partial u}{\partial t} = \varepsilon u - (1 + \nabla^2)^2 u - u^3, \quad (2.73)$$

$$u = 0, \frac{\partial^2 u}{\partial q^2} - \delta \frac{\partial u}{\partial q} = 0 \quad \text{on} \quad x = 0, L; y = 0, L. \quad (2.74)$$

Note that here q is used to denote the inward normal direction to the boundary and δ is an arbitrary parameter. The periodic problem corresponds to $\delta = 0$ and the rigid problem corresponds to $\delta = \infty$. Here it will be assumed that δ is small so that analytical progress can be made, and the effect of introducing a small component of the rigid boundary condition can be gauged. Note that the system (2.73), (2.74) possesses the same basic symmetry as the individual periodic and rigid problems.

We assume the amplitude for u is of order δ and pose an expansion of the form

$$u = \delta u_0 + \delta^2 u_1 + \delta^3 u_2 + \dots, \quad (2.75)$$

as $\delta \rightarrow 0$, with

$$\varepsilon = \varepsilon_0 + \delta \varepsilon_1 + \delta^2 \varepsilon_2 + \dots, \quad (2.76)$$

and, in order to discuss stability, we incorporate a slow time scale τ , where $t = \delta^{-2} \tau$. Substitution into (2.73), (2.74) gives, at order δ

$$(1 + \nabla^2)^2 u_0 - \varepsilon_0 u_0 = 0; \quad u_0 = \frac{\partial^2 u_0}{\partial q^2} = 0 \quad \text{on} \quad x = 0, L; \quad y = 0, L. \quad (2.77)$$

This is just the linearized periodic problem, with solution

$$u_0 = a(\tau)u_{mn} + b(\tau)u_{nm}, \varepsilon_0 = \varepsilon_{mn}, \quad (2.78)$$

where $a(\tau)$ and $b(\tau)$ are arbitrary amplitudes, u_{mn} is defined by (2.73) and ε_{mn} by (2.71). Since we are interested specifically in the possibility of repeated eigenvalues, we shall assume that $m \neq n$. The objective of the analysis is to determine the amplitude equations for a and b by continuing the analysis to higher levels of approximation.

At order δ^2 , u_1 is found to satisfy

$$(1 + \nabla^2)^2 u_1 - \varepsilon_0 u_1 = \varepsilon_1 u_0, \quad (2.79)$$

with boundary conditions

$$u_1 = 0, \quad \frac{\partial^2 u_1}{\partial x^2} = \frac{\partial u_0}{\partial x} \quad \text{on } x = 0, \quad (2.80)$$

$$u_1 = 0, \quad \frac{\partial^2 u_1}{\partial x^2} = -\frac{\partial u_0}{\partial x} \quad \text{on } x = L, \quad (2.81)$$

$$u_1 = 0, \quad \frac{\partial^2 u_1}{\partial y^2} = \frac{\partial u_0}{\partial y} \quad \text{on } y = 0, \quad (2.82)$$

$$u_1 = 0, \quad \frac{\partial^2 u_1}{\partial y^2} = -\frac{\partial u_0}{\partial y} \quad \text{on } y = L. \quad (2.83)$$

A solvability condition for this system can be derived by introducing an adjoint function

$$\bar{u}_0 = cu_{mn} + du_{nm}, \quad (2.84)$$

where c and d are arbitrary constants. Multiplication of (2.79) by \bar{u}_0 and integration over the square gives

$$\begin{aligned} \int_0^L \int_0^L \bar{u}_0 (1 + \nabla^2)^2 u_1 dx dy - \varepsilon_0 \int_0^L \int_0^L \bar{u}_0 u_1 dx dy = \\ \varepsilon_1 \int_0^L \int_0^L \bar{u}_0 u_0 dx dy. \end{aligned} \quad (2.85)$$

Integration by parts on the left-hand side and use of the boundary conditions (2.80)-(2.83) then gives

$$\begin{aligned} \int_0^L \int_0^L u_1 ((1 + \nabla^2)^2 \bar{u}_0 - \varepsilon_0 \bar{u}_0) dx dy + \int_0^L \left(\frac{\partial \bar{u}_0}{\partial x} \frac{\partial u_0}{\partial x} \Big|_{x=0} + \frac{\partial \bar{u}_0}{\partial x} \frac{\partial u_0}{\partial x} \Big|_{x=L} \right) dy \\ + \int_0^L \left(\frac{\partial \bar{u}_0}{\partial y} \frac{\partial u_0}{\partial y} \Big|_{y=0} + \frac{\partial \bar{u}_0}{\partial y} \frac{\partial u_0}{\partial y} \Big|_{y=L} \right) dx = \varepsilon_1 \int_0^L \int_0^L \bar{u}_0 u_0 dx dy. \end{aligned} \quad (2.86)$$

However, since \bar{u}_0 satisfies the same linear equation as u_0 , the first term on the left-hand side vanishes and evaluation of the remaining terms using (2.78) and (2.84) gives

$$L^{-1}(m^2 + n^2)\pi^2(ac + bd) = \frac{1}{4}\varepsilon_1 L^2(ac + bd). \quad (2.87)$$

Terms proportional to c and d must balance separately on each side, but this just fixes

$$\varepsilon_1 = 4\pi^2 L^{-3}(m^2 + n^2). \quad (2.88)$$

and does not determine the amplitudes a and b . Note that if δ is positive, this result indicates that the 'rigid' component of the boundary condition has the effect of raising the critical value of ε compared to its value for the periodic problem. The amplitudes a and b must be found by proceeding to the next order in the expansion, but before doing this it is necessary to find an explicit solution for u_1 .

Since the solution for u_1 is forced by that for u_0 , it is possible to write

$$u_1 = aU_{mn}(x, y) + bU_{nm}(x, y), \quad (2.89)$$

and

$$\varepsilon_1 = \varepsilon_{1mn} + \varepsilon_{1nm}, \quad (2.90)$$

where

$$U_{mn} = F_{mn}(y)\sin \frac{m\pi x}{L} + F_{nm}(x)\sin \frac{n\pi y}{L}, \quad (2.91)$$

and, from (2.79), F_{mn} and ε_{1mn} satisfy

$$F_{mn}'''' + 2\left(1 - \frac{m^2\pi^2}{L^2}\right)F_{mn}'' + \left[\left(1 - \frac{m^2\pi^2}{L^2}\right)^2 - \varepsilon_0\right]F_{mn} = \varepsilon_{1mn}\sin \frac{n\pi y}{L}. \quad (2.92)$$

From (2.80)-(2.83) the boundary conditions are

$$F_{mn} = 0, \quad F_{mn}'' = \frac{n\pi}{L} \quad (y = 0); \quad F_{mn} = 0, \quad F_{mn}'' = (-1)^{n+1}\frac{n\pi}{L} \quad (y = L). \quad (2.93)$$

The solution for F_{mn} exists provided that $\varepsilon_{1mn} = 4n^2\pi^2 L^{-3}$ and is given by

$$F_{mn} = \frac{n\pi}{2Lq_{mn}} \left(\frac{\cosh k_{mn}^{\frac{1}{2}}(y - \frac{1}{2}L)}{\cosh \frac{1}{2}k_{mn}^{\frac{1}{2}}L} + \frac{2y - L}{L} \cos \frac{n\pi y}{L} \right) \quad (2.94)$$

if n is odd, and

$$F_{mn} = \frac{n\pi}{2Lq_{mn}} \left(-\frac{\sinh k_{mn}^{\frac{1}{2}}(y - \frac{1}{2}L)}{\sinh \frac{1}{2}k_{mn}^{\frac{1}{2}}L} + \frac{2y - L}{L} \cos \frac{n\pi y}{L} \right) \quad (2.95)$$

if n is even, where

$$q_{mn} = \frac{(m^2 + n^2)\pi^2}{L^2} - 1 \quad (2.96)$$

and

$$k_{mn} = \frac{(2m^2 + n^2)\pi^2}{L^2} - 2. \quad (2.97)$$

For a given mode (m, n) , q_{mn} and k_{mn} are positive for low values of L and negative for high values of L . For $k_{mn} < 0$ the solutions (2.94) and (2.95) generally remain valid with the hyperbolic functions replaced by the corresponding trigonometric functions. It is evident however that the theory must be revised to deal with resonant cases for certain discrete negative values of k_{mn} and also in the case $q_{mn} = 0$ corresponding to the minimum points of the marginal stability curves in Figure 2.1. The expansions (2.75) and (2.76) would need to be modified to treat these special cases but here we focus on general values of m , n and L .

Strictly speaking, the solutions (2.94) and (2.95) can also contain an additional term $A \sin \frac{n\pi y}{L}$ where A is an arbitrary constant, but this is just equivalent to the fact that u_1 can contain an arbitrary multiple of u_0 , corresponding to a renormalization of the overall solution. We therefore proceed taking $A = 0$; it can be confirmed that if A is non-zero, it does not influence the amplitude equations for a and b determined below. Note that the value of $\varepsilon_{1mn} + \varepsilon_{1nm}$ confirms the earlier result (2.88) for ε_1 given by using the solvability condition. Note also the non-trigonometric form of F_{mn} and the asymmetry in x and y which arises from the influence of the ‘rigid’ component of the boundary conditions around the square.

At order δ^2 , u_2 is found to satisfy

$$(1 + \nabla^2)^2 u_2 - \varepsilon_0 u_2 = \varepsilon_1 u_1 + \varepsilon_2 u_0 - u_0^3 - \frac{\partial u_0}{\partial \tau}, \quad (2.98)$$

with boundary conditions

$$u_2 = 0, \quad \frac{\partial^2 u_2}{\partial x^2} = \frac{\partial u_1}{\partial x} \quad \text{on } x = 0, \quad (2.99)$$

$$u_2 = 0, \quad \frac{\partial^2 u_2}{\partial x^2} = -\frac{\partial u_1}{\partial x} \quad \text{on } x = L, \quad (2.100)$$

$$u_2 = 0, \quad \frac{\partial^2 u_2}{\partial y^2} = \frac{\partial u_1}{\partial y} \quad \text{on } y = 0, \quad (2.101)$$

$$u_2 = 0, \quad \frac{\partial^2 u_2}{\partial y^2} = -\frac{\partial u_1}{\partial y} \quad \text{on } y = L. \quad (2.102)$$

The solvability condition for this system is found by multiplying (2.98) by the adjoint function (2.84) and integrating over the square, giving

$$\begin{aligned} & \int_0^L \left(\frac{\partial \bar{u}_0}{\partial x} \frac{\partial u_1}{\partial x} \Big|_{x=0} + \frac{\partial \bar{u}_0}{\partial x} \frac{\partial u_1}{\partial x} \Big|_{x=L} \right) dy + \int_0^L \left(\frac{\partial \bar{u}_0}{\partial y} \frac{\partial u_1}{\partial y} \Big|_{y=0} + \frac{\partial \bar{u}_0}{\partial y} \frac{\partial u_1}{\partial y} \Big|_{y=L} \right) dx \\ &= \varepsilon_1 \int_0^L \int_0^L \bar{u}_0 u_1 dx dy + \varepsilon_2 \int_0^L \int_0^L \bar{u}_0 u_0 dx dy - \int_0^L \int_0^L \bar{u}_0 u_0^3 dx dy \\ & \quad - \int_0^L \int_0^L \bar{u}_0 \frac{\partial u_0}{\partial \tau} dx dy. \end{aligned} \quad (2.103)$$

All of the integrals involved in this equation can be calculated from the known expressions for u_0 , u_1 and \bar{u}_0 . From terms proportional to c , after extensive algebra and for $m \neq n$, this gives

$$\frac{1}{4} L^2 \frac{da}{d\tau} + k_1 a + k_2 b = \frac{1}{4} L^2 \varepsilon_2 a - L^2 \left(\frac{9}{64} a^3 + \frac{3}{16} ab^2 \right), \quad (2.104)$$

and from terms proportional to d ,

$$\frac{1}{4} L^2 \frac{db}{d\tau} + k_1 b + k_2 a = \frac{1}{4} L^2 \varepsilon_2 b - L^2 \left(\frac{9}{64} b^3 + \frac{3}{16} ba^2 \right), \quad (2.105)$$

where the coefficients on the left-hand side are given by

$$k_1 = (n\gamma_{mn} + m\gamma_{nm})\pi - 2\pi^2 L^{-2} (n^2 \beta_{mn} + m^2 \beta_{nm}), \quad (2.106)$$

$$k_2 = 2nm\pi^2 L^{-2} (\alpha_{mn} + \alpha_{nm}). \quad (2.107)$$

Here

$$\alpha_{mn} \equiv \int_0^L F_{mn}(y) \sin \frac{n\pi y}{L} dy = \frac{2mnL^2}{(n^2\pi^2 + 3m^2\pi^2 - 2L^2)(n^2 - m^2)} \quad (2.108)$$

if m, n are both even or both odd and $\alpha_{mn} = 0$ if m is even and n is odd (or vice versa),

$$\beta_{mn} \equiv \int_0^L F_{mn}(y) \sin \frac{m\pi y}{L} dy = \frac{(n^2\pi^2 - m^2\pi^2 + L^2)}{4(n^2\pi^2 + m^2\pi^2 - L^2)^2}, \quad (2.109)$$

and

$$\gamma_{mn} \equiv F'_{mn}(0) = \begin{cases} \frac{n\pi}{2Lq_{mn}} \left(\frac{2}{L} - k_{mn}^{\frac{1}{2}} \tanh \frac{1}{2} k_{mn}^{\frac{1}{2}} L \right), & n \text{ odd}; \\ \frac{n\pi}{2Lq_{mn}} \left(\frac{2}{L} - k_{mn}^{\frac{1}{2}} \coth \frac{1}{2} k_{mn}^{\frac{1}{2}} L \right), & n \text{ even}. \end{cases} \quad (2.110)$$

By introducing the scale transformation

$$k_2 = \frac{1}{4} L^2 k \quad (2.111)$$

and a local control parameter $\bar{\varepsilon}$ defined by

$$\bar{\varepsilon} = \varepsilon_2 - 4L^{-2}k_1, \quad (2.112)$$

the amplitude equations (2.104), (2.105) can be written in the simpler form

$$\frac{da}{d\tau} = \bar{\varepsilon}a - kb - \frac{9}{16}a^3 - \frac{3}{4}ab^2, \quad (2.113)$$

$$\frac{db}{d\tau} = \bar{\varepsilon}b - ka - \frac{9}{16}b^3 - \frac{3}{4}ba^2, \quad (2.114)$$

from which the local bifurcation structure and weakly nonlinear development can now be deduced. We first discuss steady-state solutions $a = a_s$, $b = b_s$ where the left-hand sides are set to zero.

First note that if m is even and n is odd (or vice versa) the coefficient k is zero and the equations (2.113), (2.114) are then similar to those discussed in the periodic problem in Section 2.3 (cf (2.16), (2.17)). This implies that (to within an arbitrary change of sign in u) four steady-state solutions bifurcate from $\bar{\varepsilon} = 0$, two of which are pure EO and OE modes (where either $a_s = 0$ or $b_s = 0$) and two of which are the diagonal combinations of these modes (where either $a_s = b_s$ or $a_s = -b_s$). Thus inclusion of the 'rigid' component of the boundary condition has no qualitative effect on the nature of the bifurcation in this case. This is consistent with the fact that in the rigid linearized problem (Section 2.4) such modes are still associated with repeated eigenvalues ε .

However, if m and n are either both odd or both even, the coefficient k is non-zero, being given from (2.106), (2.107) and (2.111) by

$$k = \frac{32m^2n^2\pi^4}{L^2(n^2\pi^2 + 3m^2\pi^2 - 2L^2)(m^2\pi^2 + 3n^2\pi^2 - 2L^2)}. \quad (2.115)$$

In this case the bifurcation points from the trivial solution $a_s = b_s = 0$ of (2.113), (2.114) move to separate locations $\bar{\varepsilon} = -k$ and $\bar{\varepsilon} = k$ and correspond to solutions for which $a_s = -b_s$ and $a_s = b_s$ respectively. The full nonlinear solutions of (2.113) and (2.114) are

$$a_s = -b_s = \pm \frac{4}{\sqrt{21}}(\bar{\varepsilon} + k)^{\frac{1}{2}}, \quad \bar{\varepsilon} > -k \quad (2.116)$$

and

$$a_s = b_s = \pm \frac{4}{\sqrt{21}}(\bar{\varepsilon} - k)^{\frac{1}{2}}, \quad \bar{\varepsilon} > k \quad (2.117)$$

and are equivalent to the 4-fold symmetric EE or OO solutions, consistent with the occurrence of separate eigenvalues of the linearized rigid problem in Section 2.4. Solutions of (2.113), (2.114) for which either $a_s = 0$ and $b_s \neq 0$ or $a_s \neq 0$ and $b_s = 0$, corresponding to a pure mode u_{nm} or u_{mn} , are no longer possible, but are replaced by solutions which develop from a secondary bifurcation. This can be seen by multiplying (2.113) by b_s , (2.114) by a_s and subtracting to obtain

$$(a_s^2 - b_s^2)(k + \frac{3}{16}a_sb_s) = 0. \quad (2.118)$$

The solutions for which $b_s = \pm a_s$ have already been discussed, but there are also solutions for which

$$b_s = -\frac{16k}{3a_s}. \quad (2.119)$$

From (2.113), these are given by

$$a_s = \pm \frac{2\sqrt{2}}{3}(\bar{\varepsilon} \pm (\bar{\varepsilon}^2 - 36k^2)^{\frac{1}{2}})^{\frac{1}{2}}, \quad (2.120)$$

(with b_s then determined from (2.119)) and exist for $\bar{\varepsilon} \geq 6|k|$. These four solutions bifurcate from the leading branch of (2.116), (2.117) at $\bar{\varepsilon} = 6|k|$ where $|a_s| = |b_s| = 4(\bar{\varepsilon}/3)^{\frac{1}{2}}$. As $\bar{\varepsilon}$ increases, however, one pair of solutions becomes dominated by the a_s component, so that $|a_s| \sim 4\bar{\varepsilon}^{\frac{1}{2}}/3$, $|b_s| \rightarrow 0$ as

$\bar{\varepsilon} \rightarrow \infty$ and the other pair becomes dominated by the b_s component, with $|a_s| \rightarrow 0$, $|b_s| \sim 4\bar{\varepsilon}^{1/2}/3$ as $\bar{\varepsilon} \rightarrow \infty$. Thus the pure u_{mn} and u_{nm} modes emerge on these secondary branches as $\bar{\varepsilon} \rightarrow \infty$. Note that using the measure (2.30) the overall amplitude of the solutions (2.116), (2.117) is

$$\hat{u} \sim \frac{1}{2} \delta(a_s^2 + b_s^2)^{1/2} = \sqrt{\frac{8}{21}} \delta \bar{\varepsilon}^{1/2}, \quad (2.121)$$

whereas the overall amplitude of the secondary solutions (2.119), (2.120) is slightly larger with

$$\hat{u} \sim \frac{1}{2} \delta(a_s^2 + b_s^2)^{1/2} = \frac{2}{3} \delta \bar{\varepsilon}^{1/2}. \quad (2.122)$$

Figure 2.19 shows the bifurcation diagram for the case where $m = 3$, $n = 1$ and $L = 5$, in which case $k = 0.07244$ in (2.113), (2.114). Solutions for u on the various branches, constructed from (2.78), are shown in Figure 2.20. The bifurcation diagram will look qualitatively the same for any value of k since k can be removed from the equations (2.113), (2.114) by a rescaling of ε, a, b and τ . Negative values of k are just equivalent to changing the sign of one amplitude function relative to the other.

Finally the local stability of these steady-state solutions can be examined using the method described in Section 2.3 for the periodic problem. Writing $a = a_s + \bar{A}e^{\bar{\sigma}\tau}$, $b = b_s + \bar{B}e^{\bar{\sigma}\tau}$, substituting in (2.113), (2.114) and linearizing in \bar{A} and \bar{B} yields the growth rates $\bar{\sigma}$ from the equations

$$(\bar{\sigma} - \bar{\varepsilon} + \frac{27}{16}a_s^2 + \frac{3}{4}b_s^2)\bar{A} + (k + \frac{3}{2}a_sb_s)\bar{B} = 0, \quad (2.123)$$

$$(\bar{\sigma} - \bar{\varepsilon} + \frac{27}{16}b_s^2 + \frac{3}{4}a_s^2)\bar{B} + (k + \frac{3}{2}a_sb_s)\bar{A} = 0. \quad (2.124)$$

Substituting the solutions for a_s and b_s , this shows that only the branch (2.117) or (2.118) which bifurcates first ((2.117) if $k > 0$ or (2.118) if $k < 0$) is stable, and since the maximum growth rate is given by

$$\bar{\sigma} = \frac{2}{7}(\bar{\varepsilon} - 6|k|), \quad (2.125)$$

this branch loses stability when $\bar{\varepsilon}$ reaches the value $6|k|$. At this point the secondary branches given by (2.119), (2.120) bifurcate and these have maximum growth rate

$$\bar{\sigma} = -\frac{7}{6}\bar{\varepsilon} + \left(\frac{25}{36}\bar{\varepsilon}^2 + 24k^2\right)^{1/2}, \quad (2.126)$$

which remains negative for $\bar{\varepsilon} > 6|k|$. Thus the secondary branches become the stable steady-state solutions of the system.

2.6 Nonlinear solution of the time dependent rigid problem

The time dependent form of the Swift-Hohenberg equation is a nonlinear system in two spatial variables and time. This is a non-trivial system and cannot be solved in general by analytical means. In this section we describe numerical solutions of the system. We will focus on the discretisation of the system and the various numerical methods employed, the accuracy and stability of the numerical schemes that we derive and finally the results that our scheme produces from various initial conditions.

2.6.1 Numerical scheme

The simplest approach is to use an explicit forward difference scheme in which the Swift-Hohenberg equation (2.1) is replaced by the discretised form

$$\frac{u_{i,j} - \bar{u}_{i,j}}{\Delta t} = \varepsilon \bar{u}_{i,j} - \{(1 + \nabla^2)^2 \bar{u}\}_{i,j} - \bar{u}_{i,j}^3. \quad (2.127)$$

Here $u_{i,j}$ is the solution at time $t + \Delta t$ and position $x = ih$, $y = jk$, $i = 0, \dots, M + 1$; $j = 0, \dots, N + 1$, where h and k are the step lengths in the x and y directions respectively and $(M + 1)h = (N + 1)k = L$; $\bar{u}_{i,j}$ denotes the corresponding solution at time t .

The discretisation of the term $(1 + \nabla^2)^2 \bar{u}$ is carried out using central differences exactly as in Section 2.4. This yields a scheme with truncation errors of order h^2 and k^2 in the spatial derivatives and of order Δt in the time derivative:

$$\begin{aligned} \frac{u_{i,j} - \bar{u}_{i,j}}{\Delta t} = & (\varepsilon - 1)\bar{u}_{i,j} - \frac{2}{h^2}(\bar{u}_{i+1,j} - 2\bar{u}_{i,j} + \bar{u}_{i-1,j}) \\ & - \frac{2}{k^2}(\bar{u}_{i,j+1} - 2\bar{u}_{i,j} + \bar{u}_{i,j-1}) - \frac{1}{h^4}(\bar{u}_{i+2,j} - 4\bar{u}_{i+1,j} + 6\bar{u}_{i,j} - 4\bar{u}_{i-1,j} + \bar{u}_{i-2,j}) \\ & - \frac{1}{k^4}(\bar{u}_{i,j+2} - 4\bar{u}_{i,j+1} + 6\bar{u}_{i,j} - 4\bar{u}_{i,j-1} + \bar{u}_{i,j-2}) \end{aligned}$$

$$-\frac{2}{h^2k^2}[4\bar{u}_{i,j} - 2(\bar{u}_{i+1,j} + \bar{u}_{i-1,j} + \bar{u}_{i,j+1} + \bar{u}_{i,j-1}) + \bar{u}_{i+1,j+1} + \bar{u}_{i-1,j-1} + \bar{u}_{i+1,j-1} + \bar{u}_{i-1,j+1}]$$

for $i = 1, \dots, M; j = 1, \dots, N$. (2.128)

The equation (2.128) is applied at all internal points; this requires evaluation of $\bar{u}_{i,j}$ at fictitious points outside the grid where $i = -1, i = M + 2, j = -1$ or $j = N + 2$. This is done by using the boundary conditions $\frac{\partial u}{\partial q} = 0$ on $x = 0, L$ and $y = 0, L$ which in discretised form become

$$\bar{u}_{-1,j} = \bar{u}_{1,j}, \quad \bar{u}_{M+2,j} = \bar{u}_{M,j}, \quad \bar{u}_{i,-1} = \bar{u}_{i,1}, \quad \bar{u}_{i,N+2} = \bar{u}_{i,N}.$$

(2.129)

Values of $\bar{u}_{i,j}$ in (2.128) on the boundaries are replaced using the condition $u = 0$ on $x = 0, L$ and $y = 0, L$ giving

$$\bar{u}_{0,j} = \bar{u}_{M+1,j} = \bar{u}_{i,0} = \bar{u}_{i,N+1}.$$

(2.130)

Thus (2.128) provides the solution $u_{i,j}$ at time $t + \Delta t$ at all internal grid points, and $u_{i,j}$ is zero on the boundaries. In this way the solution can be computed forwards in time, from a specified initial state

$$\bar{u}_{i,j} = U_{i,j} \quad \text{at} \quad t = 0.$$

(2.131)

Several other numerical schemes were also considered as follows. A modified Euler scheme (pseudo predictor/corrector) was developed as a possible means of increasing the time step used in the numerical scheme. The scheme takes the form

$$\hat{u}_{i,j} = \bar{u}_{i,j} + \Delta t f(\bar{u}_{i,j}),$$

(2.132)

$$u_{i,j} = \bar{u}_{i,j} + \frac{\Delta t}{2}(f(\bar{u}_{i,j}) + f(\hat{u}_{i,j})) = \frac{1}{2}(\bar{u}_{i,j} + \hat{u}_{i,j}) + \Delta t f(\hat{u}_{i,j})$$

(2.133)

where $f(\bar{u}_{i,j})$ is the right-hand side of (2.127) and $u_{i,j}$ is the corrected value of the solution at time $t + \Delta t$.

The Dufort-Frankel leapfrog method was also considered with a view to improving stability. This is a three-time-level scheme but for a fourth-order equation in two spatial variables is not generally explicit and is therefore more difficult to implement than for a second-order equation.

The use of a Crank-Nicolson scheme was also considered. This again is an implicit scheme which would allow larger time steps to be used and would have order Δt^2 truncation error in the time derivative. However the nonlinearity of the system would necessitate an iterative process at each time step. As the main aim is to identify steady-state solutions, it was decided to limit the use of implicit schemes to the steady state system (see Section 2.7 below).

2.6.2 Accuracy and validation

We expect that for the fourth order equation (2.127), and provided $h = k$, the forward-difference scheme described above will be stable provided that

$$\Delta t \leq \kappa h^4, \quad (2.134)$$

where κ is a constant. Temporal and spatial errors will be compounded and the numerical scheme will quickly become unstable and diverge if this condition is not met.

A number of experiments were carried out to test the validity of (2.134) and to estimate a value of κ . These were done for the case $L = 1$ and $\varepsilon = 2000$ using a 10x10 grid ($M = N = 9$), a 20x20 grid ($M = N = 19$) and a 40x40 grid ($M = N = 39$). This is a case where the solution approaches a non-zero steady-state as $t \rightarrow \infty$. For the 10x10 grid using a random initial state $U_{i,j}$ it was found after numerous runs testing Δt that for $\Delta t \geq 0.0000032$ the scheme is unstable, giving an approximation for κ of 0.032. This was tested by running the numerical scheme using a finer mesh (40x40) and again examining the stable area. The solution was found to be stable for $\Delta t = 1.289 \times 10^{-8}$, in agreement with the criterion $\Delta t \leq \kappa h^4$ with $\kappa = 0.032$ and $h = 0.025$. Computations with the 20x20 grid also confirmed this criterion. We thus have a suitable estimate of the restriction on Δt for a defined mesh resolution to use in the numerical work. Because the Swift-Hohenberg equation is fourth order, extremely small time steps are needed to maintain stability in the forward difference scheme.

The modified Euler scheme (2.132) and (2.133) produced the same steady-state solution at $L = 1$, $\varepsilon = 2000$ to 6 decimal places but it was found after

Grid size	u_{num}	u_{true}
10x10	38.970028	
20x20	37.339985	36.79663733
40x40	36.802868	36.65839067

Table 2.4: Central values of u_{num} and u_{true} , for various grid sizes with $L = 1$ and $\varepsilon = 2000$.

some testing that Δt could not be increased to any significant degree in comparison to its value for the forward Euler scheme (2.126) and therefore the modified scheme was not used further.

The next set of tests were designed to determine how the steps h and k affect the accuracy of the solution. Table 2.4 gives results for $L = 1$, $\varepsilon = 2000$ on three different grids ($M = N = 9$, $M = N = 19$, $M = N = 39$) showing the steady state value of the single cell solution at the centre of the square. It also shows the solution predicted using an h^2 -extrapolation of the results based on the formula

$$u_{num} = u_{true} + h^2 A \quad (2.135)$$

where u_{num} is the numerical solution and A is a constant. Values of u_{true} in Table 2.4 are calculated using the numerical results for the given grid and the grid of doubled step size. This analysis suggests that the results for the 10x10 mesh are up to 5.9 percent in error, for the 20x20 grid the error is 1.47 percent and for the 40x40 grid the error is only 0.3 percent. Despite the large value of ε the qualitative nature of the solution is preserved even on a 10x10 grid. For more complex patterns it can be expected that finer grids will be necessary to adequately resolve the solution.

2.6.3 Results

The time-dependent system was used to allow the solution to evolve to non-linear steady-state solutions of the Swift-Hohenberg equation. By computing steady-state solutions for a range of values of ε , at fixed L , the nonlinear development from the linear onset solutions identified in Section 2.4 can be obtained.

It is also possible to examine how the time evolution depends on the initial state (2.131) specified at $t=0$. Results were obtained for several different initial states $u = U(x, y)$ at $t = 0$, including

$$U(x, y) = U_0 \sin \frac{m\pi x}{L} \sin \frac{n\pi y}{L}, \quad (2.136)$$

with U_0 , m and n specified and

$$U(x, y) = R(i, j) \quad \text{at } x = ih, \quad y = jk, \quad (2.137)$$

where $R(i, j)$ is taken as a random real value in the range $-1 < R < 1$ at each grid point (i, j) . Different initial states can be used, to some extent, to generate steady-state solutions of a particular form. This is because solutions of (2.1), (2.2) which are initially even or odd in x or y retain that symmetry at later times. However, in practice if the steady-state solution is an unstable state, truncation errors in the numerical computation destroy the symmetry and lead to an asymmetric temporal evolution, with the solution tending to a stable steady-state at large time. This means that the present time-dependent method cannot be used to obtain all of the steady-state solutions of the system (2.1), (2.2).

Results were obtained for several different sizes of square and details are given here for the cases $L = 5, 5\pi, 30$ and 16π .

(a) $L = 5$

Figures 2.21-2.26 show contours of steady-state solutions and time evolution graphs for the case $L = 5$. These were mostly obtained using 10×10 and 20×20 meshes and a time step Δt of 0.0001.

Figure 2.21 shows a solution with EE symmetry, which is the solution generally achieved using a random initial profile, $U(x, y) = R(i, j)$ or a symmetric initial profile such as $U = x(L - x)y(L - y)$, indicating that it is a stable steady-state. At high values of ε the nonlinear solution has a plateau form with the main variation in u occurring near the boundaries. The height of the plateau is given by $u \approx \varepsilon^{\frac{1}{2}}$ as $\varepsilon \rightarrow \infty$, corresponding to a balance between the terms εu and u^3 in the Swift-Hohenberg equation. Convergence to the steady-state solution occurs faster at higher values of ε , as can be seen from Figure 2.22.

The pattern of Figure 2.23 was achieved by using the initial profile $U(x, y) = \sin \frac{\pi x}{L} \sin \frac{2\pi y}{L}$ and $h = k = 0.25$. The pattern is a 2-cell parallel structure with EO symmetry, and is comparable with the pattern of the linearized solution u_1 for $L = 5$ of Figure 2.12. It was only possible to track this solution for $\varepsilon \geq 60$; for $\varepsilon < 60$ the solution converged to the one-cell solution of Figure 2.21. Figure 2.24 shows the evolution with time of the solution (in this case the solution at the centre of the square remains zero for all t and so \hat{u} , defined by (2.30), is used as a measure of the amplitude of the solution). For $\varepsilon = 200$ the convergence of the solution to its steady-state form is slower than for the one-cell solution of Figure 2.21.

An initial profile of the form $U(x, y) = \sin \frac{2\pi x}{L} \sin \frac{2\pi y}{L}$ was used to try and generate a four-cell OO solution of the form observed in the linearized solution of Figure 2.14. This led to a rather interesting three-cell diagonal steady-state solution shown in Figure 2.25. The solution in Figure 2.25 was only found for $\varepsilon \geq 141.5$ on a 10x10 grid. However, several simulations on finer grids (20x20 and 40x40) were inconclusive as the solution in Figure 2.25 could not be found on these finer grids. Figure 2.26 shows the time evolution to the steady-state solutions of Figure 2.25. In fact the solution almost converges to the OO mode, but then undergoes a second stage of evolution to the diagonal mode, which is presumably more stable. The diagonal mode appears to be a combination of the one-cell EE mode and the four-cell OO mode.

(b) $L = 5\pi$

Figures 2.27-2.30 show contours of solutions for the case $L = 5\pi$. These were obtained with a 32x32 grid ($h = k = 0.49087$) and a time step Δt of 0.00001. Random initial conditions were used for most of the computations in this subsection and this led to a number of different steady-state patterns, as shown in Figures 2.27, 2.28 and 2.30. In some cases the steady-state pattern found at one value of ε was used as an initial state for computations at other values of ε .

The 4-cell parallel mode of Figure 2.27 has OE symmetry. This steady-state pattern was first found when performing numerical simulations using a random initial state with $\varepsilon = 0.18$ and was also readily found at higher values of ε . The amplitude of the cells increases with ε .

Figure 2.28 shows a steady-state 5-cell diagonal mode achieved using a random initial state over a range of values of ε . Figure 2.29 shows the pattern evolution to steady-state through time for the case where $\varepsilon = 0.3$.

The steady-state contours of Figure 2.30 are the product of simulations using an initial profile $U(x, y) = |R(i, j)|$. This mode was only found for $\varepsilon \geq 0.37$. It is even about $x = \frac{1}{2}L$ but has no symmetry in the y direction.

Finally, Figure 2.31 shows a centrosymmetric steady-state pattern found at $\varepsilon = 0.855$ and a non-symmetric steady-state pattern found at $\varepsilon = 1.248$. Similar stable patterns can be found for other reasonably high values of ε .

(c) $L = 30$

Figures 2.32-2.34 show contours of steady state solutions for the case $L = 30$. These were all obtained using a 32 x32 mesh and a time step Δt of 0.001. Random initial conditions were used for the computations and this led to various steady state patterns.

Figure 2.32 shows steady-state solutions found in the range $\varepsilon = 0.028$ to $\varepsilon = 0.08$. This 12-cell diagonal mode is associated with the linearized solution u_3 of Figure 2.13 and as ε increases the cells spread across the square to fill the opposite corners.

Figure 2.33 shows steady solutions found in the range $\varepsilon = 0.09$ to $\varepsilon = 0.14$. The 12-cell diagonal mode is still found at $\varepsilon = 0.09$ and versions without symmetry about the second diagonal are found at higher ε . In addition, a new centrosymmetric mode is found for $\varepsilon \geq 0.11$.

Figure 2.34 shows steady solutions found in the range $\varepsilon = 0.16$ to $\varepsilon = 0.22$. These include non-symmetric diagonal modes ($\varepsilon = 0.18, \varepsilon = 0.22$), centrosymmetric modes ($\varepsilon = 0.16, \varepsilon = 0.17$) and a non-symmetric mode ($\varepsilon = 0.21$).

(d) $L = 16\pi$

Figures 2.35 and 2.36 show the contours of a steady-state solution and its time evolution for the case $L = 16\pi$ with $\varepsilon = 0.1$. These results were obtained with a 96x96 grid ($h = k = 0.523599$), a time step Δt of 0.001 and a random initial profile $U(x, y) = R(i, j)$.

2.7 Nonlinear solution of the steady-state rigid problem

Consider the steady-state Swift-Hohenberg equation

$$\varepsilon u - (1 + \nabla^2)^2 u - u^3 = 0, \quad (2.138)$$

with boundary conditions

$$u = \frac{\partial u}{\partial q} = 0 \quad \text{on} \quad x = 0, L \quad \text{and} \quad y = 0, L. \quad (2.139)$$

In this section we describe a numerical scheme for solving this problem based on Newton iteration, and present results for several values of L .

2.7.1 Numerical scheme

We discretise the system on to a uniform grid in x and y , as in the solution of the linearized system in Section 2.4. The equation (2.136) can then be expressed in the form

$$F_{i,j} \equiv \varepsilon u_{i,j} - \{(1 + \nabla^2)^2 u\}_{i,j} - u_{i,j}^3 = 0. \quad (2.140)$$

Since this is a nonlinear system, it can be solved by performing a Newton iteration:

$$F_{i,j} + \sum_{I,J} \frac{\partial F_{i,j}}{\partial u_{I,J}} \delta u_{I,J} = 0, \quad (2.141)$$

to obtain the Newton increments $\delta u_{i,j}$ at each grid point. These are then used to produce an improved approximation $u_{i,j} + \delta u_{i,j}$ to the solution. The iterative process is continued until all of the Newton increments tend to zero, to within some specified tolerance. The advantages of this method over the time-dependent scheme of Section 2.6 are that it can find both stable and unstable steady-states, it can significantly reduce computation times and it allows solutions to be tracked as a function of ε in a relatively straightforward manner.

In (2.140), the middle term is discretised in exactly the same way as in Section 4.1, so that

$$F_{i,j} = (\varepsilon - 1)u_{i,j} - \frac{2}{h^2}(u_{i+1,j} - 2u_{i,j} + u_{i-1,j}) - \frac{2}{k^2}(u_{i,j+1} - 2u_{i,j} + u_{i,j-1})$$

$$\begin{aligned}
& -\frac{1}{h^4} [u_{i+2,j} - 4u_{i+1,j} + 6u_{i,j} - 4u_{i-1,j} + u_{i-2,j}] \\
& -\frac{1}{k^4} [u_{i,j+2} - 4u_{i,j+1} + 6u_{i,j} - 4u_{i,j-1} + u_{i,j-2}] \\
& -\frac{2}{h^2k^2} [4u_{i,j} - 2(u_{i+1,j} + u_{i-1,j} + u_{i,j+1} + u_{i,j-1}) \\
& \quad + u_{i+1,j+1} + u_{i-1,j-1} + u_{i+1,j-1} + u_{i-1,j+1}] \\
& \quad \text{for } i = 1, \dots, M; j = 1, \dots, N. \quad (2.142)
\end{aligned}$$

Using the boundary conditions (2.52) and (2.53), this implies that $F_{i,j}$ is defined at all internal grid points. The partial derivatives $\frac{\partial F_{i,j}}{\partial u_{i,j}}$ appearing in (2.141) can now be calculated, and provide the $(MN)^2$ elements of the matrix P in the matrix equation

$$P \underline{\delta u} = -\underline{F} \quad (2.143)$$

obtained from (2.141). Here $\underline{\delta u}$ is the column vector of unknowns:

$$\underline{\delta u} = \begin{pmatrix} \delta u_{1,1} \\ \delta u_{2,1} \\ \vdots \\ \delta u_{M,1} \\ \delta u_{1,2} \\ \vdots \\ \delta u_{M,2} \\ \vdots \\ \delta u_{1,N} \\ \vdots \\ \delta u_{M,N} \end{pmatrix} \quad (2.144)$$

F is the column vector

$$\underline{F} = \begin{pmatrix} F_{1,1} \\ F_{2,1} \\ \vdots \\ F_{M,1} \\ F_{1,2} \\ \vdots \\ F_{M,2} \\ \vdots \\ F_{1,N} \\ \vdots \\ F_{M,N} \end{pmatrix} \quad (2.145)$$

and P is the matrix

$$P = A - \varepsilon I + Q, \quad (2.146)$$

where A is the matrix defined by (2.56)-(2.66). The additional contributions arising from the nonlinear term $-u_{i,j}^3$ in (2.142) are contained in the matrix Q , which is defined by

$$Q = \begin{pmatrix} Q_1 & 0 & \dots & \dots & \dots & \dots & 0 & 0 & 0 & 0 \\ \dots & Q_2 & \dots & \dots & \dots & \dots & \dots & 0 & 0 & 0 \\ \dots & 0 & 0 \\ \dots & 0 \\ \dots & \dots \\ \dots & \dots \\ 0 & \dots \\ 0 & 0 & \dots \\ 0 & 0 & 0 & \dots & \dots & \dots & \dots & \dots & Q_{N-1} & 0 \\ 0 & 0 & 0 & 0 & \dots & \dots & \dots & \dots & 0 & Q_N \end{pmatrix} \quad (2.147)$$

where

$$Q_j = \begin{pmatrix} -3u_{1,j}^2 & 0 & \dots & \dots & \dots & \dots & 0 & 0 & 0 & 0 & 0 \\ \ddots & -3u_{2,j}^2 & \ddots & \ddots & \ddots & \ddots & \ddots & 0 & 0 & 0 & 0 \\ \ddots & 0 & 0 & 0 \\ \ddots & 0 & 0 \\ \ddots & 0 \\ \ddots & \ddots \\ 0 & \ddots \\ 0 & 0 & \ddots \\ 0 & 0 & 0 & \ddots & \ddots & \ddots & \ddots & \ddots & -3u_{M-1,j}^2 & 0 & 0 \\ 0 & 0 & 0 & 0 & \dots & \dots & \dots & \dots & 0 & -3u_{M,j}^2 & 0 \end{pmatrix} \quad (2.148)$$

Note that P is a symmetric matrix.

Two methods were used to solve the matrix equation (2.143). In the first, Gauss-Seidel iteration was applied, starting from an initial guess $\delta u_{i,j} = 0$ for all i, j . Although this method worked successfully in a number of simple cases and required minimal computer storage, it did not prove to be robust, and convergence was generally very slow because of the large number of equations involved. The second approach was to use a direct method based on Gauss elimination. This proved reliable and was therefore adopted for all subsequent calculations.

The Newton iteration was implemented generally by using the linearized solution of Section 2.4 as an initial guess for $u_{i,j}$, and, once convergence to within a specified tolerance had been achieved, by incrementing the value of ϵ and using the previous solution for $u_{i,j}$ as the next initial guess. For most calculations a tolerance of

$$\sum_{i=1}^M \sum_{j=1}^N \delta u_{i,j}^2 < 10^{-3}, \quad (2.149)$$

was applied to ensure adequate convergence of the Newton iteration. Results from the time-dependent calculations of Section 2.6 were used as a check on the numerical scheme.

2.7.2 Accuracy

Results were tested for accuracy using different step sizes, $L = 5$ and $\varepsilon = 1.285$ for various grids. These indicated reasonable agreement. Checks were also made to ensure that calculations of the nonlinear system were consistent with the bifurcation points predicted by the linear analysis of Section 2.4.

2.7.3 Results

Results were obtained for various values of L and are described in detail here for the cases $L = 5$, 5π and 30 . A convenient single measure of the amplitude of the nonlinear solution is \hat{u} , as defined in (2.30), and this was computed numerically as

$$\hat{u} = \left(\frac{1}{(M+1)(N+1)} \sum_{i=1}^M \sum_{j=1}^N u_{i,j}^2 \right)^{\frac{1}{2}} \quad (2.150)$$

using the trapezium rule. An alternative measure is to use the value of u at the centre of the square, but this is not useful for solutions with odd symmetry.

(a) $L = 5$

Figure 2.37 shows a bifurcation diagram of steady-state solutions for the case $L = 5$ obtained using a 32×32 mesh ($h = k = 0.15625$). The leading branch bifurcates at $\varepsilon = 1.090$, and consists of a solution with EE symmetry, consistent with the results of Section 2.4. Figure 2.38 shows contours of u for branch EE1 of Figure 2.37 at various values of ε . The amplitude \hat{u} increases with ε and the pattern remains in the form of a single cell which develops a plateau region at the centre when ε is large.

The second and third branches both bifurcate at $\varepsilon = 4.901$ where there is a repeated eigenvalue of the linearized system. Figure 2.39 shows the nonlinear solution with larger amplitude, branch D1, which is a 2-cell diagonal mode. Again as ε increases the pattern remains the same in symmetry and general appearance and the amplitude \hat{u} increases. Figure 2.40 shows the other solution which bifurcates at $\varepsilon = 4.901$ which is a 2-cell parallel mode with OE symmetry (branch OE1). The nonlinear results obtained here confirm the existence of the diagonal and OE modes predicted in the linear analysis of

Section 2.4 although it is interesting to note that, in contrast to the periodic problem, it is the diagonal mode here which has a larger amplitude.

The fourth branch bifurcates at $\varepsilon = 12.248$ and has OO symmetry. Figure 2.41 shows contours of u on this branch (branch OO1) at various values of ε . Again the pattern does not change with increasing ε , and the amplitude \hat{u} increases. This branch was also computed by solving the problem on the quarter domain $0 \leq x \leq \frac{1}{2}L$, $0 \leq y \leq \frac{1}{2}L$ with boundary conditions $u = \frac{\partial^2 u}{\partial q^2} = 0$ applied on the internal edges $x = \frac{1}{2}L$ and $y = \frac{1}{2}L$. Since these are equivalent to periodic boundary conditions, the modifications needed to the numerical scheme are similar to those mentioned in Section 2.4. The results were useful in providing an additional check on the numerical scheme.

The fifth and sixth branches (EE2 and EE3) bifurcate at $\varepsilon = 19.178$ and $\varepsilon = 19.573$ respectively. These two branches are solutions with EE symmetry and are consistent with the patterns predicted by the linearized analysis of Section 2.4. Again as ε is increased the patterns remain the same in symmetry and general appearance and the amplitudes increase. Contours are shown in Figures 2.42 and 2.43.

(b) $L = 5\pi$

The nonlinear results of this section are for the case $L = 5\pi$ and were obtained mainly with a 32x32 mesh ($h = k = 0.49087$). Figure 2.44 shows a bifurcation diagram of steady-state solutions that were found. We first discuss solutions that bifurcate from the trivial solution $u = 0$.

The first branch, branch OO1 of Figure 2.44, has OO symmetry and bifurcates at $\varepsilon = 0.107$, consistent with the linear numerical results of Section 2.4. Figure 2.45 shows the contours of this solution for increasing ε . The amplitude increases and the pattern retains the same form as ε increases.

The second branch bifurcates at $\varepsilon = 0.116$ and is also a non-repeated root of the linear system. Figure 2.46 shows this nonlinear solution (branch EE1 of Figure 2.44) which has EE symmetry and is basically a 9-cell structure similar to the (3,3) mode of the periodic problem.

The third and fourth branches of Figure 2.44 bifurcate at $\varepsilon = 0.119$ where there is a repeated eigenvalue of the linear system. Figure 2.47 shows the contours of u for the solution with diagonal symmetry (branch D1), which is consistent with the 6-cell linearized form of u_3 predicted in Section 2.4. The

other solution predicted by the linear analysis, which has OE symmetry is shown in Figure 2.48.

The fifth and sixth branches both bifurcate at $\varepsilon = 0.1434$, and again are solutions arising from a repeated OE mode of the linearized system. Figure 2.49 shows contours of u on branch OE2 which has OE symmetry and is associated with the solution u_1 of the linearized system. This pattern is somewhat like the (3,2) mode of the periodic problem. The branch of solutions D2 with diagonal symmetry, is shown in Figure 2.50.

The seventh branch OO2 has OO symmetry and contours of u are shown in Figure 2.51.

We now discuss nonlinear solutions which do not bifurcate from the trivial solution, taking them in order of their appearance as ε increases. The existence of such modes is indicated by reference to the time-dependent analysis of Section 2.6 because many of the solutions found there do not have patterns which identify with any of the seven branches listed above. These nonlinear modes were located by using the steady-state solutions found in Section 2.6 as initial guesses in the Newton scheme. In each case the entire branch of steady-state solutions could then be tracked by incrementing the value of ε backwards and forwards from its initial value.

The first solution to arise nonlinearly is a secondary bifurcation from the primary mode OO1 which appears at $\varepsilon = 0.1345$. This solution has diagonal symmetry and is the 5-cell diagonal mode of Figure 2.28. It is designated D_S1 (D for 'diagonal', S for 'secondary') in Figure 2.44. Its amplitude \hat{u} is larger than that of the primary mode OO1 from which it bifurcates, explaining why it is seen in the time-dependent calculations. Contour plots are shown in Figure 2.52 and demonstrate how the diagonal pattern evolves by breaking the symmetry of the OO pattern.

Another solution to arise nonlinearly is a fold bifurcation at $\varepsilon = 0.1707$. This has OE symmetry and its upper branch OE_F^U1 (F for 'fold', U for 'upper') is the stable 4-cell parallel mode reported in the time-dependent calculations of Figure 2.27. The lower branch OE_F^L1 also consists of 4 cells but these become less 'parallel' as ε increases. Patterns on the upper branch are shown in Figure 2.53 and on the lower branch in Figure 2.54. The solutions were found by starting from a point on the upper branch and tracking

backwards in ε until the vertex of the fold bifurcation was eventually located (using extremely small steps in ε) at $\varepsilon = 0.1707$; for lower values of ε the solution converged to mode OO1. In order to track the solution down past the vertex and on to the lower branch, the solution at each grid point was regarded as a function of \hat{u} , allowing a linear extrapolation to be used to provide an initial guess for the Newton iteration at the first point on the lower branch. Thereafter, the solution could be tracked forwards in ε , initially using extremely small steps. Figure 2.55 shows the solution in the neighbourhood of the vertex.

Another solution to arise nonlinearly is a secondary bifurcation from the mode EE1 which appears at $\varepsilon = 0.336$. This solution has even symmetry in one direction only and is therefore designated E_S1 in Figure 2.44. It is the mode reported in the time-dependent calculations of Figure 2.30. Contour plots are shown in Figure 2.56 and demonstrate how the pattern evolves from the EE pattern by breaking the symmetry in one direction.

Finally, another nonlinear solution appears as a fold bifurcation at $\varepsilon = 0.6318$. This has centrosymmetry and contour plots on its upper and lower branches (designated C_F^U1 and C_F^L1) are shown in Figures 2.57 and 2.58 respectively. This is the mode reported in the left-hand contour plot of Figure 2.31 in the time-dependent calculations. The patterns on the two branches differ very little, although slight differences are discernible when ε reaches 0.854. The solution was tracked around the vertex using the same method as for branch OE_F1 ; Figure 2.59 shows the solution in the neighbourhood of the vertex.

It is almost inevitable that other nonlinear solutions appear through secondary bifurcations and fold bifurcations within the range of ε shown in Figure 2.44. However, those described here are likely to be of greatest significance as they give rise to solutions, some of which, from the time-dependent analysis, are stable states. The results of Figure 2.44 show that the amplitudes \hat{u} of the various stable modes are extremely close, explaining why the diagonal, parallel and centrosymmetric modes are all observable in the time-dependent calculations. In fact the leading linear onset solution, which is an OO mode, has largest amplitude only for a very restricted range of ε ($0.107 < \varepsilon < 0.13$); thereafter, solutions containing longer, more coherent

cells (diagonal, parallel or curved) are preferred states of the system.

(c) $L = 30$

A less comprehensive set of results is reported in this section for the case $L = 30$, obtained using a 32×32 grid ($h = k = 0.9375$). Figure 2.60 shows a bifurcation diagram of steady-state solutions that were found. Again solutions that bifurcate from the trivial solution $u = 0$ are discussed first.

The first two branches bifurcate at $\varepsilon = 0.0255$ and correspond to a repeated eigenvalue of the linear system. One of those branches has OE symmetry (associated with the onset solution u_1 shown in Figure 2.13) and the other has diagonal symmetry (associated with the onset solution u_3 shown in Figure 2.13). Only the diagonal mode D1, which from the time-dependent calculations shown in Figure 2.32 is expected to be stable, is shown in Figure 2.60. Contour plots on this branch are shown in Figure 2.61. The solution consists of 12 cells and as ε increases there is tendency for these to spread laterally to fill the square.

The third branch EE1 bifurcates at $\varepsilon = 0.0258$, consistent with the eigenvalue of the linear system shown in Figure 2.11, and at onset consists of 11 cells on each diagonal. Contour plots for this branch are shown in Figure 2.62. As ε increases the outer cells spread laterally to fill the corners and the central region becomes dominated by square cells formed by the interaction of the two diagonal sets; this solution was not observed in the time-dependent calculations and may not be stable.

The fourth branch, OO1, bifurcates at $\varepsilon = 0.026$, consistent with the eigenvalue of the linear system shown in Figure 2.15, and at onset consists of 10 cells on each diagonal, separated by a central saddle point. Contour plots for this branch are shown in Figure 2.63. As ε increases, the central region again becomes dominated by square cells.

Two nonlinear solutions, which do not bifurcate from the trivial solution $u = 0$, were also located. The first of these, EE_F1 , appears as a fold bifurcation at $\varepsilon = 0.0455$ and on the upper branch (EE_F^U1) consists of a 9-cell parallel mode, as shown in Figure 2.64. This solution was found in the time-dependent calculations of Figure 2.34 at $\varepsilon = 0.19$, suggesting that it is stable. On the lower branch (EE_F^L1) the parallel structure becomes less well-ordered as ε increases, as shown in the contour plots of Figure 2.65, and the solution

is likely to be unstable.

A second fold bifurcation (C_F1) was located at $\varepsilon = 0.0666$ and is a centrosymmetric mode of the type observed in the time-dependent calculations of Figure 2.33 at $\varepsilon = 0.11$ and $\varepsilon = 0.13$. Contour plots on the upper branch (C_F^U1) are shown in Figure 2.66 and on the lower branch (C_F^L1) in Figure 2.67.

These two fold bifurcations are similar to those observed in the case $L = 5\pi$, suggesting that they are a generic feature of convection patterns in square cavities.

2.8 Discussion

Pattern formation in a square has been investigated by solving the two-dimensional Swift-Hohenberg equation analytically and numerically for periodic, quasi-periodic and rigid boundary conditions. One of the aims of the study has been to establish the preferred structure and orientation of the pattern, especially in cases where the square is sufficiently large for many cells to be accommodated. In this section we give a summary of the main results.

For periodic boundary conditions the results of Section 2.3 show that solutions onset in the form of parallel-cell solutions (i.e. cells with boundaries parallel to the sides of the square) with EE, OO, OE (or EO) symmetry. Apart from the parallel-cell solutions that already have 4-fold rotational symmetry, all of the other modes appear at repeated eigenvalues of ε which, in the OE/EO case, gives rise to further onset solutions with diagonal symmetry and, in the EE or OO case, give rise to further onset solutions with 4-fold rotational symmetry. However, a weakly nonlinear analysis shows that these non-parallel solutions are all unstable, having lower amplitude than the corresponding modes that bifurcate at the same value of ε . As the size of the square (measured by the non-dimensional parameter L) increases the most dangerous mode continually changes so that on average the parallel onset pattern contains an increasingly large number of cell boundaries in both directions, the specific number depending on the precise value of L .

For the rigid problem, the linear theory of Section 2.4 again reveals so-

lutions with EE, OO, OE (or EO) symmetry. Like the periodic case, the OE/EO modes appear at repeated eigenvalues of ε , giving rise to further onset solutions with diagonal symmetry, the existence of which is confirmed by nonlinear computations in Section 2.7. In the rigid case, however, these diagonal solutions can have larger amplitude than the corresponding OE or EO solution. Also in contrast to the periodic case there are in general no repeated eigenvalues with EE or OO symmetry - in the rigid problem all EE and OO modes appear with 4-fold rotational symmetry at distinct eigenvalues. In Section 2.5 this qualitative difference is investigated by studying a quasi-periodic system containing a small element of the rigid boundary condition. This confirms that the influence of the rigid condition is to render the repeated OO and EE eigenvalues of the linearized periodic system distinct and instead the corresponding parallel modes of the periodic problem emerge as a secondary bifurcation of the primary mode.

Another important difference between the rigid and periodic systems is that in the rigid case the most dangerous mode of the linearized system does not continually change as L increases. Instead there is a competition between just three modes, one with EE symmetry, one with OO symmetry and one with OE/EO or diagonal (D) symmetry. These modes interweave as L changes and the pattern best 'fits' the square, so that each becomes the most dangerous mode for particular intervals of L . The pattern associated with each mode also changes as L changes, facilitating the incorporation of additional cells as L increases. This leads to patterns at large values of L that consist of cells along, and with axes orthogonal to, the diagonals of the square. For the EE, OO and OE/EO modes the cells are positioned along both diagonals whereas for the diagonal mode D they are positioned along one diagonal. These results are consistent with the idea that in large planform systems with rigid boundaries, roll patterns occupy the region spanning points of the boundary of maximum separation.

The results for the linearized rigid problem not only emphasize the prevalence of diagonal structures but also the notable lack of parallel-cell solutions. The existence of nonlinear parallel modes and other modes is, however, confirmed by the time-dependent calculations presented in Section 2.6. These show that as ε increases a whole range of nonlinear stable steady states can

in fact be found, including diagonal modes, parallel modes, modes with centrosymmetry and modes with no symmetry. The question of analyzing the nonlinear bifurcation structure of these modes is addressed in Section 2.7. For relatively low values of L (e.g. $L = 5$) and moderate values of ε this structure is reasonably straightforward and the results confirm the existence of supercritical nonlinear branches of solutions which bifurcate from the linearized eigenvalues and have EE, OO, OE/EO or D symmetry.

As L increases, more modes fit into the square at low values of ε and the complexity of the bifurcation structure is evident from results obtained for $L = 5\pi$ and $L = 30$. These indicate that in addition to the modes stemming from the linear eigenvalues there are other important nonlinear modes that arise through secondary bifurcations and fold bifurcations. In the case $L = 30$ the primary solution is a diagonal mode and in the case $L = 5\pi$, where the primary mode is an OO solution with 4-fold symmetry, it rapidly gives way to a diagonal mode through a secondary bifurcation. In both cases, at higher ε , a parallel mode and then a centrosymmetric mode enter through fold bifurcations, with the time-dependent calculations indicating that the upper branches of these modes are stable. Other stable states were also found, consistent with the idea of complex patterns evolving through symmetry breaking. The various nonlinear patterns reflect a preference for long coherent cells (either straight or curved) thereby minimizing cell boundaries within the interior of the domain. At the boundaries of the domain, the preference is for cells to approach orthogonally, avoiding extended areas of weak convection there.

A more comprehensive set of nonlinear solutions is needed in order to identify all the generic features of the bifurcation diagram for general values of L . However, it is conjectured that diagonal modes with an even number of cells generally bifurcate from the trivial solution at an OE eigenvalue and that diagonal modes with an odd number of cells generally appear as secondary bifurcations through a nonlinear interaction between EE and OO modes. Parallel and centrosymmetric modes with an odd or even number of cells generally appear through fold bifurcations. Further work is needed to confirm these ideas and to carry out a stability analysis of nonlinear solutions.

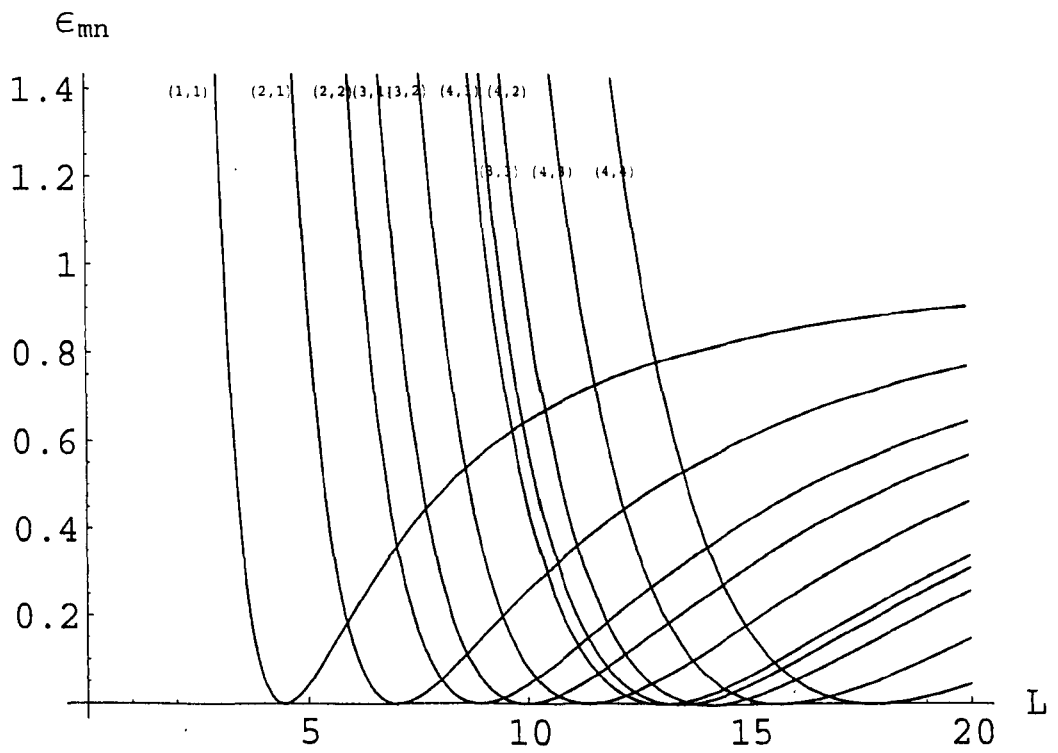


Figure 2.1: The first ten branches of the eigenvalues ϵ_{mn} as functions of L . Branches are labelled (m,n) .

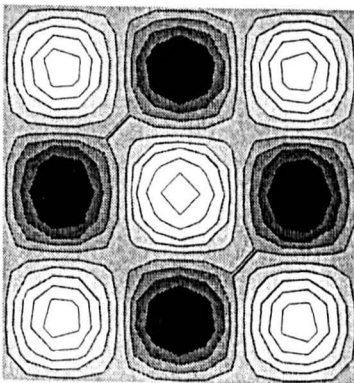
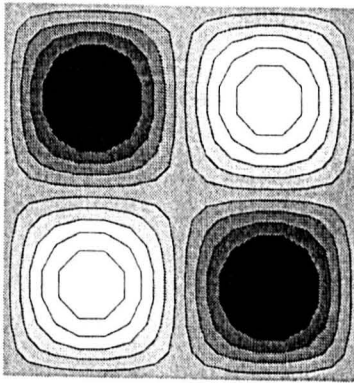
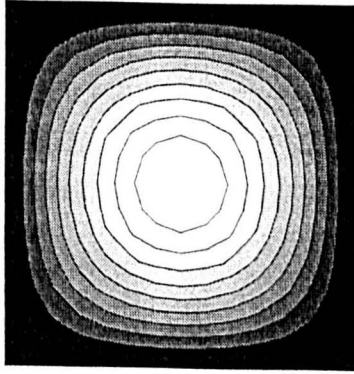


Figure 2.2: Contour plots of the solutions (2.19) for $(m,n)=(1,1)$, $(2,2)$, $(3,3)$.

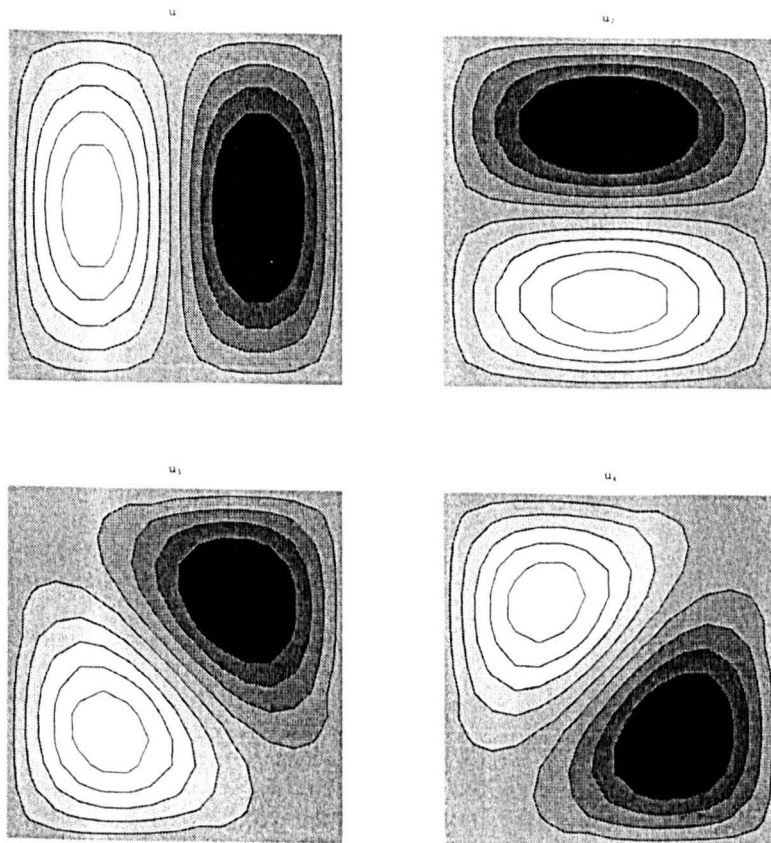


Figure 2.3: Contour plots for $m = 2$ and $n = 1$ of solutions u_1 , u_2 , u_3 and u_4 .

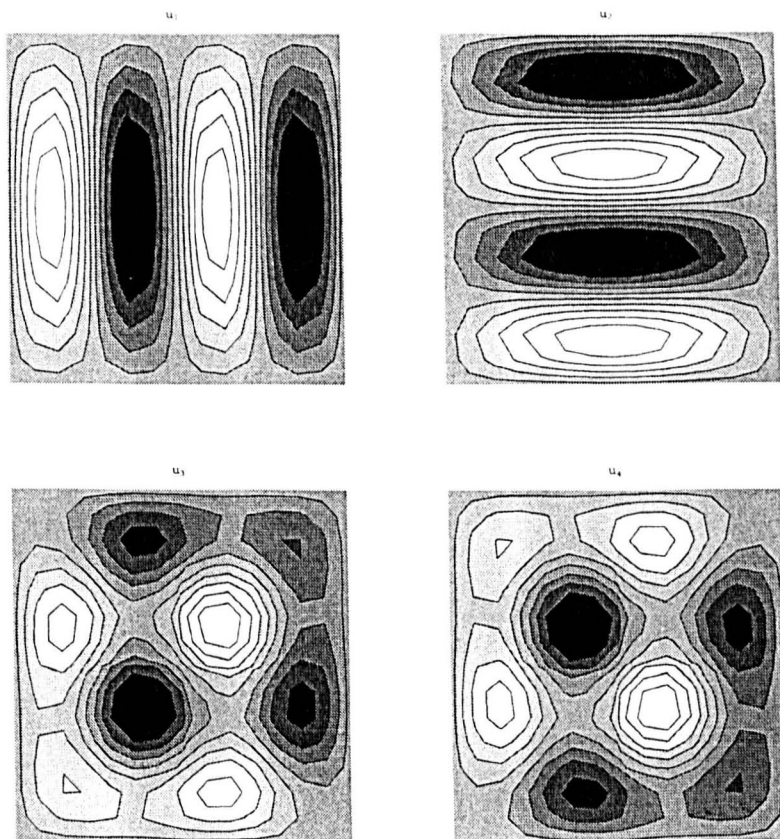


Figure 2.4: Contour plots for $m = 4$ and $n = 1$ of solutions u_1 , u_2 , u_3 and u_4 .

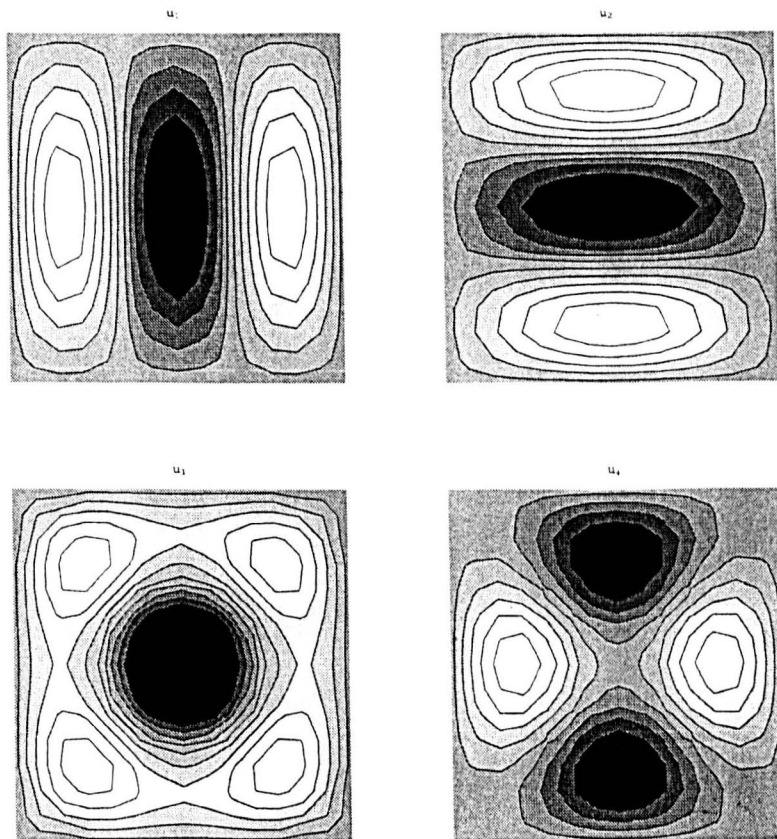


Figure 2.5: Contour plots for $m = 3$ and $n = 1$ of solutions u_1 , u_2 , u_3 and u_4 .

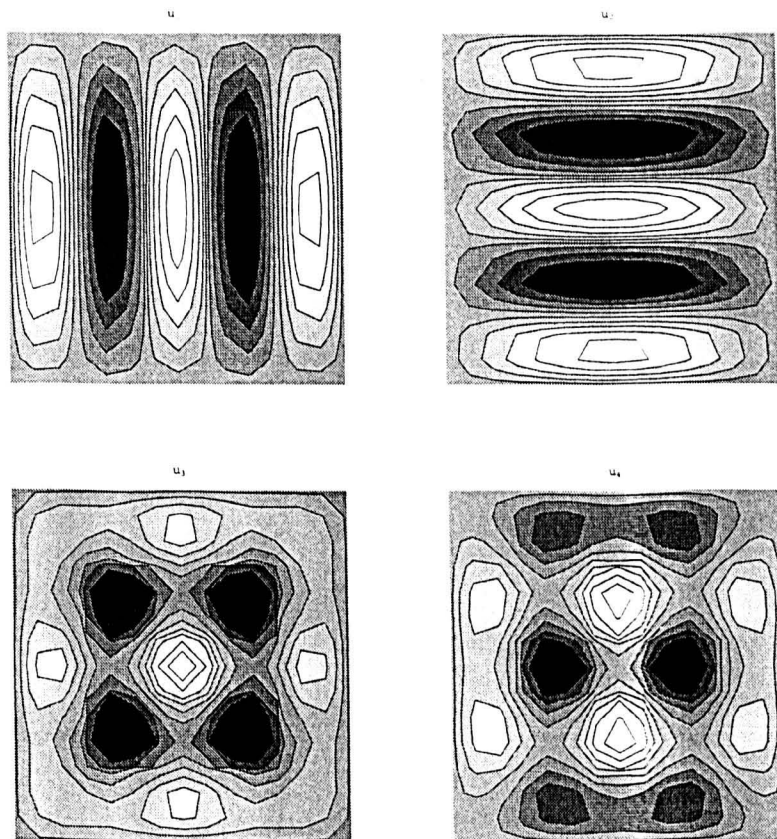


Figure 2.6: Contour plots for $m = 5$ and $n = 1$ of solutions u_1 , u_2 , u_3 and u_4 .

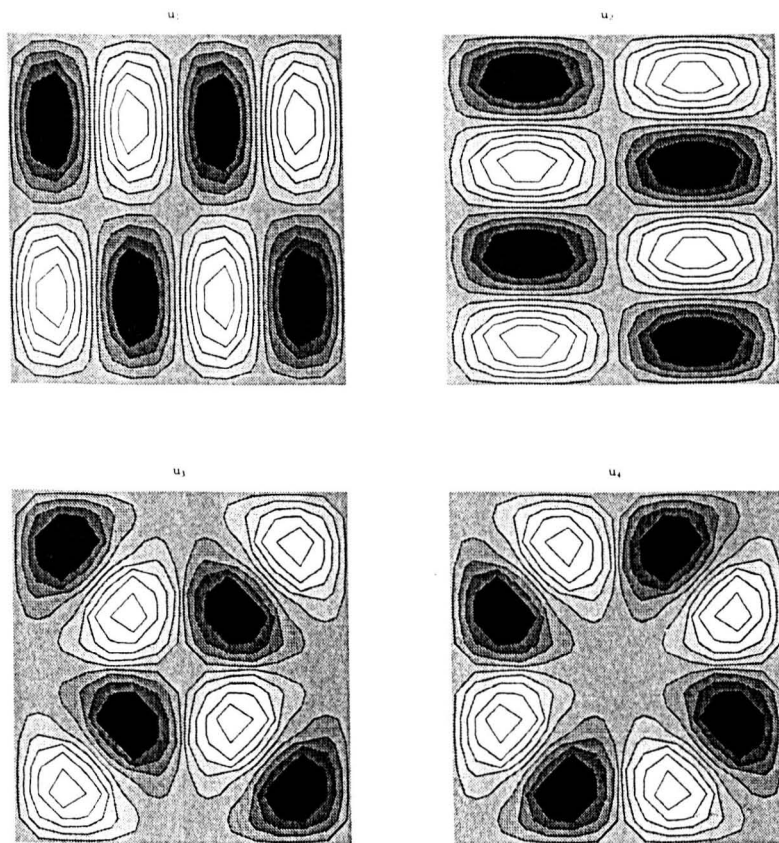


Figure 2.7: Contour plots for $m = 4$ and $n = 2$ of solutions u_1 , u_2 , u_3 and u_4 .

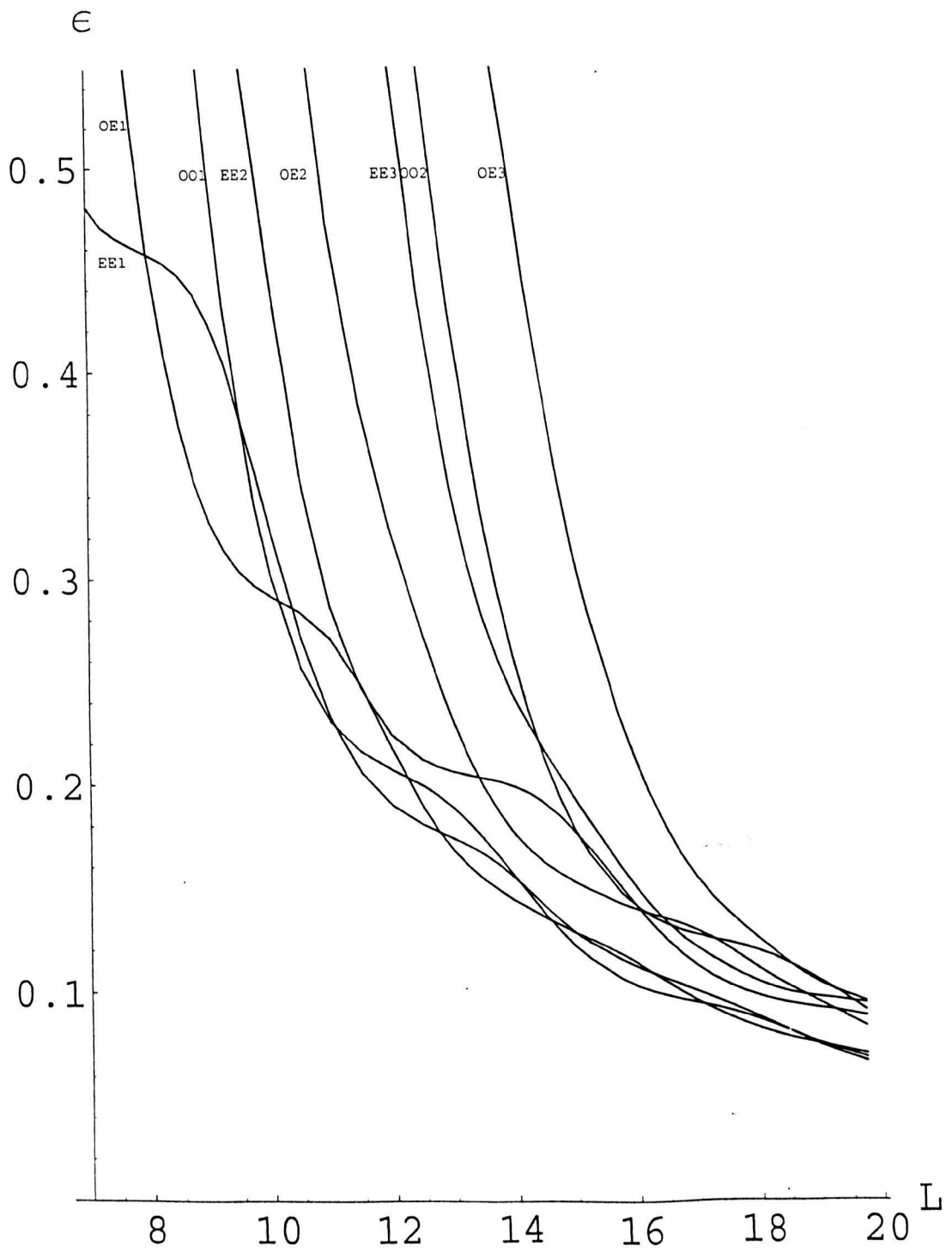


Figure 2.8: The first eight branches of the eigenvalues ϵ as functions of L obtained using a 20x20 grid.

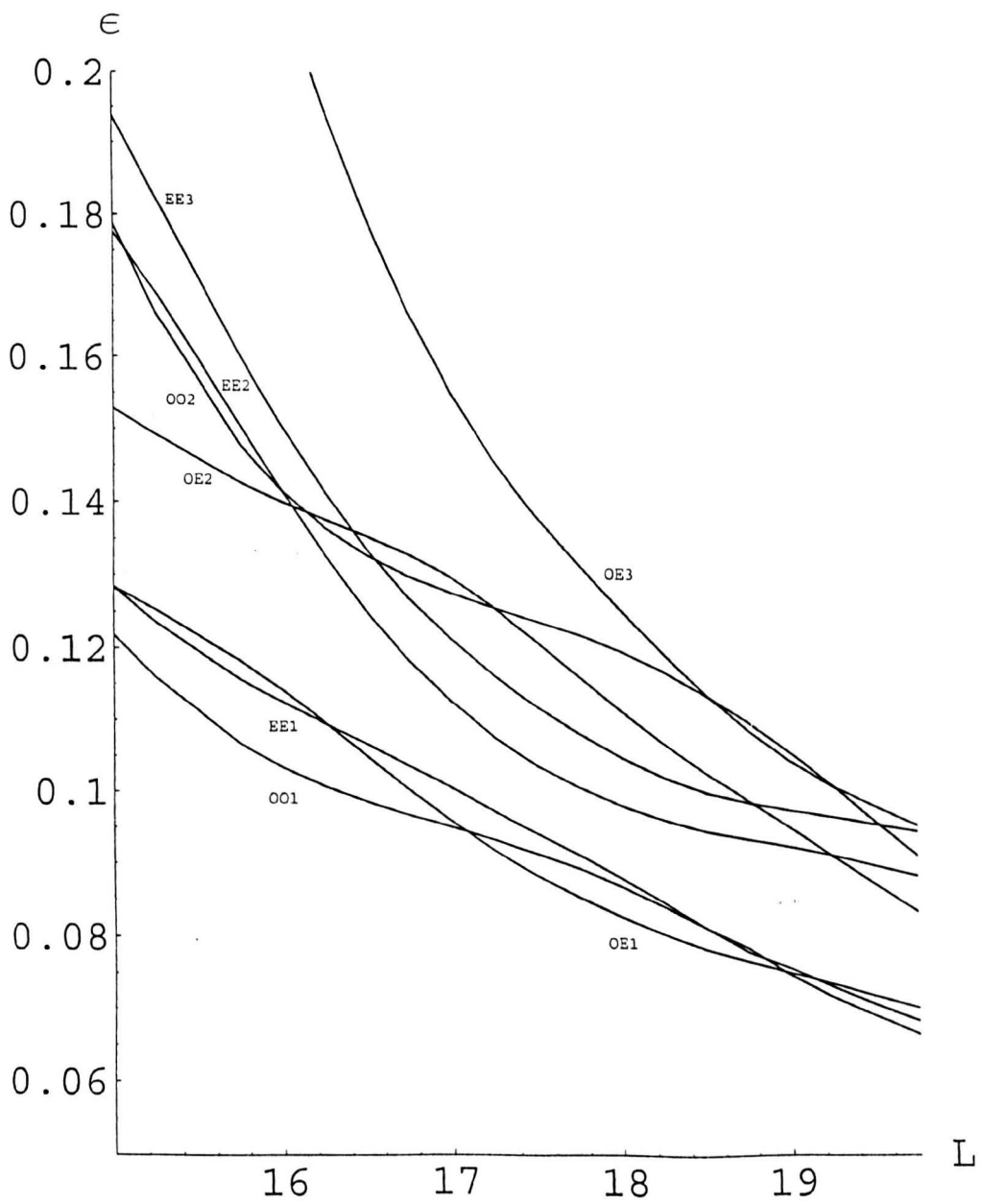


Figure 2.9: The first eight branches of the eigenvalues ϵ as functions of L in the region $15 < L < 20$ obtained using a 40×40 grid.

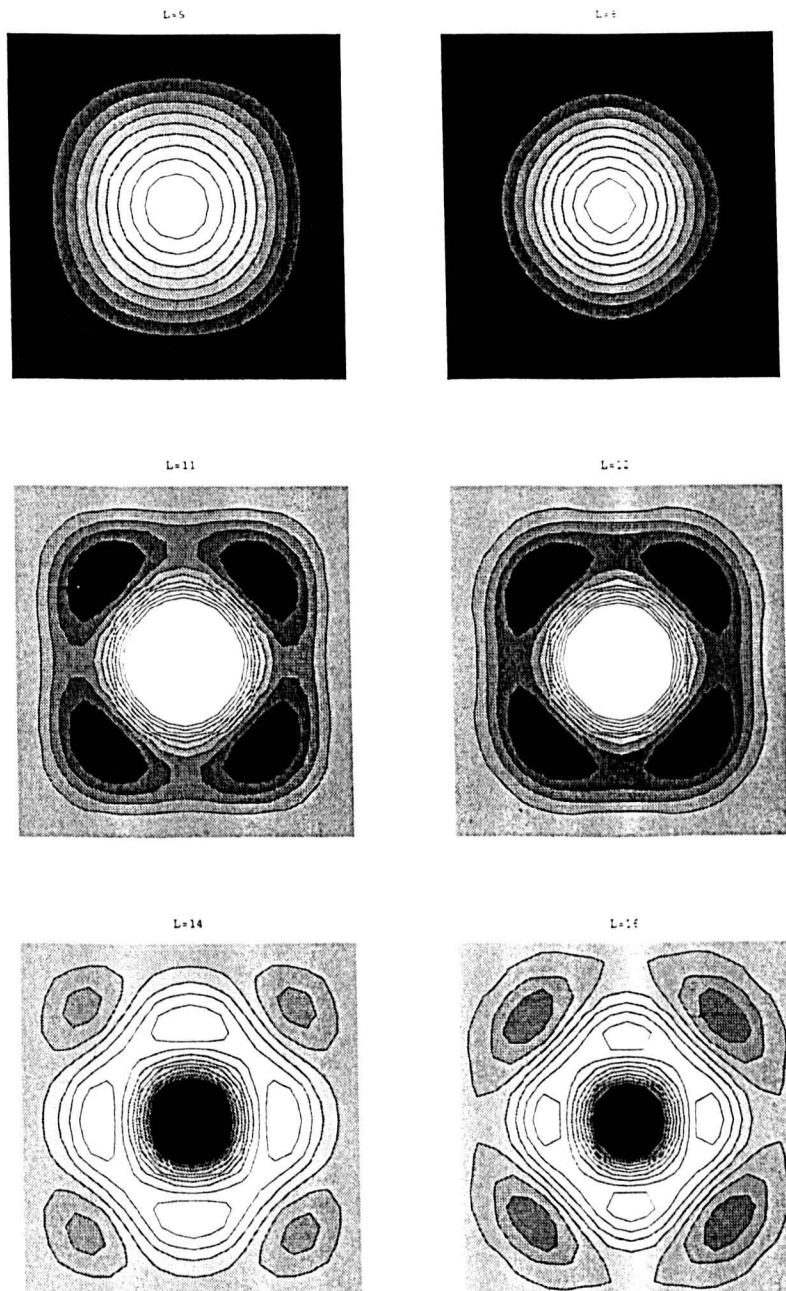


Figure 2.10: Sequence of patterns on branch EE1 for $L = 5, 8, 11, 12, 14, 16$.

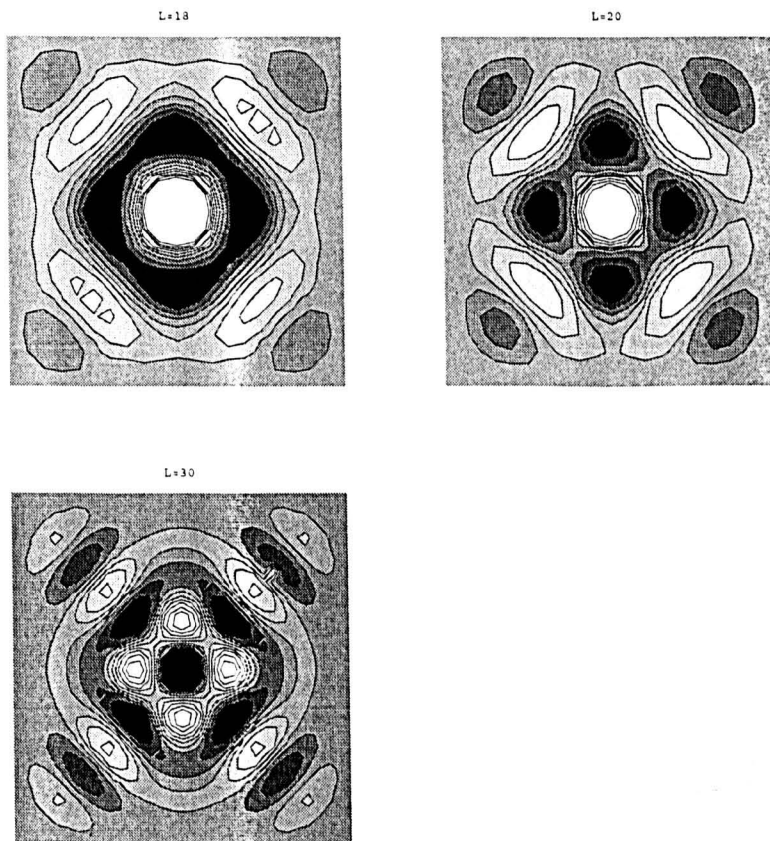


Figure 2.11: Sequence of patterns on branch EE1 for $L = 18, 20, 30$.

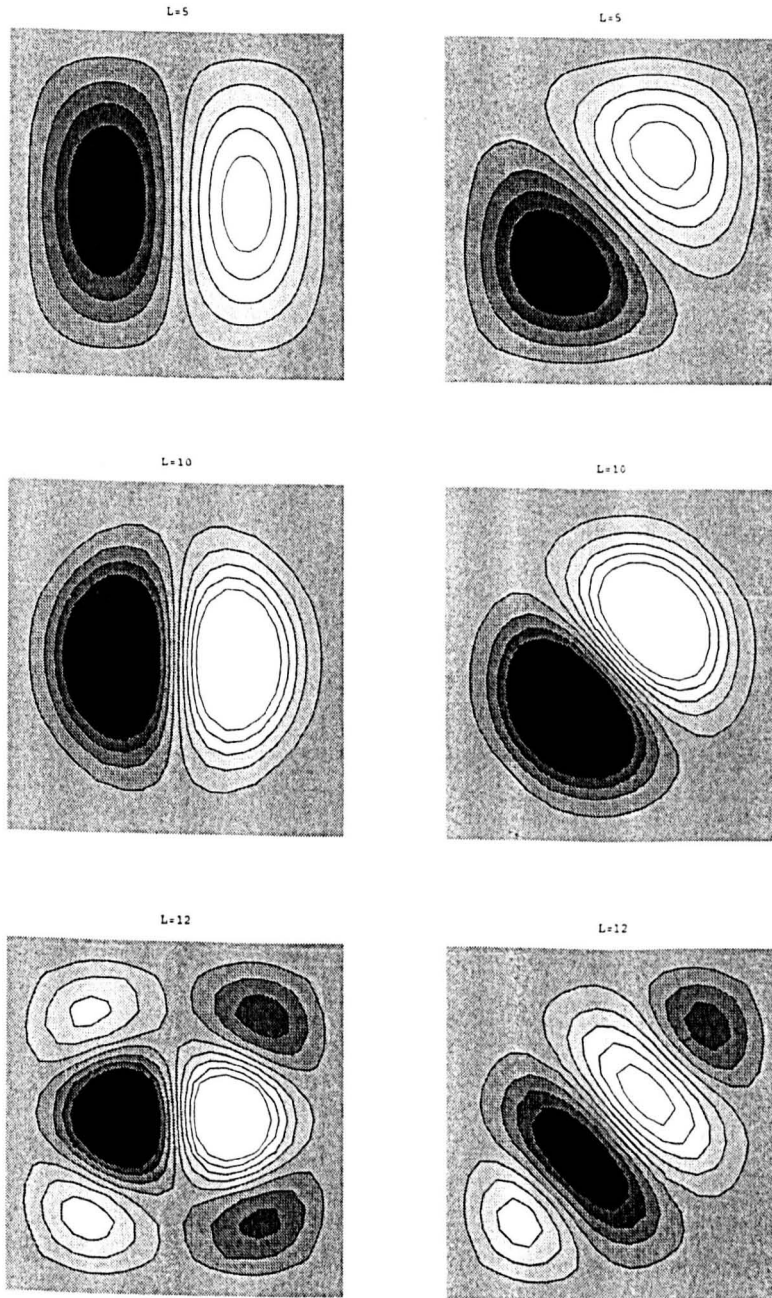


Figure 2.12: Sequence of patterns on branch OE1 for $L = 5, 10, 12$. The OE solution u_1 is shown on the left and the diagonal solution u_3 on the right.

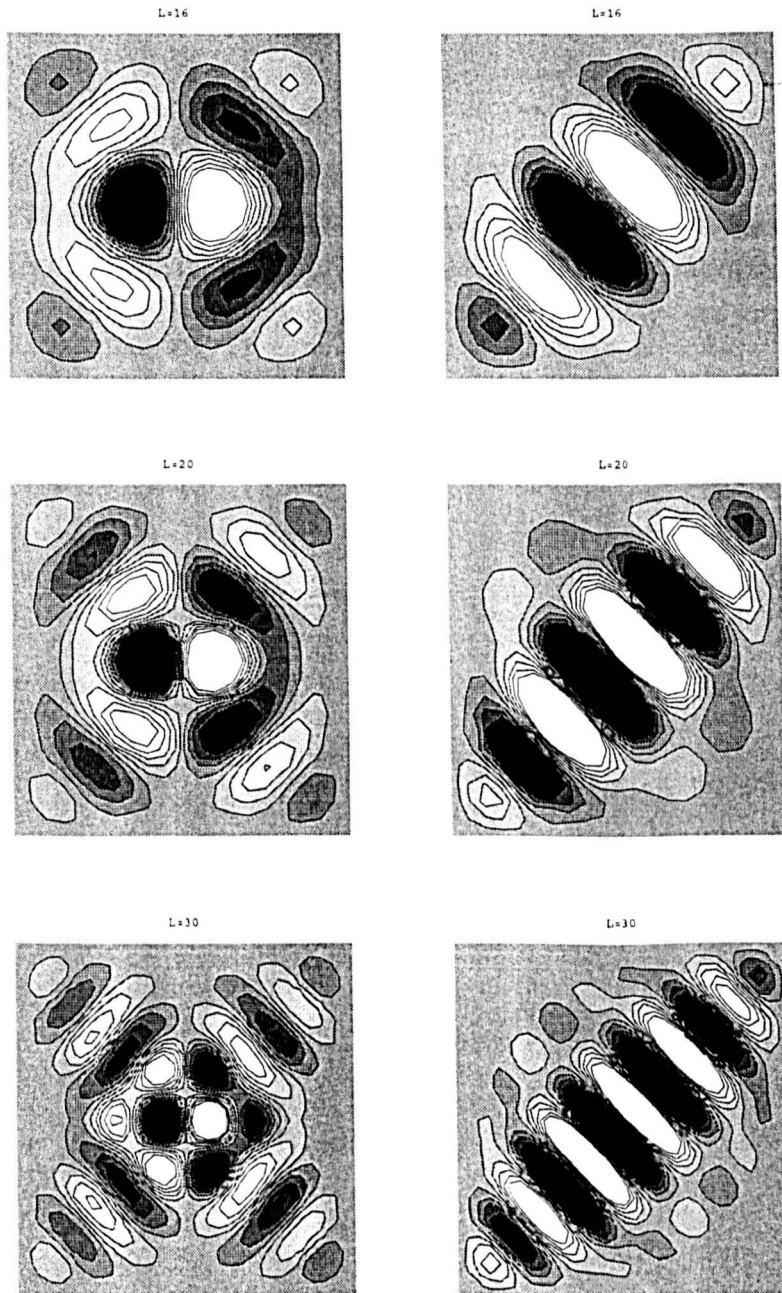


Figure 2.13: Sequence of patterns on branch OE1 for $L = 16, 20, 30$. The OE solution u_1 is shown on the left and the diagonal solution u_3 on the right.

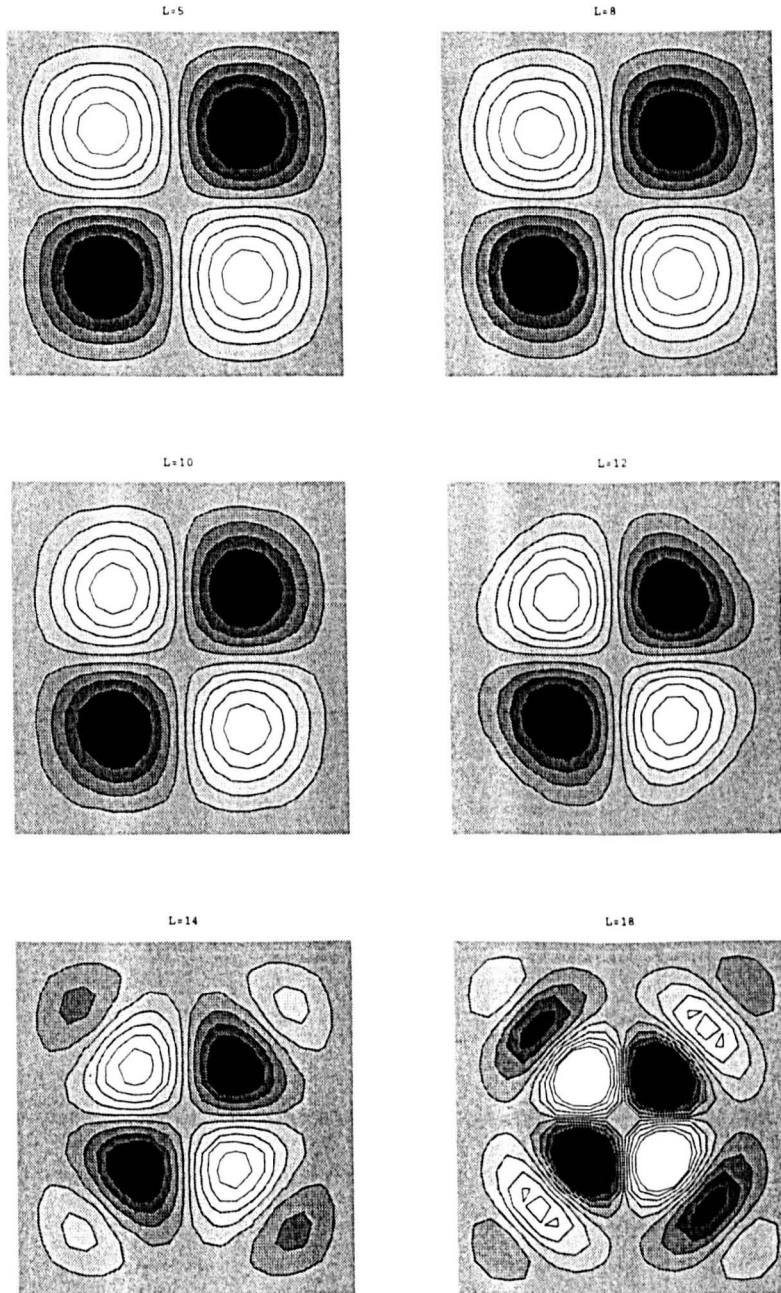


Figure 2.14: Sequence of patterns on branch OO1 for $L = 5, 8, 10, 12, 14, 18$.

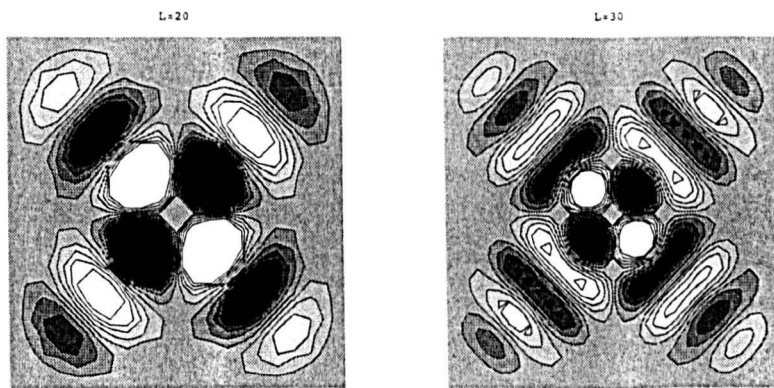


Figure 2.15: Sequence of patterns on branch OO1 for $L = 20, 30$.

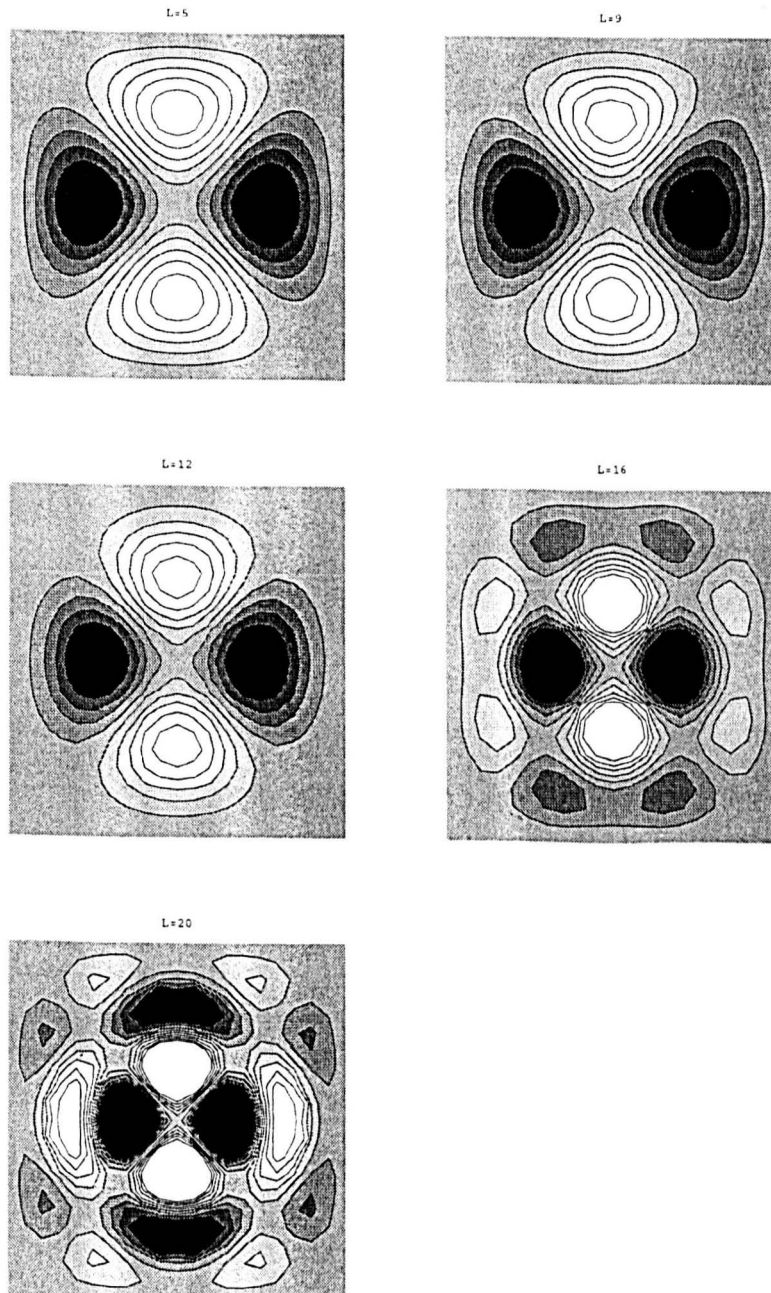


Figure 2.16: Sequence of patterns on branch EE2 for $L = 5, 9, 12, 16, 20$.

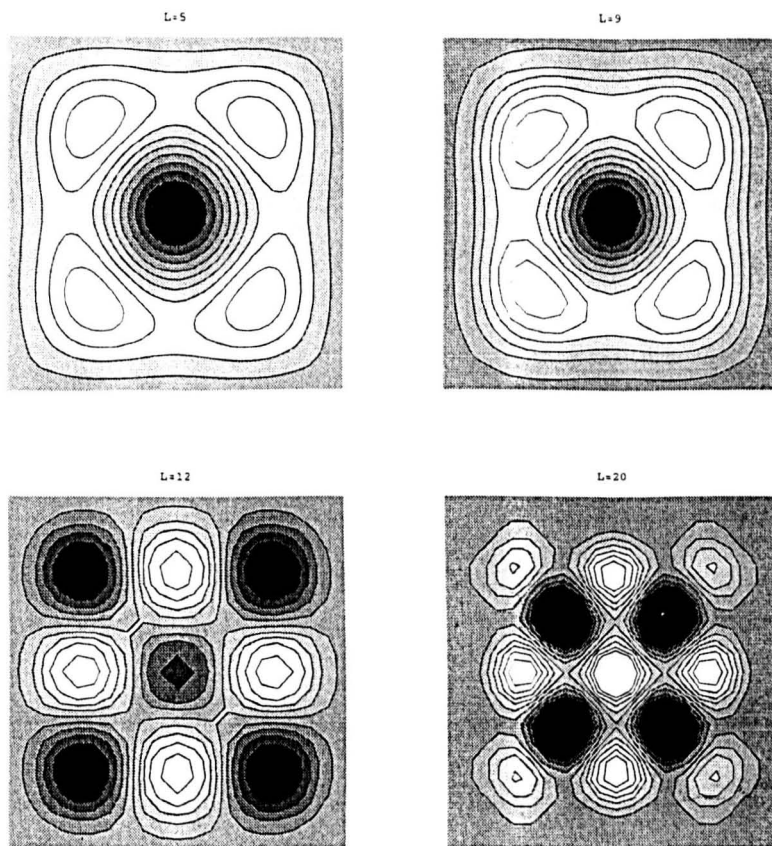


Figure 2.17: Sequence of patterns on branch EE3 for $L = 5, 9, 12, 20$.

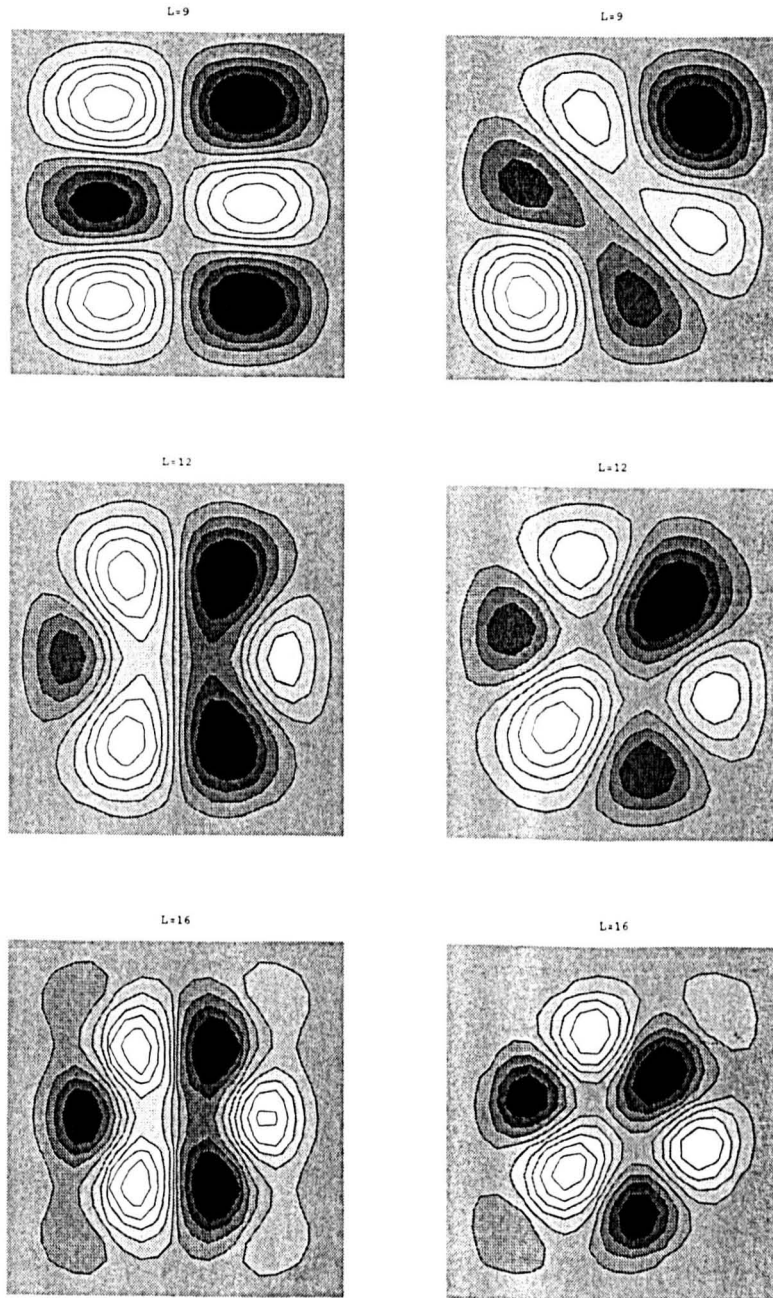


Figure 2.18: Sequence of patterns on branch OE2 for $L = 9, 12, 16$. The OE solution u_1 is shown on the left and the diagonal solution u_3 on the right.

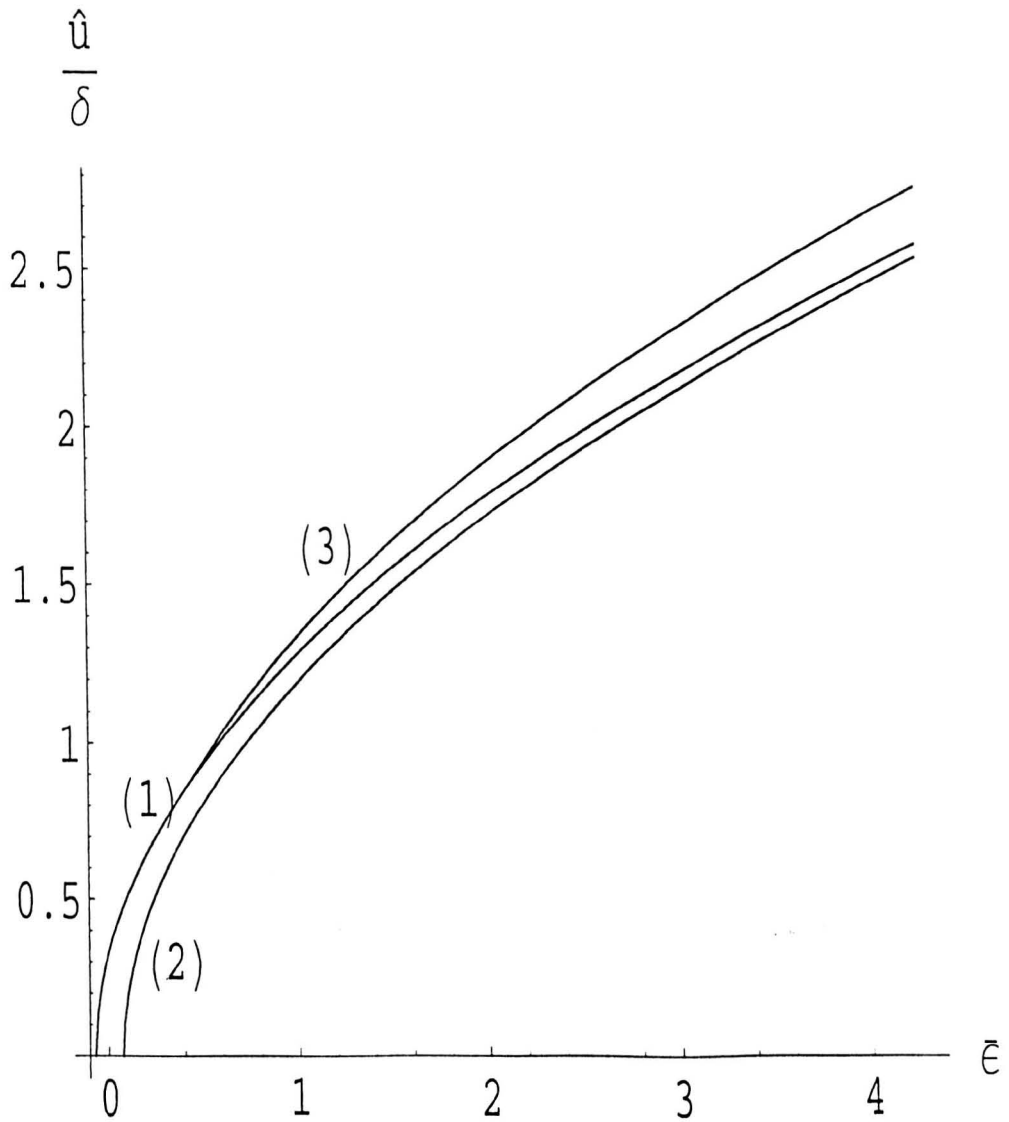


Figure 2.19: Bifurcation diagram for the case $m = 3$, $n = 1$, $L = 5$ where $k = 0.07244$. Branch (1) corresponds to the solutions $a_s = -b_s$, branch (2) corresponds to the solutions $a_s = b_s$ and branch (3) corresponds to the solutions given by (2.119), (2.120).

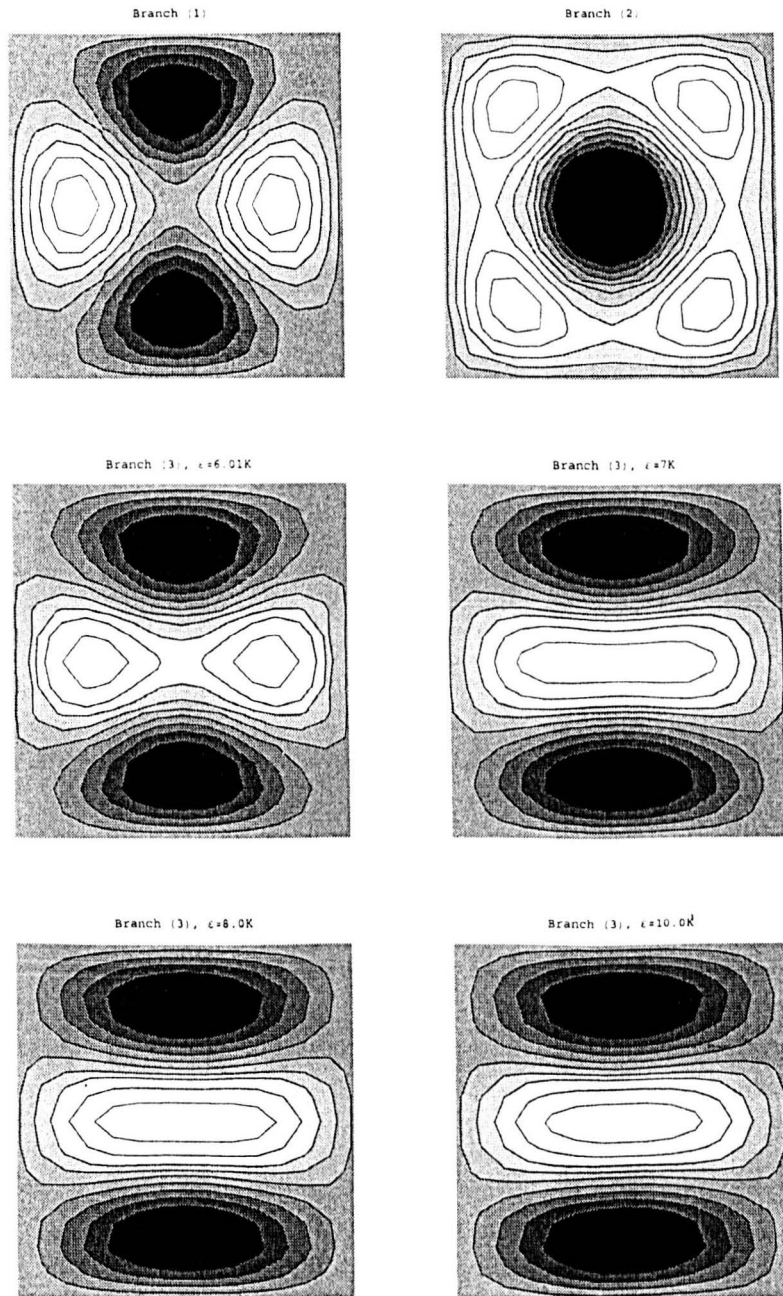


Figure 2.20: Contours of u on the various branches of Figure 2.19. The patterns on branch (3) are shown for various values of $\bar{\epsilon}$, whereas those on branches (1) and (2) are independent of $\bar{\epsilon}$.

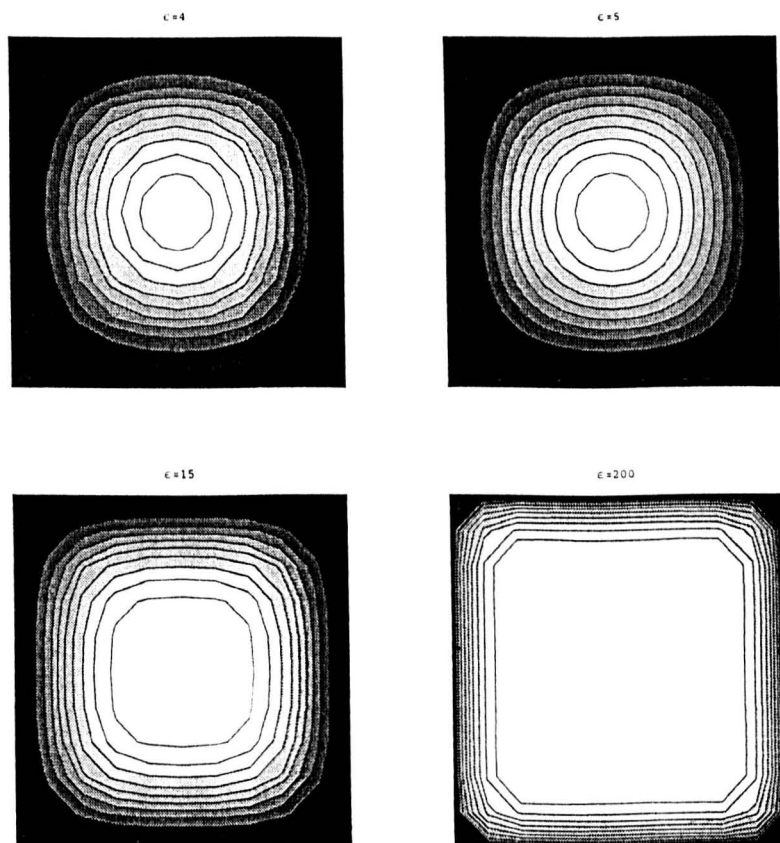


Figure 2.21: Contours of steady-state solutions u for $L = 5$, obtained with an initial state $U(x, y) = x(L - x)y(L - y)$.

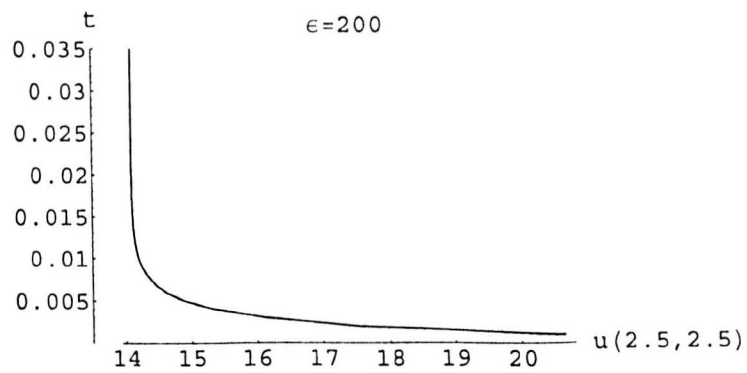
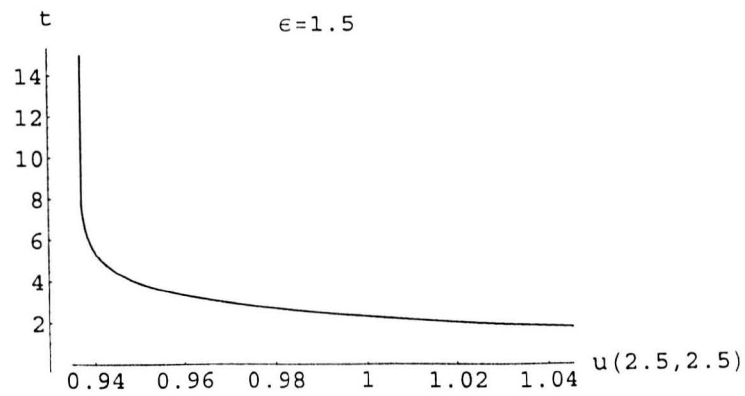


Figure 2.22: Time evolution of two steady-state solutions of the type shown in Figure 2.21.

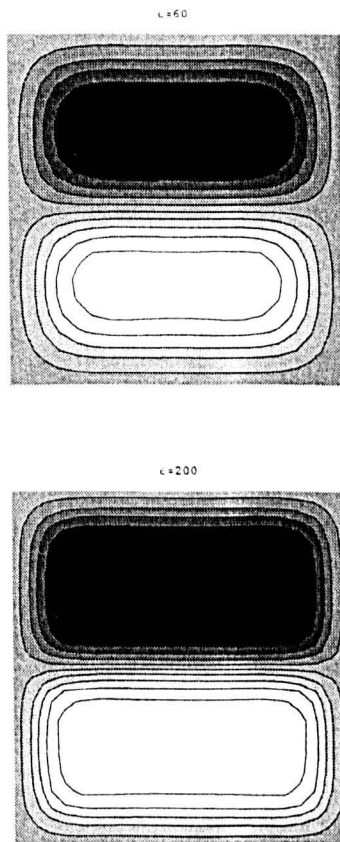


Figure 2.23: Contours of steady-state solutions u for $L = 5$, obtained with an initial state $U(x, y) = \sin\left(\frac{\pi x}{L}\right) \sin\left(\frac{2\pi y}{L}\right)$.

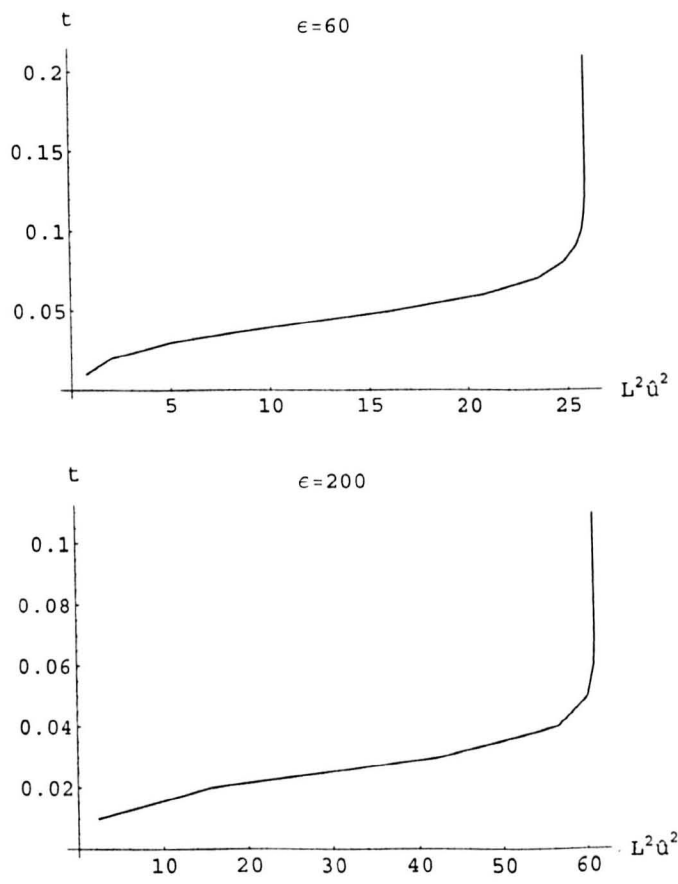


Figure 2.24: Time evolution of the steady-state solutions shown in Figure 2.23.

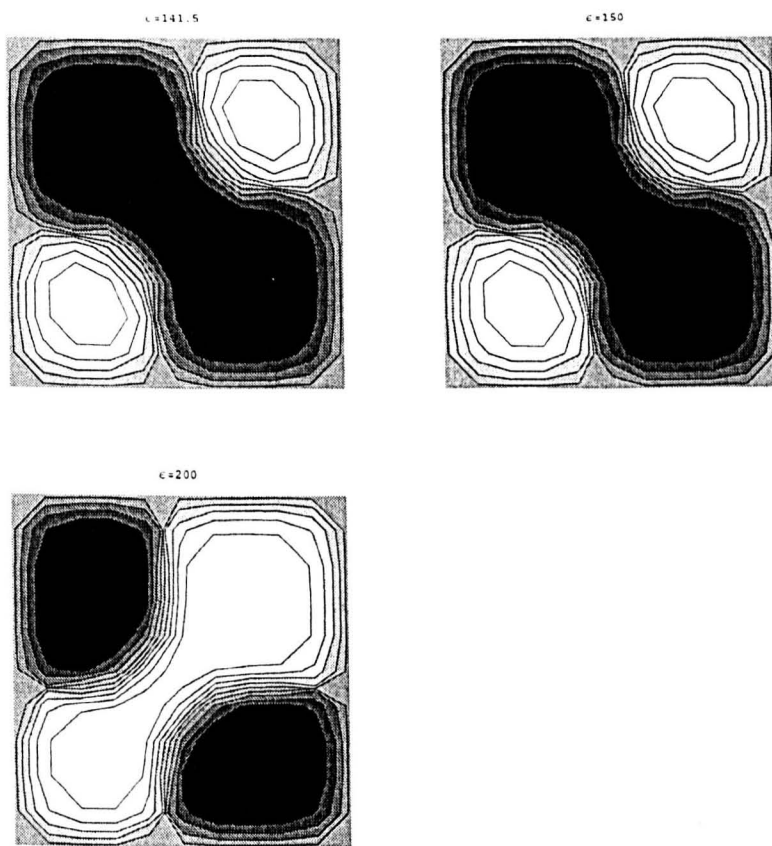


Figure 2.25: Contours of steady-state solutions u for $L = 5$, obtained with an initial state $U(x, y) = \sin\left(\frac{2\pi x}{L}\right) \sin\left(\frac{2\pi y}{L}\right)$.

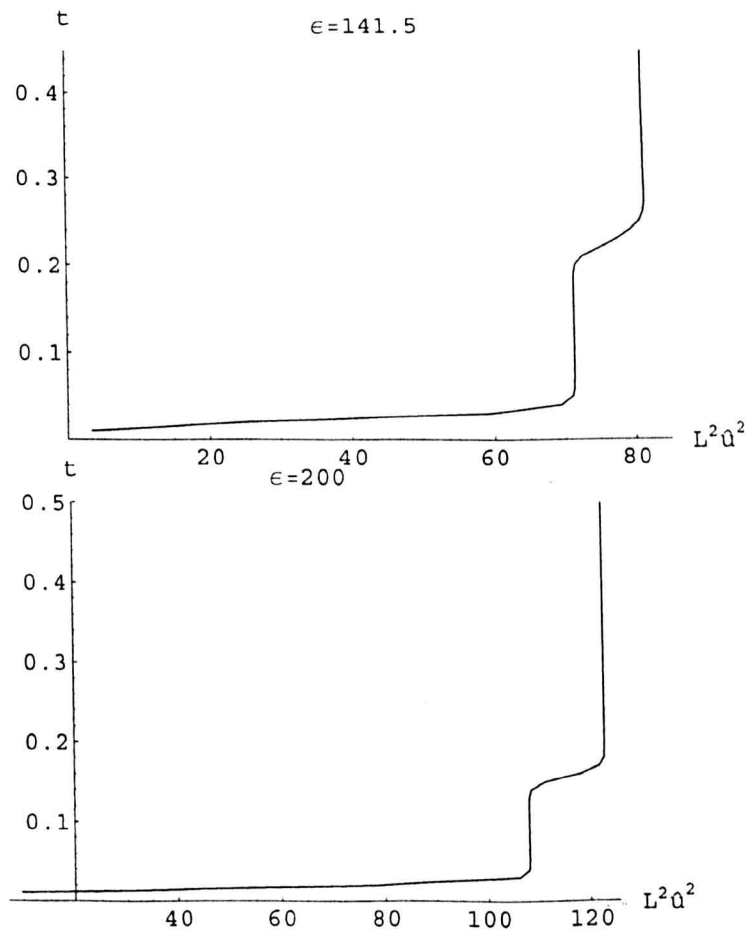


Figure 2.26: Time evolution of two of the steady-state solutions shown in Figure 2.25.

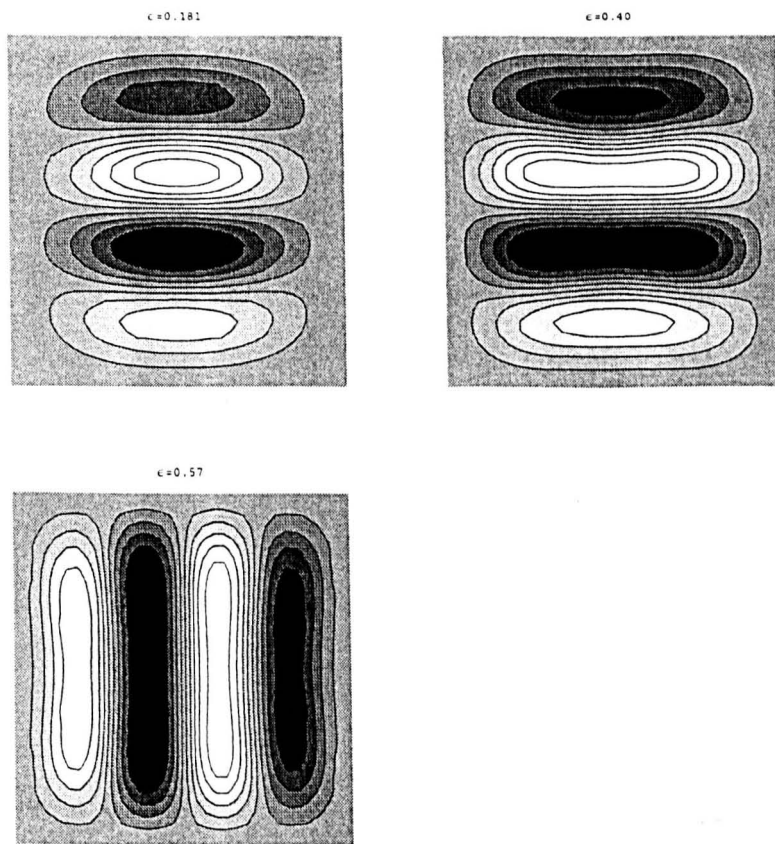


Figure 2.27: Contours of steady-state solutions u for $L = 5\pi$, obtained with an initial state $U(x, y) = R(i, j)$.

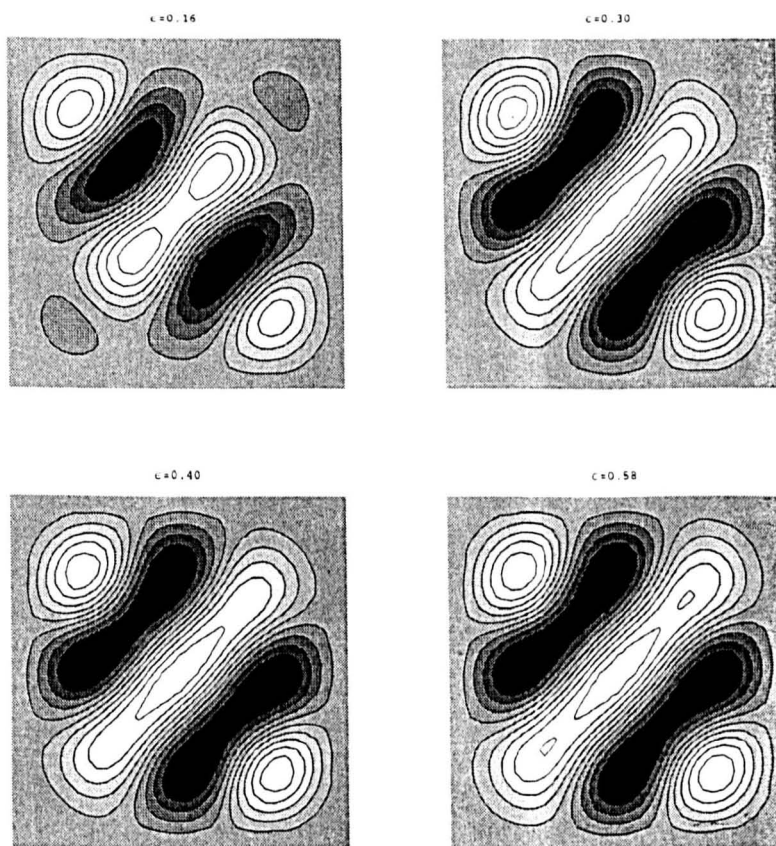


Figure 2.28: Contours of steady-state solutions u for $L = 5\pi$, obtained with an initial state $U(x, y) = R(i, j)$.

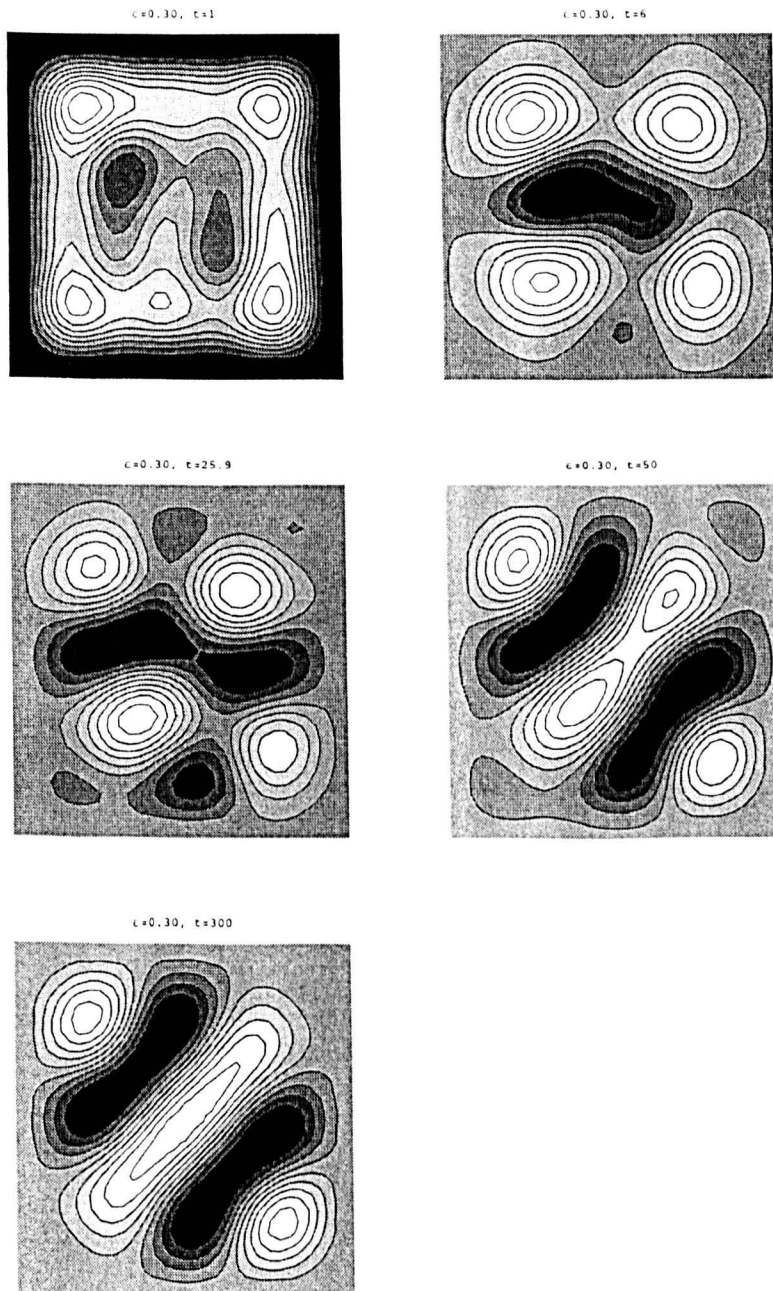


Figure 2.29: Contours of u at various times t in the evolution leading to the steady-state solution for $\epsilon = 0.30$ shown in Figure 2.28 .

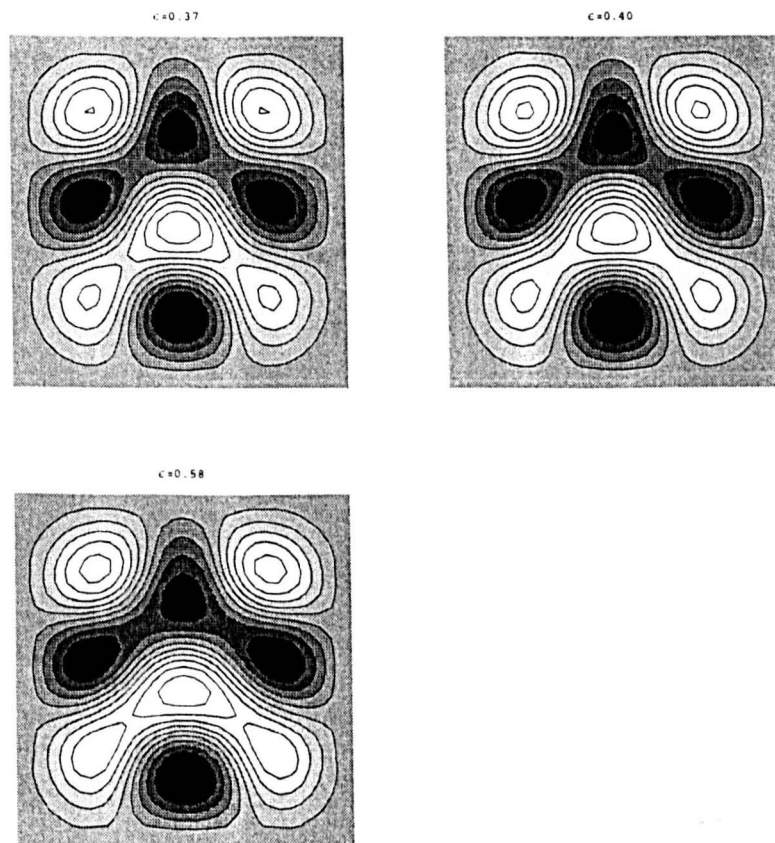


Figure 2.30: Contours of steady-state solutions u for $L = 5\pi$, obtained with an initial state $U(x, y) = |R(i, j)|$.

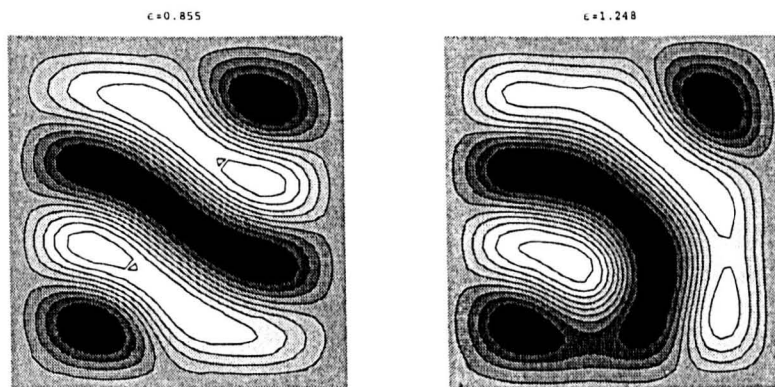


Figure 2.31: Contours of steady-state solutions u for $L = 5\pi$, obtained with an initial state $U(x, y) = R(i, j)$.

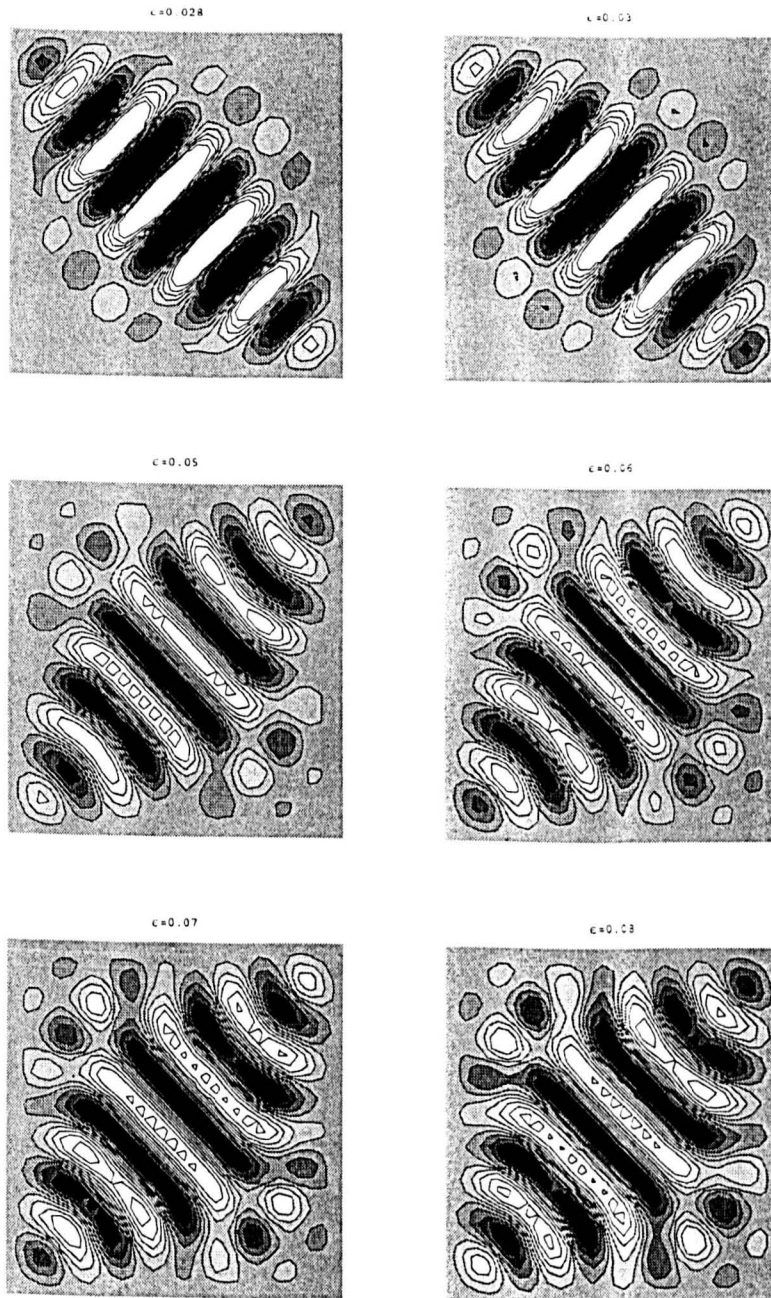


Figure 2.32: Contours of steady-state solutions u for $L = 30$, obtained with an initial state $U(x, y) = R(i, j)$.

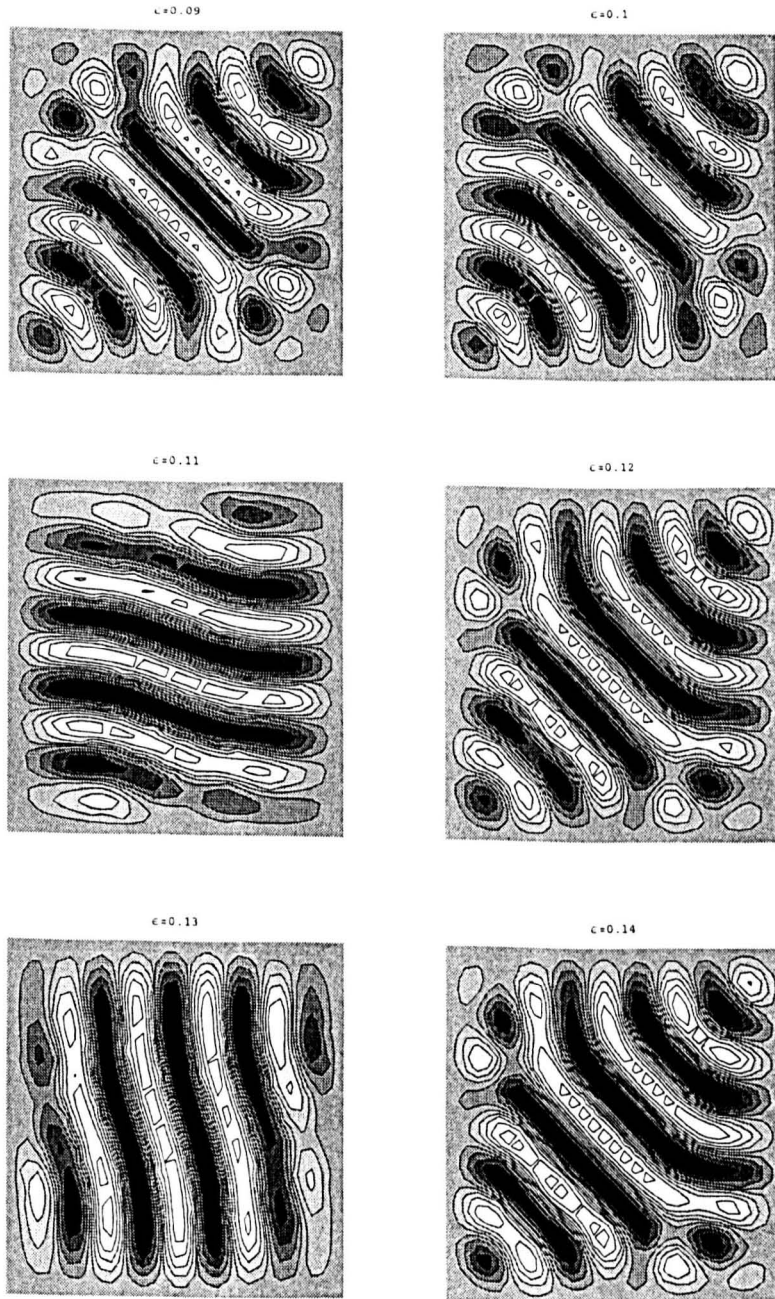


Figure 2.33: Contours of steady-state solutions u for $L = 30$, obtained with an initial state $U(x, y) = R(i, j)$.

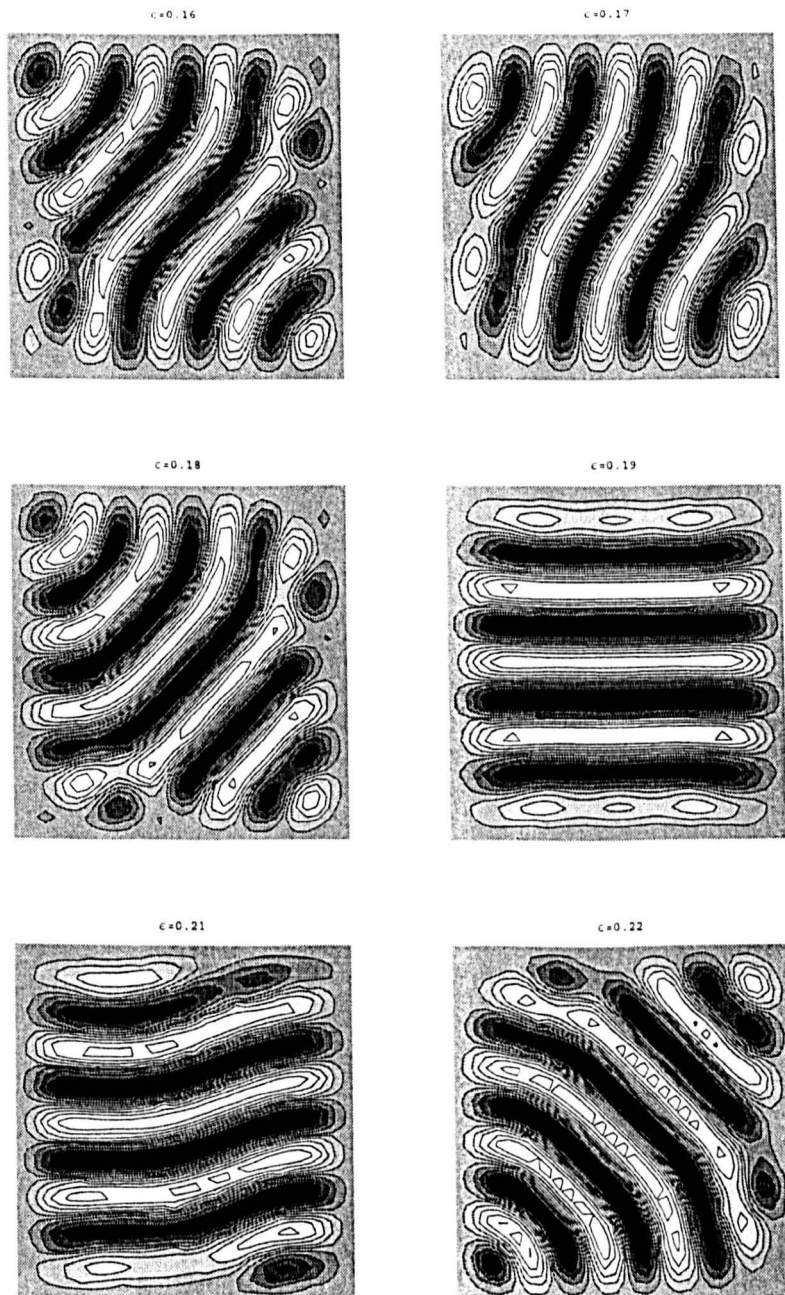


Figure 2.34: Contours of steady-state solutions u for $L = 30$, obtained with an initial state $U(x, y) = R(i, j)$.

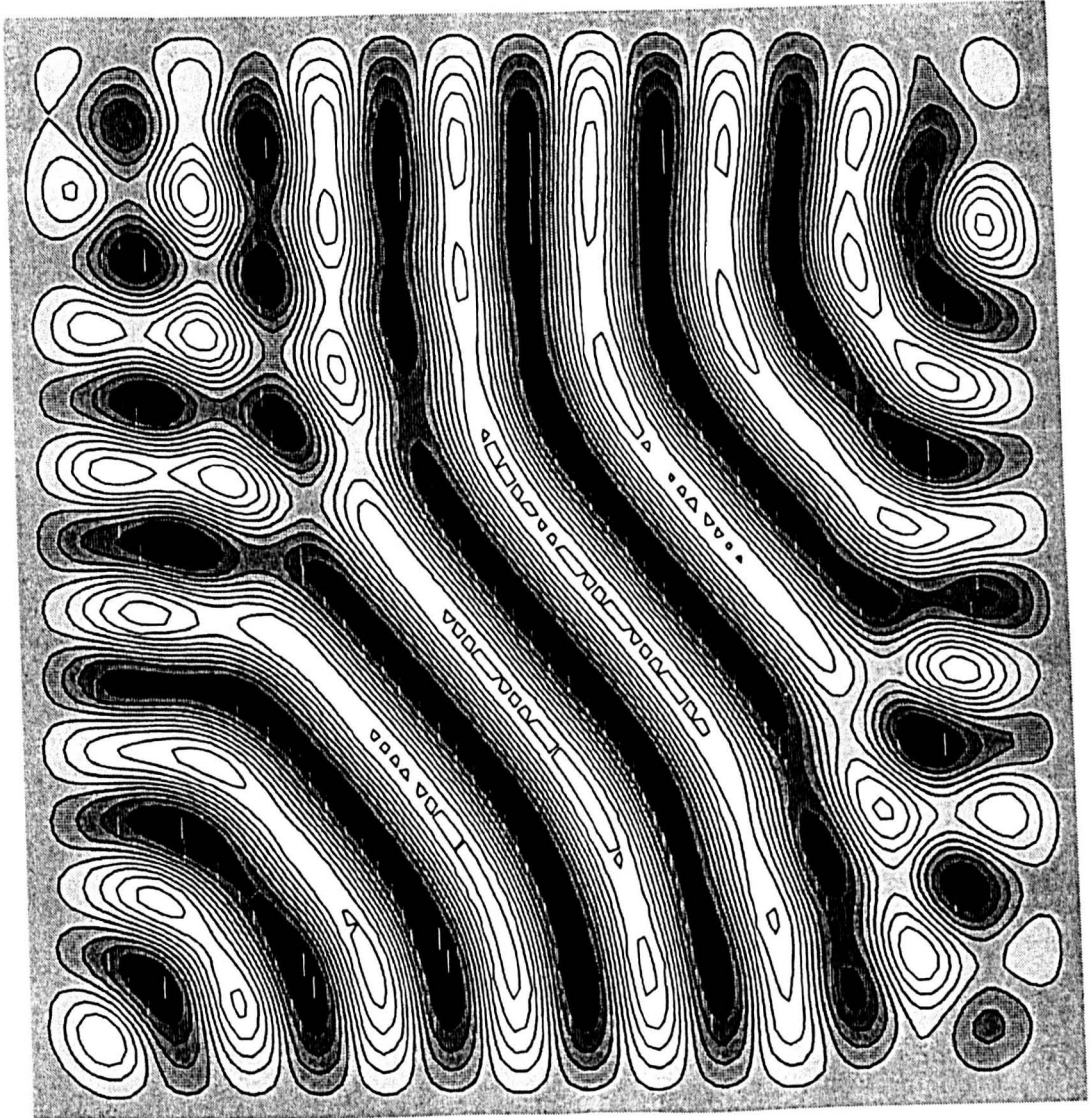


Figure 2.35: Contours of a steady-state solution u for $L = 16\pi$ and $\varepsilon = 0.1$, obtained with an initial state $U(x, y) = R(i, j)$.

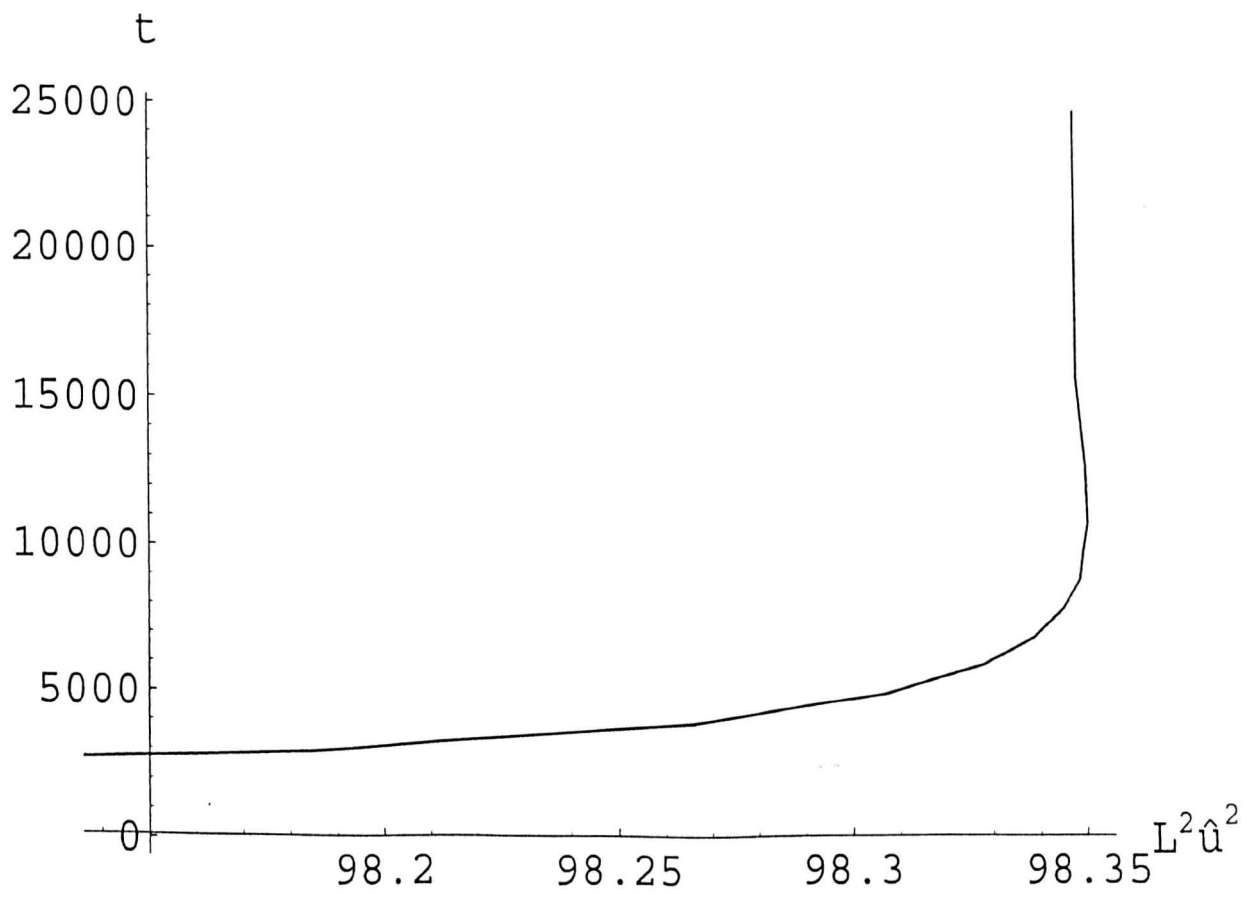


Figure 2.36: Time evolution of the steady-state solution shown in Figure 2.35.

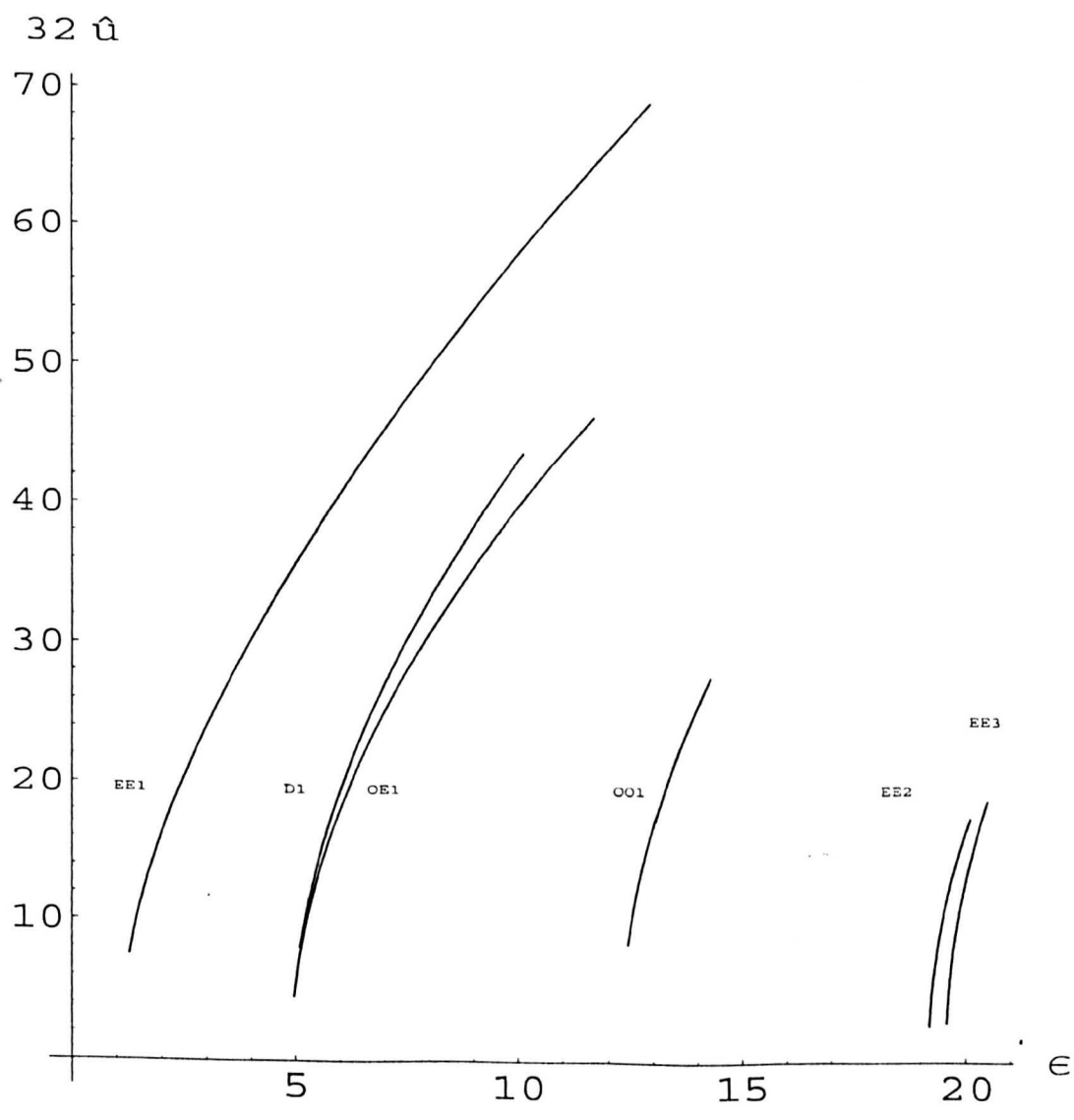


Figure 2.37: Bifurcation diagram for the case $L = 5$.

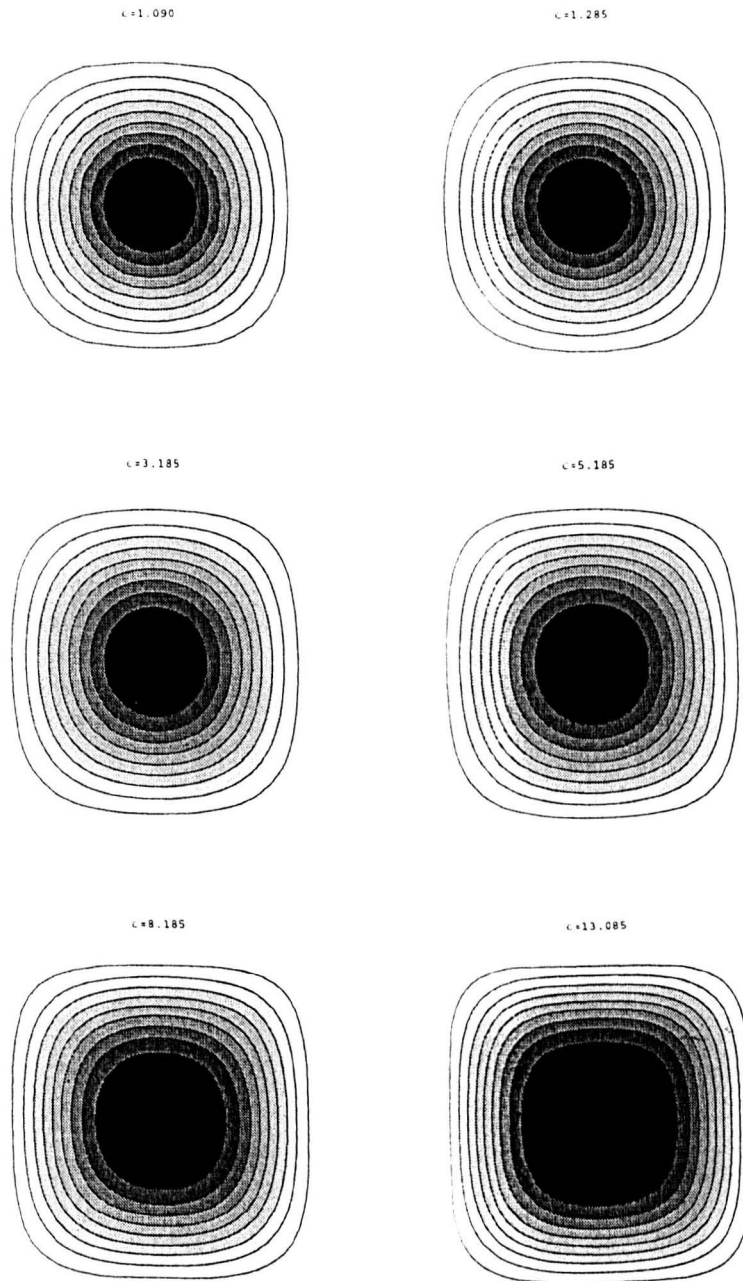


Figure 2.38: Contour plots of solutions u on branch EE1 for increasing ϵ and $L = 5$.

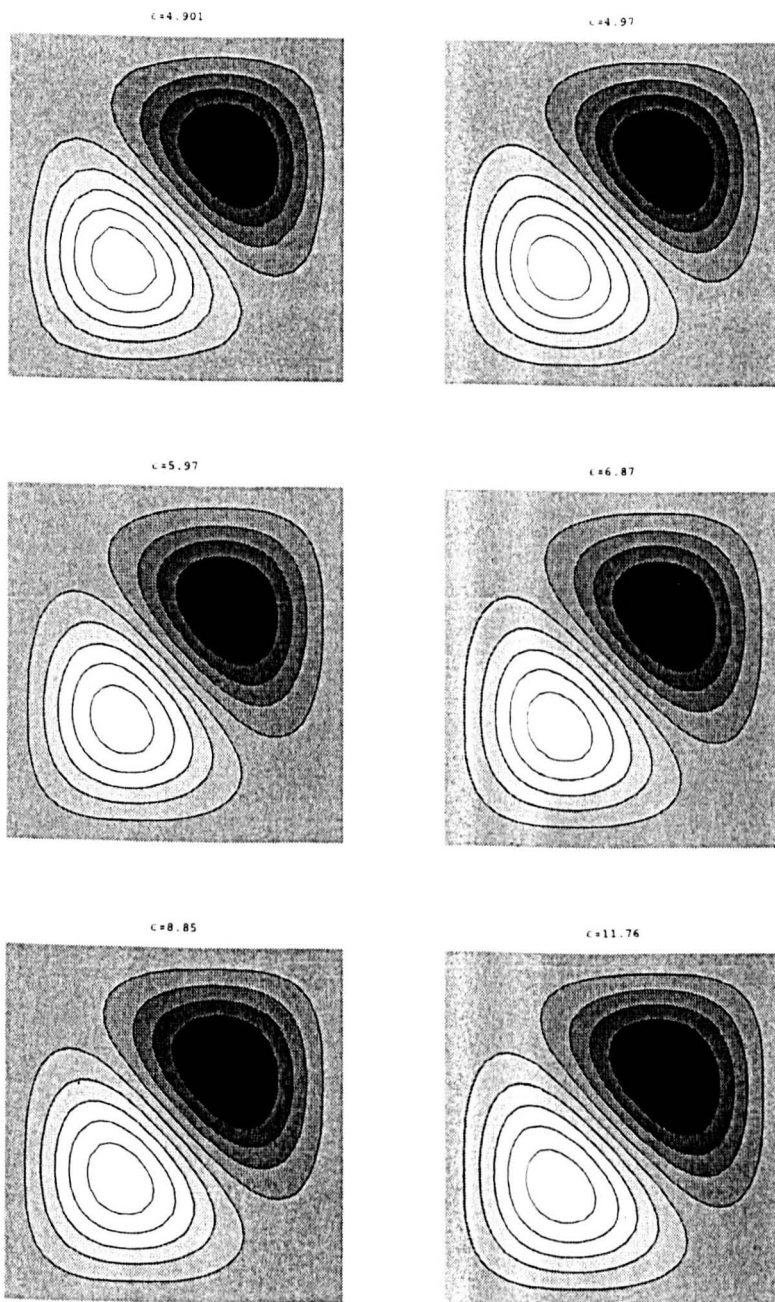


Figure 2.39: Contour plots of solutions u on branch D1 for increasing ϵ and $L = 5$.

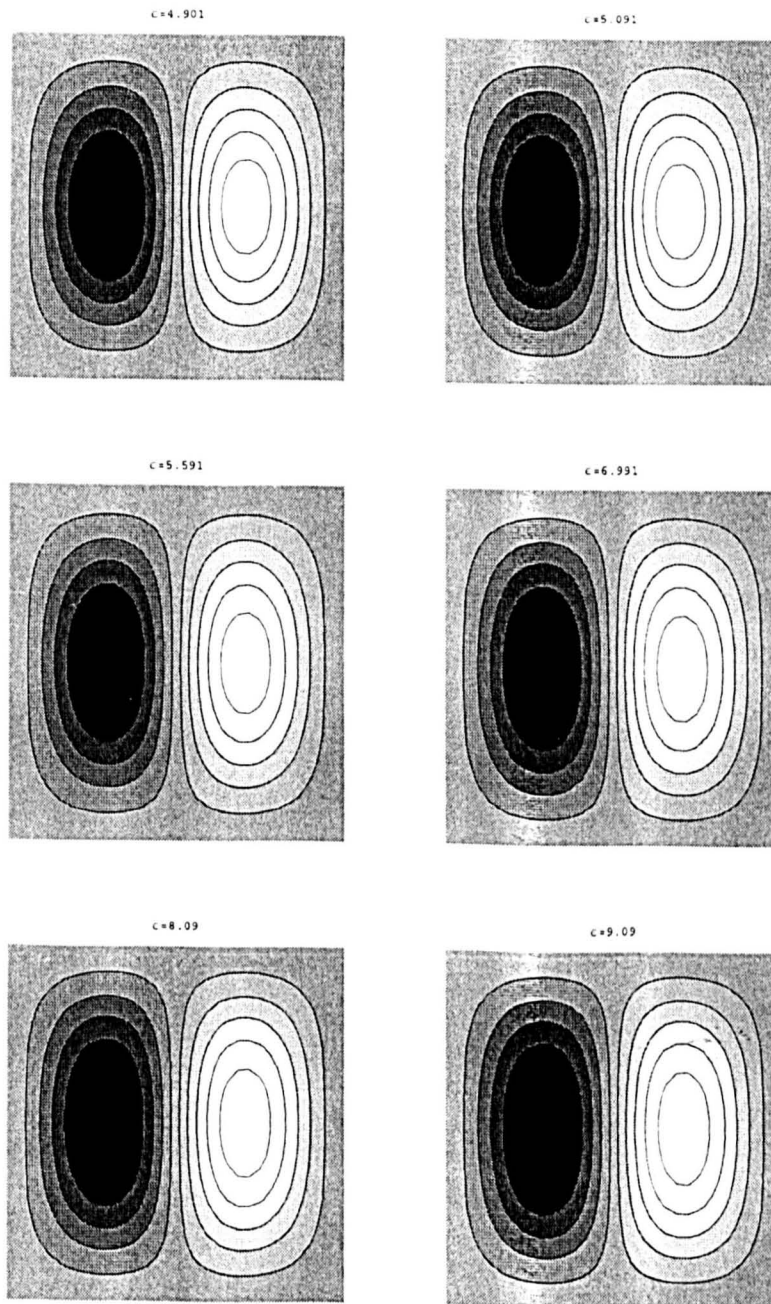


Figure 2.40: Contour plots of solutions u on branch OE1 for increasing ε and $L = 5$.

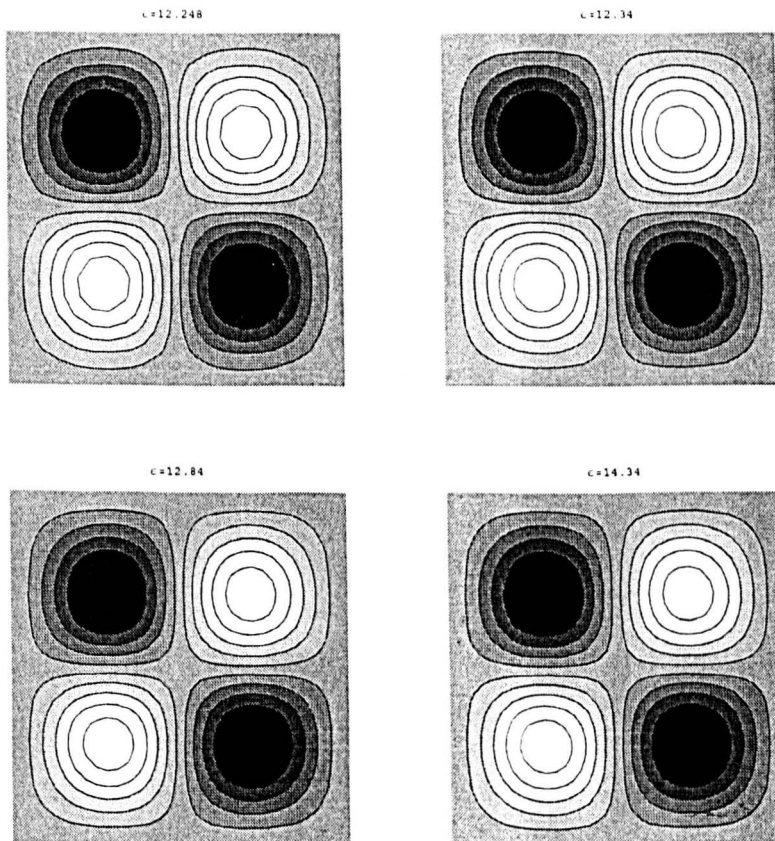


Figure 2.41: Contour plots of solutions u on branch OO1 for increasing ε and $L = 5$.

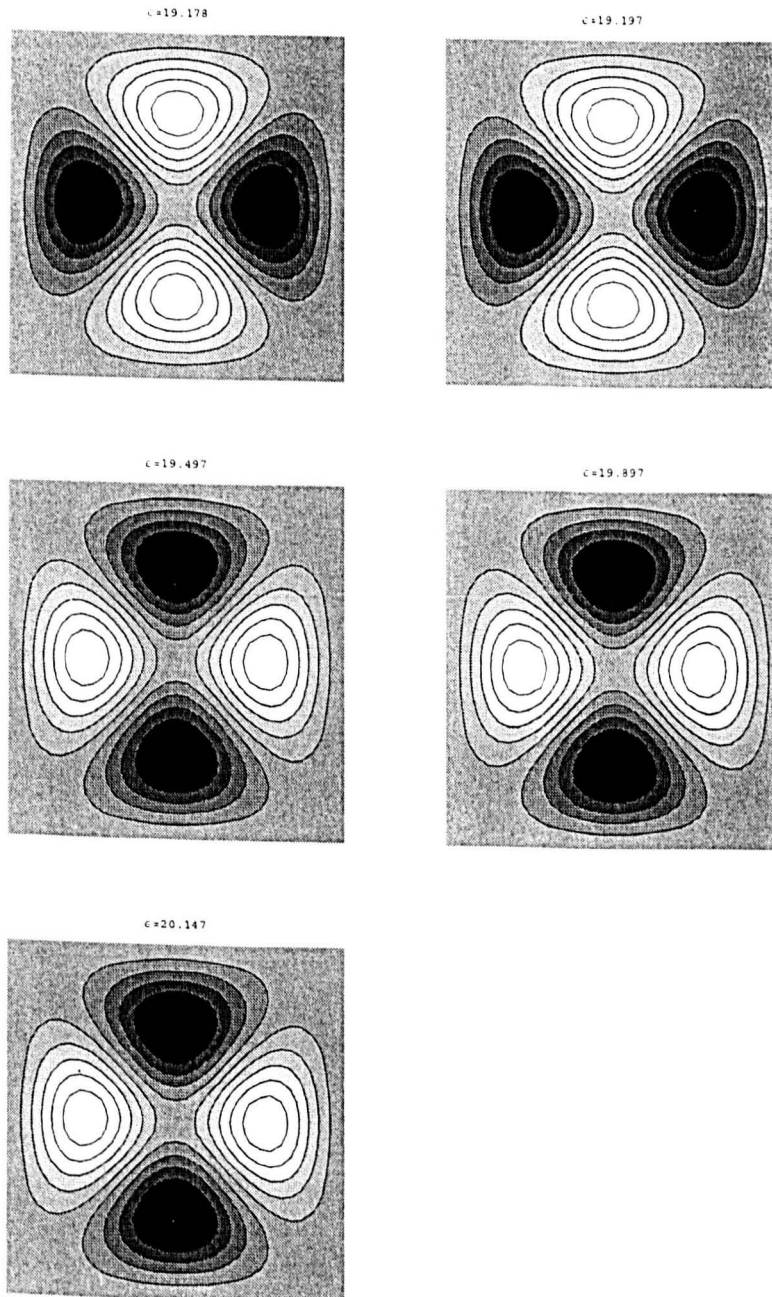


Figure 2.42: Contour plots of solutions u on branch EE2 for increasing ε and $L = 5$.

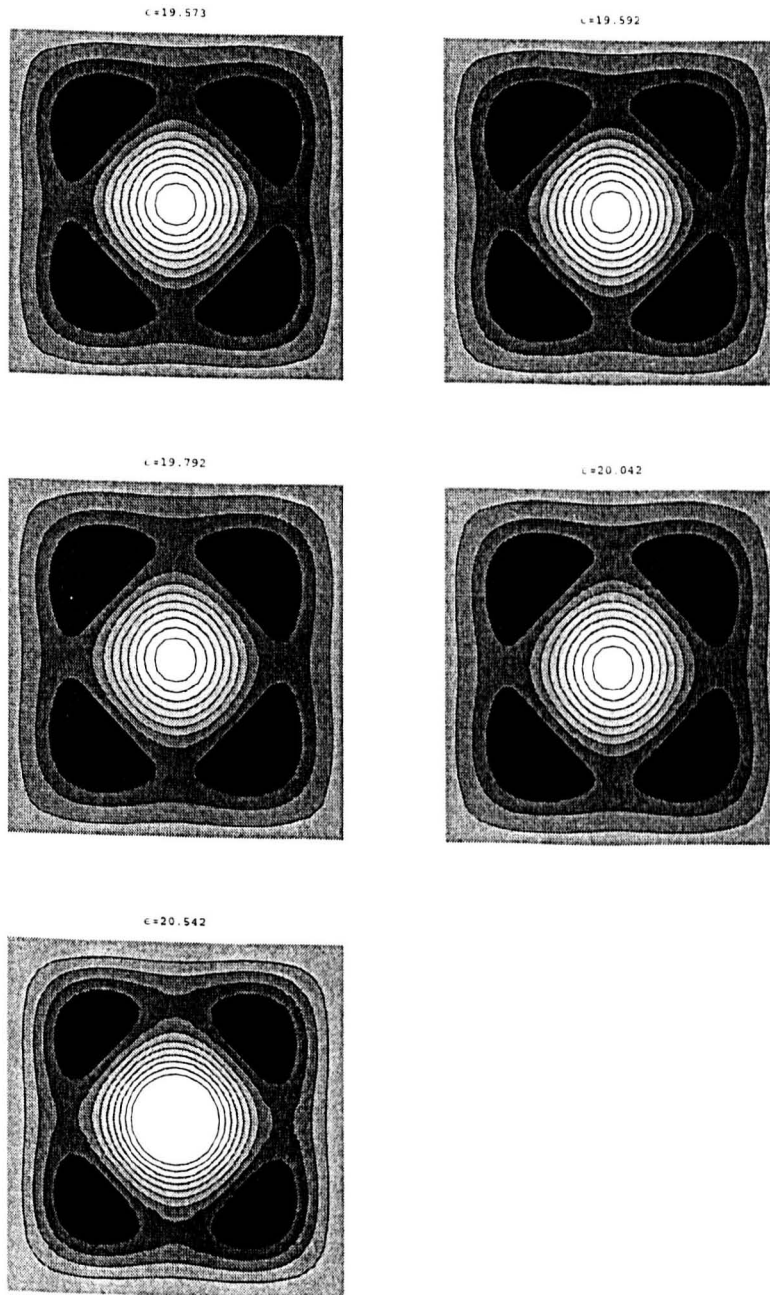


Figure 2.43: Contour plots of solutions u on branch EE3 for increasing ϵ and $L = 5$.

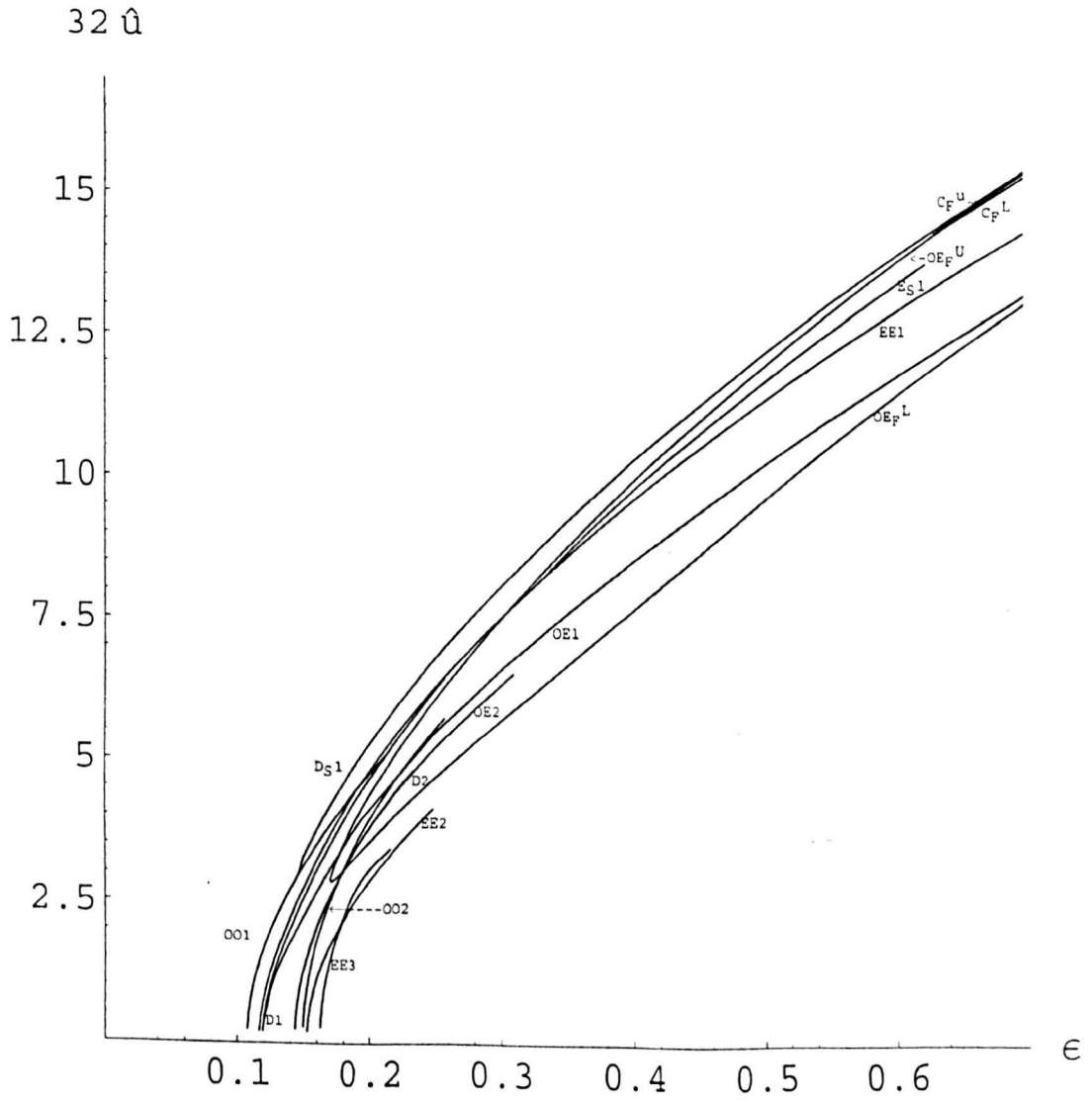


Figure 2.44: Bifurcation diagram for the case $L = 5\pi$.

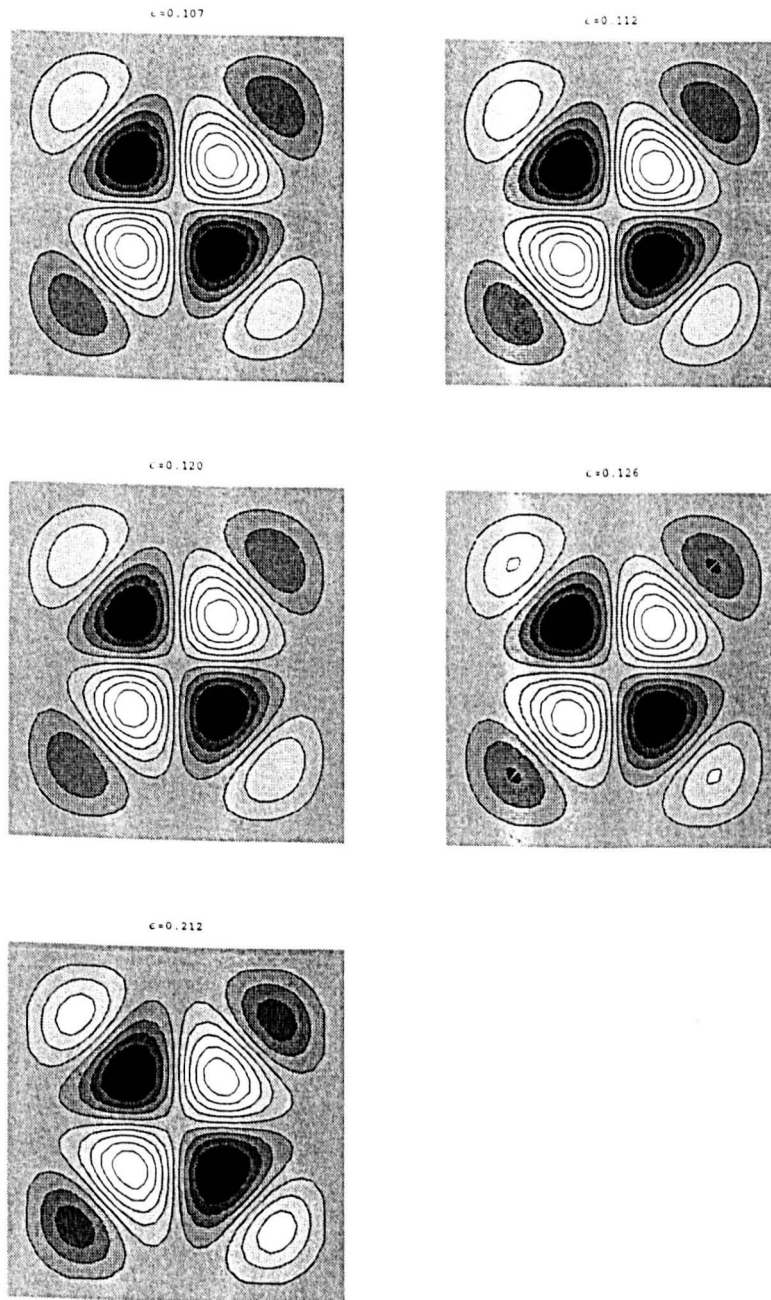


Figure 2.45: Contour plots of solutions u on branch OO1 for increasing ε and $L = 5\pi$.

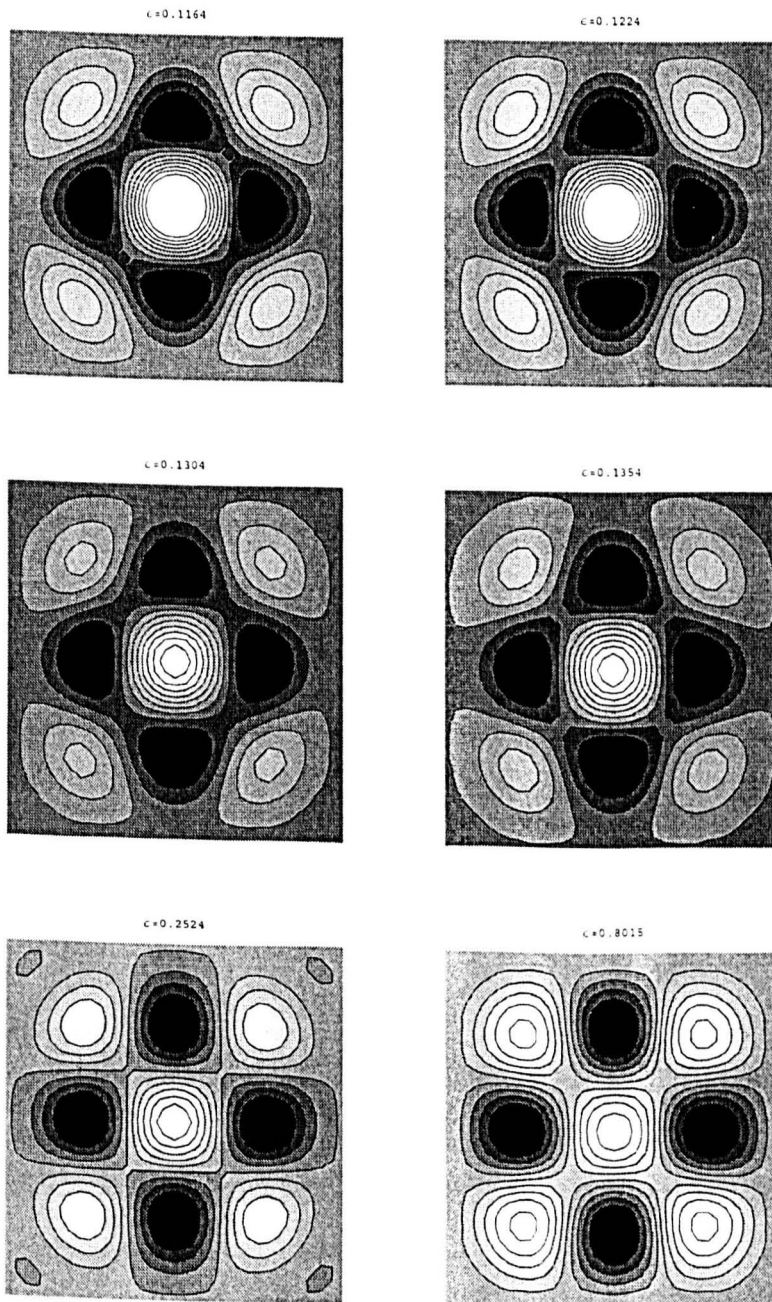


Figure 2.46: Contour plots of solutions u on branch EE1 for increasing ε and $L = 5\pi$.

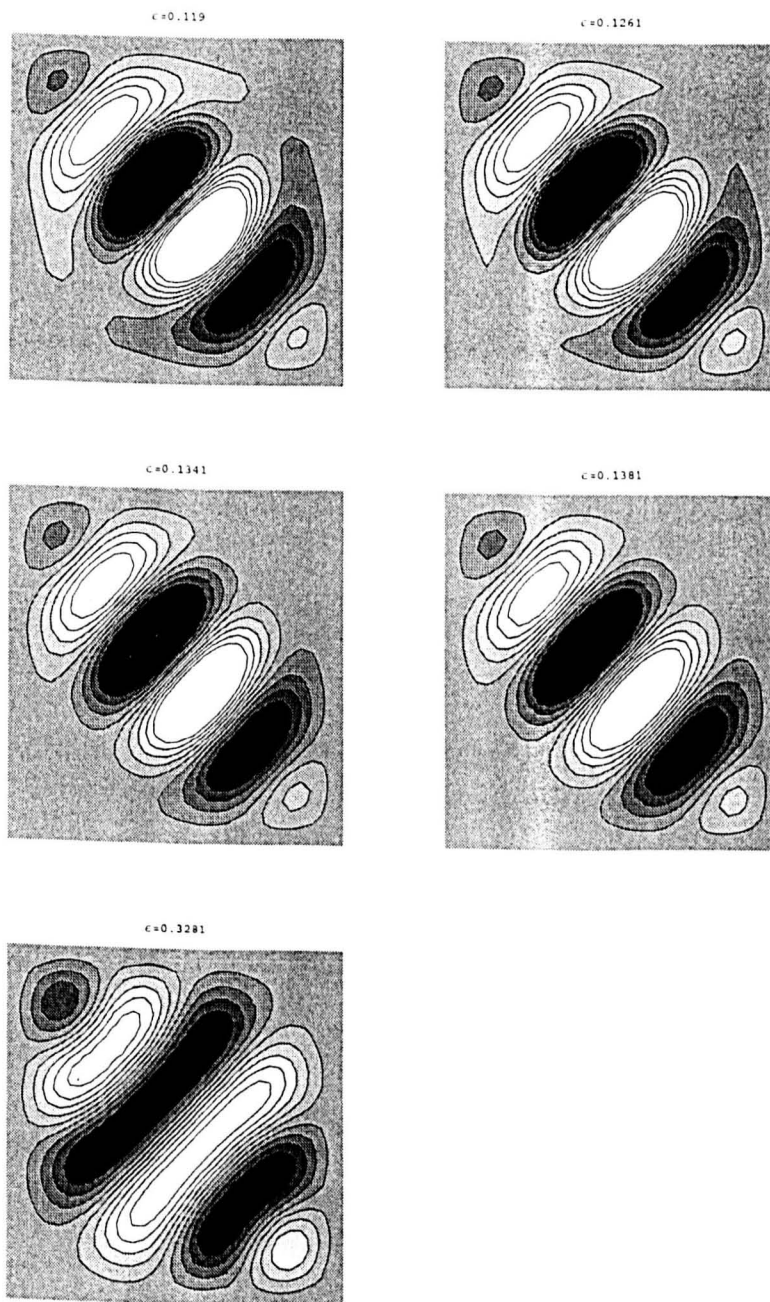


Figure 2.47: Contour plots of solutions u on branch D1 for increasing ε and $L = 5\pi$.

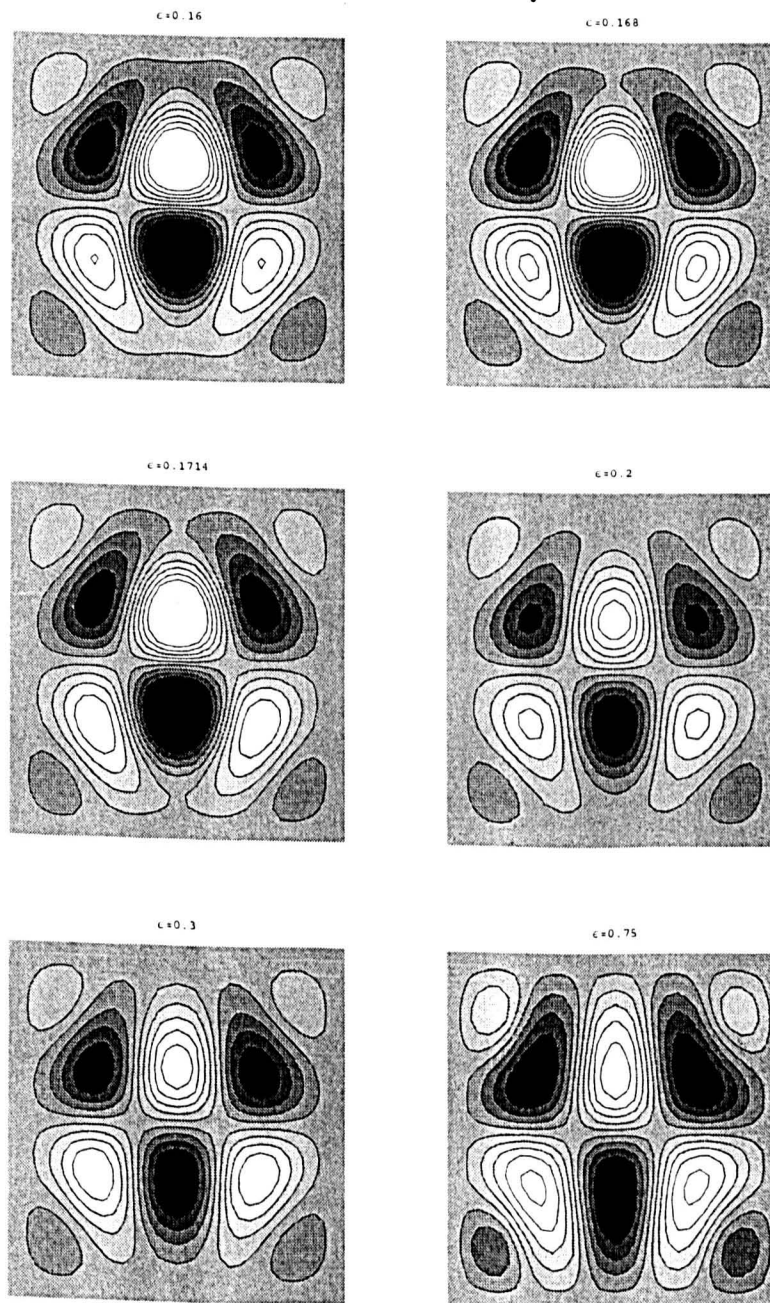


Figure 2.48: Contour plots of solutions u on branch OE1 for increasing ϵ and $L = 5\pi$.

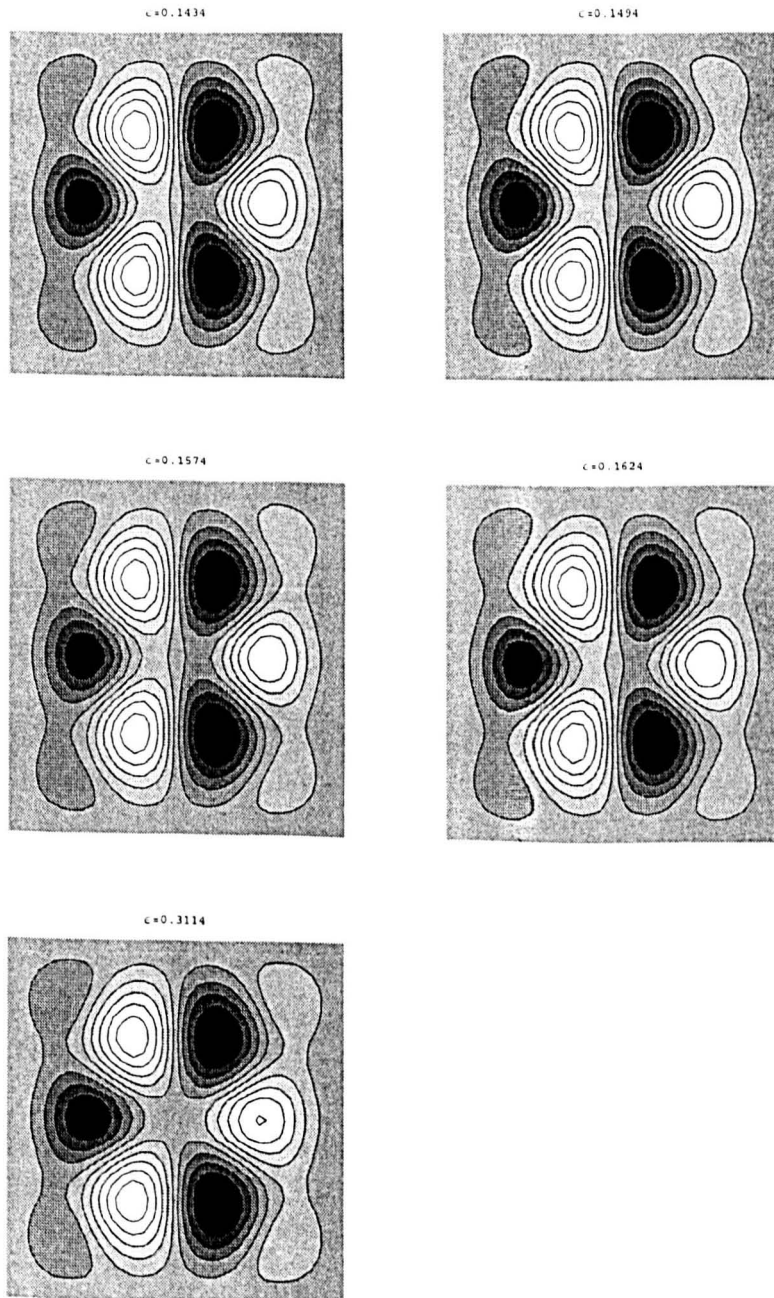


Figure 2.49: Contour plots of solutions u on branch OE2 for increasing ε and $L = 5\pi$.

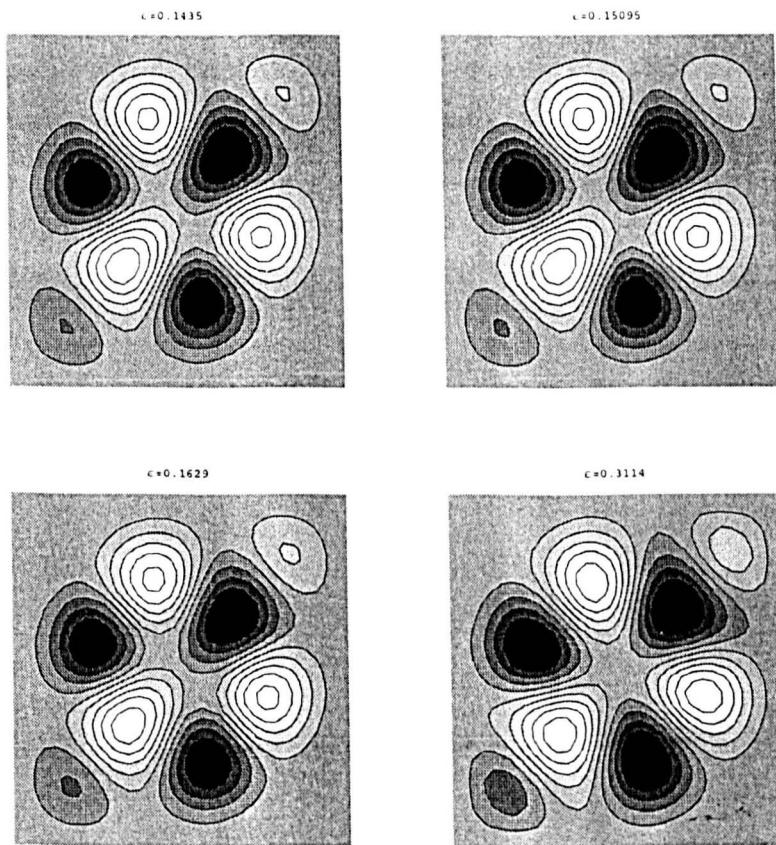


Figure 2.50: Contour plots of solutions u on branch D2 for increasing ϵ and $L = 5\pi$.

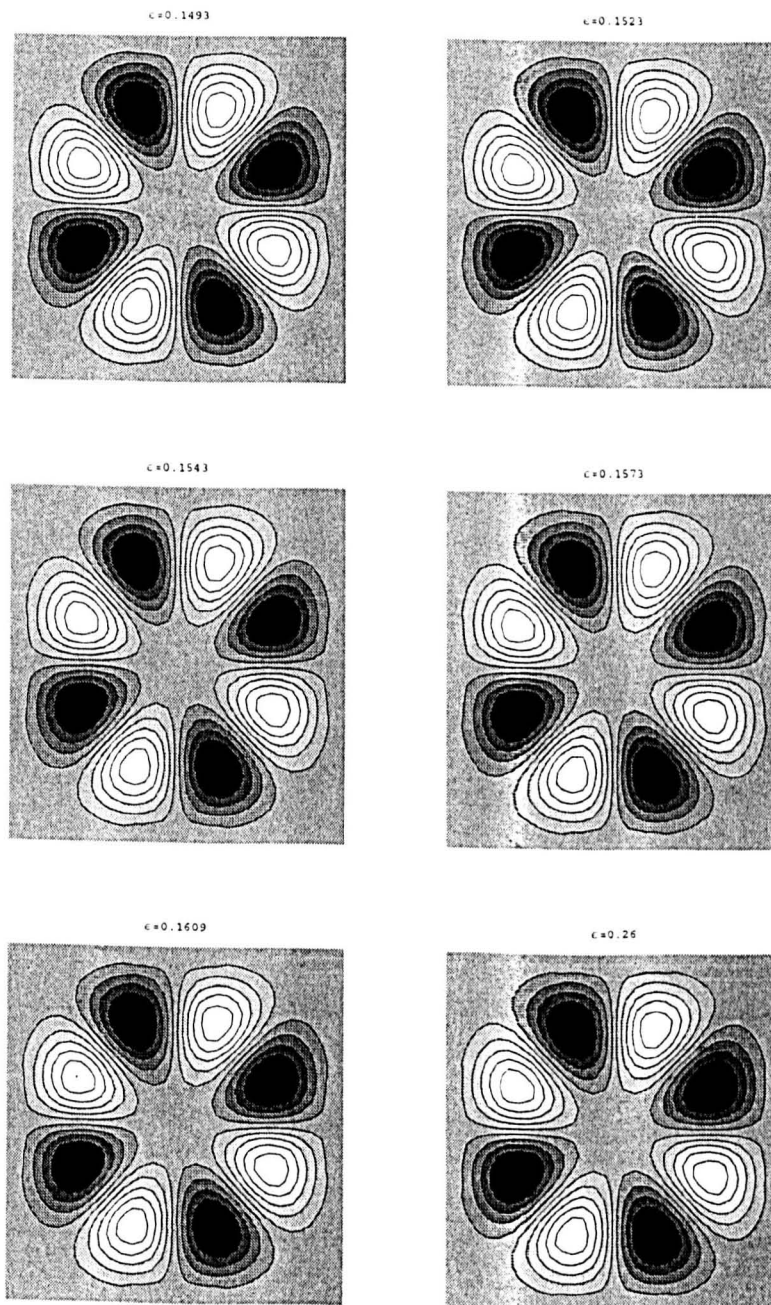


Figure 2.51: Contour plots of solutions u on branch OO2 for increasing ε and $L = 5\pi$.

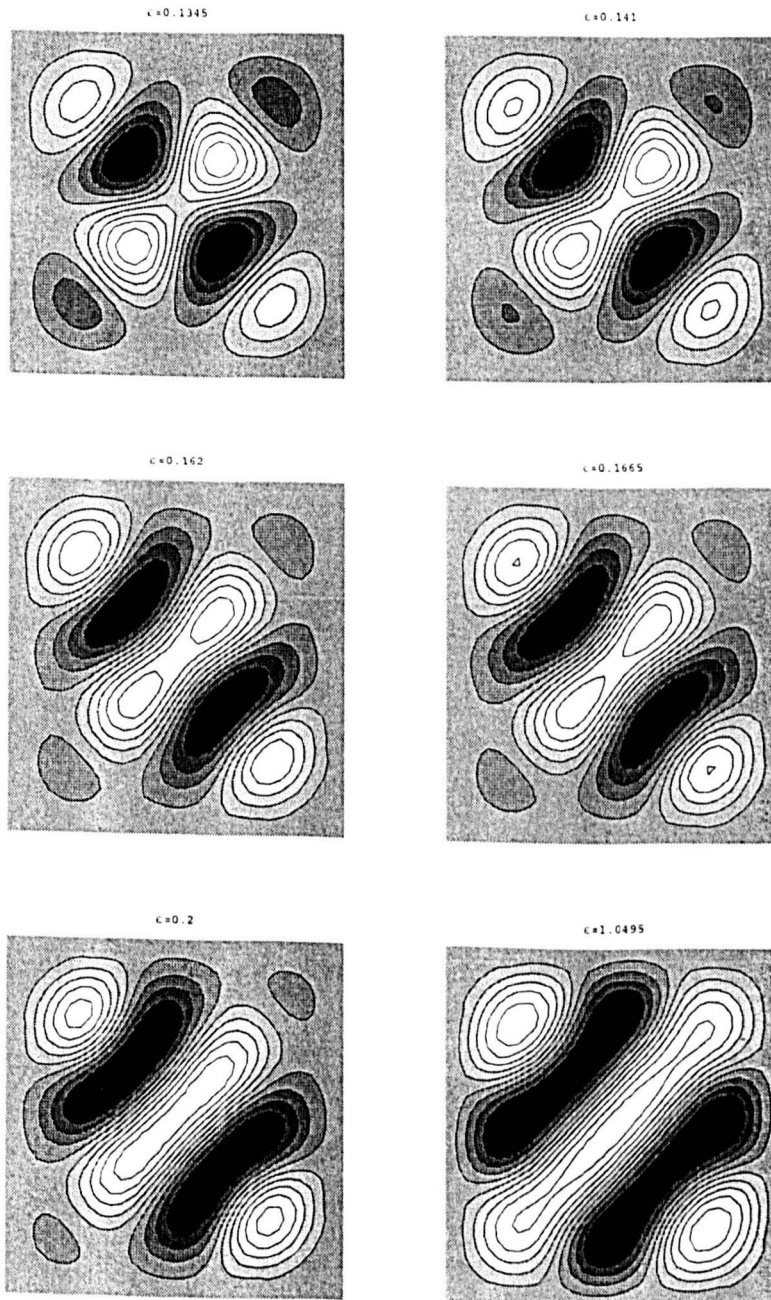


Figure 2.52: Contour plots of solutions u on branch D_{S1} for increasing ϵ and $L = 5\pi$.

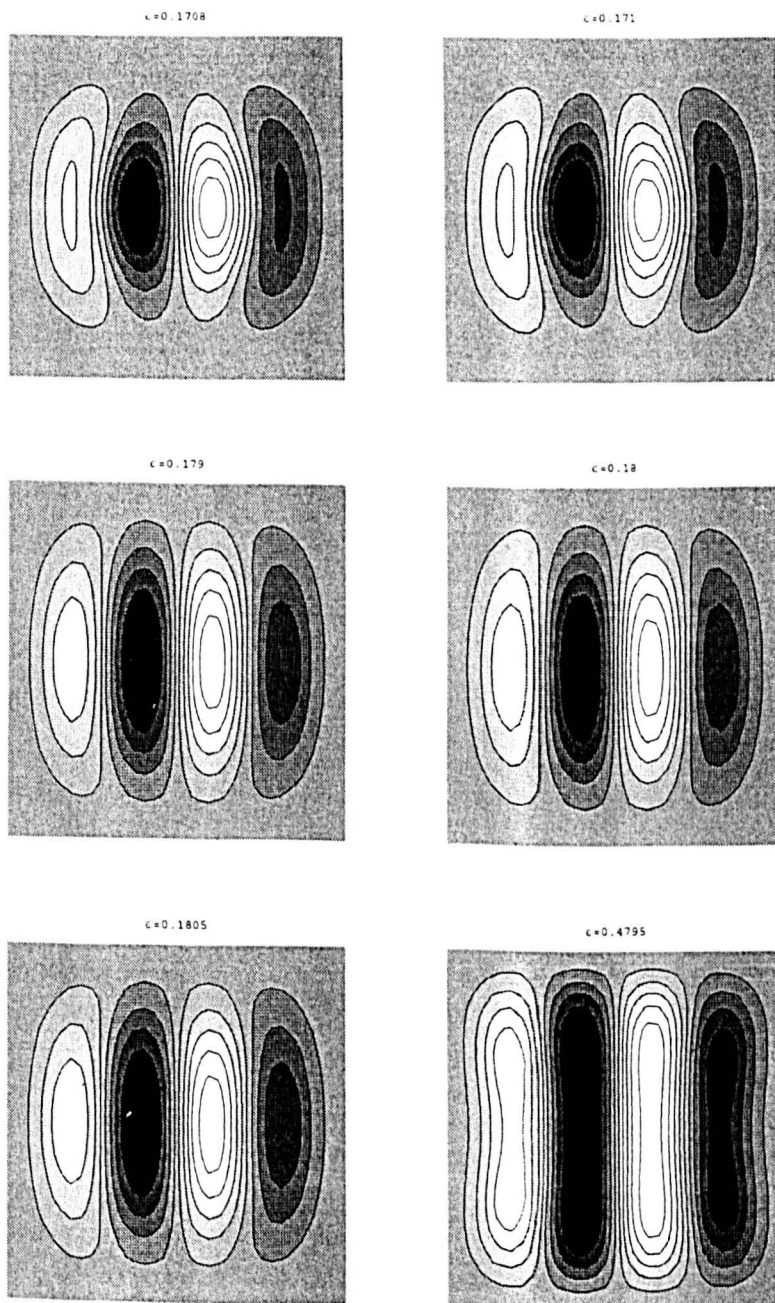


Figure 2.53: Contour plots of solutions u on branch OE_F^U1 for increasing ϵ and $L = 5\pi$.

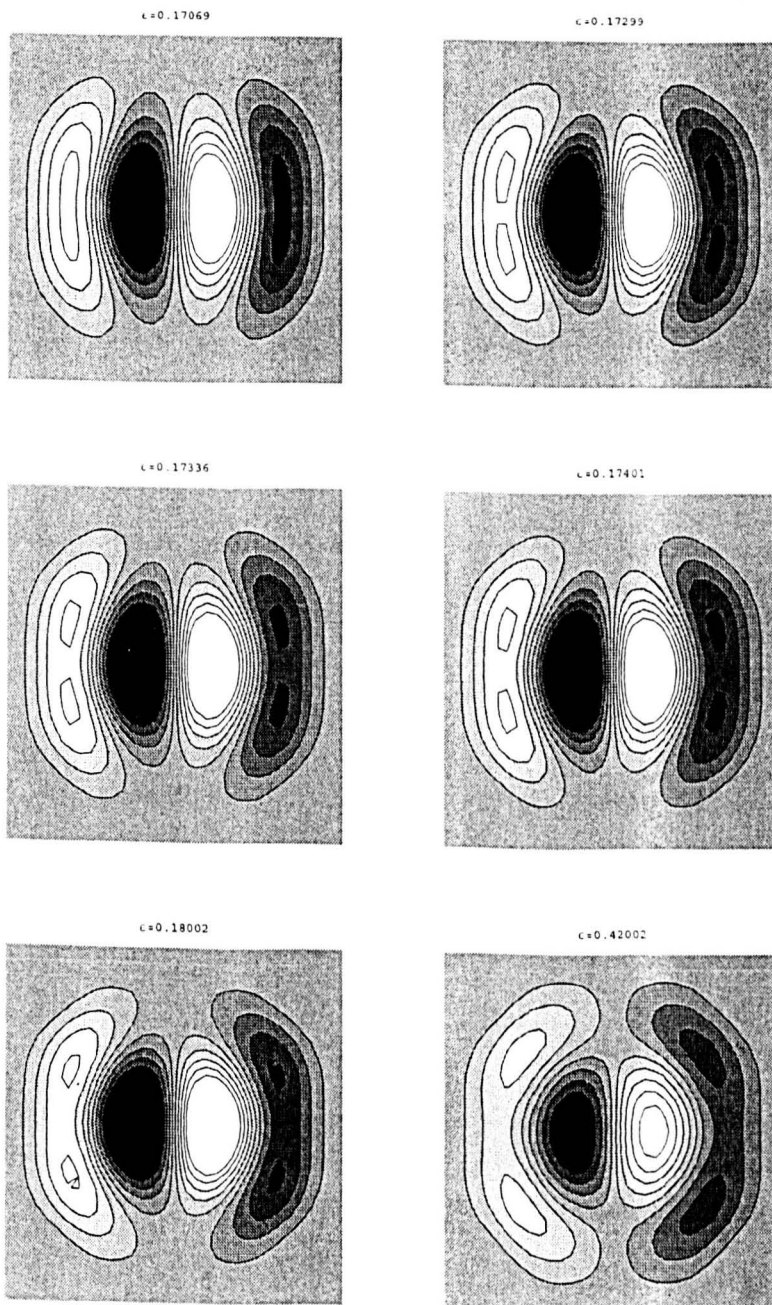


Figure 2.54: Contour plots of solutions u on branch OE_F^L for increasing ε and $L = 5\pi$.

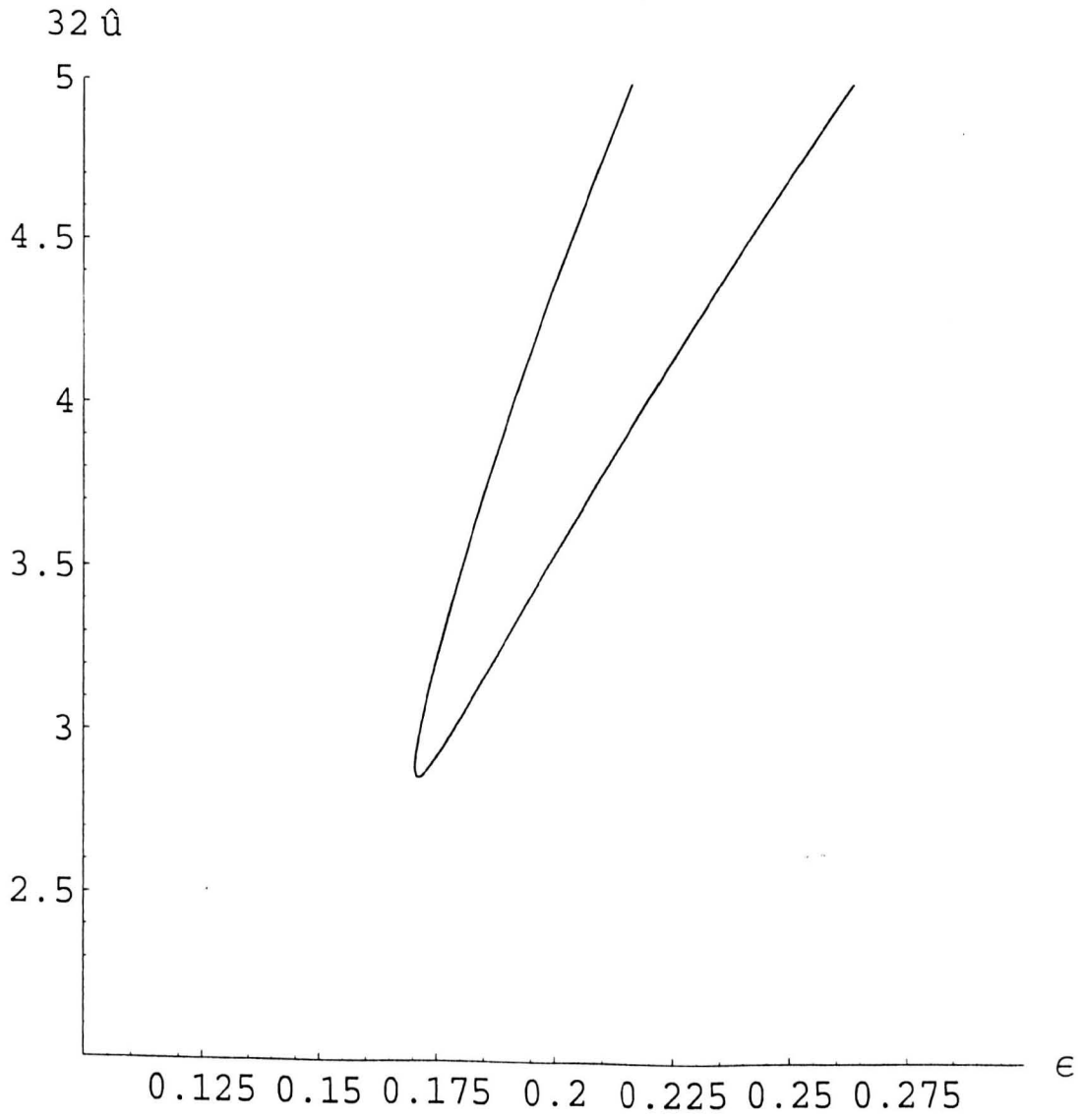


Figure 2.55: The fold bifurcation of branch OE_{F1} near $\epsilon = 0.170$.

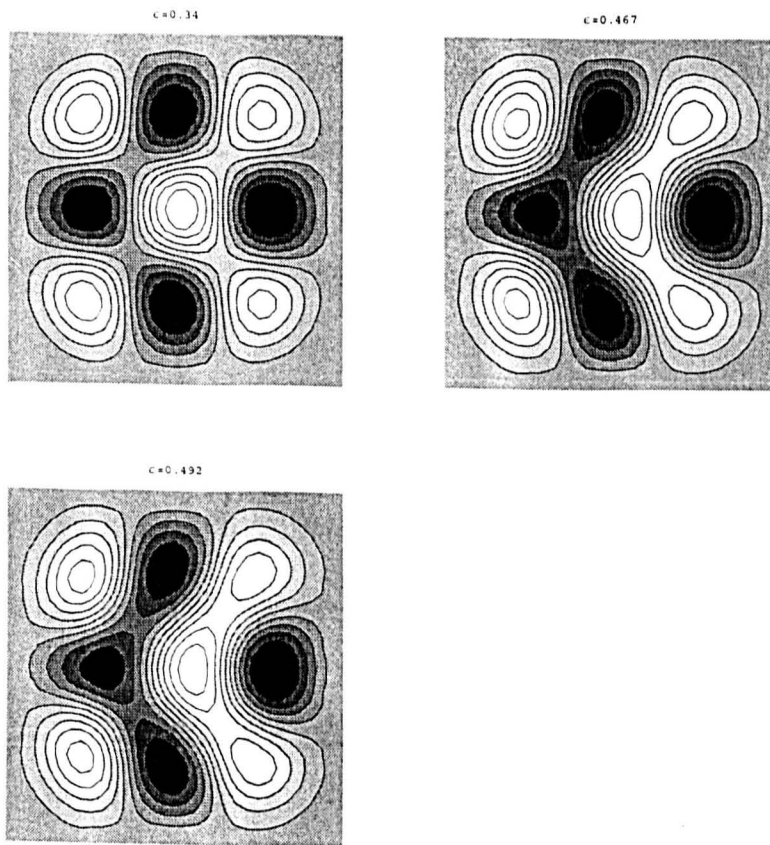


Figure 2.56: Contour plots of solutions u on branch E_{S1} for increasing ε and $L = 5\pi$.

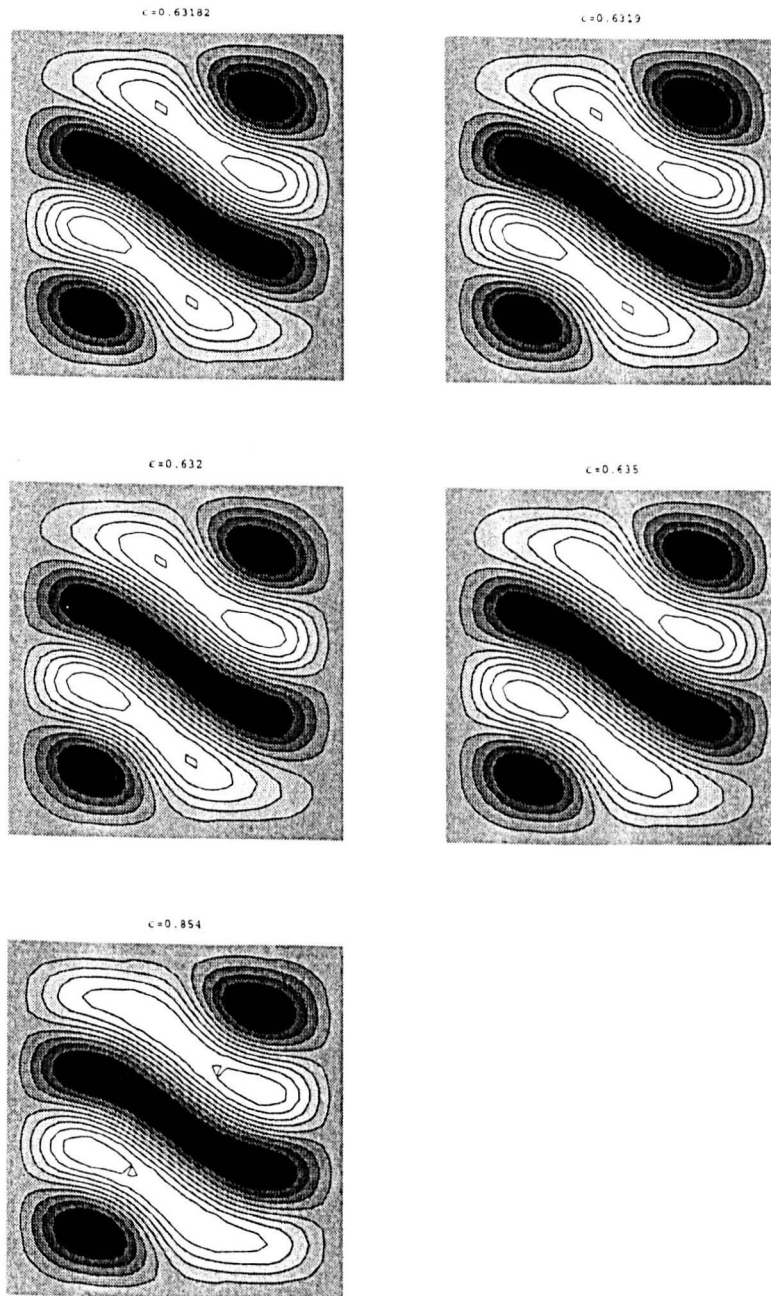


Figure 2.57: Contour plots of solutions u on branch C_F^U for increasing ϵ and $L = 5\pi$.

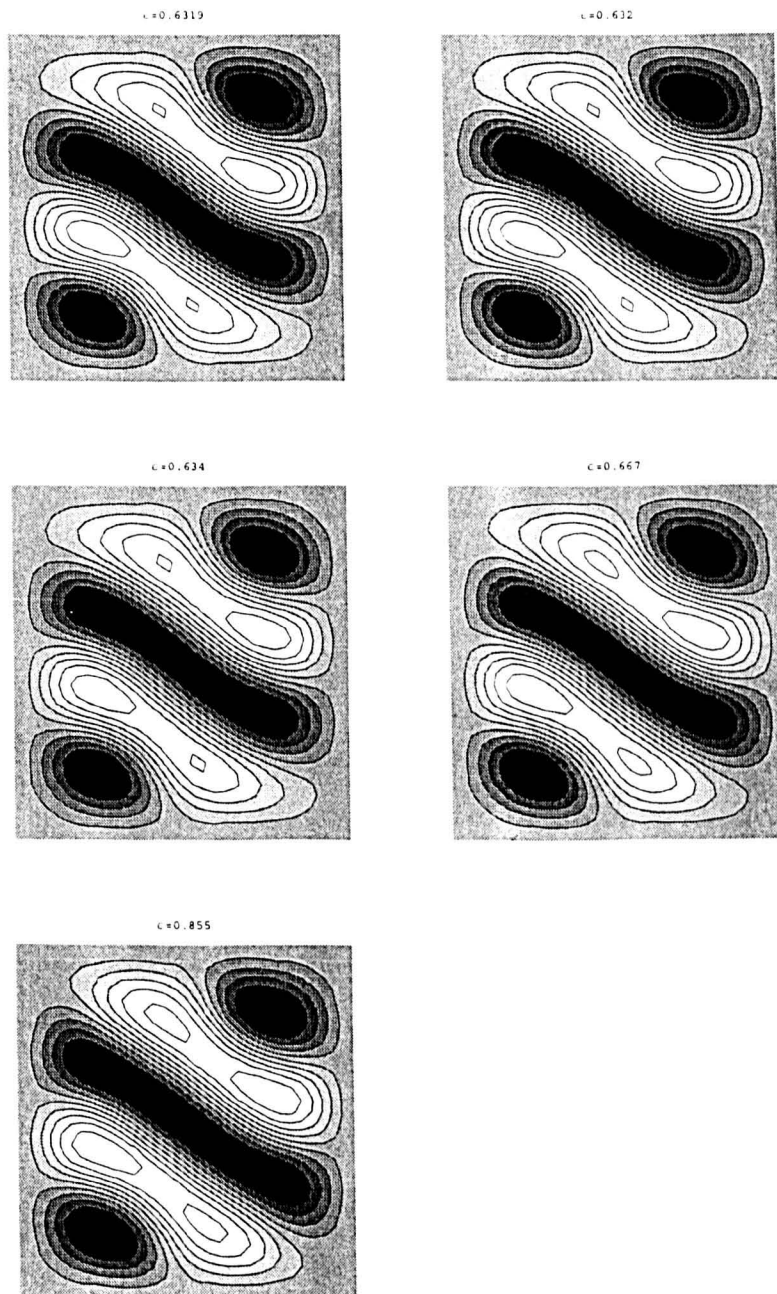


Figure 2.58: Contour plots of solutions u on branch $C_F^L 1$ for increasing ϵ and $L = 5\pi$.

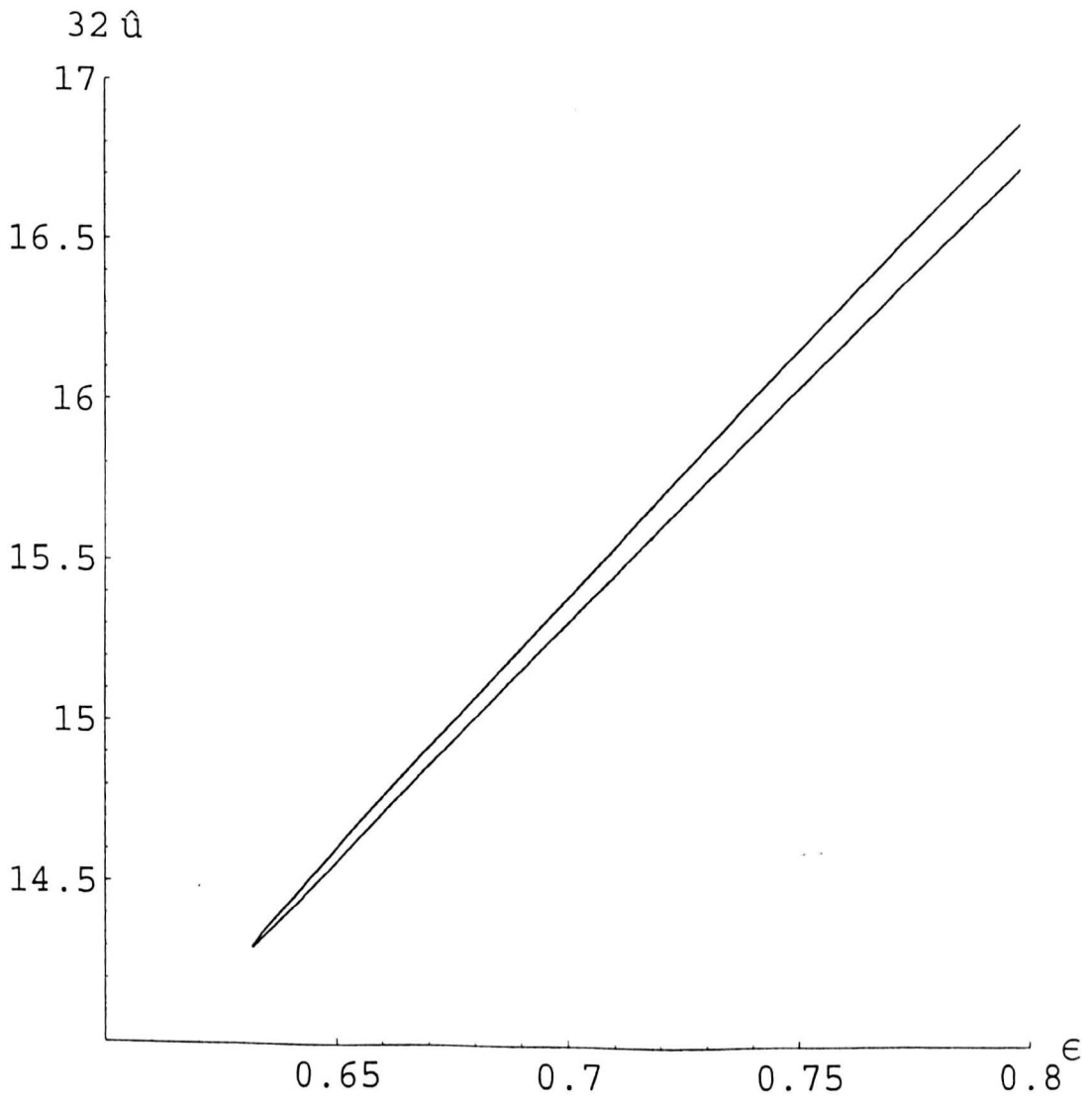


Figure 2.59: The fold bifurcation of branch C_{F1} near $\epsilon = 0.6318$.

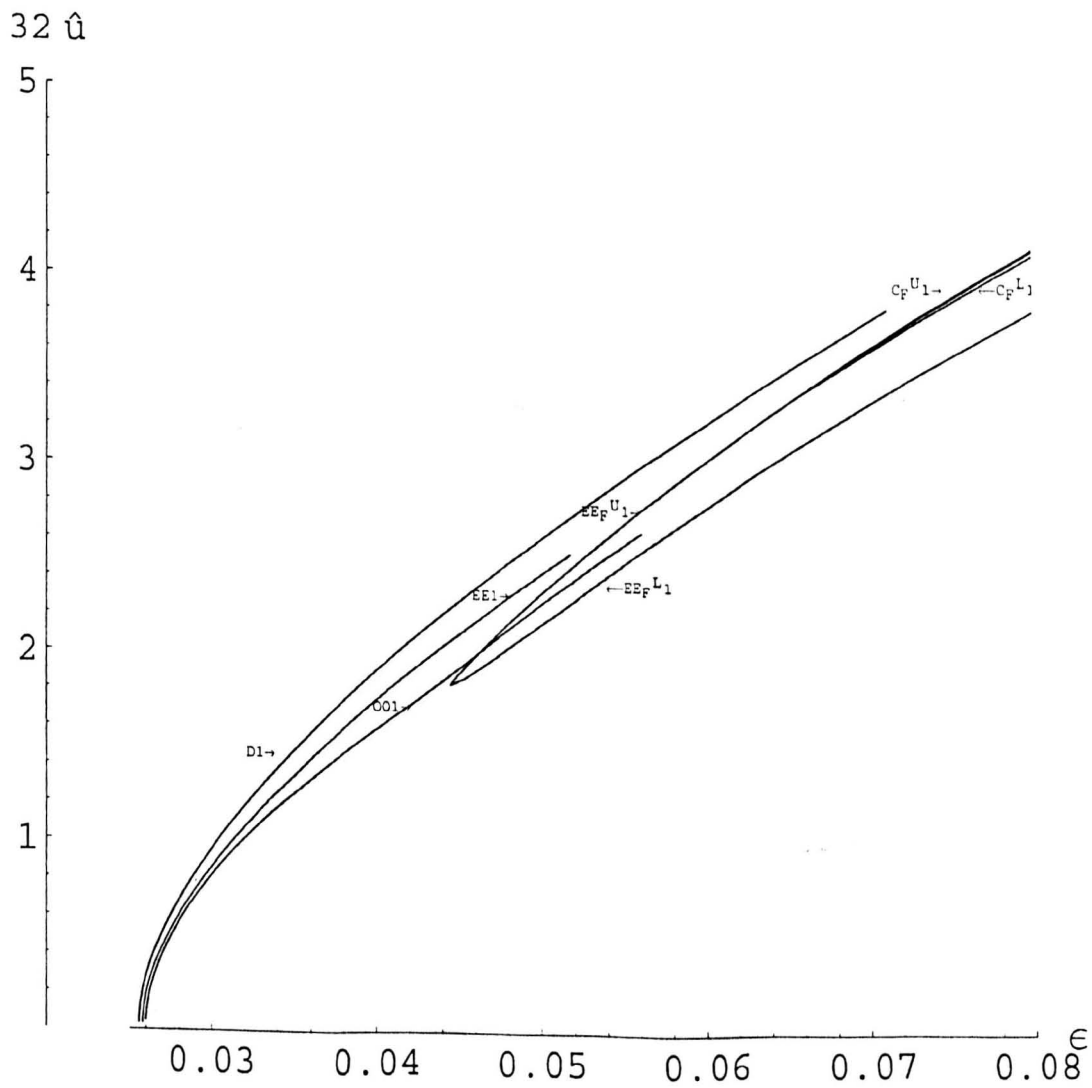


Figure 2.60: Bifurcation diagram for the case $L = 30$.

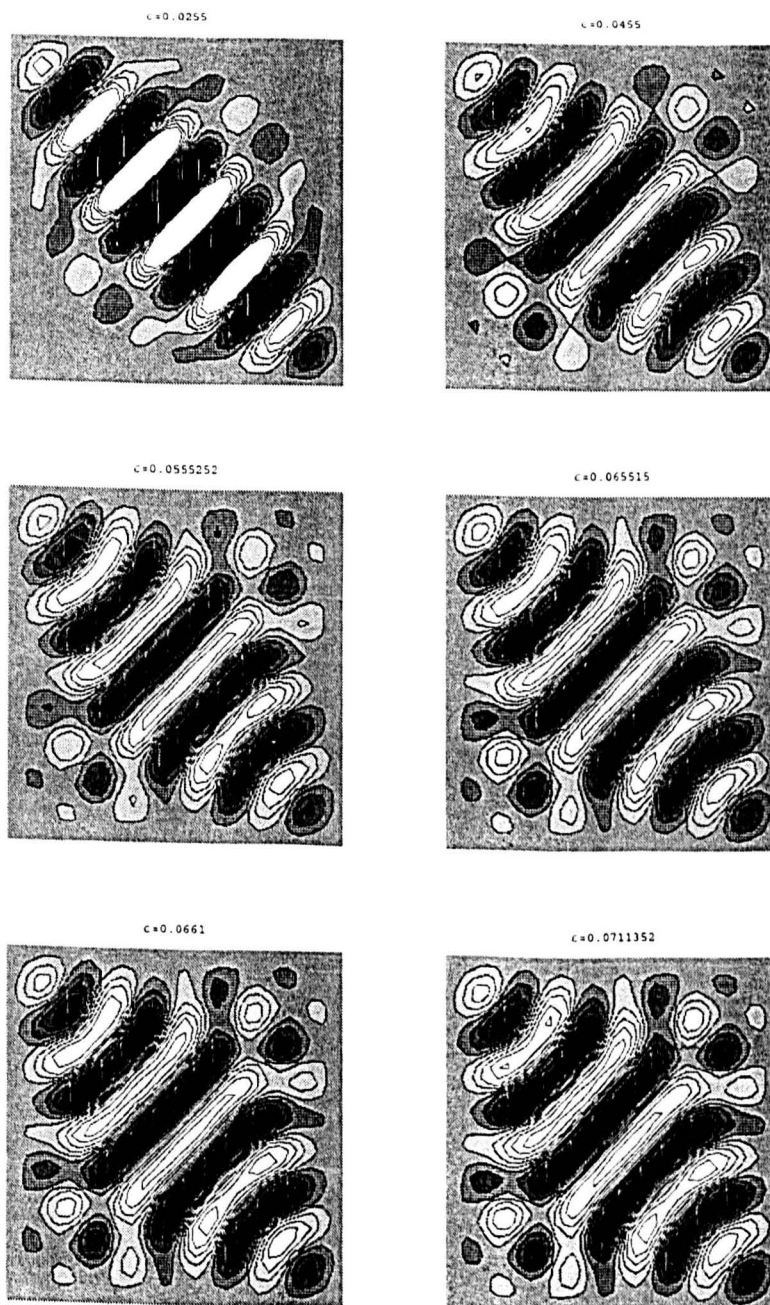


Figure 2.61: Contour plots of solutions u on branch D1 for increasing ϵ and $L = 30$.

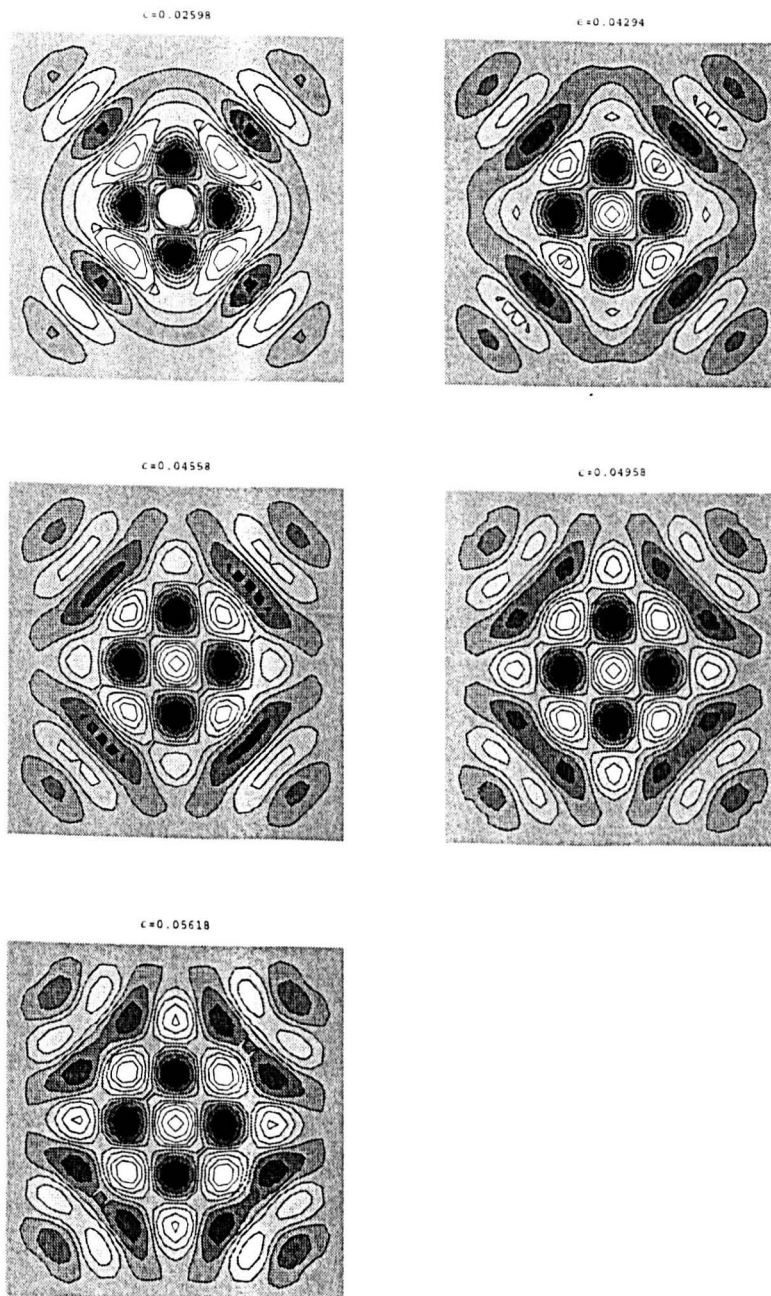


Figure 2.62: Contour plots of solutions u on branch EE1 for increasing ε and $L = 30$.

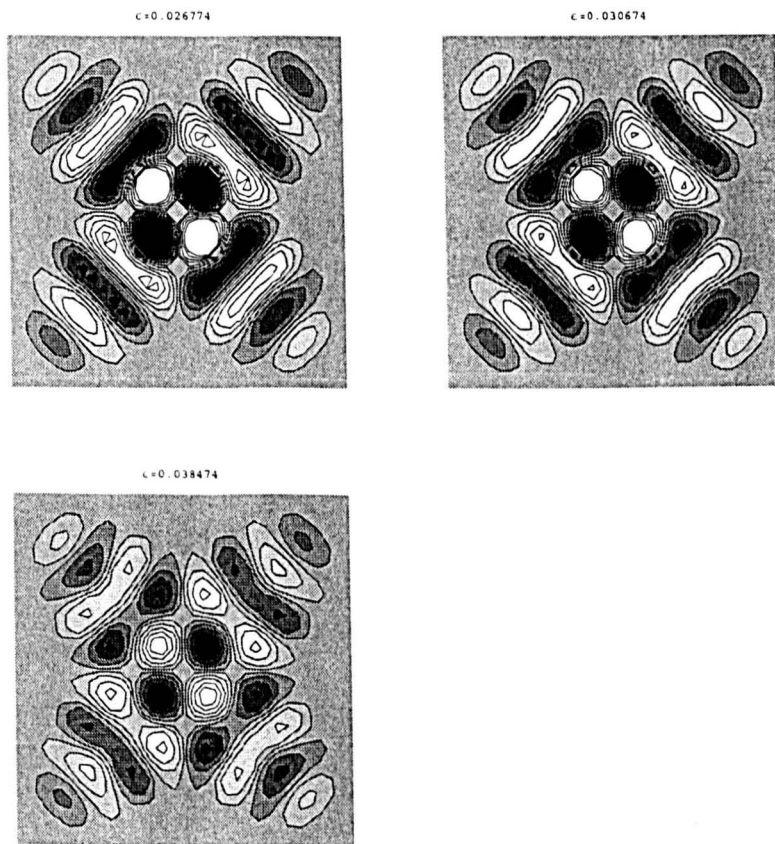


Figure 2.63: Contour plots of solutions u on branch OO1 for increasing ε and $L = 30$.

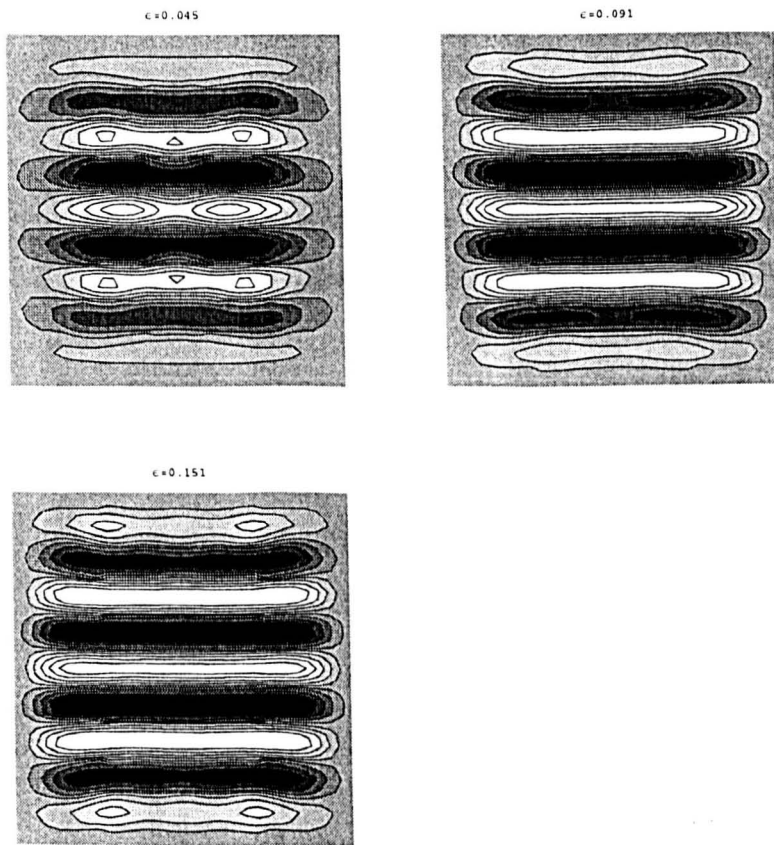


Figure 2.64: Contour plots of solutions u on branch $EE_F^U 1$ for increasing ϵ and $L = 30$.

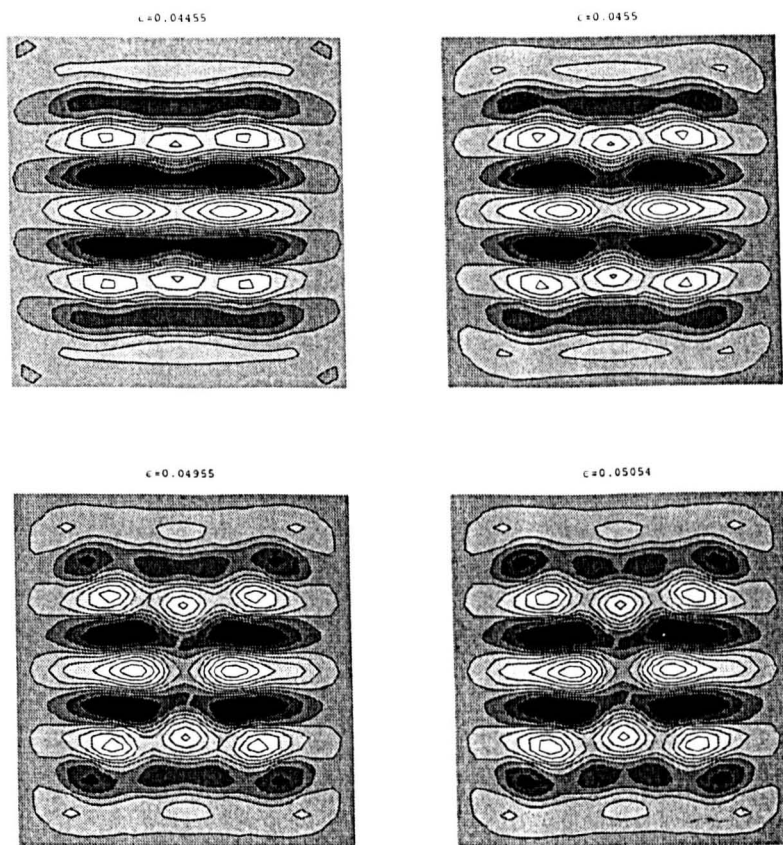


Figure 2.65: Contour plots of solutions u on branch $EE_F^L 1$ for increasing ε and $L = 30$.

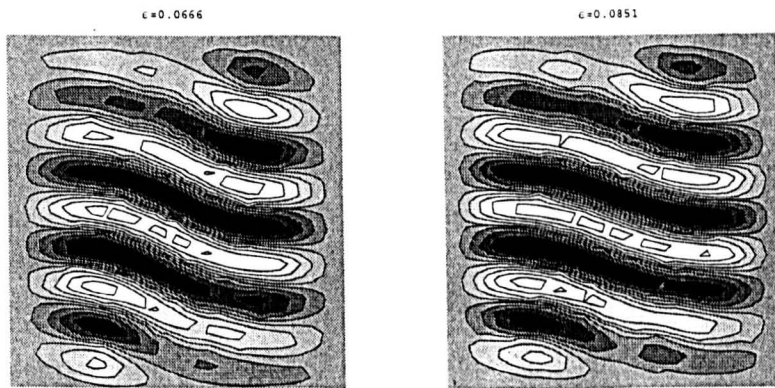


Figure 2.66: Contour plots of solutions u on branch C_F^U1 for increasing ϵ and $L = 30$.

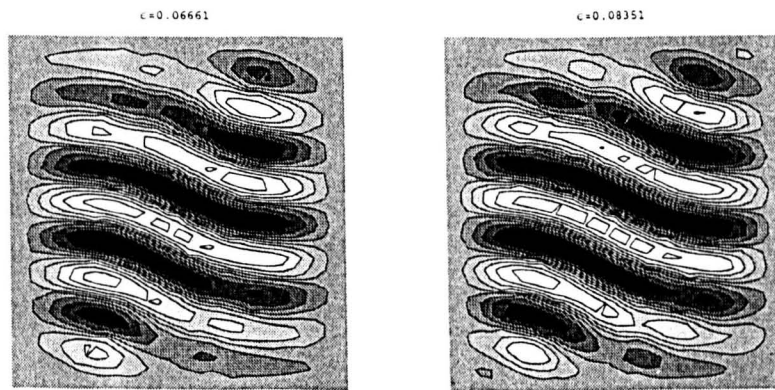


Figure 2.67: Contour plots of solutions u on branch C_F^L1 for increasing ϵ and $L = 30$.

Chapter 3

Pattern Formation in Large Squares

3.1 Introduction

Pattern formation in a square with sides of length L has been investigated by solving the 2D Swift-Hohenberg equation numerically for rigid boundary conditions. One of the aims of this study has been to establish the preferred structure and orientation of the pattern, especially in the cases where the square is sufficiently large for many cells to be accommodated. This chapter will investigate the idea that in large planform systems with rigid boundaries, roll patterns can occupy the region spanning points of the boundary of maximum separation, in other words with axes orthogonal to the diagonals of the square. This type of pattern has already been observed in the numerical solutions for the square in Chapter 2 and appears to be the leading mode of convection as $L \rightarrow \infty$.

This study will attempt to gain insight by making use of asymptotic methods, based on the assumptions that the lateral dimensions of the container are much larger than the characteristic wavelength of convection and that the solution is weakly nonlinear. Since we are considering large squares in which many cells can be accommodated, a solution near onset is sought in terms of an envelope function which modulates the amplitude and phase of a set of rolls with axes perpendicular to the diagonal. The problem is for-

mulated in Section 3.2 and the equation for the envelope function is derived in Section 3.3. The boundary conditions for this function are determined by considering corner regions in Section 3.4, where the solution adjusts to the wall conditions. In Section 3.5 a Fourier transform method together with a solvability condition leads to a closed system for the transform of the envelope function. Solutions of this system are found in Sections 3.6 and 3.7. Further properties of the asymptotic structure of the solution in the corners are investigated analytically in Section 3.8 and show how reflection at the walls generates a local cross-roll structure. The results are summarized in Section 3.9

3.2 Formulation of the problem

The Swift-Hohenberg equation is

$$\frac{\partial u}{\partial t} = \varepsilon u - (1 + \nabla^2)^2 u - u^3, \quad (3.1)$$

where t is the non-dimensional time, $\nabla^2 = \frac{\partial^2}{\partial x^2} + \frac{\partial^2}{\partial y^2}$ where x and y are non-dimensional Cartesian coordinates, ε is a control parameter and $u(x, y, t)$ is a scalar field. The domain is a square with sides of length L and the conditions

$$u = \frac{\partial u}{\partial q} = 0 \quad (3.2)$$

on the boundary where q is used to denote the inward normal direction to the boundary.

It is convenient in this chapter to choose the origin of the coordinates x, y at the centre of the square, with the x axis directed along one of the diagonals, as shown in Figure 3.1. A parameter l is introduced such that the diagonal is defined by $-l \leq x \leq l, y = 0$ and then $L = \sqrt{2}l$.

This chapter is concerned with an asymptotic description of the solution for u as $l \rightarrow \infty$, focusing on the structure of the leading modes of convection as the control parameter ε increases. Figure 3.1 shows the main regions of the proposed solution structure. A core region of width $y \sim l^{\frac{1}{2}}$ lies along the diagonal and contains rolls with axes in the y direction. At each end of the core region are corner regions of size $x \pm l \sim l^{\frac{1}{2}}$ and $y \sim l^{\frac{1}{2}}$ and within

these further adjustments occur in wall regions on a length scale of order one normal to the boundaries of the square.

The main ingredients of the structure proposed here are based on the weakly nonlinear theory developed by Daniels (2000) for the onset of convection in arbitrarily-shaped domains. In that theory the boundary of the domain is assumed to be smooth and the convection pattern forms along the diameter of the domain, the straight line of maximum length spanning the domain. At the ends of the diameter the boundary is described locally by the equations

$$\frac{x \mp l}{l} = \mp c_{\pm} \left(\frac{y}{l}\right)^2 \quad (3.3)$$

where the parameters c_{\pm} are a measure of the local curvature of the boundary. This leads to the onset of convection when ε reaches a critical value

$$\varepsilon = \frac{\pi^2}{l^2} + \frac{\delta}{l^3} + \dots, \quad l \rightarrow \infty, \quad (3.4)$$

with the parameter δ depending on c_{\pm} . The leading term in (3.4) represents the fact that the presence of the boundaries, distance $2l$ apart, gives rise to an increase in the critical value of ε relative to its value ($\varepsilon=0$) for an infinite layer. The correction term involving δ is the additional increase in ε needed to allow for inward curvature of the boundaries at each end of the diameter. In the limit of large boundary curvature ($c_{\pm} \rightarrow \infty$) Daniels (2000) showed that, at onset, $\delta \sim c_{\pm}$ and that the lateral extent of the rolls in the y direction is of order $l^{\frac{1}{2}}$ and independent of c_{\pm} . Although this theory cannot be applied directly to the case of a square because of the non-smooth nature of the boundary, it can be used to estimate the likely effect on (3.4). In the case of the square, $x \mp l$ and y are of comparable magnitudes near the corners. With $y \sim l^{\frac{1}{2}}$ it follows from (3.3) that if $x \mp l \sim l^{\frac{1}{2}}$ also then $c_{\pm} \sim l^{\frac{1}{2}}$. Since $\delta \sim c_{\pm}$ as $c_{\pm} \rightarrow \infty$ it follows that for the square it can be expected that the onset of convection will occur when $\delta \sim l^{\frac{1}{2}}$ and so we set

$$\varepsilon = \frac{\pi^2}{l^2} + \frac{\delta_1}{l^{\frac{5}{2}}} \quad (3.5)$$

where δ_1 is an order one parameter. A further implication is that the magnitude of u in the core region is of order $(\varepsilon - \frac{\pi^2}{l^2})^{\frac{1}{2}} \sim l^{-\frac{5}{4}}$. The expansion of the solution in the core region is considered next.

3.3 Core expansion

A solution in the core region is assumed in the form

$$u = l^{-\frac{5}{4}}u_0 + l^{-\frac{7}{4}}u_1 + l^{-\frac{9}{4}}u_2 + l^{-\frac{11}{4}}u_3 + l^{-\frac{13}{4}}u_4 + l^{-\frac{15}{4}}u_5 + \dots \quad (3.6)$$

where $u_i = u_i(x, X, Y, \tau)$ are functions of x and the scaled variables $X = x/l$, $Y = y/l^{\frac{1}{2}}$ and $\tau = t/l^{\frac{5}{2}}$. These are chosen to accommodate a modulation of the roll pattern along the diagonal ($-1 < X < 1$), the decay of the roll pattern on the lateral scale $y \sim l^{\frac{1}{2}}$ corresponding to $-\infty < Y < \infty$ and the temporal evolution of the weakly nonlinear solution near onset. Justification for the precise scalings in l will become clear in due course. The expansion (3.6) is substituted into the governing equation (3.3) with the control parameter ε expressed in the form (3.5), leading to a series of problems for u_0, u_1, \dots

At order $l^{-\frac{5}{4}}$, u_0 is found to satisfy the equation

$$L(u_0) \equiv \frac{\partial^4 u_0}{\partial x^4} + 2 \frac{\partial^2 u_0}{\partial x^2} + u_0 = 0 \quad (3.7)$$

and the relevant solution is

$$u_0 = A_0(X, Y, \tau)e^{ix} + A_0^*(X, Y, \tau)e^{-ix} \quad (3.8)$$

where A_0 is a complex amplitude function and $*$ denotes complex conjugate. This solution represents a set of rolls with axes orthogonal to the diagonal whose amplitude and phase are modulated by the function A_0 .

At order $l^{-\frac{7}{4}}$, u_1 is found to satisfy the equation $L(u_1) = 0$ and the relevant solution is

$$u_1 = A_1(X, Y, \tau)e^{ix} + A_1^*(X, Y, \tau)e^{-ix}, \quad (3.9)$$

where A_1 is a further complex amplitude function.

At order $l^{-\frac{9}{4}}$, u_2 is found to satisfy the equation

$$L(u_2) = -4 \frac{\partial^4 u_0}{\partial x^3 \partial X} - 4 \frac{\partial^2 u_0}{\partial x \partial X} - 2 \frac{\partial^2 u_0}{\partial Y^2} - 2 \frac{\partial^4 u_0}{\partial x^2 \partial Y^2}. \quad (3.10)$$

From (3.8), the terms on the right-hand side sum to zero, so that

$$u_2 = A_2(X, Y, \tau)e^{ix} + A_2^*(X, Y, \tau)e^{-ix}, \quad (3.11)$$

where A_2 is a further complex amplitude function.

At order $l^{-\frac{11}{4}}$, u_3 is found to satisfy

$$L(u_3) = -4 \frac{\partial^4 u_1}{\partial x^3 \partial X} - 4 \frac{\partial^2 u_1}{\partial x \partial X} - 2 \frac{\partial^2 u_1}{\partial Y^2} - 2 \frac{\partial^4 u_1}{\partial x^2 \partial Y^2} \quad (3.12)$$

and again the right-hand side terms sum to zero, giving

$$u_3 = A_3(X, Y, \tau) e^{ix} + A_3^*(X, Y, \tau) e^{-ix}, \quad (3.13)$$

where A_3 is a further complex amplitude function.

At order $l^{-\frac{13}{4}}$, u_4 is found to satisfy

$$\begin{aligned} L(u_4) = & -4 \frac{\partial^4 u_2}{\partial x^3 \partial X} - 4 \frac{\partial^2 u_2}{\partial x \partial X} - 2 \frac{\partial^2 u_2}{\partial Y^2} - 2 \frac{\partial^4 u_2}{\partial x^2 \partial Y^2} \\ & + \pi^2 u_0 - 6 \frac{\partial^4 u_0}{\partial x^2 \partial X^2} - 4 \frac{\partial^4 u_0}{\partial x \partial X \partial Y^2} - \frac{\partial^4 u_0}{\partial Y^4} - 2 \frac{\partial^2 u_0}{\partial X^2}. \end{aligned} \quad (3.14)$$

A bounded solution for u_4 requires that the terms on the right-hand side (which are proportional to $e^{\pm ix}$) sum to zero, and substitution for u_0 from (3.8) and u_2 from (3.11) shows that A_0 satisfies the equation

$$4 \left(\frac{\partial}{\partial X} - \frac{i}{2} \frac{\partial^2}{\partial Y^2} \right)^2 A_0 + \pi^2 A_0 = 0. \quad (3.15)$$

The assumed scaling for $y \sim l^{\frac{1}{2}}$ ensures that the Y derivatives appear in this equation along with the X derivatives, essential in allowing a solution for A_0 that decays as $Y \rightarrow \pm\infty$. This solution will be considered in Section 3.5.

At order $l^{-\frac{15}{4}}$, u_5 is found to satisfy

$$\begin{aligned} L(u_5) = & -4 \frac{\partial^4 u_3}{\partial x^3 \partial X} - 4 \frac{\partial^2 u_3}{\partial x \partial X} - 2 \frac{\partial^2 u_3}{\partial Y^2} - 2 \frac{\partial^4 u_3}{\partial x^2 \partial Y^2} \\ & + \pi^2 u_1 - 6 \frac{\partial^4 u_1}{\partial x^2 \partial X^2} - 4 \frac{\partial^4 u_1}{\partial x \partial X \partial Y^2} - \frac{\partial^4 u_1}{\partial Y^4} - 2 \frac{\partial^2 u_1}{\partial X^2} \\ & + \delta_1 u_0 - u_0^3 - \frac{\partial u_0}{\partial \tau}. \end{aligned} \quad (3.16)$$

A bounded solution for u_5 requires that the terms proportional to $e^{\pm ix}$ on the right-hand side sum to zero; substitution from (3.8), (3.9) and (3.13) shows that A_1 satisfies the equation

$$4 \left(\frac{\partial}{\partial X} - \frac{i}{2} \frac{\partial^2}{\partial Y^2} \right)^2 A_1 + \pi^2 A_1 = \frac{\partial A_0}{\partial \tau} - \delta_1 A_0 + 3 A_0 |A_0|^2. \quad (3.17)$$

The scalings in (3.5), (3.6) and of the time t ensure that the terms in A_0 involving δ_1 , nonlinear effects and the time derivative appear on the right-hand side of (3.17). The solution of (3.17) is considered in Section 3.5.

3.4 Corner regions

The corner region near $x=-l$ is defined by $|Y| \leq X_- < \infty$ where $y=l^{\frac{1}{2}}Y$ and $x=-l+l^{\frac{1}{2}}X_-$. Since the scale in x is much larger than the critical wavelength of the roll pattern, this corner region contains many rolls and the solution must match with that in the core region as $X_- \rightarrow \infty$. In the core region it will be assumed that the leading order amplitude function A_0 approaches zero as $X \rightarrow \pm 1$ so that

$$A_0(\pm 1, Y, \tau) = 0. \quad (3.18)$$

This is consistent with the usual behaviour in finite domains with rigid lateral boundaries (Daniels 1977a) and is needed to ensure that the wall conditions (3.2) can be satisfied (see Section 3.8 below). This implies that as $X \rightarrow -1$ the core amplitude function has the behaviour

$$A_0 \sim (X+1) \frac{\partial A_0}{\partial X}(-1, Y, \tau), \quad (3.19)$$

giving rise to a solution in the corner region of the form

$$u = l^{-\frac{7}{4}} u_0^-(x, X_-, Y, \tau) + \dots \quad (3.20)$$

as $l \rightarrow \infty$.

The required solution for u_0^- can be found by an expansion procedure similar to that of Section 3.3 but allowing for the new scaling of X_- in place of X . Since the analysis is essentially the same but with X_- in place of X , it can be inferred that the required solution for u_0^- is

$$u_0^- = A_0^-(X_-, Y, \tau) e^{ix} + A_0^{-*}(X_-, Y, \tau) e^{-ix} \quad (3.21)$$

where the amplitude equation equivalent to (3.15) is dominated by the X_- derivative, giving

$$\frac{\partial^2 A_0^-}{\partial X_-^2} = 0. \quad (3.22)$$

Matching with (3.19) requires that

$$A_0^- \sim X_- \frac{\partial A_0}{\partial X}(-1, Y, \tau) \quad \text{as} \quad X_- \rightarrow \infty \quad (3.23)$$

and the other boundary condition for A_0^- is that it vanishes on the boundary of the square, so that

$$A_0^- = 0 \quad \text{on} \quad X_- = |Y|, \quad -\infty < Y < \infty. \quad (3.24)$$

This is necessary to allow the solution to adjust to the wall conditions (3.2) in the wall regions, to be considered in Section 3.8. From (3.22) - (3.24) the solution for A_0^- is

$$A_0^- = (X_- - |Y|) \frac{\partial A_0}{\partial X}(-1, Y, \tau). \quad (3.25)$$

The corner region at $x=l$ is defined by $-\infty < X_+ \leq -|Y|$ where $x = l + l^{\frac{1}{2}} X_+$ and the solution there is

$$u = l^{-\frac{7}{4}} u_0^+(x, X_+, Y, \tau) + \dots \quad (3.26)$$

as $l \rightarrow \infty$, where

$$u_0^+ = A_0^+(X_+, Y, \tau) e^{ix} + A_0^{+*}(X_+, Y, \tau) e^{-ix} \quad (3.27)$$

and

$$A_0^+ = (X_+ + |Y|) \frac{\partial A_0}{\partial X}(1, Y, \tau). \quad (3.28)$$

Matching between the corner solutions (3.25), (3.28) and the core solution now implies that the core amplitude function A_1 must satisfy the boundary conditions

$$A_1(\pm 1, Y, \tau) = \pm |Y| \frac{\partial A_0}{\partial X}(\pm 1, Y, \tau). \quad (3.29)$$

If the core functions $\frac{\partial A_0}{\partial X}(\pm 1, Y, \tau)$ are smooth functions of Y that are non-zero at $Y = 0$, it follows that the corner solutions (3.25) and (3.28) have a discontinuous gradient in Y across $Y = 0$. This is a consequence of the lack of Y derivatives in the governing equation (3.22) and can be expected to be smoothed out on a smaller lateral scale $y \sim l^{\frac{1}{2}}$ within each corner region, where the y derivatives in the governing equations become significant. The details of the solution in this region are not considered here.

3.5 Fourier transform theory

From the results of Sections 3.3 and 3.4 a local onset of convection requires a solution of

$$4\left(\frac{\partial}{\partial X} - \frac{i}{2} \frac{\partial^2}{\partial Y^2}\right)^2 A_0 + \pi^2 A_0 = 0 \quad (3.30)$$

for which $A_0=0$ at $X = \pm 1$ and $A_0 \rightarrow 0$ as $Y \rightarrow \pm\infty$. Such solutions can conveniently be represented using a Fourier transform in Y ,

$$\bar{A}_0(X, \omega, \tau) = \int_{-\infty}^{\infty} A_0(X, Y, \tau) e^{i\omega Y} dY \quad (3.31)$$

and it follows from (3.30) that \bar{A}_0 satisfies

$$\bar{L}(\bar{A}_0) \equiv 4\left(\frac{\partial}{\partial X} + \frac{i\omega^2}{2}\right)^2 \bar{A}_0 + \pi^2 \bar{A}_0 = 0 \quad (3.32)$$

so that

$$\bar{A}_0 = a(\omega, \tau) e^{-\frac{i\omega^2 X}{2}} \cos\left(\frac{\pi X}{2}\right) \quad (3.33)$$

where $a(\omega, \tau)$ is an arbitrary function of τ and the transform variable ω . A single Fourier component of frequency ω would correspond to a roll whose axis lies at an angle $\omega/l^{\frac{1}{2}}$ to the y direction. The function a must be determined by considering the problem for A_1 which consists of the equation

$$4\left(\frac{\partial}{\partial X} - \frac{i}{2} \frac{\partial^2}{\partial Y^2}\right)^2 A_1 + \pi^2 A_1 = \frac{\partial A_0}{\partial \tau} - \delta_1 A_0 + 3A_0 |A_0|^2 \quad (3.34)$$

together with the boundary conditions given by (3.29) and the requirement that $A_1 \rightarrow 0$ as $Y \rightarrow \pm\infty$. It follows that the transform $\bar{A}_1(X, \omega, \tau)$ of A_1 must satisfy

$$\bar{L}(\bar{A}_1) = \bar{R}(X, \omega, \tau) \quad (3.35)$$

where \bar{R} is the transform of the right-hand side of (3.34), together with

$$\bar{A}_1(\pm 1, \omega, \tau) = \bar{D}_{\pm}(\omega, \tau) \quad (3.36)$$

where \bar{D}_{\pm} are the transforms of the right-hand sides of (3.29).

The adjoint function for \bar{A}_0 is $e^{\frac{i\omega^2 X}{2}} \cos(\frac{\pi X}{2})$ and so the problem for \bar{A}_1 has a solution only if the solvability condition

$$\int_{-1}^1 \bar{R} e^{\frac{i\omega^2 X}{2}} \cos\left(\frac{\pi X}{2}\right) dX = 2\pi(\bar{D}_+ e^{\frac{i\omega^2}{2}} + \bar{D}_- e^{-\frac{i\omega^2}{2}}) \quad (3.37)$$

is satisfied. Given that \bar{A}_0 is known in terms of $a(\omega, \tau)$, this is an equation for the unknown function $a(\omega, \tau)$:

$$\frac{\partial a}{\partial \tau} = \delta_1 a + 2\pi(\bar{D}_+ e^{\frac{i\omega^2}{2}} + \bar{D}_- e^{-\frac{i\omega^2}{2}}) - 3I_0 \quad (3.38)$$

where

$$I_0(\omega, \tau) = \int_{-1}^1 H_0(X, \omega, \tau) e^{\frac{i\omega^2 X}{2}} \cos\left(\frac{\pi X}{2}\right) dX, \quad (3.39)$$

$$H_0(X, \omega, \tau) = \int_{-\infty}^{\infty} A_0 |A_0|^2 e^{i\omega Y} dY, \quad (3.40)$$

$$A_0(X, Y, \tau) = \frac{\cos \frac{\pi X}{2}}{2\pi} \int_{-\infty}^{\infty} a(\omega, \tau) e^{-\frac{i\omega^2 X}{2} - i\omega Y} d\omega \quad (3.41)$$

and

$$\bar{D}_{\pm}(\omega, \tau) = \pm \int_{-\infty}^{\infty} |Y| \frac{\partial A_0}{\partial X}(\pm 1, Y, \tau) e^{i\omega Y} dY \quad (3.42)$$

where

$$\frac{\partial A_0}{\partial X}(\pm 1, Y, \tau) = \mp \frac{1}{4} \int_{-\infty}^{\infty} a(\omega, \tau) e^{\mp \frac{i\omega^2}{2} - i\omega Y} d\omega. \quad (3.43)$$

The system (3.38) - (3.43) admits solutions of the form

$$a(\omega, \tau) = r(\omega, \tau) e^{i\theta} \quad (3.44)$$

where r is real and the phase θ is constant. In this case

$$A_0 = e^{i\theta} A, \quad H_0 = e^{i\theta} H, \quad I_0 = e^{i\theta} I, \quad \bar{D}_- = e^{i\theta} D, \quad \bar{D}_+ = e^{i\theta} D^* \quad (3.45)$$

and r is the solution of the system

$$\frac{\partial r}{\partial \tau} = \delta_1 r + 2\pi (D e^{-\frac{i\omega^2}{2}} + D^* e^{\frac{i\omega^2}{2}}) - 3I \quad (3.46)$$

where

$$I(\omega, \tau) = \int_{-1}^1 H(X, \omega, \tau) e^{\frac{i\omega^2 X}{2}} \cos\left(\frac{\pi X}{2}\right) dX \quad (3.47)$$

$$H(X, \omega, \tau) = \int_{-\infty}^{\infty} A |A|^2 e^{i\omega Y} dY \quad (3.48)$$

$$A(X, Y, \tau) = \frac{\cos \frac{\pi X}{2}}{2\pi} \int_{-\infty}^{\infty} r(\omega, \tau) e^{-\frac{i\omega^2 X}{2} - i\omega Y} d\omega \quad (3.49)$$

and

$$D(\omega, \tau) = - \int_{-\infty}^{\infty} |Y| F(Y, \tau) e^{i\omega Y} dY \quad (3.50)$$

where

$$F(Y, \tau) = \frac{1}{4} \int_{-\infty}^{\infty} r(\omega, \tau) e^{\frac{i\omega^2}{2} - i\omega Y} d\omega. \quad (3.51)$$

Solutions are required for which

$$r \rightarrow 0 \quad \text{as} \quad \omega \rightarrow \pm\infty. \quad (3.52)$$

The value of the phase constant θ is arbitrary but is expected to be determined at higher order in the expansion of the solution for u as $l \rightarrow \infty$ (see, for example, Daniels 1978) with $\theta = 0$ corresponding to solutions for u_0 even in x , and $\theta = \frac{\pi}{2}$ corresponding to solutions for u_0 odd in x .

The system (3.46) - (3.52) has real solutions r that are even or odd functions of ω , the nonlinear term I appearing in (3.46) being real in this case. This follows because if $r(\omega, \tau) = r(-\omega, \tau)$ then A is even in Y and its real and imaginary parts are even and odd in X respectively, whilst if $r(\omega, \tau) = -r(-\omega, \tau)$ then A is odd in Y and its real and imaginary parts are odd and even in X respectively. In either case it then follows that the real and imaginary parts of H are even and odd in X respectively and thence that the imaginary part of I is zero. Solutions of the steady linearised version of (3.46) are found in Section 3.6 and of the full nonlinear system in Section 3.7.

3.6 Linear Solution

In this section solutions of the steady linearised version of (3.46),

$$\delta_1 r + 2\pi(De^{-\frac{i\omega^2}{2}} + D^* e^{\frac{i\omega^2}{2}}) = 0 \quad (3.53)$$

are found subject to the boundary conditions (3.52). This is an eigenvalue problem for δ_1 , with the lowest value of δ_1 and the corresponding eigenfunction $r = r(\omega)$ defining the onset of convection.

3.6.1 Solution method

Solutions of (3.53) were found using a Fourier series representation

$$r = \sum_{n=1}^{\infty} r_n \sin n\pi\bar{\omega} \quad (3.54)$$

where

$$\bar{\omega} = \frac{1}{2}(1 + \tanh \omega), \quad 0 < \bar{\omega} < 1. \quad (3.55)$$

This ensures the smooth decay of the eigenfunction r to zero as $\omega \rightarrow \pm\infty$ (that is, as $\bar{\omega} \rightarrow 1$ and $\bar{\omega} \rightarrow 0$).

From (3.51),

$$F = \sum_{n=1}^{\infty} r_n F_n(Y) \quad (3.56)$$

where $F_n = F_{nr} + iF_{ni}$ and

$$F_{nr} = \frac{1}{4} \int_{-\infty}^{\infty} \left(\cos \frac{\omega^2}{2} \cos \omega Y + \sin \frac{\omega^2}{2} \sin \omega Y \right) \sin n\pi\bar{\omega} d\omega, \quad (3.57)$$

$$F_{ni} = \frac{1}{4} \int_{-\infty}^{\infty} \left(\sin \frac{\omega^2}{2} \cos \omega Y - \cos \frac{\omega^2}{2} \sin \omega Y \right) \sin n\pi\bar{\omega} d\omega \quad (3.58)$$

and then (3.50) gives

$$D = \sum_{n=1}^{\infty} r_n D_n(\omega) \quad (3.59)$$

where $D_n = D_{nr} + iD_{ni}$ and

$$D_{nr} = - \int_{-\infty}^{\infty} |Y| (F_{nr} \cos \omega Y - F_{ni} \sin \omega Y) dY, \quad (3.60)$$

$$D_{ni} = - \int_{-\infty}^{\infty} |Y| (F_{ni} \cos \omega Y + F_{nr} \sin \omega Y) dY. \quad (3.61)$$

Equation (3.53) is now decomposed into individual modes as

$$\delta_1 r_m + 4\pi \sum_{n=1}^{\infty} r_n b_{mn} = 0 \quad (m = 1, 2, \dots) \quad (3.62)$$

where

$$b_{mn} = 2 \int_0^1 \left(D_{nr} \cos \frac{\omega^2}{2} + D_{ni} \sin \frac{\omega^2}{2} \right) \sin m\pi\bar{\omega} d\bar{\omega} \quad (3.63)$$

or, in matrix form,

$$\left(\mathbf{B} + \frac{\delta_1}{4\pi} \mathbf{I} \right) \mathbf{r} = 0 \quad (3.64)$$

where \mathbf{B} is the matrix with elements b_{mn} , \mathbf{I} is the identity matrix and \mathbf{r} is the column vector with elements r_m .

From (3.57) and (3.58), F_{nr} and F_{ni} are even in Y for odd values of n and odd in Y for even values of n . It follows from (3.60) and (3.61) that D_{nr} and D_{ni} are even in ω for odd values of n and odd in ω for even values of n . Thus $b_{mn} = 0$ when n is odd and m is even, and when m is odd and n is even. It follows that one set of eigensolutions is obtained with $r_n = 0$ for even n , corresponding to eigenfunctions $r(\omega)$ that are even functions of ω , and another set with $r_n = 0$ for odd n , corresponding to eigenfunctions $r(\omega)$ that are odd functions of ω .

3.6.2 Results

The matrix eigenvalue problem (3.64) was solved using a standard Mathematica routine. The system was truncated to N modes and the matrix elements b_{mn} calculated using Simpson's rule in the integrals (3.57), (3.58), (3.60), (3.61) and (3.63). For the integrations in ω the integrals were transformed to the variable $\bar{\omega}$ and the domain $0 \leq \bar{\omega} \leq 1$ subdivided into equal intervals. The integrands oscillate rapidly as $\bar{\omega} \rightarrow 0$ and $\bar{\omega} \rightarrow 1$ and the integrations were performed from $\bar{\omega} = \bar{\epsilon}$ to $\bar{\omega} = 1 - \bar{\epsilon}$ with the parameter $\bar{\epsilon}$ chosen sufficiently small (typically $\bar{\epsilon} = 0.01$) to provide an accurate evaluation; the integrands are bounded as $\bar{\omega} \rightarrow 0$ and $\bar{\omega} \rightarrow 1$ and so contributions to the integrals from the neighbourhood of $\bar{\omega} = 0$ and $\bar{\omega} = 1$ are small. The integration over Y in (3.60) and (3.61) was performed typically with a step size $\Delta Y = 0.1$ and various outer boundaries $Y = \pm Y_\infty$ with Y_∞ ranging from 10 to 80. The integrations in $\bar{\omega}$ were performed with the same number of steps as those in Y . Results were obtained for a range of truncation levels up to $N = 28$, at which point reasonable convergence was achieved.

Table 3.1 shows the dependence of the leading eigenvalue δ_1 on the truncation level and the outer boundary Y_∞ . Results for the first six eigenvalues δ_1 and the corresponding eigenvectors \mathbf{r} obtained for a truncation level $N = 28$ and outer boundary $Y_\infty = 80$ are shown in Table 3.2. The leading eigenvalue is calculated to be $\delta_1 = 15.5$ to three significant figures. The leading eigenfunction $r(\omega)$ is constructed from (3.54) and the real and imaginary parts of the corresponding amplitude function $A(X, Y)$ calculated from (3.49) are shown in Figure 3.2. Figure 3.3 shows the solution for u_0 calculated from (3.8) in the case where L is taken as 30 and $\theta = 0$. The corresponding results for the second eigenvalue $\delta_2 = 31.5$ are shown in Figures 3.4 and 3.5.

3.6.3 Comparison with numerical results

The asymptotic results obtained here can be compared with the linearised solutions of the Swift-Hohenberg equation reported in Section 2.4. Setting $l = L/\sqrt{2}$ in (3.5), the present asymptotic theory predicts linear solutions at

$$\epsilon \sim \frac{2\pi^2}{L^2} + \frac{2^{\frac{5}{4}}\delta_1}{L^{\frac{5}{2}}}, \quad L \rightarrow \infty \quad (3.65)$$

N	$Y_\infty = 10$	$Y_\infty = 20$	$Y_\infty = 40$	$Y_\infty = 80$
2	19.2215		19.2224	
4	16.8609	16.8604	16.8614	
6	16.0670	16.0954	16.0973	
8	15.7127	15.7709	15.7741	
10		15.6183	15.6226	
12		15.5421	15.5495	
14		15.5048	15.5152	
16			15.5009	15.5091
18			15.4969	15.5061
20			15.4982	15.5082
22			15.5015	15.5123
24			15.5066	15.5171
26			15.5097	15.5216
28			15.5154	15.5254

Table 3.1: Dependence of the leading eigenvalue δ_1 on the outer boundary Y_∞ and the truncation level N for $\Delta Y = 0.1$.

δ_1	15.5254	41.1787	67.5581	δ_1	31.4948	53.5543	82.3752
r_1	-0.7918	0.1126	-0.0008	r_2	-0.5651	-0.0000	0.0083
r_3	-0.4317	-0.3644	-0.0180	r_4	-0.4711	-0.0357	-0.1317
r_5	-0.2911	-0.4247	0.1850	r_6	-0.3860	0.2505	0.4552
r_7	-0.2102	-0.4089	-0.4860	r_8	-0.3177	-0.4846	-0.1082
r_9	-0.1567	-0.3720	0.0473	r_{10}	-0.2628	-0.0680	-0.3789
r_{11}	-0.1189	-0.3297	0.3766	r_{12}	-0.2179	0.3219	-0.3238
r_{13}	-0.0909	-0.2874	0.3464	r_{14}	-0.1806	0.3752	-0.1266
r_{15}	-0.0696	-0.2472	0.1364	r_{16}	-0.1492	0.2039	0.0820
r_{17}	-0.0530	-0.2096	-0.0948	r_{18}	-0.1224	-0.0300	0.2400
r_{19}	-0.0399	-0.1747	-0.2650	r_{20}	-0.0992	-0.2227	0.3294

Table 3.2: The leading six eigenvalues and the first ten non-zero elements of the corresponding eigenvectors obtained with $\Delta Y = 0.1, Y_\infty = 80$ and a truncation level $N = 28$.

and these are shown in Figure 3.6 for the first two eigenvalues δ_1 listed in Table 3.2, along with the linearised solutions of the Swift-Hohenberg equation displayed in Figure 2.8. These indicate good agreement. The leading eigenvalue $\delta_1 = 15.5$ is associated with the first group of branches; the distinction between the different modes (EE, OO and EO/OE/D) identified in Section 2.3 corresponds to the possibility of selecting the phase as $\theta = 0$ or $\theta = \frac{\pi}{2}$ and is expected to give rise to the next correction to ε in (3.65) which is likely to be a term of order L^{-3} (cf Daniels 1978). The value of this correction term is expected to be different for each of the three symmetries (EE, OO and EO/OE/D), providing the three distinct curves.

The diagonal pattern predicted by the asymptotic theory is consistent with that observed in the Swift-Hohenberg calculations. The single diagonal mode corresponds to the mode D1 observed in Figure 2.13. Superposition of the asymptotic structure along one diagonal with a similar structure along the other diagonal of the square gives rise to the OE,EO,OO and EE modes observed in Figures 2.11–2.15. Although the asymptotic theory is nonlinear, such a superposition is permissible because the two diagonal structures only interact with each other where they intersect at the centre of the square. Because this interaction occurs over a short length scale (x and y of order $l^{\frac{1}{2}}$) it does not affect the leading order solution - the pattern observed in this central region is therefore just the linear superposition of the two sets of orthogonal rolls.

The second eigenvalue $\delta_1 = 31.5$ is associated with the second group of branches; here the amplitude function is odd in Y and so sets of double cells are predicted along the diagonals.

3.7 Nonlinear solution

In this section solutions of the full nonlinear version of (3.46),

$$\frac{\delta r}{\delta \tau} = \delta_1 r + 2\pi(De^{-\frac{i\omega^2}{2}} + D^*e^{\frac{i\omega^2}{2}}) - 3I \quad (3.66)$$

are found subject to the boundary conditions (3.24).

3.7.1 Solution method

The Fourier series representation

$$r = \sum_{n=1}^{\infty} r_n \sin n\pi\bar{\omega} \quad (3.67)$$

with

$$\bar{\omega} = \frac{1}{2}(1 + \tanh \omega), \quad 0 < \bar{\omega} < 1 \quad (3.68)$$

was again used but now with $r_n = r_n(\tau)$ functions of the time τ . Provided r is an even or odd function of ω the nonlinear term I is real and can be expressed as a Fourier series

$$I(\omega, \tau) = \sum_{n=1}^{\infty} c_n \sin n\pi\bar{\omega} \quad (3.69)$$

where the coefficients $c_n = c_n(\tau)$ are given by

$$c_n = 2 \int_0^1 I(\omega, \tau) \sin n\pi\bar{\omega} d\bar{\omega}, \quad (3.70)$$

Equation (3.66) therefore gives a system of ordinary differential equations:

$$\frac{\delta r_m}{\delta \tau} = \delta_1 r_m + 4\pi \sum_{n=1}^{\infty} r_n b_{mn} - 3c_m, \quad m = 1, 2, \dots \quad (3.71)$$

to be solved for the individual modes r_m . These equations are coupled through both the linear terms involving the coefficients b_{mn} calculated in Section 3.6 and the nonlinear terms c_m given by (3.70) where I must be calculated in terms of $r_m, m = 1, 2, \dots$ using (3.18) - (3.20).

An Euler forward difference scheme was used to solve (3.71), so that the solution at time $\tau = (j+1)\Delta\tau$ is obtained in terms of that at time $\tau = j\Delta\tau$ from the formulae

$$r_{m,j+1} = r_{m,j} + \Delta\tau [\delta_1 r_{m,j} + 4\pi \sum_{n=1}^{\infty} r_{n,j} b_{mn} - 3c_{m,j}], \quad m = 1, 2, \dots, \quad (3.72)$$

where $\Delta\tau$ is the time step. The solution is allowed to evolve in time until a steady state is attained. The linearised solution of Section 3.6 with a suitably chosen amplitude was used to provide an initial state at $\tau = 0$, starting with a value of δ_1 somewhat greater than the critical value identified in Section 3.6.

Once a steady state was achieved the value of δ_1 was incremented and the new steady-state values of r_m used as the initial state for the next computation.

The various integrations involved in (3.70) and (3.18) - (3.20) were performed using Simpson's rule and results were tested for accuracy using different step sizes in $X, Y, \bar{\omega}$ and τ , and different outer boundaries $\pm Y_\infty$ for the integration in Y . Results were also obtained for various truncation levels N in the Fourier representation.

3.7.2 Results

Figure 3.7 shows a plot of the steady state solution for r at $\omega = 0$ as a function of δ_1 for the leading mode that bifurcates at $\delta_1 = 15.5$. This was obtained using a truncation level $N = 10$ and with 20 steps in X and 100 steps in $\bar{\omega}$ and Y in the integration formulae with $Y_\infty = 5$. A time step $\Delta\tau = 0.005$ was used and convergence to a steady-state solution was achieved typically to within an error of 0.005 in the value of r when $\tau = 1$, although this time increased significantly in the neighbourhood of the bifurcation point, $\delta_1 = 15.5$. Plots of the steady-state solution for the real and imaginary parts of A at $\delta_1 = 23$ constructed from (3.49) are shown in Figure 3.8. As δ_1 increases the solution increases in amplitude and spreads outwards from the diagonal. Figure 3.9 shows the steady-state solutions for u_0 constructed from (3.8) at $\delta_1 = 18$ and $\delta_1 = 45$ in the case when L is taken as 30 and $\theta = 0$. Here it is seen that the curvature of the roll pattern decreases as δ_1 increases.

3.8 Wall regions

In this section it is confirmed that the assumptions made in Sections 3.3 and 3.4 concerning the behaviour of the core and the corner region solutions are consistent with satisfaction of the wall conditions (3.2).

First, recall that in the corner region near $x = -l$ the solution is given by

$$u = l^{-\frac{7}{4}} u_0^-(x, X_-, Y, \tau) + \dots \quad (3.73)$$

as $l \rightarrow \infty$, where

$$u_0^- = A_0^-(X_-, Y, \tau)e^{ix} + A_0^{-*}(X_-, Y, \tau)e^{-ix} \quad (3.74)$$

and

$$A_0^- = (X_- - |Y|)f(Y, \tau). \quad (3.75)$$

where we introduce

$$f(Y, \tau) = \frac{\partial A_0}{\partial X}(-1, Y, \tau). \quad (3.76)$$

Then

$$f(Y, \tau) = e^{i\theta} F(Y, \tau) \quad (3.77)$$

where θ is the arbitrary phase constant and F is the function defined in (3.51). Plots of the real and imaginary parts of the steady-state solution for F for various values of δ_1 on the leading branch of solutions computed in Section 3.7 are shown in Figure 3.10.

As $X_- \rightarrow |Y|$ the amplitude function A_0^- approaches zero and the solution for u undergoes a further adjustment within wall regions whose width is comparable with that of individual rolls. The proposed structure is shown in Figure 3.1. In order to describe the solution within the wall regions it is convenient to introduce the new coordinates ξ and η aligned with the walls, defined by

$$x + l = \frac{\eta + \xi}{\sqrt{2}}, \quad y = \frac{\eta - \xi}{\sqrt{2}}. \quad (3.78)$$

Wall region Ia (see Figure 3.1) then occupies the domain $0 \leq \eta < \infty$, $0 \leq \tilde{\xi} < \infty$ where $\tilde{\xi} = \xi/l^{1/2}$. The solution there is

$$u = l^{-9/4} \tilde{u}(\xi, \eta, \tilde{\xi}, \tau) + \dots \quad (3.79)$$

as $l \rightarrow \infty$ where \tilde{u} satisfies the linearised version of the Swift-Hohenberg equation

$$(1 + \nabla^2)^2 \tilde{u} = 0 \quad (3.80)$$

with $\nabla^2 = \frac{\partial^2}{\partial \xi^2} + \frac{\partial^2}{\partial \eta^2}$. Matching with the incident x -roll pattern given by (3.73)-(3.75) requires that

$$\tilde{u} \sim \sqrt{2}\eta [f(-\tilde{\xi}/\sqrt{2}, \tau)e^{i(-l + \frac{\eta + \xi}{\sqrt{2}})} + f^*(-\tilde{\xi}/\sqrt{2}, \tau)e^{-i(-l + \frac{\eta + \xi}{\sqrt{2}})}], \eta \rightarrow \infty \quad (3.81)$$

and the wall conditions (3.2) require that

$$\tilde{u} = \frac{\partial \tilde{u}}{\partial \eta} = 0 \quad \text{on} \quad \eta = 0. \quad (3.82)$$

Satisfaction of the wall conditions requires the generation of a reflected (y -roll) component and a solution for \tilde{u} can be found in the form

$$\tilde{u} = (a + b\eta)e^{i(\frac{\eta+\xi}{\sqrt{2}})} + (a^* + b^*\eta)e^{-i(\frac{\eta+\xi}{\sqrt{2}})} + (c + d\eta)e^{i(\frac{\eta-\xi}{\sqrt{2}})} + (c^* + d^*\eta)e^{-i(\frac{\eta-\xi}{\sqrt{2}})} \quad (3.83)$$

where a, b, c and d are complex functions of τ and $\tilde{\xi}$ to be determined. From (3.81) it follows that

$$b = \sqrt{2}f(-\tilde{\xi}/\sqrt{2}, \tau)e^{-il}, \quad d = 0 \quad (3.84)$$

and then from (3.82),

$$a + c^* = 0, \quad b + \frac{i}{\sqrt{2}}(a - c^*) = 0. \quad (3.85)$$

Thus

$$a = if(-\tilde{\xi}/\sqrt{2}, \tau)e^{-il}, \quad c = if^*(-\tilde{\xi}/\sqrt{2}, \tau)e^{il} \quad (3.86)$$

and the solution for \tilde{u} is

$$\tilde{u} = (i + \sqrt{2}\eta)fe^{i(-l + \frac{\eta+\xi}{\sqrt{2}})} + (-i + \sqrt{2}\eta)f^*e^{i(l - \frac{\eta+\xi}{\sqrt{2}})} + if^*e^{i(l + \frac{\eta-\xi}{\sqrt{2}})} - ife^{-i(l + \frac{\eta-\xi}{\sqrt{2}})} \quad (3.87)$$

where $f = f(-\tilde{\xi}/\sqrt{2}, \tau)$.

A similar solution can be found in wall region Ib, which occupies the domain $0 \leq \xi \leq \infty, 0 \leq \tilde{\eta} \leq \infty$ where $\tilde{\eta} = \eta/l^{1/2}$. Here

$$u = l^{-9/4}\tilde{u}(\xi, \eta, \tilde{\eta}, \tau) + \dots \quad (3.88)$$

as $l \rightarrow \infty$ where \tilde{u} again satisfies (3.80). Matching with the incident x -roll pattern requires that

$$\tilde{u} \sim \sqrt{2}\xi[f(\tilde{\eta}/\sqrt{2}, \tau)e^{i(-l + \frac{\eta+\xi}{\sqrt{2}})} + f^*(\tilde{\eta}/\sqrt{2}, \tau)e^{-i(-l + \frac{\eta+\xi}{\sqrt{2}})}], \quad \xi \rightarrow \infty \quad (3.89)$$

and the wall conditions (3.2) require that

$$\tilde{u} = \frac{\partial \tilde{u}}{\partial \xi} = 0 \quad \text{on} \quad \xi = 0. \quad (3.90)$$

The relevant solution is

$$\tilde{u} = (i + \sqrt{2}\xi)fe^{i(-l + \frac{\eta+\xi}{\sqrt{2}})} + (-i + \sqrt{2}\xi)f^*e^{i(l - \frac{\eta+\xi}{\sqrt{2}})} + if^*e^{i(l + \frac{\xi-\eta}{\sqrt{2}})} - ife^{-i(l + \frac{\xi-\eta}{\sqrt{2}})}. \quad (3.91)$$

where $f = f(\tilde{\eta}/\sqrt{2}, \tau)$.

The last two terms in (3.87) and (3.91) represent the generation of a y -roll component, a result of the reflection of the incident x -roll pattern at the edges of the square. This y -roll component emerges into the main corner region I where, together with the finite parts of the x -roll component in (3.87) and (3.91), generates a term of order $l^{-9/4}$ in the expansion (3.73):

$$u = l^{-7/4}u_0^- + l^{-9/4}u_1^- + \dots \quad (3.92)$$

as $l \rightarrow \infty$. The solution for u_1^- therefore contains both x and y -roll components associated with complex amplitude functions A_1^- and B_1^- respectively:

$$u_1^- = A_1^-(X_-, Y, \tau)e^{ix} + A_1^{-*}(X_-, Y, \tau)e^{-ix} + B_1^-(X_-, Y, \tau)e^{iy} + B_1^{-*}(X_-, Y, \tau)e^{-iy}. \quad (3.93)$$

The amplitude equations for A_1^- and B_1^- can be derived in the usual way, allowing for the $l^{1/2}$ length scales associated with X and Y , to obtain

$$\frac{\partial^2 A_1^-}{\partial X_-^2} = \frac{\partial^3 A_0^-}{\partial X_- \partial Y^2} \quad (3.94)$$

and

$$\frac{\partial^2 B_1^-}{\partial Y^2} = 0. \quad (3.95)$$

The component A_1^- is just a small correction to the x -roll pattern in the corner region but B_1^- represents the leading-order y -roll component. Boundary conditions for B_1^- are provided by matching with (3.87) and (3.91) at $Y = -X_-$ and $Y = X_-$, respectively. Since $\tilde{\xi} = \sqrt{2}X_-$ at $Y = -X_-$ and $\tilde{\eta} = \sqrt{2}X_-$ at $Y = X_-$, this gives

$$B_1^- = if^*(-X_-, \tau)e^{il} \quad \text{at} \quad Y = -X_- \quad (3.96)$$

and

$$B_1^- = -if(X_-, \tau)e^{-il} \quad \text{at} \quad Y = X_-. \quad (3.97)$$

Thus the required solution of (3.95) is

$$B_1^- = \alpha(X_-, \tau)Y + \beta(X_-, \tau) \quad (3.98)$$

where

$$\alpha = -\frac{i}{2X_-} \{f(X_-, \tau)e^{-il} + f^*(-X_-, \tau)e^{il}\}, \quad (3.99)$$

$$\beta = \frac{i}{2} \{f^*(-X_-, \tau)e^{i\ell} - f(X_-, \tau)e^{-i\ell}\}. \quad (3.100)$$

The solution for B_1^- decays at the inner edge of the corner region because $f(X_-, \tau)$ and $f(-X_-, \tau)$ tend to zero (exponentially) as $X_- \rightarrow \infty$. Thus the y -roll component identified here is confined to the corner region and has no impact on the core expansion. A similar solution can be derived for corner region II at the opposite end of the diagonal. It is observed from (3.99) that α is generally singular as $X_- \rightarrow 0$ so that the solution for B_1^- has a term proportional to Y/X_- as $X_- \rightarrow 0$. This is consistent with the existence of an inner corner region $\eta \sim \xi \sim 1$ formed by the junction of the two wall regions; the details of the solution in this region are not considered here.

For the leading branch of solutions, where the steady-state form of $f = e^{i\theta}F$ is an even function of Y (with F as shown in Figure 3.10) it follows that $\alpha = i\alpha_i$ is purely imaginary and $\beta = \beta_r$ is purely real in (3.99) (3.100). Thus the y -roll component in the corner region has the form

$$u \sim l^{-9/4}(B_1^- e^{iy} + B_1^{-*} e^{-iy}) = 2l^{-9/4}(\alpha_i Y \sin y + \beta_r \cos y) \quad (3.101)$$

and is thus an even function of y . The structure obtained here confirms that the assumptions made in Sections 3.3 and 3.4 concerning the behaviour of the core and corner region solutions are consistent with satisfaction of the wall conditions (3.2). The rigid boundaries of the square require that the core and corner-region amplitude functions tend to zero as the edges of the square are approached, where the motion is weak. The other main effect of the corners is to generate a cross-roll component within a distance of order $l^{1/2}$ of the corner although this is weaker, by order $l^{-1/2}$, than the main roll pattern there.

3.9 Discussion

In this chapter the question of whether the onset of convection in a square domain takes the form of a local solution concentrated along the diagonals has been investigated. A Fourier transform technique is used to derive a closed system governing disturbances which to a first approximation take the form of rolls with axes aligned perpendicular to the diagonals. These

axes extend a distance of order $l^{1/2}$ which is small compared with the size l of the square. The structure is similar to that proposed by Daniels (2000) for the case of an arbitrary domain with a smooth boundary except that here the corners of the square must be taken into account. A local structure has been found that allows the solution to adjust via a main corner region discussed in Section 3.4 and wall regions discussed in Section 3.8 to the full boundary conditions at the walls. An interesting feature of this structure is the generation of a weak cross-roll pattern perpendicular to the main roll pattern.

The asymptotic structure discussed here focuses on one diagonal of the square but because of the local nature of the solution, solutions corresponding to rolls along both diagonals can just be constructed by superposition. Because the two patterns overlap only on a short $l^{1/2} \times l^{1/2}$ length scale at the centre of the square, to leading order they have no effect upon each other at least within the weakly nonlinear regime considered here.

The predicted critical value of ε given by (3.65) compares well with the numerical results of Section 2.4 for large L . The leading order asymptotic theory described here does not distinguish between solutions with EE, OO, OE or D symmetry. It is envisaged that this group of branches in Figure 2.8 has the same critical value of ε to the order given in (3.65) but that the EE, OO and OE/D symmetries will be distinguished by different higher order terms in the expansion (3.65). It is beyond the scope of the present work to carry out the necessary analysis to find these higher order terms.

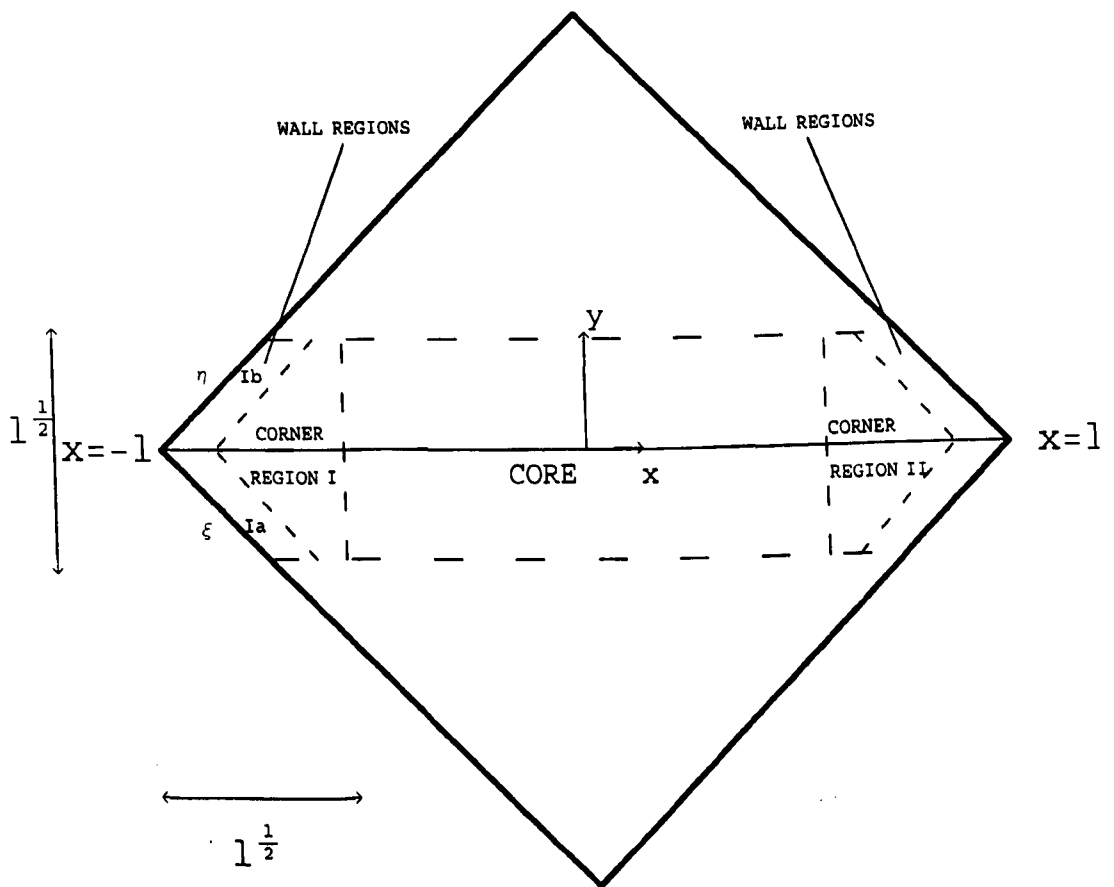


Figure 3.1: Schematic diagram of the asymptotic structure for large L , showing the diagonal from $x = -l$ to $x = l$ and the core region of width order $l^{1/2}$.

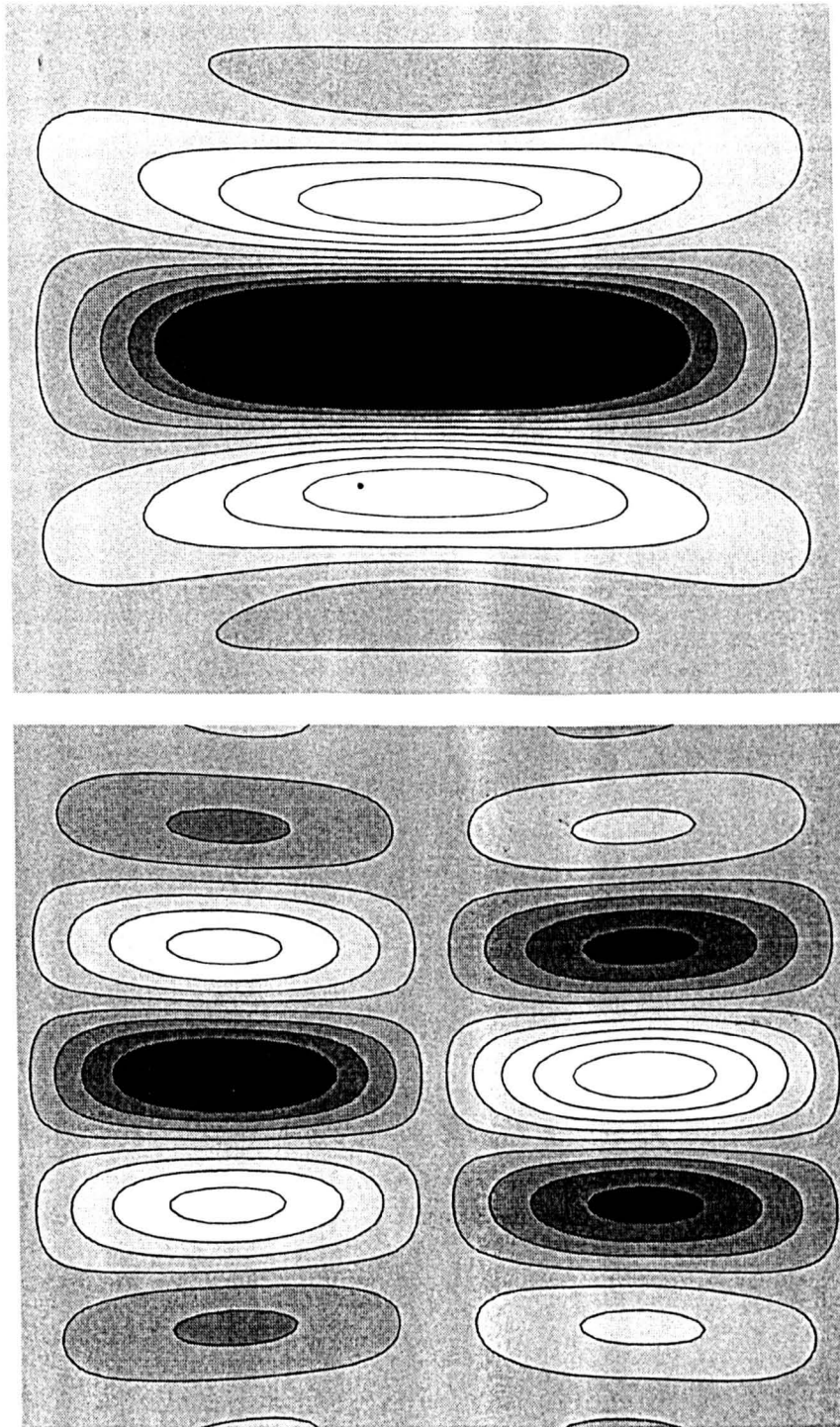


Figure 3.2: Contours of the real and imaginary parts of the amplitude function $A(X, Y)$ in the domain $-1 < X < 1$, $-5 < Y < 5$ for the leading mode at onset ($\delta_1 = 15.5$).

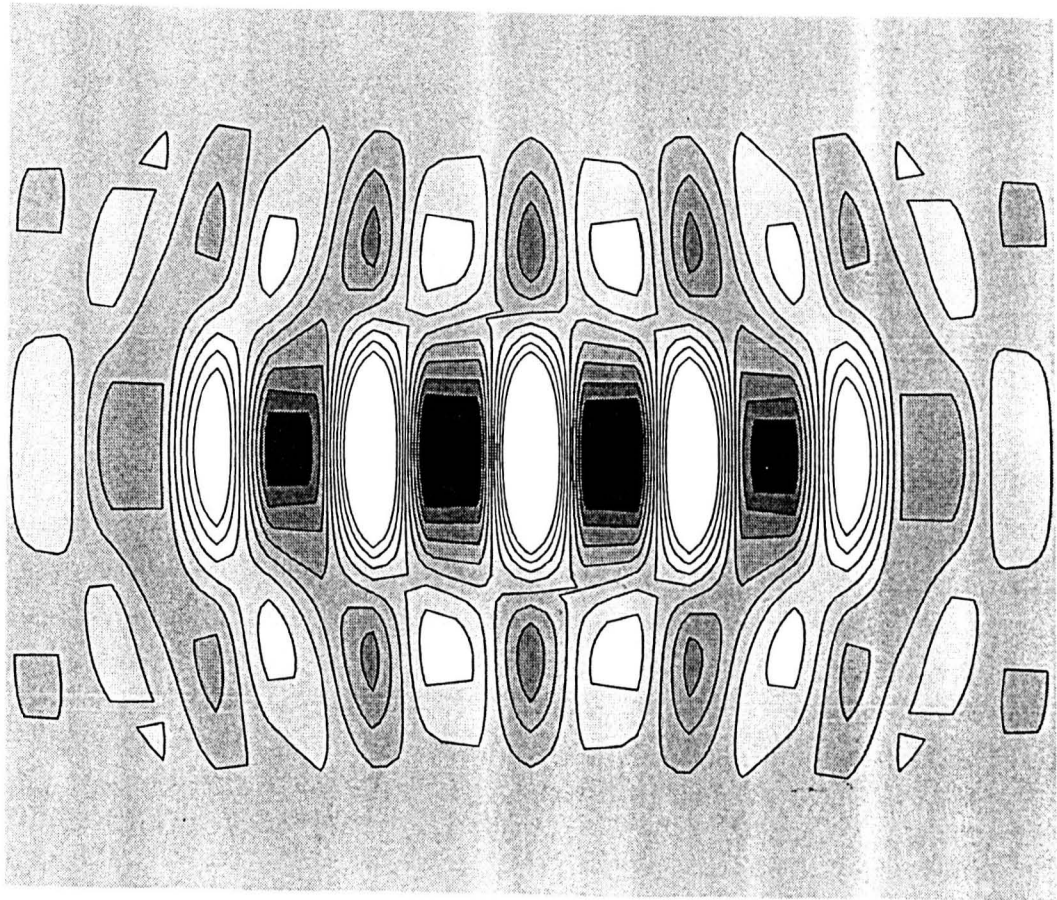


Figure 3.3: Contours of u_0 for the leading eigenfunction constructed from (3.8) with $L = 30$ and $\theta = 0$ in the domain $-1 < X < 1$, $-5 < Y < 5$.

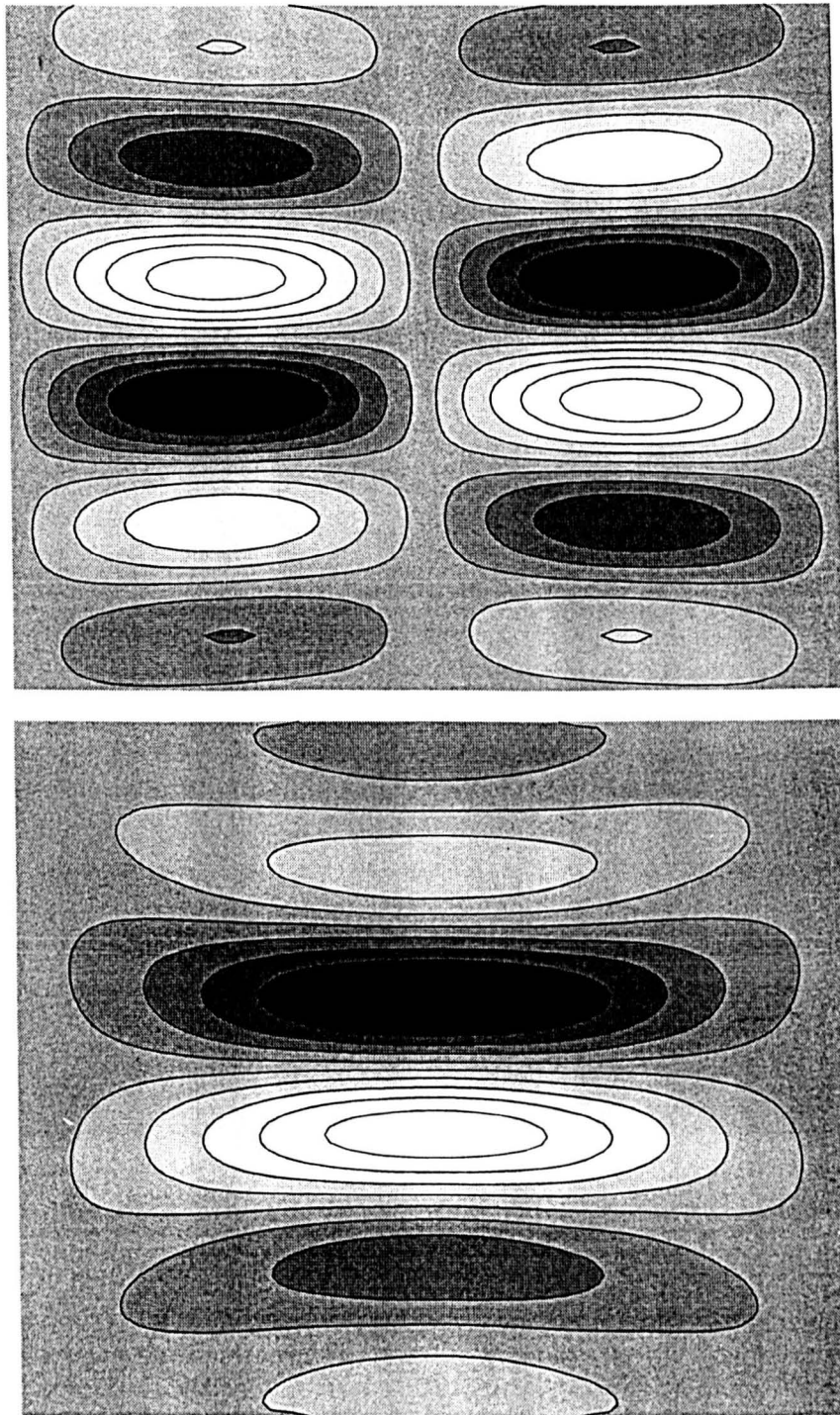


Figure 3.4: Contours of the real and imaginary parts of the amplitude function $A(X, Y)$ in the domain $-1 < X < 1$, $-5 < Y < 5$ for the second mode at onset ($\delta_1 = 31.5$).

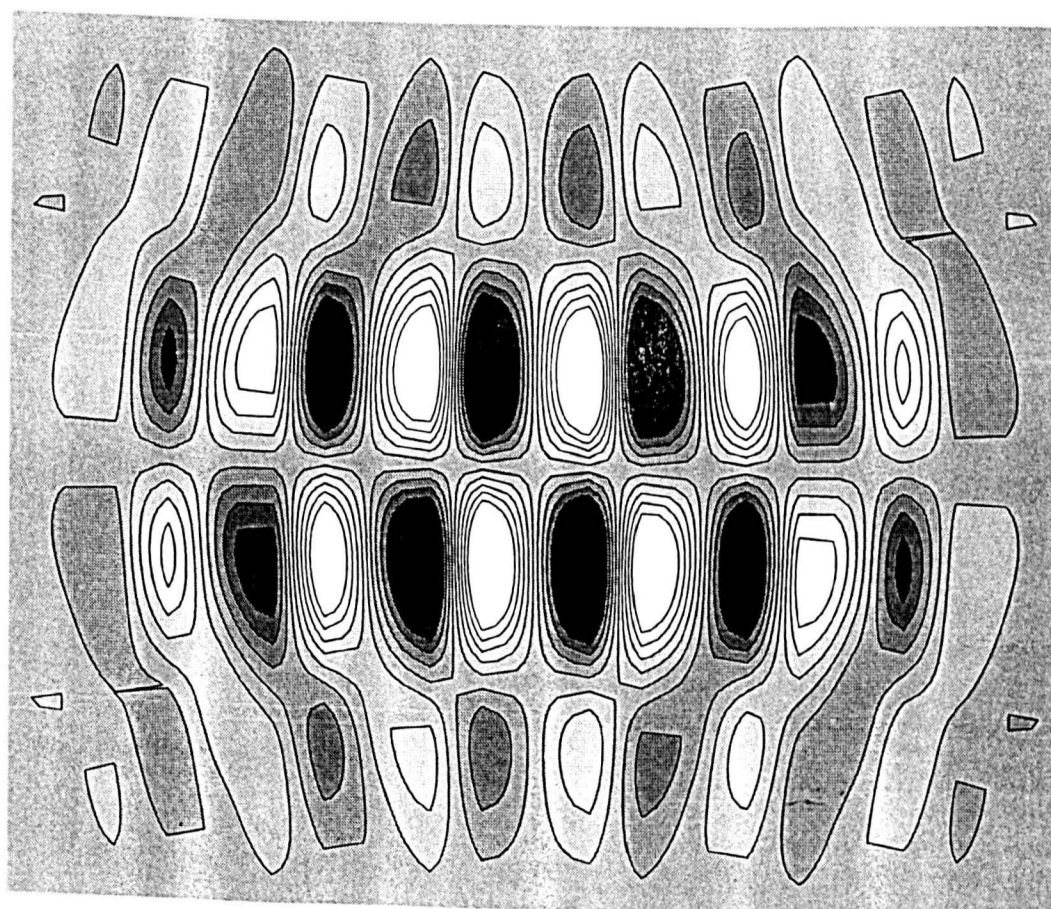


Figure 3.5: Contours of u_0 for the second eigenfunction constructed from (3.8) with $L = 30$ and $\theta = 0$ in the domain $-1 < X < 1$, $-5 < Y < 5$.

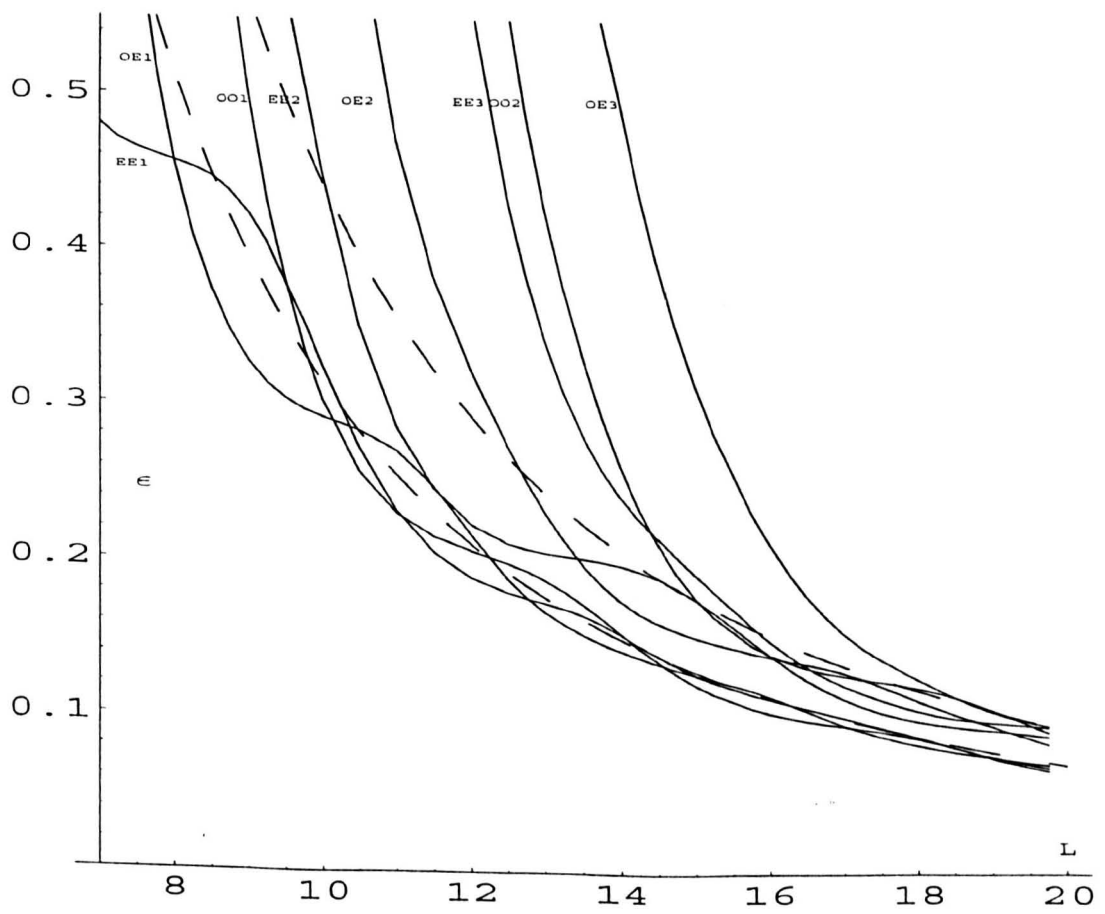


Figure 3.6: Comparison of the asymptotic theory (dashed curves) with the numerical results for the two leading eigenvalues.

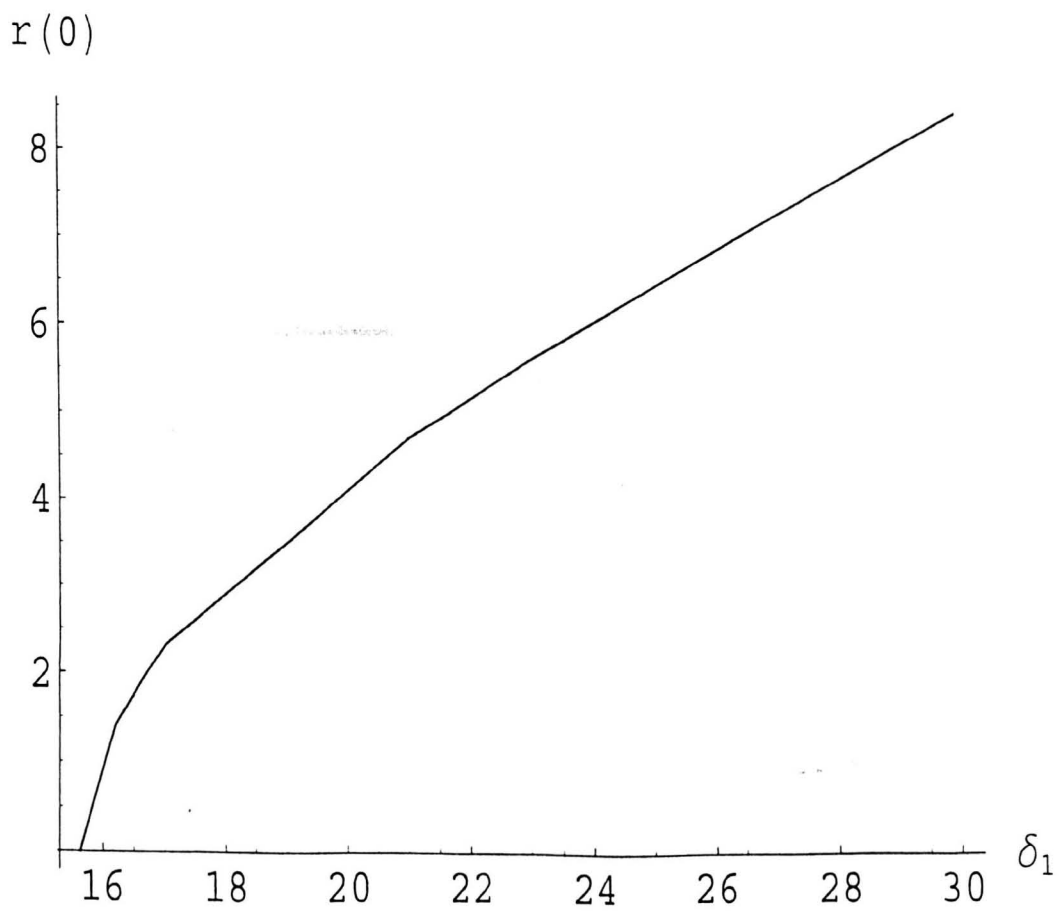


Figure 3.7: $r(0)$ versus δ_1 for the leading branch of solutions.

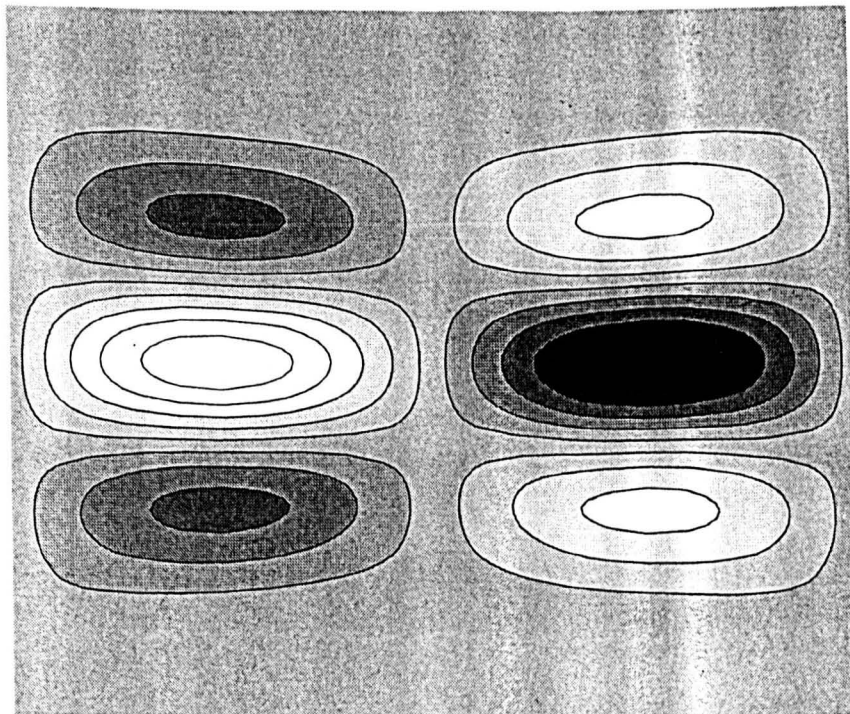
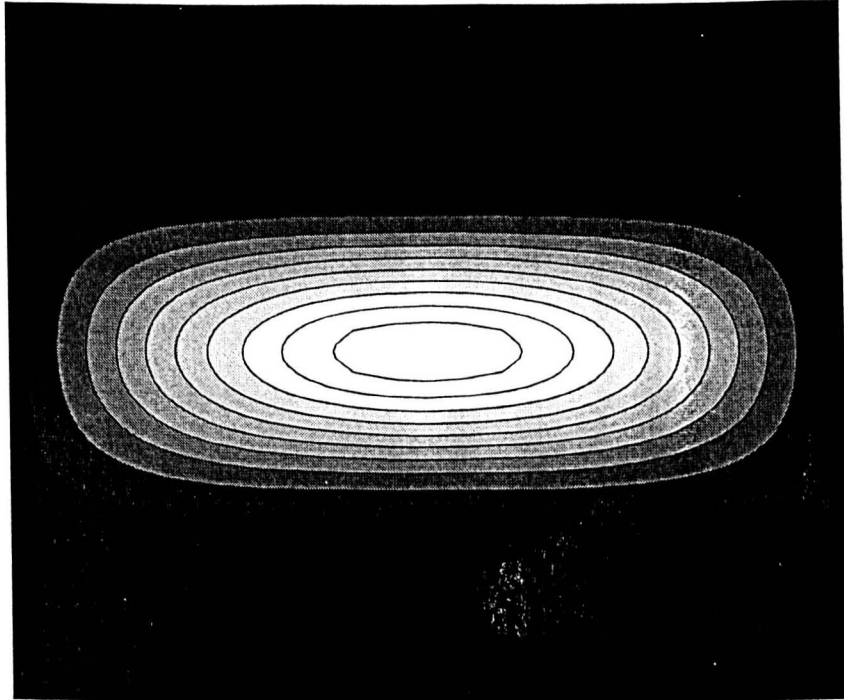


Figure 3.8: Contours of the real and imaginary parts of the amplitude function $A(X, Y)$ in the domain $-1 < X < 1, -5 < Y < 5$ for the leading mode at $\delta_1 = 23$.

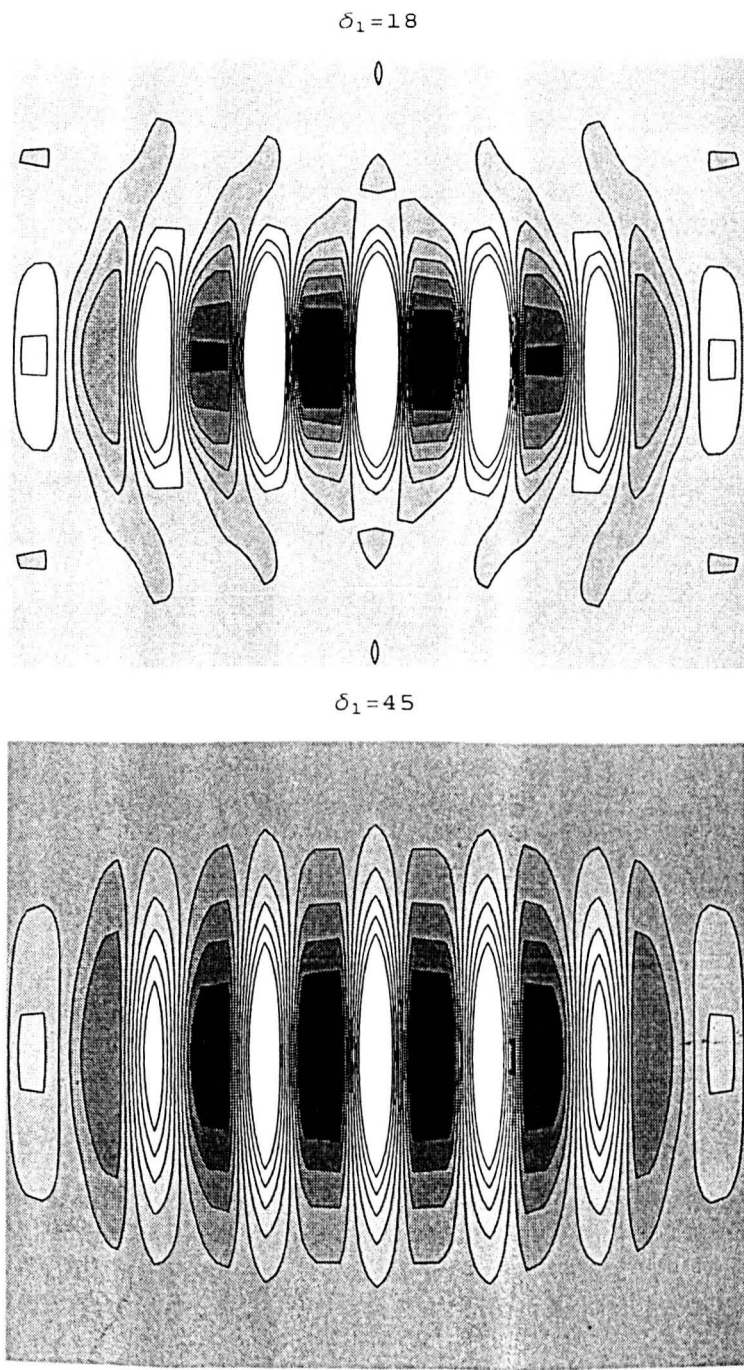


Figure 3.9: Contours of u_0 for $\delta_1 = 18, 45$ on the leading solution branch constructed from (3.8) with $L = 30$ and $\theta = 0$ in the domain $-1 < X < 1, -5 < Y < 5$.

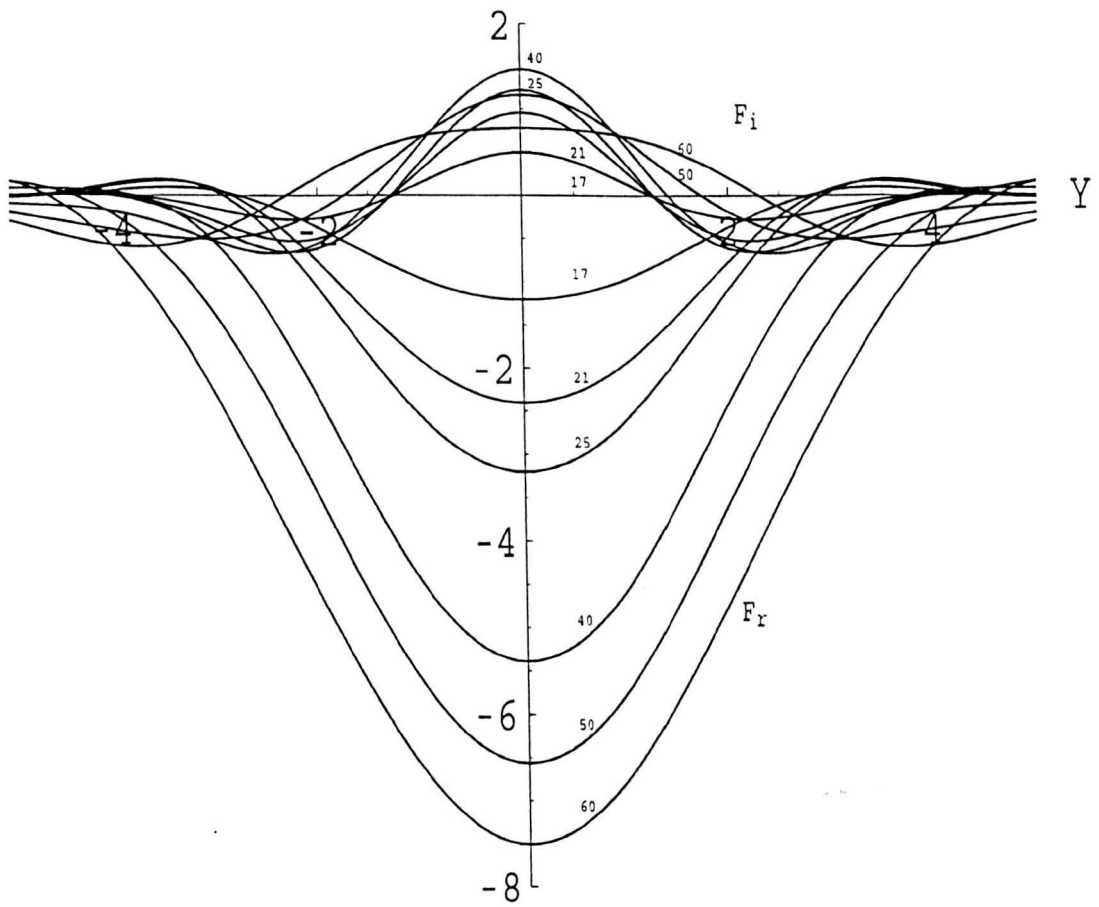


Figure 3.10: Real and imaginary parts of $F(Y)$ for the leading solution branch at $\delta_1 = 17, 21, 25, 40, 50, 60$.

Chapter 4

Convection Patterns in Rectangles

4.1 Introduction

In this chapter the numerical investigation of the rigid problem of Chapter 2 is extended to the case of a rectangular geometry $0 \leq x \leq L, 0 \leq y \leq M$. Detailed results are obtained for two aspect ratios $M/L = 0.75$ and $M/L = 0.5$ and are described in Sections 4.3 and 4.4 respectively. One of the main objectives is to see whether onset now occurs in the form of rolls parallel to the shorter side as in the Galerkin calculations for the equivalent Rayleigh-Bénard problem by Davis (1967) and Catton (1970). Such patterns are also predicted for moderately large planforms (containing up to about 6 rolls) by experiments such as those of Stork and Muller (1972), Buhler, Kirchartz and Oertel (1979) and Kirchartz and Oertel (1988). However for large planforms ($L \rightarrow \infty, M \rightarrow \infty$) the asymptotic theory of Daniels (2000) suggests that at onset rolls may form along the diagonals of the rectangle indicating a possible transition between parallel roll solutions and this more complicated roll structure as L and M become large. The asymptotic theory of Daniels (2000) does not allow for corners and so is not immediately applicable to the case of a rectangle; modifications to the theory similar to those of Chapter 3 to allow for this are considered in Chapter 5.

4.2 Formulation of the problem

The Swift-Hohenberg equation is

$$\frac{\partial u}{\partial t} = \varepsilon u - (1 + \nabla^2)^2 u - u^3, \quad (4.1)$$

where t is the non-dimensional time, $\nabla^2 = \frac{\partial^2}{\partial x^2} + \frac{\partial^2}{\partial y^2}$ where x and y are non-dimensional Cartesian coordinates, ε is a control parameter and $u(x, y, t)$ is a scalar field.

The geometry that we are considering is a rectangle $0 \leq x \leq L$, $0 \leq y \leq M$ with the equivalent of rigid lateral boundaries so that on the boundary u and its derivative normal to the boundary vanish:

$$u = \frac{\partial u}{\partial q} = 0 \quad \text{on} \quad x = 0, L \quad \text{and} \quad y = 0, M. \quad (4.2)$$

Note that here q is used to denote the inward normal direction.

4.3 Results for aspect ratio 0.75

In this section results are described for the case $M/L = 0.75$.

4.3.1 Linear solution

Results were obtained for values of M in the range 6 to 30 using the method described in detail in Section 2.4 and grids of 32×24 . Figure 4.1 shows the eigenvalues ε plotted as a function of M for the first seven modes. The curves in Figure 4.1 are labelled according to their symmetry properties and their order at low values of L . Each branch corresponds to an eigensolution u with EE, OO, OE or EO symmetry. Unlike the square problem, there are no repeated eigenvalues for solutions with EO and OE symmetry and diagonal modes are absent. As L increases, the various branches of Figure 4.1 interweave as a particular mode ‘best fits’ the size of the rectangle. It appears that in the rectangular geometry the most dangerous mode is confined to one of two branches EE1 or OE1 for moderate L . At larger L , the various branches appear to divide into distinct groups - branches EE1, OE1, EO1

and OO1 constitute the first group and members of the second group include branches EE2, OE2, OO2 and EO2. This behaviour is similar to that found for the square problem of Chapter 2.

We now investigate in more detail the patterns corresponding to each of the leading branches specified above, and how they evolve as functions of M . Branch EE1 has EE symmetry and at low values of M consists of a single cell. Contours of the eigenfunction u associated with this branch at various values M are shown in Figures 4.2 and 4.3. It is the dominant mode for $M < 6.48$, for $8.4 < M < 10.1$ and then again when M reaches 12.48; at large M it continues to interweave with branches OE1, EO1 and OO1. The pattern changes in an interesting manner as M increases; in the region $6.48 < M < 8.16$ (where it is not the leading mode) it develops two new cells parallel to the shorter side. In the region $10.24 < M < 12.24$ it develops four new cells in the corners which eventually join up at $M \approx 12.36$ to form two rolls placed parallel to the shorter sides of the rectangle and hence the EE1 mode becomes a (5,1) roll structure. A computation for $M = 30$ (Figure 4.3) shows that the EE1 mode has developed into a roll solution consisting of two main components concentrated along the diagonals of the rectangle.

Branch OE1 contains solutions with OE symmetry, and contours of the solution at various values of M along branch OE1 are shown in Figures 4.4 and 4.5. At low values of M the solution is a 2 - roll parallel mode resembling the solution of Section 2.4 for the square with $L = 5$. The OE1 mode is dominant for $6.48 < M < 8.4$, $10.32 < M < 12.48$ and then again for $14.64 < M < 15.36$. As M increases, the (2,1) OE1 mode gains additional cells in all four corners which in the region $8.88 < M < 9.84$ join up to give a (4,1) parallel mode at $M \approx 9.92$. It repeats this process of adding new cells in corners in the region $12.48 < M < 13.92$ (it is not the dominant mode here) and as a result develops an additional two parallel rolls at $M \approx 12.08$ to become a (6,1) mode. At large M , a diagonal structure emerges similar to that of the EE1 mode.

Branch EO1, which has EO symmetry, is shown in Figures 4.6 and 4.7. It is not the leading mode in the region $6 < M < 15.12$ but reaches the rank of second-most dominant solution at $M \approx 15.12$. At low values of M it is very similar in structure to branch OE1, being a 2-cell (1,2) parallel mode

in the region $6 < M < 8.4$. As we increase M , we gradually observe the formation of four new cells in the corners of the rectangle and by $M \approx 9.84$ we can describe the pattern to be a typical (3,2) structure. At $M \approx 13.8$, the pattern on branch EO1 has again gradually evolved and is now a (5,2) mode. At large L it develops a diagonal structure.

Branch OO1 has OO symmetry and contours of u at various values of M are shown in Figures 4.8 and 4.9. At low values of M the pattern is reminiscent of the (2,2) mode seen in the $L = 5$ square (Section 2.4). Unlike in the square mode, OO1 does not become the dominant mode for moderate M . In the region $10.32 < M < 11.76$ it develops new cells in the corners, sitting at both ends of the diagonals to become a (4,2) mode. When $M = 15.12$, branch OO1 has again grown an extra four new cells and is seen to be a (6,2) solution. For large M it develops a diagonal structure.

The next group of branches also contains solutions with EE, EO, OE and OO symmetry. Figures 4.10, 4.11 and 4.12 show contours of u at various values of M on the branches EE2, EO2 and OE2.

Branch EE2 has EE symmetry and is shown in Figure 4.10. In the region $6 < M < 7.2$, we can describe the pattern on branch EE2 to be a typical (3,1) mode similar to the solution of branch EE1 of Figure 4.2. As we increase M past $M = 7.2$, we can find most interestingly that the outer rolls are growing whilst pinching the middle roll. The outer rolls continue to grow until they manage to merge hence completely annihilating the middle roll. Two new cells, parallel to the longer sides, appear at the top and bottom of the rectangle and the pattern on branch EE2 for $M \approx 9.12$ can be described as a (1,3) parallel roll structure. In the region $12 < M < 15.12$, the solution on branch EE2 loses its appearance as a typical parallel roll pattern by developing six new cells.

Branch EO2 has EO symmetry and contours of u are shown in Figure 4.11. For low M , we can describe the pattern as a (3,2) solution reminiscent of the patterns seen on branch EO1 of Figures 4.6 and 4.7. As we increase M we find the solution on branch EO2 goes through a similar metamorphosis as described above for branch EE2, in that the outer cells grow and force the middle cells to decay. This results in the solution that can be described as a (1,2) parallel roll solution for $M \approx 10.8$. In the region of $10.8 < M < 12.96$,

the pattern develops two new cells parallel to the longest sides and thus branch EO2 has become a (1,4) parallel roll solution. The pattern develops a further four new cells in the region $12.96 < M < 15.12$ and hence loses its parallel roll structure.

Branch OE2 has OE symmetry and solutions are shown in Figure 4.12. Again for low M the pattern on branch OE2 can be described as a (4,1) parallel roll solution but changes appearance as M increases in the same manner as branches EE2 and EO2.

4.3.2 Nonlinear time-dependent solutions

The method described in detail in Section 2.6.1 was used to compute the time evolution of the system for $M = 15.12$ and $M = 30$.

(a) $M = 15.12$

Figures 4.13 - 4.19 show contours of steady-state solutions for the case $M = 15.12$. These were mostly obtained using a 32×24 mesh and a time step Δt of 0.005 with $h = k = 0.63$. Figures 4.13 and 4.14 show contours of u with OE symmetry, which is the solution generally achieved using a random initial profile, $U(x, y) = R(i, j)$ in the region $0.077 < \varepsilon < 0.09$, indicating that it is a stable steady-state. This pattern is a 6-cell parallel structure and is comparable with the pattern of the linearized solution u for $M = 15.12$ of Figure 4.5. For $\varepsilon > 0.09$, the solution would either converge to branch OE1 or alternatively jump to another mode which is described next.

Figures 4.15 and 4.16 show contours of a rather interesting steady-state solution. This solution has centrosymmetry and is a 6-cell mode; it is not directly associated with the linearized solutions of Section 4.3.1.

The patterns of Figure 4.17 were achieved by using the initial profile $U(x, y) = \sin \frac{7\pi x}{L} \sin \frac{\pi y}{M}$. The solution has EE symmetry and is a 5-cell parallel mode. This particular initial profile was chosen in order to establish whether a 7-cell parallel mode with EE symmetry exists nonlinearly (the investigation of Section 4.3.1 did not yield a 7-cell parallel linear mode with EE symmetry for $M = 15.12$). Instead we obtained the 5-cell mode which is comparable with the pattern of the linearized solution u for $M = 15.12$ of Figure 4.3. Having not found a 7-cell parallel mode for $\varepsilon < 0.9$, we tried the same initial

profile in the region $\varepsilon > 2.1$.

Figure 4.18 shows a steady-state with EE symmetry achieved by using the initial profile $U(x, y) = \sin \frac{7\pi x}{L} \sin \frac{\pi y}{M}$ in the region $2.1 < \varepsilon < 2.185$. It is predominantly a 5-roll mode where the first and fifth rolls are pinched towards the corners by small centrally placed cells. This solution is not comparable to any of the linearized solutions of Section 4.3.1.

It was finally established in the region $2.19 < \varepsilon < 2.5$ using the initial profile $U(x, y) = \sin \frac{7\pi x}{L} \sin \frac{\pi y}{M}$ that there exists a 7-roll parallel mode with EE symmetry. The contours of this solution are shown in Figure 4.19.

Figures 4.20-4.22 show several other steady-state solutions with some or no symmetry achieved using a random initial profile $U(x, y) = R(i, j)$ in the region $0.2 < \varepsilon < 2.085$.

(b) $L = 40$

Figures 4.23-4.25 show contours of solutions for the case $M = 30$. These were obtained using a 40×30 grid ($h = k = l$) and a time step Δt of 0.03. Random initial conditions were used for all computations in this subsection and this led to three different steady-state patterns. In some cases the steady-state pattern found at one value of ε was used as an initial state for computations at other values of ε . Figure 4.23 shows a steady-state pattern at $\varepsilon = 0.017$ that is comparable with the contours of the linearized solution of Figure 4.5. This pattern was not found at higher values of ε using a random initial state. Figure 4.24 shows steady solutions for a 13-cell parallel mode with EE symmetry found in the range $0.022 < \varepsilon < 0.135$. In addition a 14-cell centrosymmetric mode is presented in Figure 4.25. The solutions shown in Figures 4.24 and 4.25 are not directly comparable with the linear onset modes of Section 4.3.1.

4.3.3 Nonlinear steady-state solutions

The method described in detail in Section 2.7.1 was used to track steady-state solutions of the system for $M = 15.12$ and $M = 30$.

(a) $M = 15.12$

Figure 4.26 shows a bifurcation diagram of steady-state solutions for the case $M = 15.12$ using a 32×24 mesh with $h = k = 0.63$. The leading

branch bifurcates at $\varepsilon = 0.078$ and consists of a solution with OE symmetry, consistent with the results of Section 4.3.1. Figure 4.27 shows contours of u for the leading branch OE1 of Figure 4.26 at various values of ε . The amplitude \hat{u} defined as

$$\hat{u} = \left(\frac{1}{LM} \int_0^L \int_0^M u^2 dx dy \right)^{1/2} \quad (4.3)$$

increases with ε , and the pattern expands to fill the rectangle as ε is increased, resulting in six well-formed rolls at large ε . This is consistent with the time-dependent results of Figures 4.13 and 4.14. The second branch bifurcates at $\varepsilon = 0.0837$ and has EO symmetry. Figure 4.28 shows contours of u on this branch at various values of ε . This is a (5,2) mode. Again as ε increases the pattern remains the same in general appearance and the amplitude \hat{u} increases. The third branch, branch EE1 of Figure 4.26, has EE symmetry and bifurcates at $\varepsilon = 0.0845$, also consistent with the results of Section 4.3.1. Contours are shown in Figure 4.29. This is the (5,1) mode obtained in the time-dependent results of Figure 4.17. As ε increases the cells seem to fit the rectangle better by losing their curvature and straightening so that the axes of the rolls are parallel to the shorter sides of the rectangle. The fourth branch bifurcates at $\varepsilon = 0.0905$ and has OO symmetry. Figure 4.30 shows contours of u on this branch at various values of ε . This is essentially a (6,2) mode. As ε increases the cells near the shorter sides adopt an "L" shape so that they are perpendicular to both sides of the rectangle. The fifth, sixth and seventh branches (OE2, EE2 and OO2) bifurcate at $\varepsilon = 0.109$, $\varepsilon = 0.117$ and $\varepsilon = 0.124$ respectively, consistent with the linear analysis of Section 4.3.1. Contours of u are shown in Figures 4.31, 4.32 and 4.33.

We now discuss nonlinear solutions which do not bifurcate from the trivial solution. The first nonlinear mode was located by using the steady-state solution found in Section 4.3.2 (Figure 4.14) as the initial guess in the Newton iteration scheme. The entire branch of steady-state solutions could be tracked by incrementing the value of ε backwards and forwards from its initial value. This branch is a secondary bifurcation from the primary mode OE1 which appears at $\varepsilon = 0.0885$ and has centrosymmetry. Its amplitude \hat{u} is larger than that of the primary mode OE1 from which it bifurcates, explaining why it is so prominent in the time-dependent calculations. Contour plots are

shown in Figures 4.34 and 4.35 and demonstrate how the centrosymmetric pattern evolves by breaking the symmetry of the OE pattern. The solution is designated C_S1 (C for ‘centrosymmetric’, S for ‘secondary’) in Figure 4.26. Another solution appears as a fold bifurcation at $\varepsilon = 1.249$. This has EE symmetry and contours of its upper and lower branches, designated EE_F^U1 and EE_F^L2 (F for ‘fold’, U for ‘upper’, L for ‘lower’), are shown in Figures 4.36 and 4.38 respectively. This is the pattern represented in the contour plot of Figure 4.18 in the time-dependent calculations. The patterns on the upper and lower branches differ very little although slight differences are discernible in that the small cells adjacent to the short sides have larger amplitude on the upper branch for comparable ε . The solutions were found by starting from a point on the upper branch and tracking backwards in ε until the vertex of the fold bifurcation was eventually located (using extremely small steps in ε) at $\varepsilon = 1.249$; for lower values of ε the solution converged to mode $EE1$. In order to track the solution down past the vertex and onto the lower branch, the solution at each grid point was regarded as a function of \hat{u} , allowing a linear extrapolation to be used to provide an initial guess for the Newton iteration at the first point on the lower branch. Thereafter, the solution could be tracked forwards in ε , initially using extremely small steps.

Another solution to arise nonlinearly is a fold bifurcation at $\varepsilon = 2.186$. This has EE symmetry and its upper branch, EE_F^U2 is the stable 7-cell parallel mode reported in the time-dependent calculations of Figure 4.19. The lower branch EE_F^L2 also consists of seven cells. Patterns on the upper branch are shown in Figure 4.38 and on the lower branch in Figure 4.39. The solution was tracked around the vertex using the same extrapolation method as for branches EE_F1 .

There will be a number of other nonlinear solutions appearing through secondary and fold bifurcations within the range of ε used for Figure 4.26. However, those described here are likely to be of greatest significance as they give rise to solutions some of which, from the time dependent analysis, are stable states. Figure 4.26 shows that the amplitudes \hat{u} of the various stable modes are extremely close, explaining why the parallel and centrosymmetric modes are all observable in the time dependent calculations. In fact the leading linear mode, which is an OE solution, has largest amplitude only

for a very restricted range of ε ($0.078 < \varepsilon < 0.088$); thereafter solutions containing larger, more coherent cells (diagonal, parallel or curved) are the preferred states of the system.

(b) $M = 30$

A set of results is reported in this subsection for the case of $M = 30$, obtained using a 40×30 grid ($h = k = 1$). Figure 4.40 shows a bifurcation diagram of steady-state solutions that were found. The solutions that bifurcate in the linear regime are discussed first. The first branch bifurcates at $\varepsilon = 0.01696$ and corresponds to a mode with OE symmetry (associated with the onset solution u shown in Figure 4.5). This pattern is also comparable to that found in the time dependent calculations, Figure 4.23. Contour plots of this branch are shown in Figure 4.41. The solution consists of ten curved rolls but with main components distributed along the diagonals and the central region forming three distinct sets of cells, the outer two of which form arcs relative to the larger sides. The second branch, OO1, bifurcates at $\varepsilon = 0.016997$ and at onset consists of two arcs of twelve cells (see Figure 4.9). It was not possible to find nonlinear solutions for this branch using the Newton iteration scheme as the solution would always converge to branch EO1. This may be due to the fact that branches EO1 and OO1 onset very close to each other. The third branch, EO1, bifurcates very close to the second branch at $\varepsilon = 0.017008$ consistent with the linear analysis of Section 4.3.1. At onset the pattern consists of two arcs of eleven small cells. Contour plots for this branch are shown in Figure 4.42. The fourth branch, EE1, bifurcates at $\varepsilon = 0.01724$ and at onset consists of a pattern similar to that of branch OE1. Contour plots for this branch are shown in Figure 4.43. Branches EO1, OO1 and EE1 were not observed in the time dependent calculations and may not be stable, except possibly for a very small range of ε close to onset.

Two nonlinear solutions which do not bifurcate from the trivial solution $u = 0$ were also located. The first of these, C_S1 , consists of a centrosymmetric mode of the type observed in the time dependent calculations (Figure 4.25). This branch does not appear as a fold bifurcation but as a secondary bifurcation from the primary mode OE1 at $\varepsilon = 0.01715$. Its amplitude \hat{u} is larger than that of the primary mode OE1, explaining why this stable mode is seen in the time dependent calculations. Contours of u are shown in Fig-

ures 4.44 and 4.45 describing its interesting metamorphosis from branch OE1 into a diagonally dominant mode. The second nonlinear solution, EE_F1 , is a fold bifurcation at $\varepsilon = 0.0194$ and consists of a 13-roll parallel solution as shown in Figures 4.46 and 4.47. This solution was found first in the time dependent calculations (Figure 4.24, $\varepsilon = 0.037$) suggesting that it is stable. On the lower branch (EE_F^L1) the parallel rolls become curved as ε increases, as shown in the contour plots of Figure 4.47, and the solution is likely to be unstable.

4.4 Results for aspect ratio 0.5

An extensive set of results was also obtained for the case $M/L = 0.5$. These revealed bifurcation structures similar to those of the case $M/L = 0.75$ and some of the main results are shown in Figures 4.48-4.66. Figure 4.48 shows the first seven branches of the eigenvalue ε as a function of M . Interweaving again occurs along with the grouping together of the leading eigenfunctions of each type of symmetry (EE1, OE1, OO1, EO1) as M increases. This process, leading again to diagonal structures at large M , now occurs over a larger range of M because with $M/L = 0.5$ there is less room for the diagonal cell distributions to fit into the rectangle than with $M/L = 0.75$. However for sufficiently large M the same structure emerges. Figures 4.49-4.52 show sequences of patterns on each of the four leading branches. At moderate values of M rolls roughly parallel to the shorter side of the rectangle are the preferred pattern.

Figures 4.53-4.59 show nonlinear steady-state patterns obtained at various values of ε as a result of time-dependent computations from a random initial state with $M = 10$. These include EE and OE states (Figures 4.53, 4.54), centrosymmetric states (Figure 4.55), solutions even in one dimension only (Figures 4.56) and solutions with no symmetry (Figures 4.57-4.59). Corresponding results for $M = 30$ include an EE steady state shown in Figure 4.60 and a centrosymmetric steady state shown in Figure 4.61. Figures 4.62-4.66 show nonlinear steady-state solutions tracked using the Newton iteration code. A bifurcation diagram showing the leading EE, OE and OO modes for the case $M = 10$ is shown in Figure 4.62 and two fold bifurcations associated

with centrosymmetric modes (C_F1) and (C_F2) are shown in Figures 4.63 and 4.64. A bifurcation diagram for the case $M = 30$ is shown in Figure 4.65 and contour plots for the leading mode OE1 and the centrosymmetric mode C_S1 which is a secondary bifurcation from OE1 are shown in Figure 4.66.

4.5 Discussion

The steady-state structure and time-evolution of solutions of the Swift-Hohenberg equation in a rectangular domain $0 \leq x \leq L$, $0 \leq y \leq M$ with rigid boundary conditions have been investigated. Results have been obtained for a range of values of L and M focusing on two aspect ratios $M/L = 0.75$ and $M/L = 0.5$.

As far as the linearized eigensolutions are concerned the main difference from the four-fold symmetric case of the square is that solutions now arise with the four distinct symmetries EE, OO, OE and EO. The critical values ε for these solutions interweave as functions of M forming into groups of four as $M \rightarrow \infty$. At low and moderate values of M the preferred patterns are typically parallel roll solutions consistent with the original theoretical predictions for the Rayleigh-Bénard system by Davis (1967) and Catton (1970) and with experiments such as those by Stork and Muller (1972) and others.

At large M the preferred linear patterns develop into the more complex diagonal structures of the type already discussed for the square domain. However as ε increases above critical this quickly gives way to a more diagonally dominant centrosymmetric structure typically via a secondary bifurcation of the type illustrated in Figures 4.45 and 4.66. This centrosymmetric pattern dominated by one diagonal is consistent with the type of steady-state solutions found by Greenside and Coughran (1984, figure 10) in a large planform rectangular domain.

For more moderate values of M , roll patterns parallel to the shorter sides tend to be one of the preferred states and may develop as nonlinear solutions either from the linear eigensolutions of the system or as fold bifurcations at supercritical values of ε . As ε increases, strongly aligned parallel roll states with differing numbers of rolls become available and these can also be subject to cross-roll effects near the shorter ends. Stable centrosymmetric solutions

also occur as ε increases at moderate values of M as do more complex asymmetric patterns. In general the preference is for coherent roll structures (as opposed to individual cells) with straight rolls parallel to the shorter sides particularly prevalent for moderately sized planforms and diagonally oriented curved roll structures prevalent for large planforms. An asymptotic analysis for large planform rectangular domains is undertaken in the next chapter.

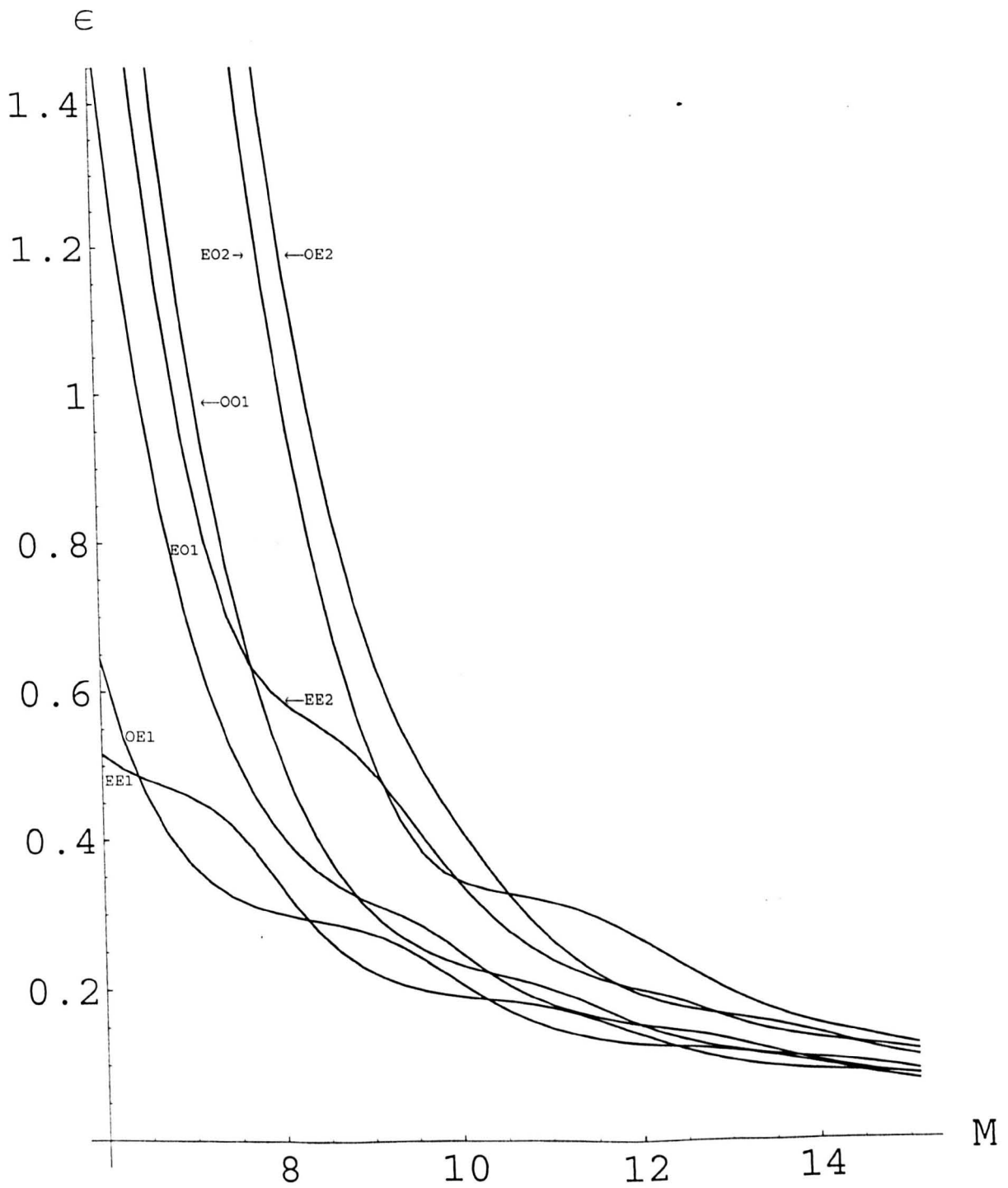


Figure 4.1: The first seven branches of the eigenvalues ϵ as functions of M for $M/L = 0.75$ obtained using a 32×24 grid.

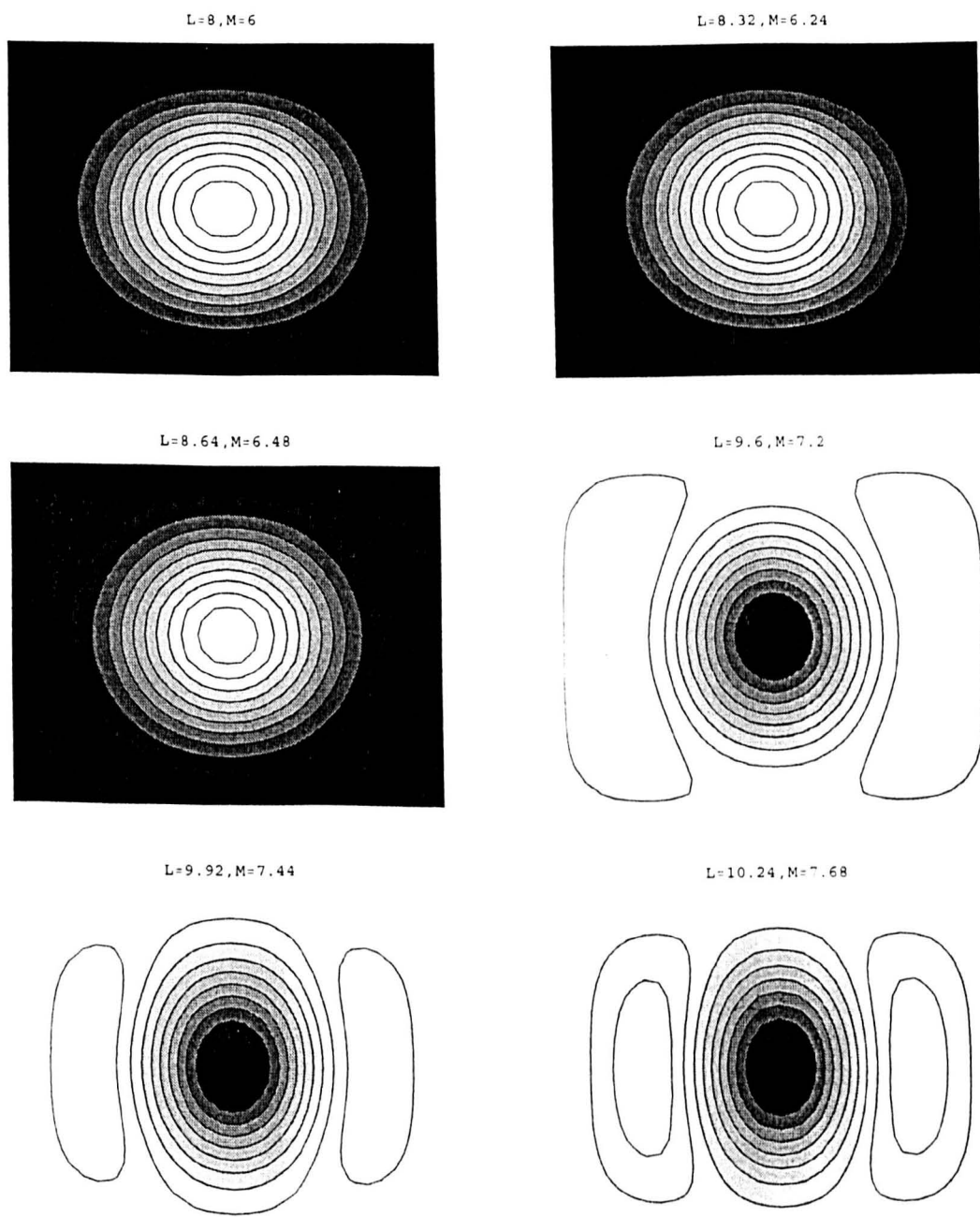


Figure 4.2: Sequence of patterns on branch EE1 for $M = 6.624, 6.48, 7.2, 7.44, 7.68$.

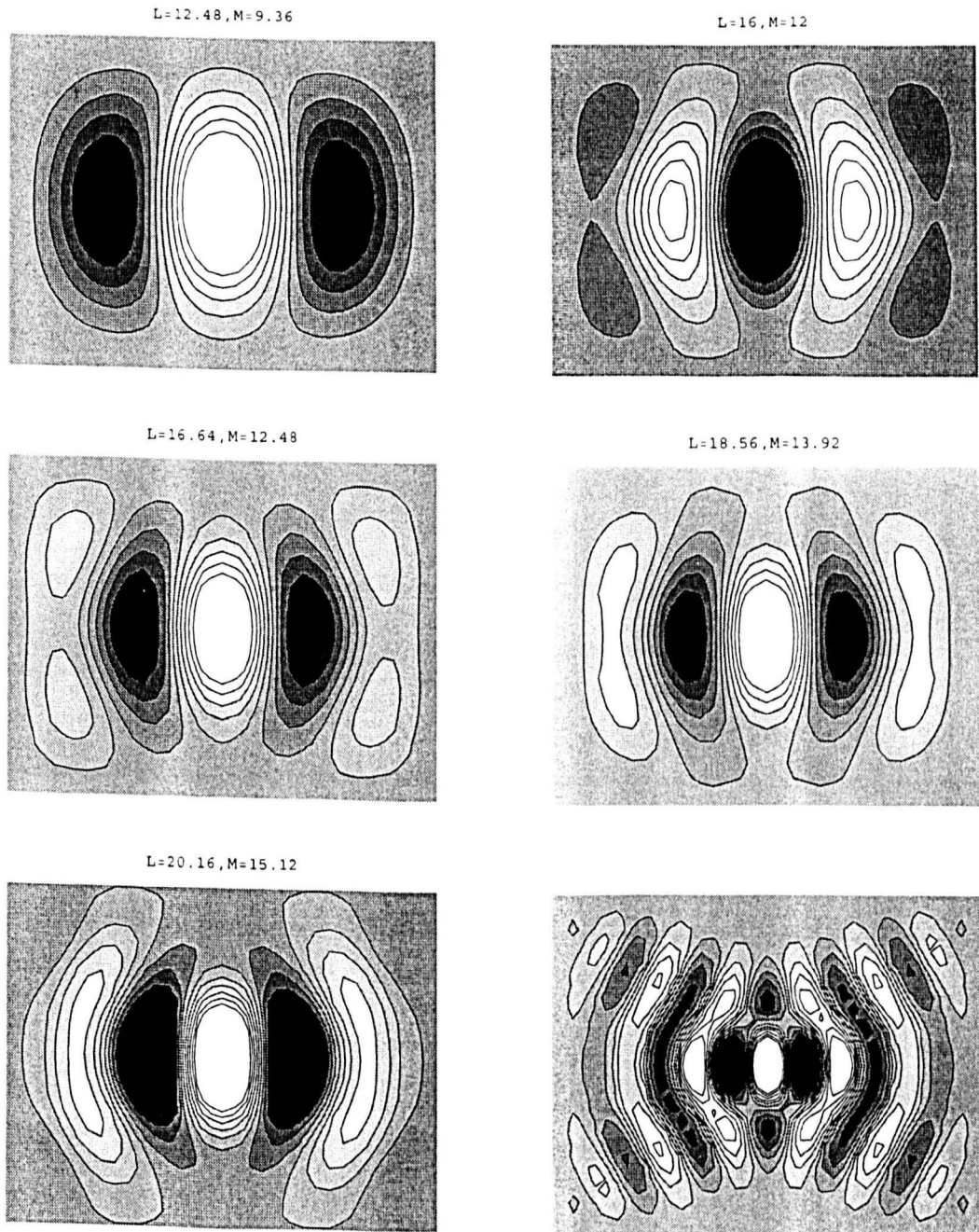


Figure 4.3: Sequence of patterns on branch EE1 for $M = 9.36, 12, 12.48, 13.92, 15.12, 30$.

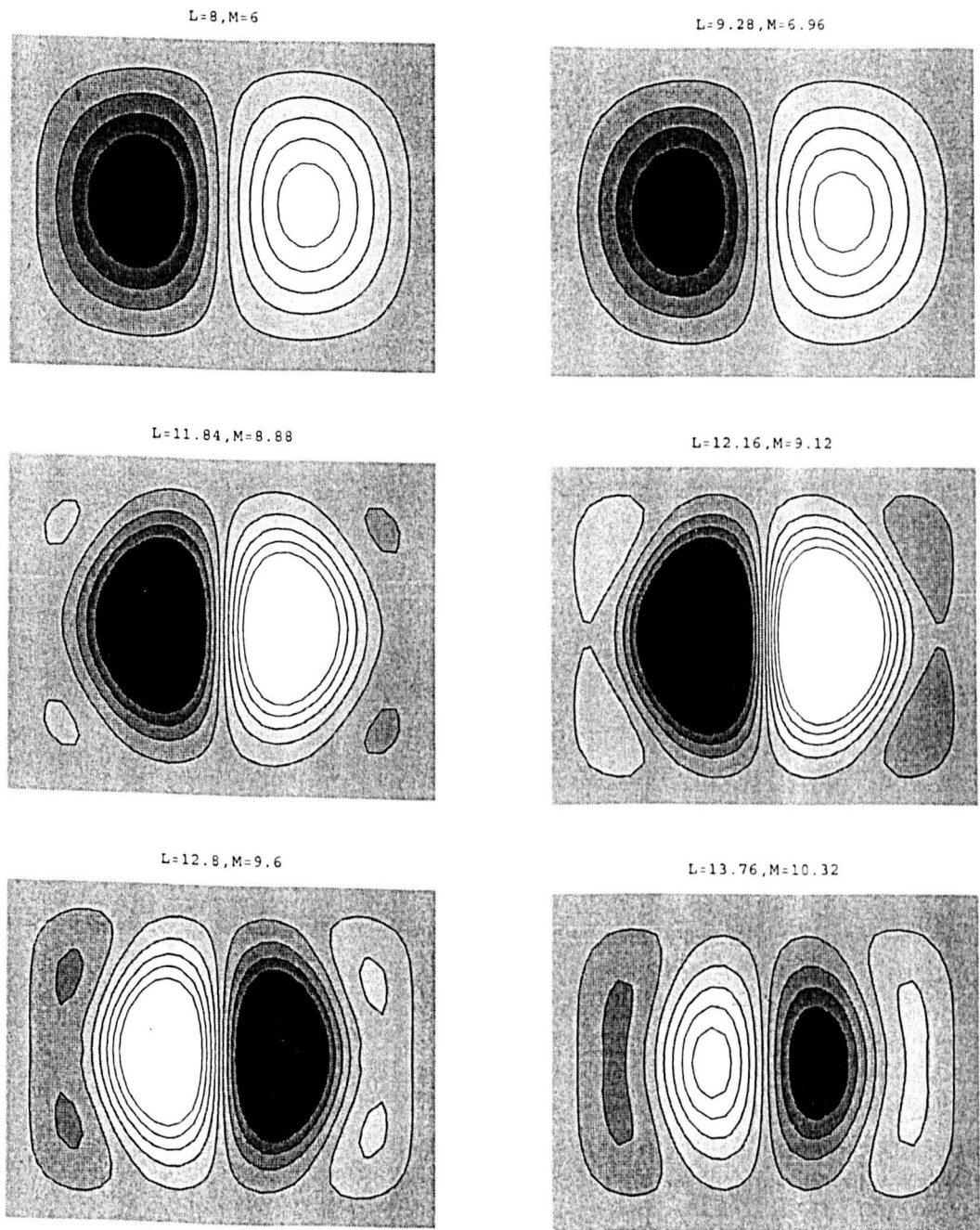


Figure 4.4: Sequence of patterns on branch OE1 for $M = 6.696, 8.88, 9.12, 9.6, 10.32$.

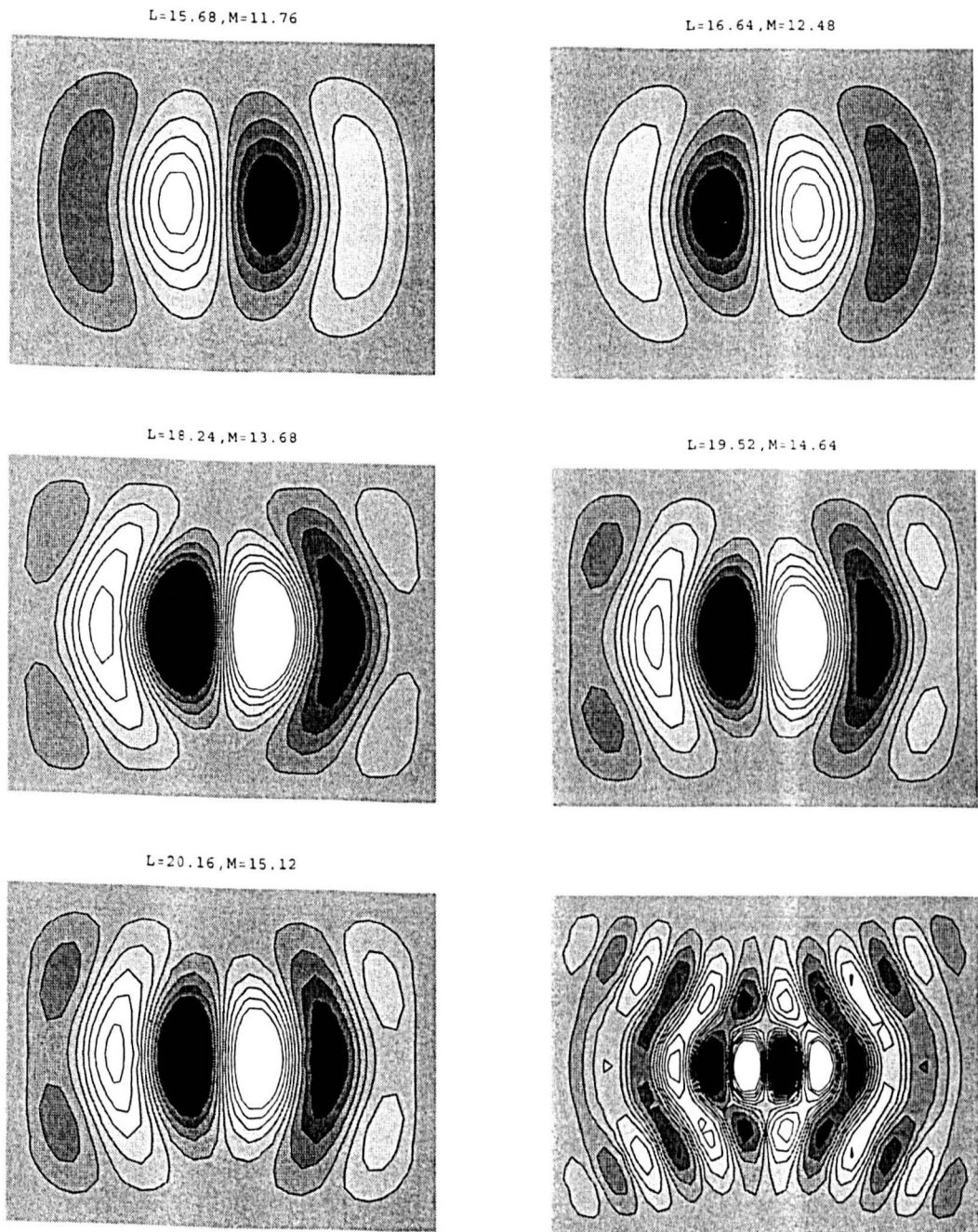


Figure 4.5: Sequence of patterns on branch OE1 for $M = 11.76, 12.48, 13.68, 14.64, 15.12, 30$.

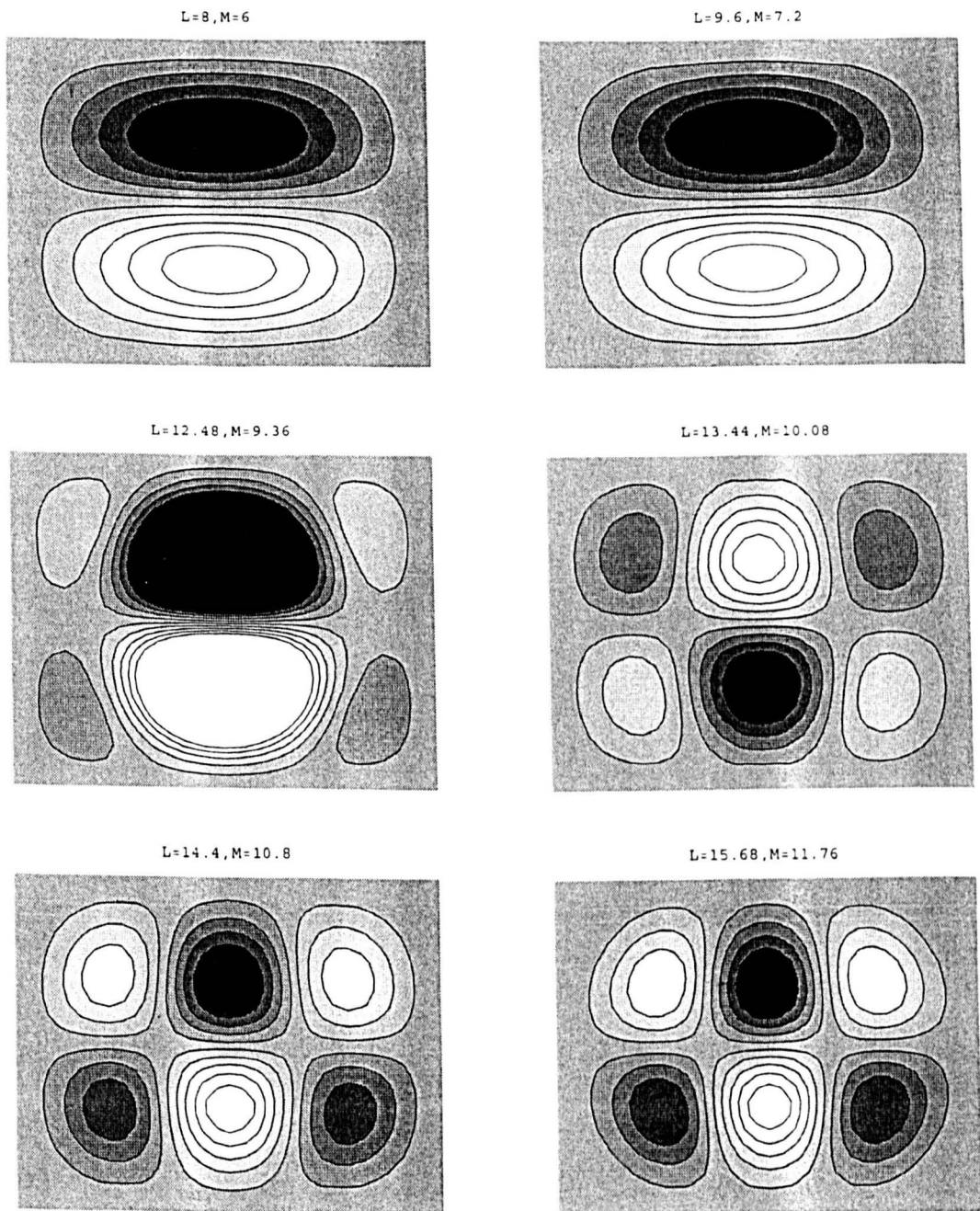


Figure 4.6: Sequence of patterns on branch EO1 for $M = 6, 7.2, 9.36, 10.08, 10.8, 11.76$.

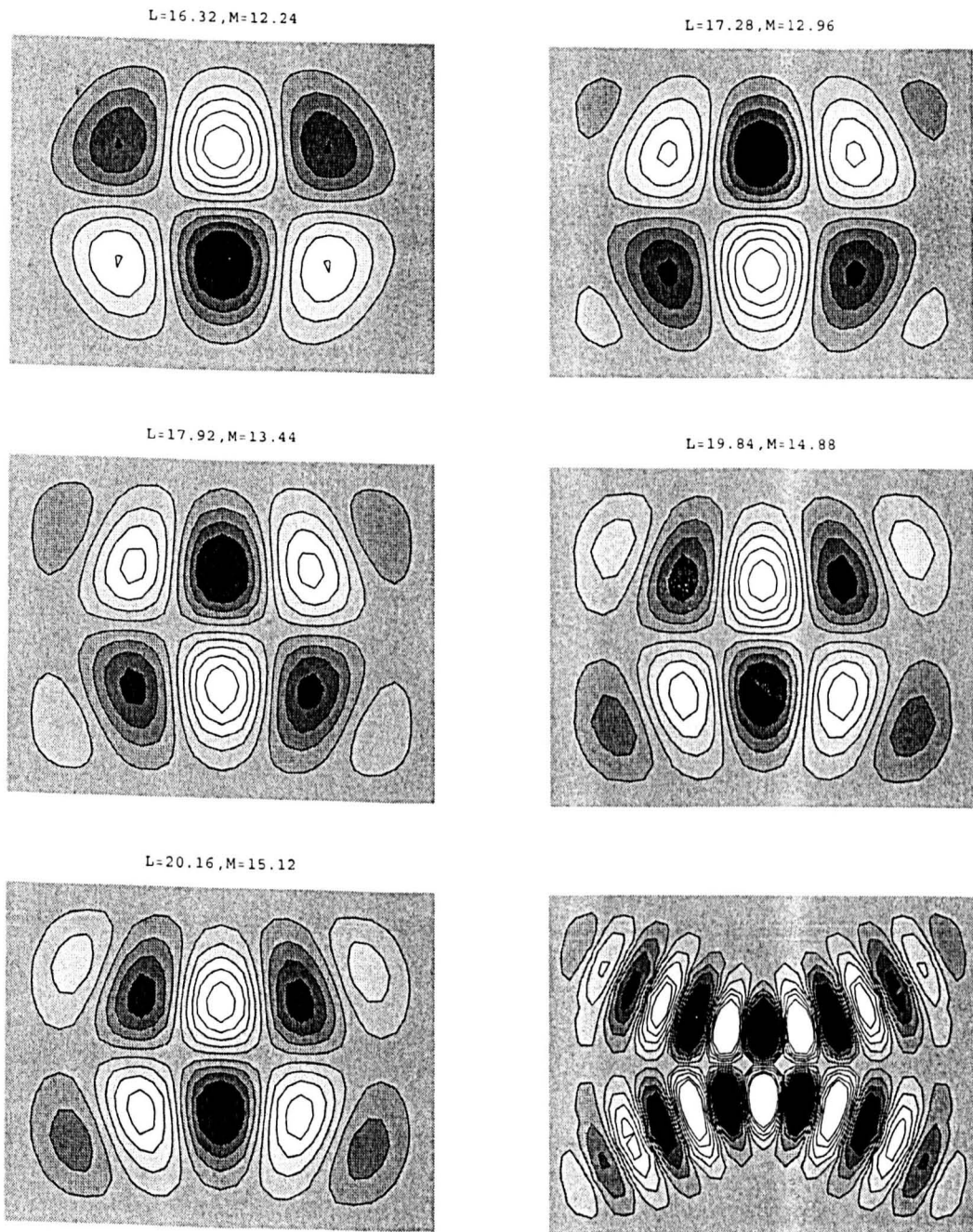


Figure 4.7: Sequence of patterns on branch EO1 for $M = 12.24, 12.96, 13.44, 14.88, 15.12, 30$.

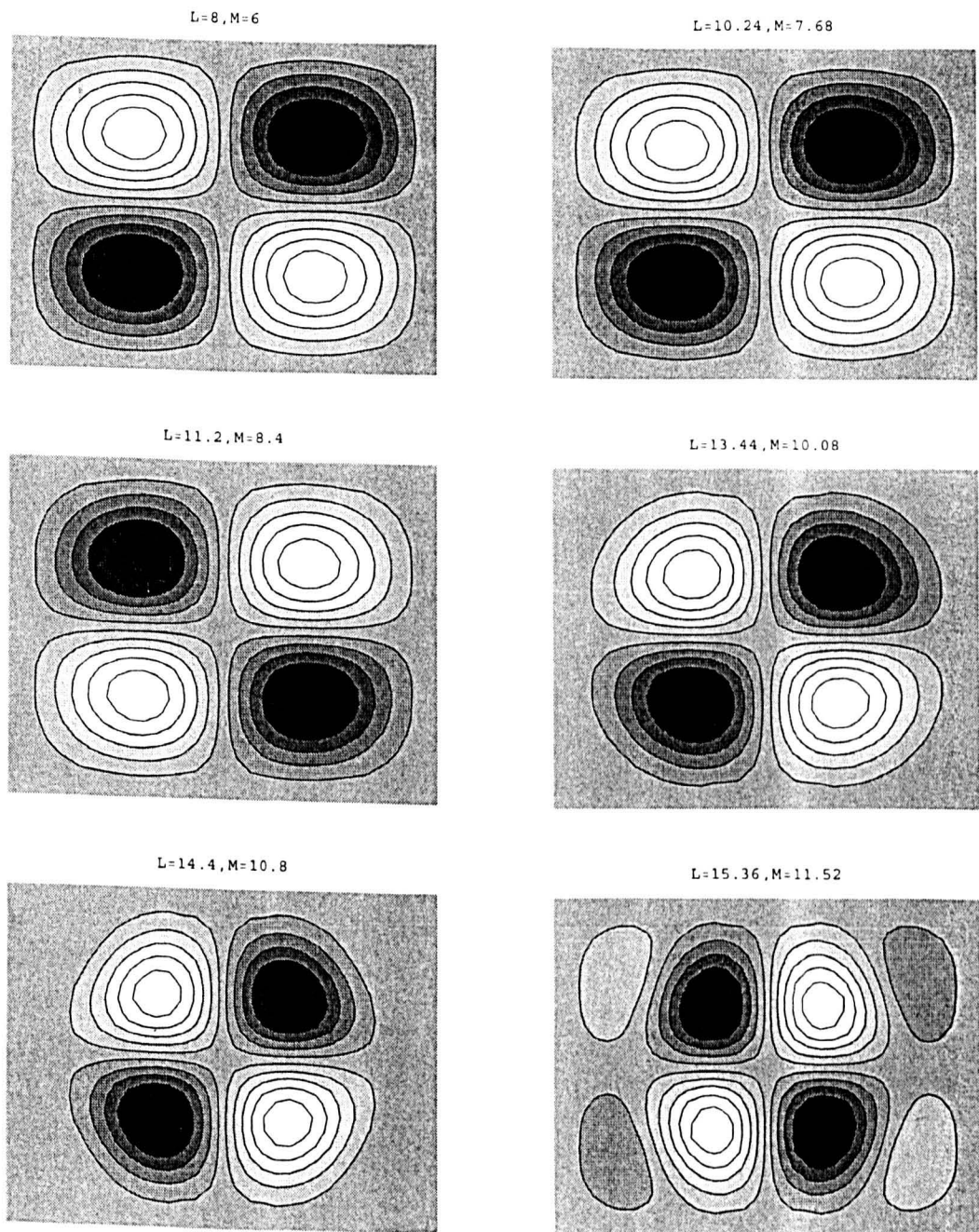


Figure 4.8: Sequence of patterns on branch OO1 for $M = 6, 7.68, 8.4, 10.08, 10.8, 11.52$.

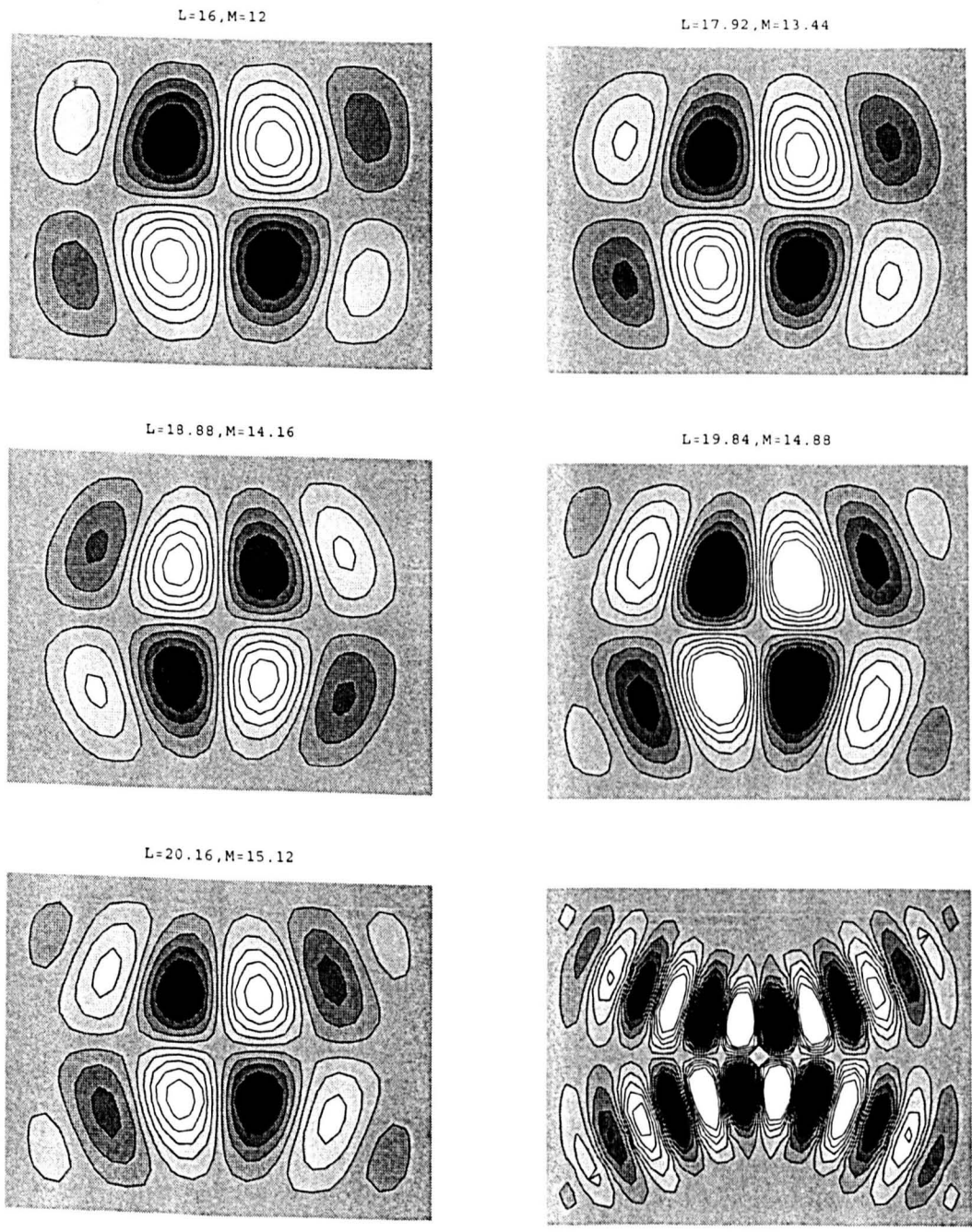


Figure 4.9: Sequence of patterns on branch OO1 for $M = 12, 13.44, 14.16, 14.88, 15.12, 30$.

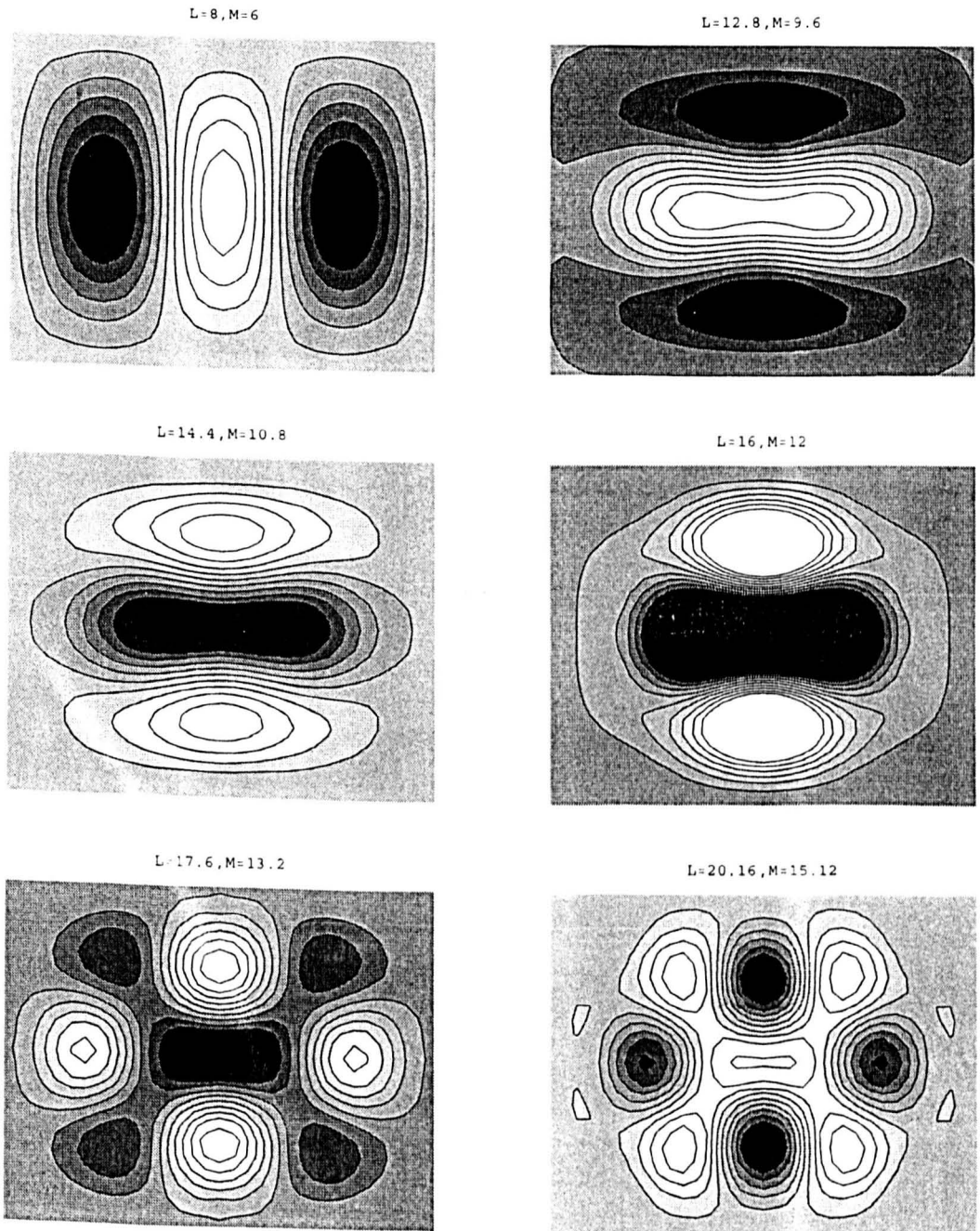


Figure 4.10: Sequence of patterns on branch EE2 for $M = 6, 9.6, 10.8, 12, 13.2, 15.12$.

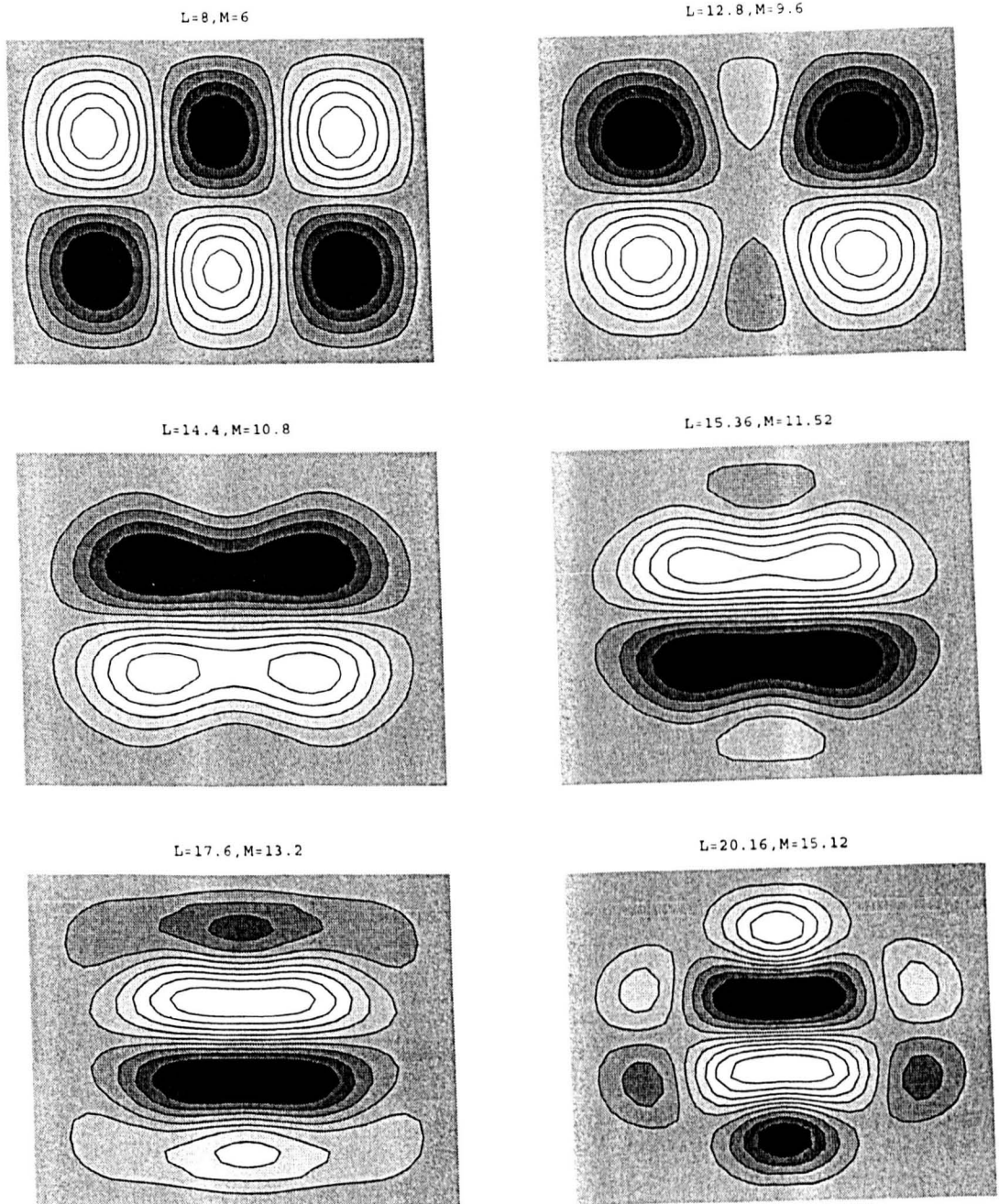


Figure 4.11: Sequence of patterns on branch EO2 for $M = 6.9.6, 10.8, 11.52, 13.2, 15.12$.

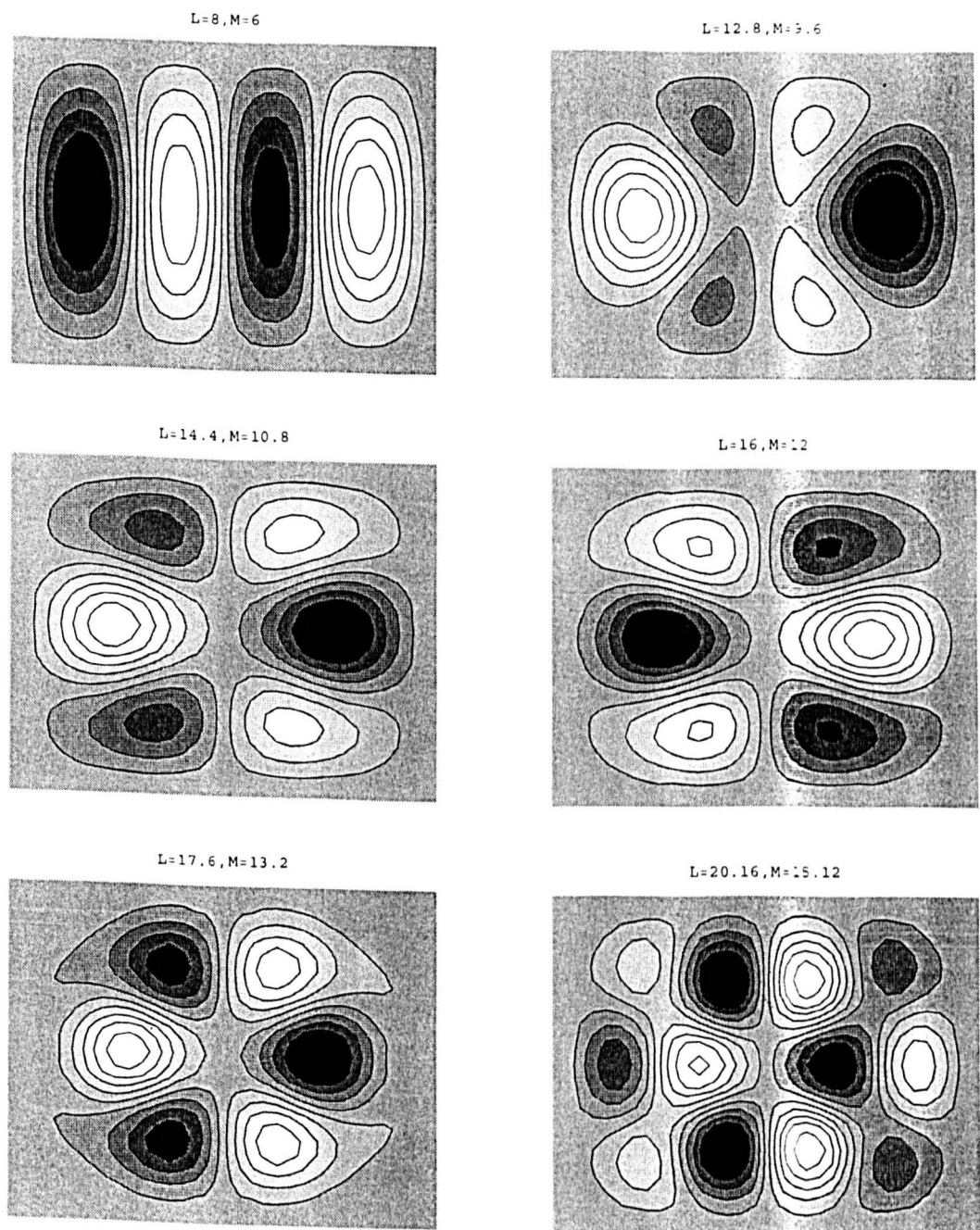


Figure 4.12: Sequence of patterns on branch OE2 for $M = 6.9.6, 10.8, 12, 13.2, 15.12$.

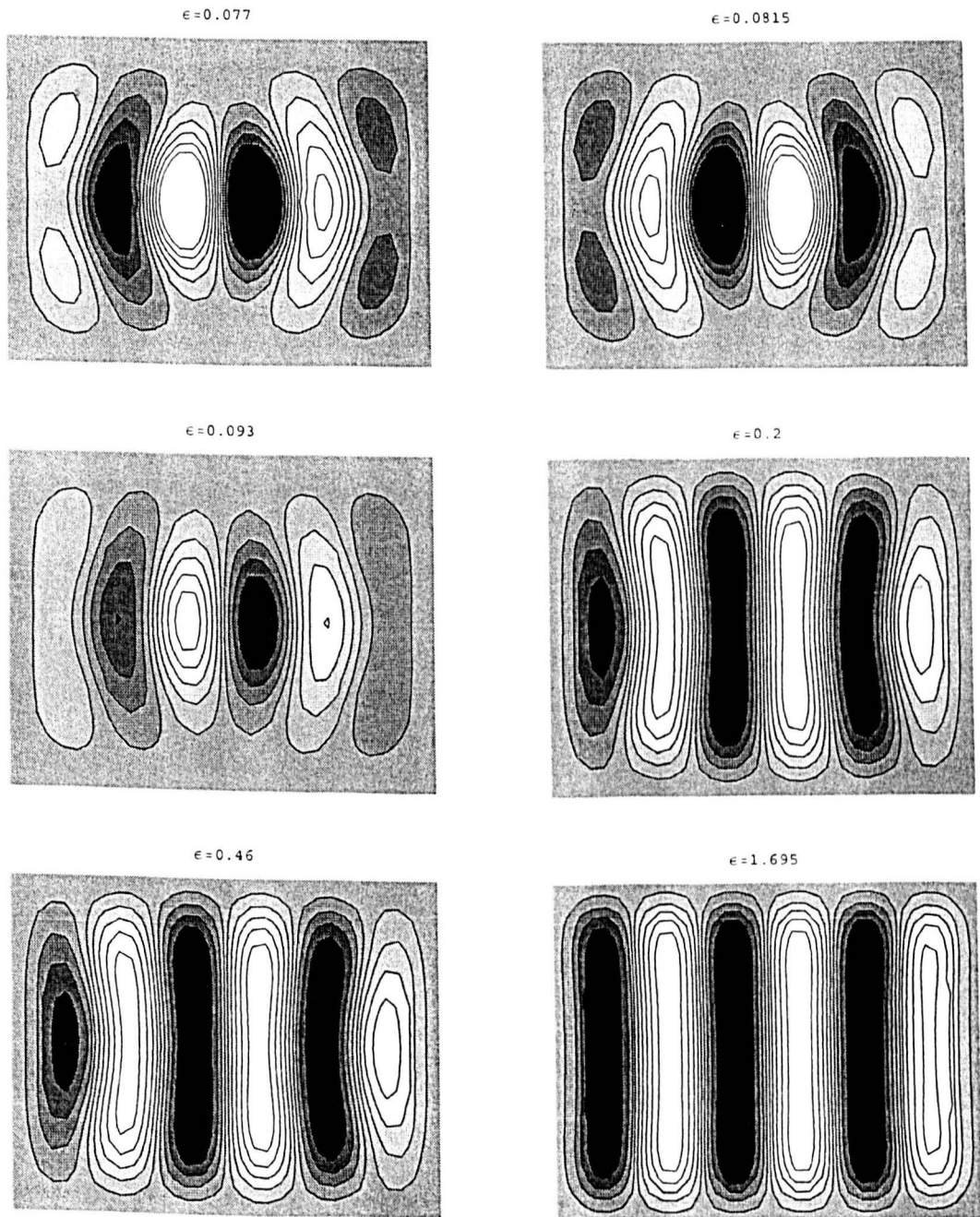


Figure 4.13: Contours of steady-state solutions u for $M = 15.12$ obtained with an initial state $U(x, y) = R(i, j)$.

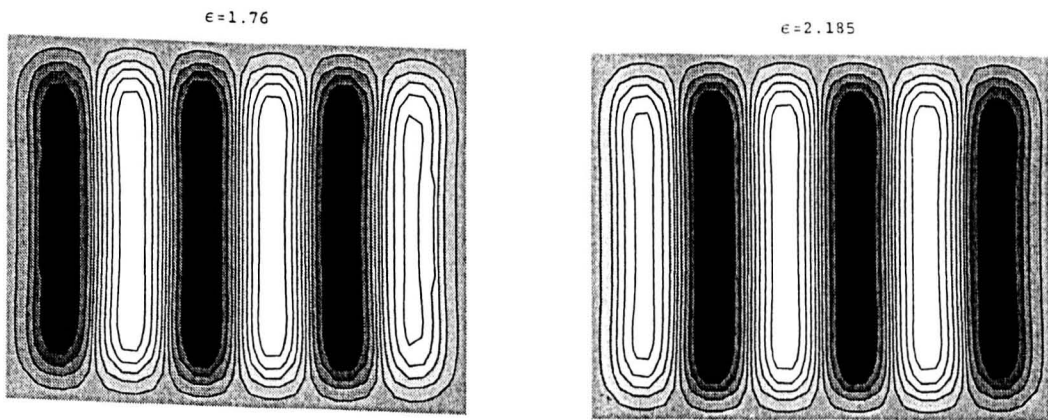


Figure 4.14: Contours of steady-state solutions u for $M = 15.12$ obtained with an initial state $U(x, y) = R(i, j)$.

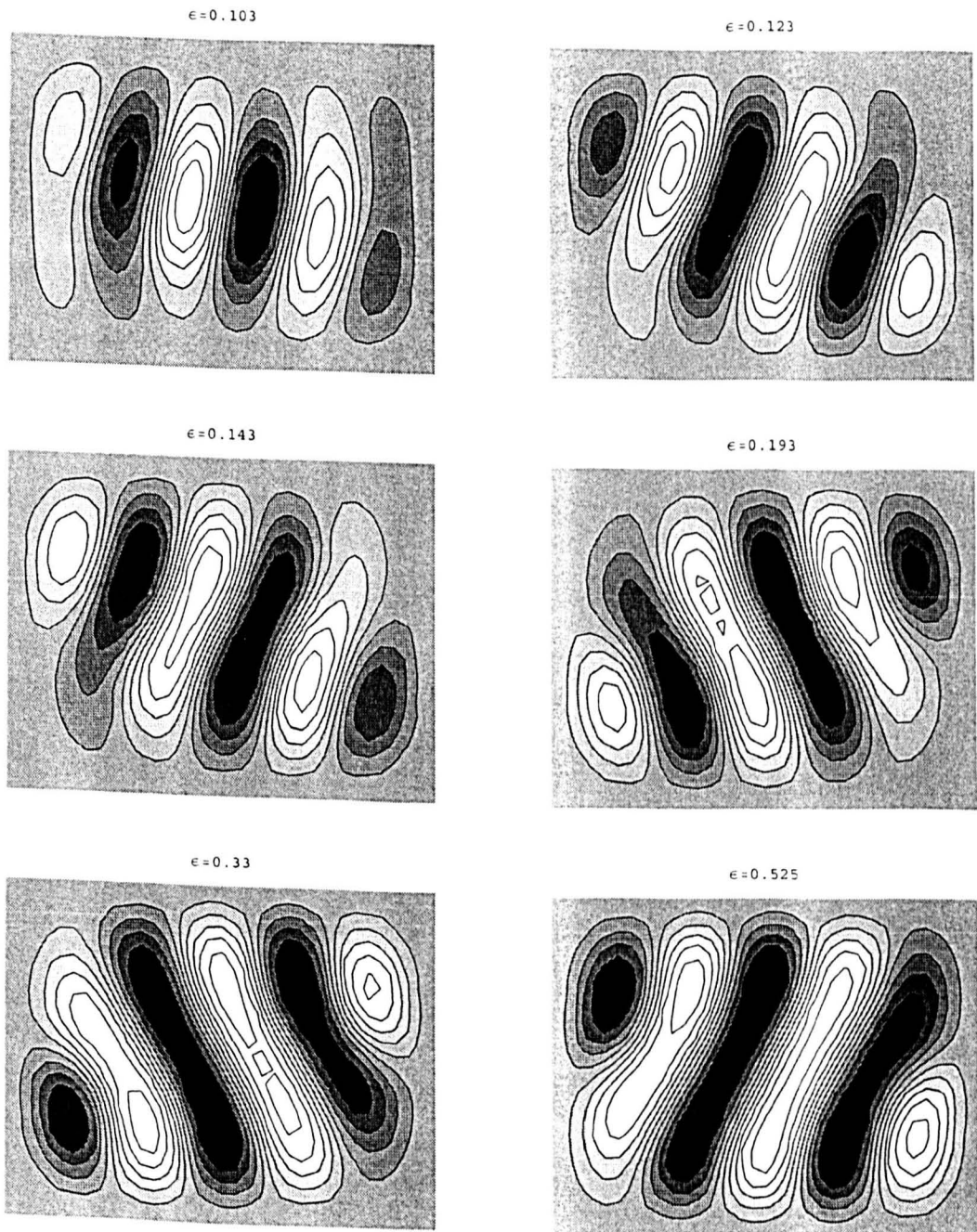


Figure 4.15: Contours of steady-state solutions u for $M = 15.12$ obtained with an initial state $U(x, y) = R(i, j)$.

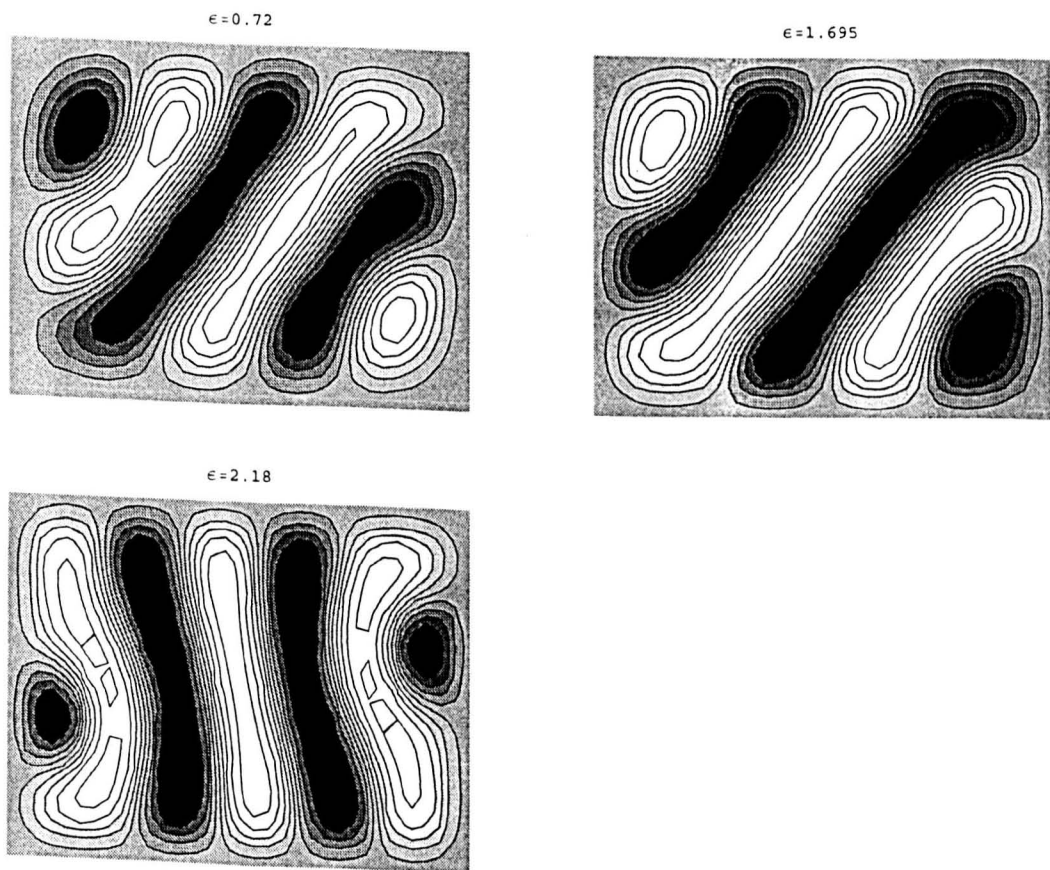


Figure 4.16: Contours of steady-state solutions u for $M = 15.12$ obtained with an initial state $U(x, y) = R(i, j)$.

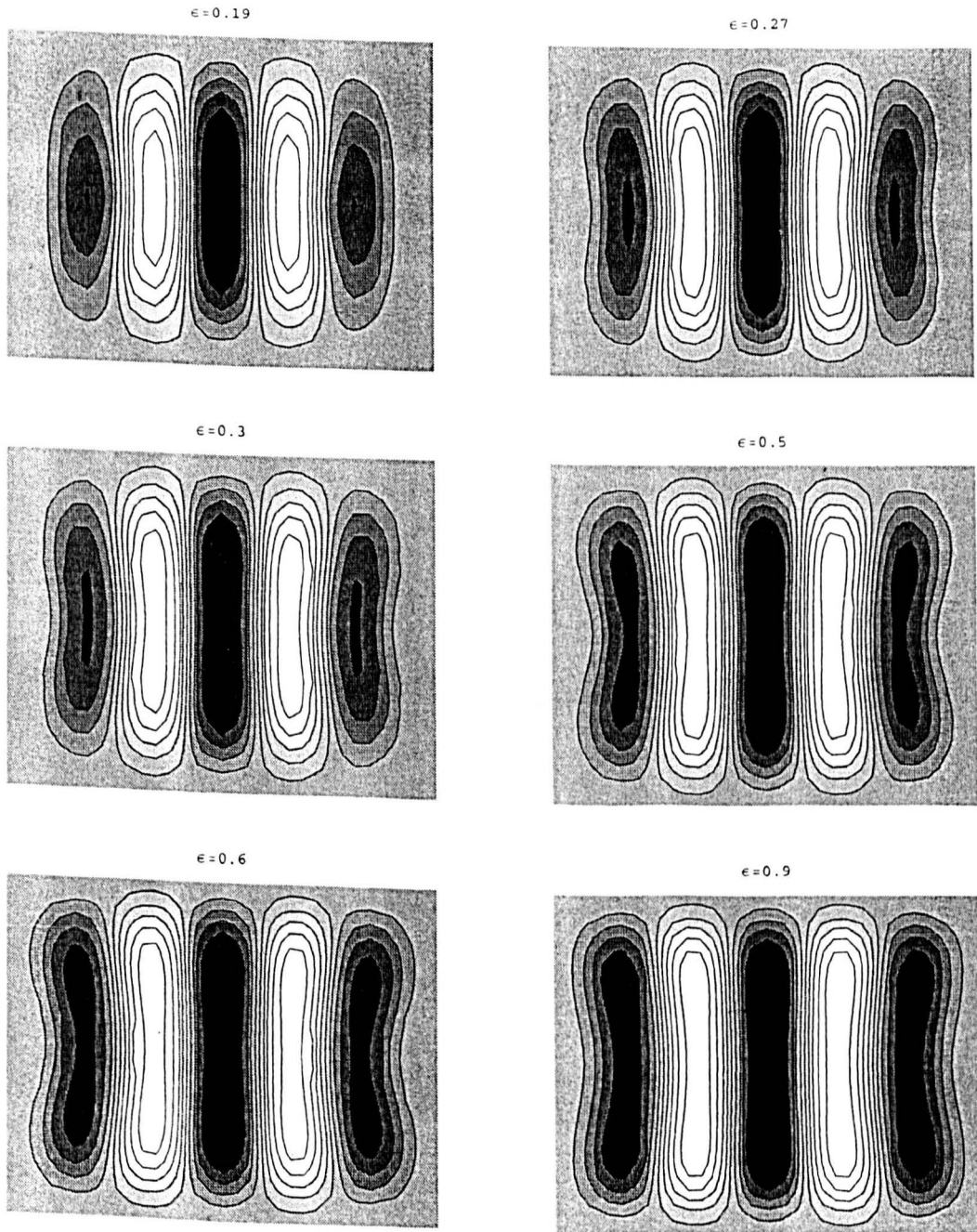


Figure 4.17: Contours of steady-state solutions u for $M = 15.12$ obtained with an initial state $U(x, y) = \sin \frac{7\pi x}{L} \sin \frac{\pi y}{M}$.

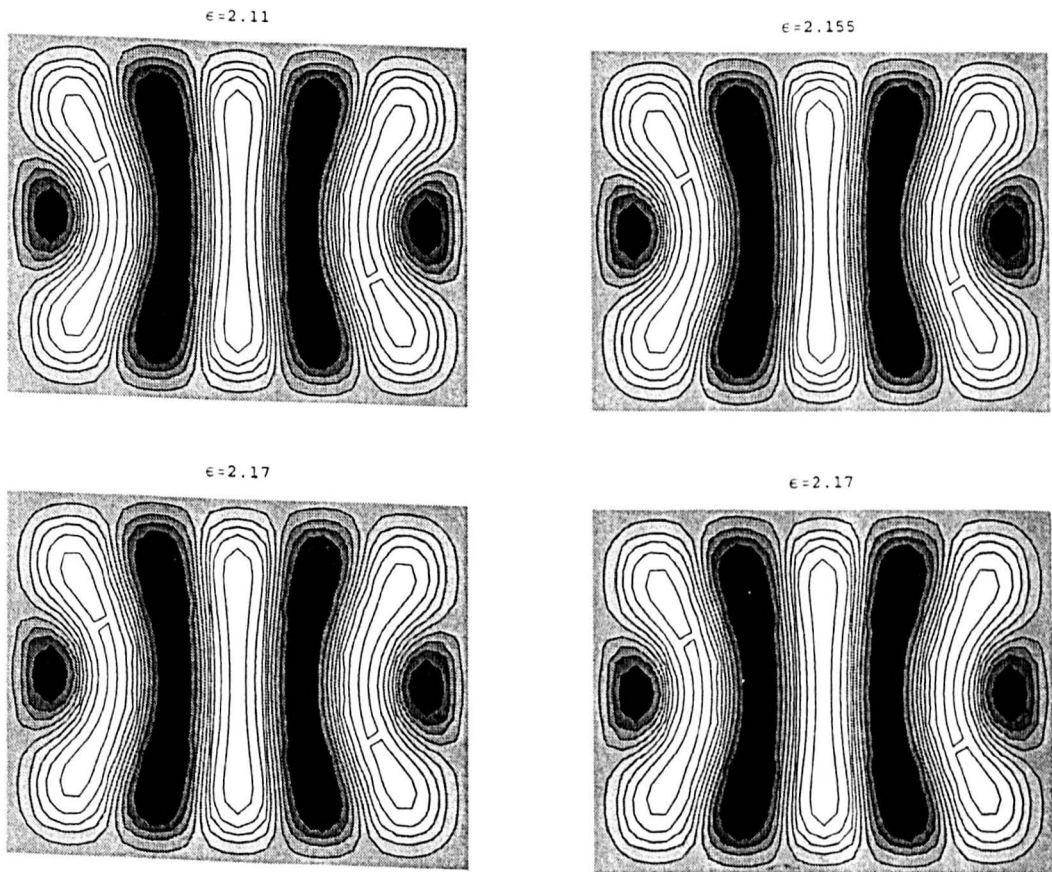


Figure 4.18: Contours of steady-state solutions u for $M = 15.12$ obtained with an initial state $U(x, y) = \sin \frac{7\pi x}{L} \sin \frac{\pi y}{M}$.

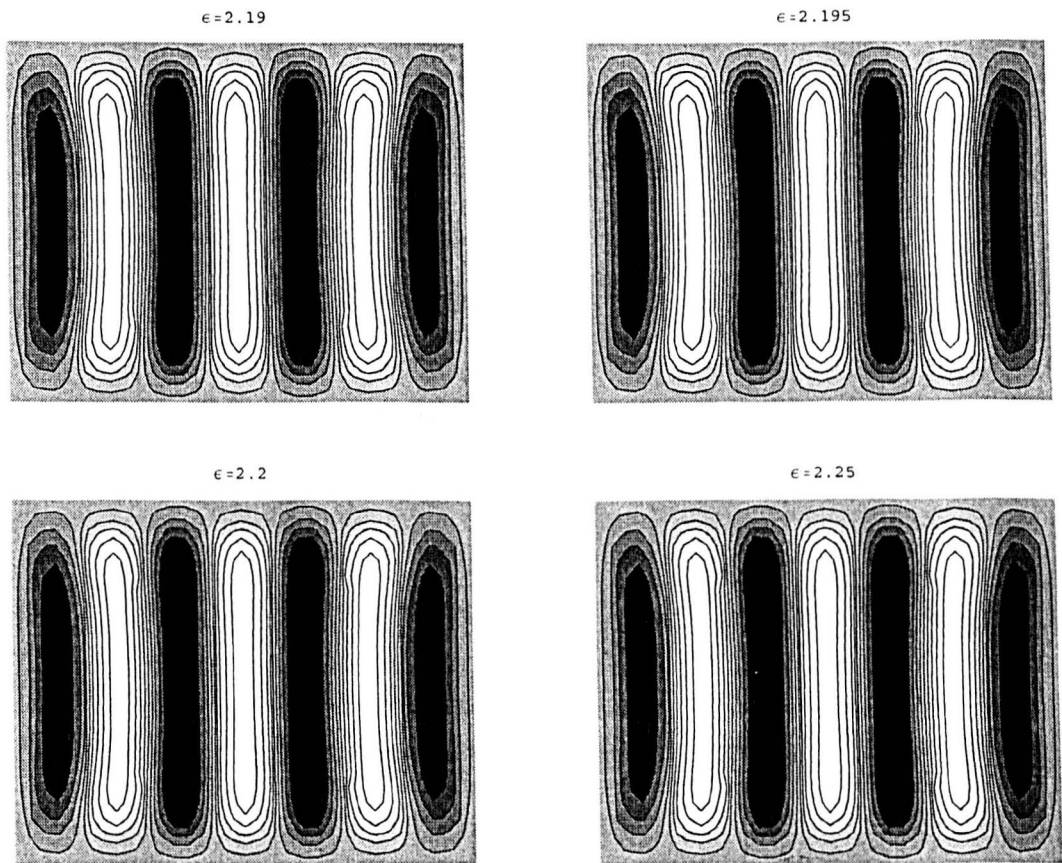


Figure 4.19: Contours of steady-state solutions u for $M = 15.12$ obtained with an initial state $U(x, y) = \sin\left(\frac{7\pi x}{L}\right) \sin\frac{\pi y}{M}$.

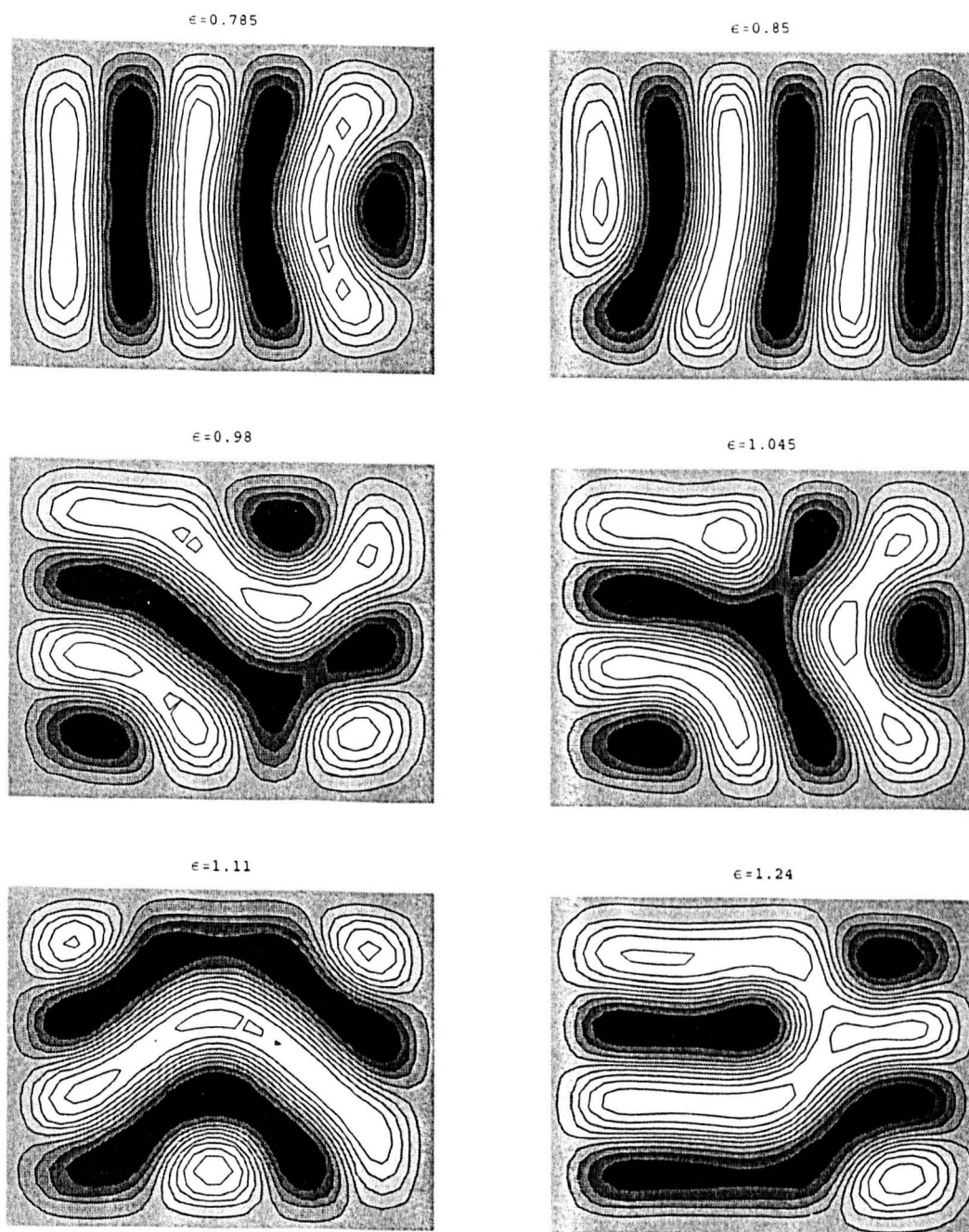


Figure 4.20: Contours of steady-state solutions u for $M = 15.12$ obtained with an initial state $U(x, y) = R(i, j)$.

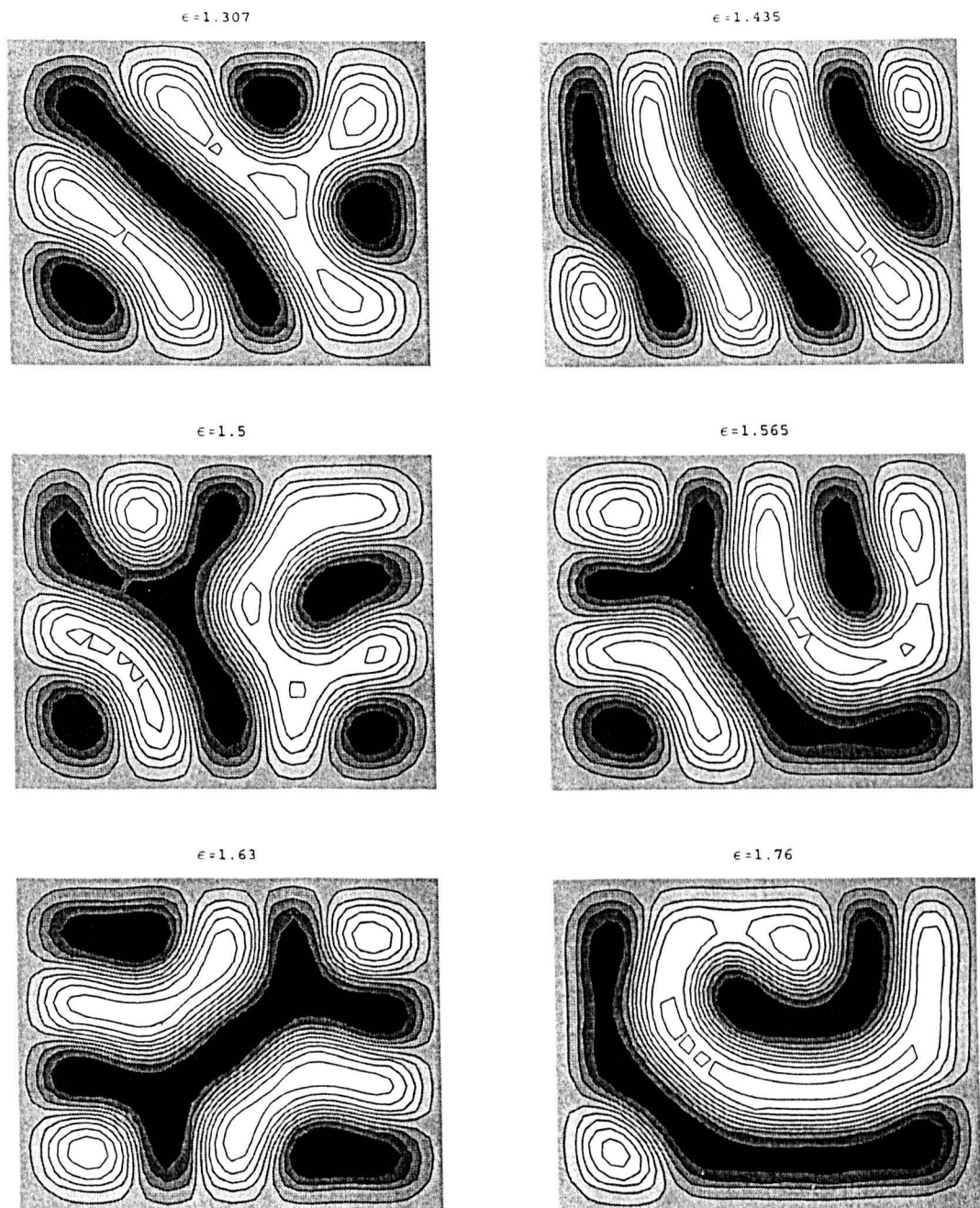


Figure 4.21: Contours of steady-state solutions u for $M = 15.12$ obtained with an initial state $U(x, y) = R(i, j)$.

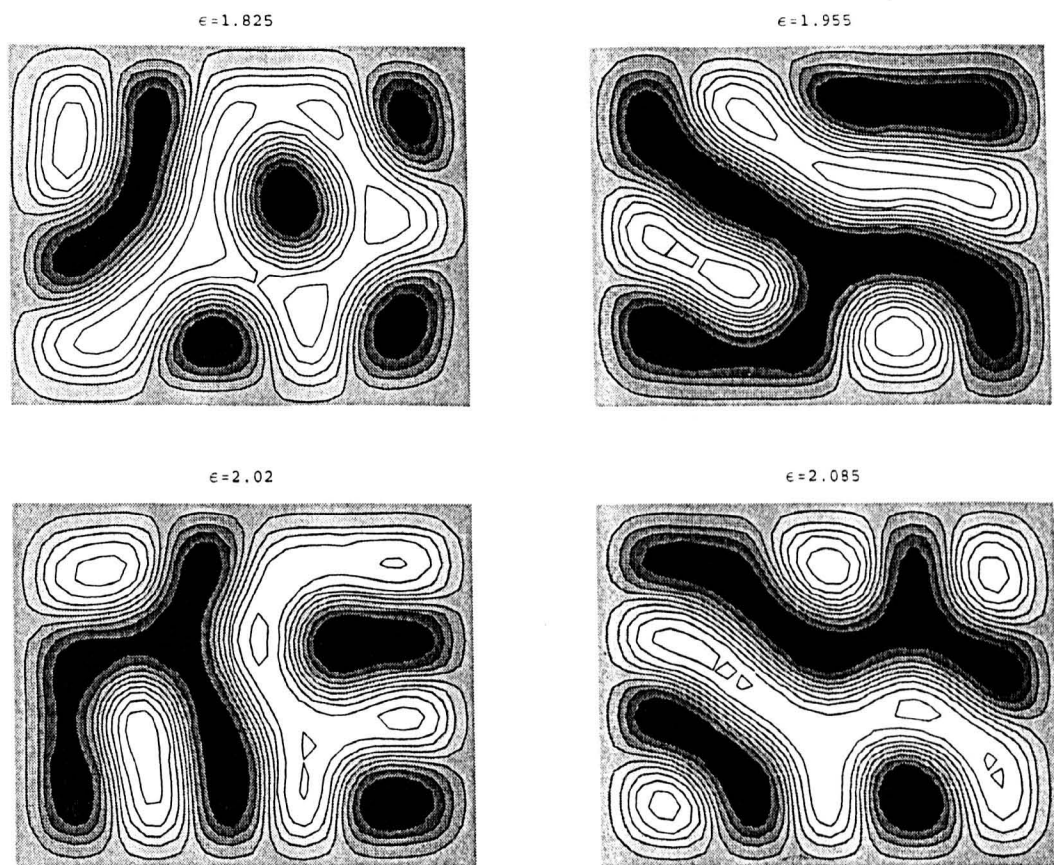


Figure 4.22: Contours of steady-state solutions u for $M = 15.12$ obtained with an initial state $U(x, y) = R(i, j)$.

$\epsilon=0.017$

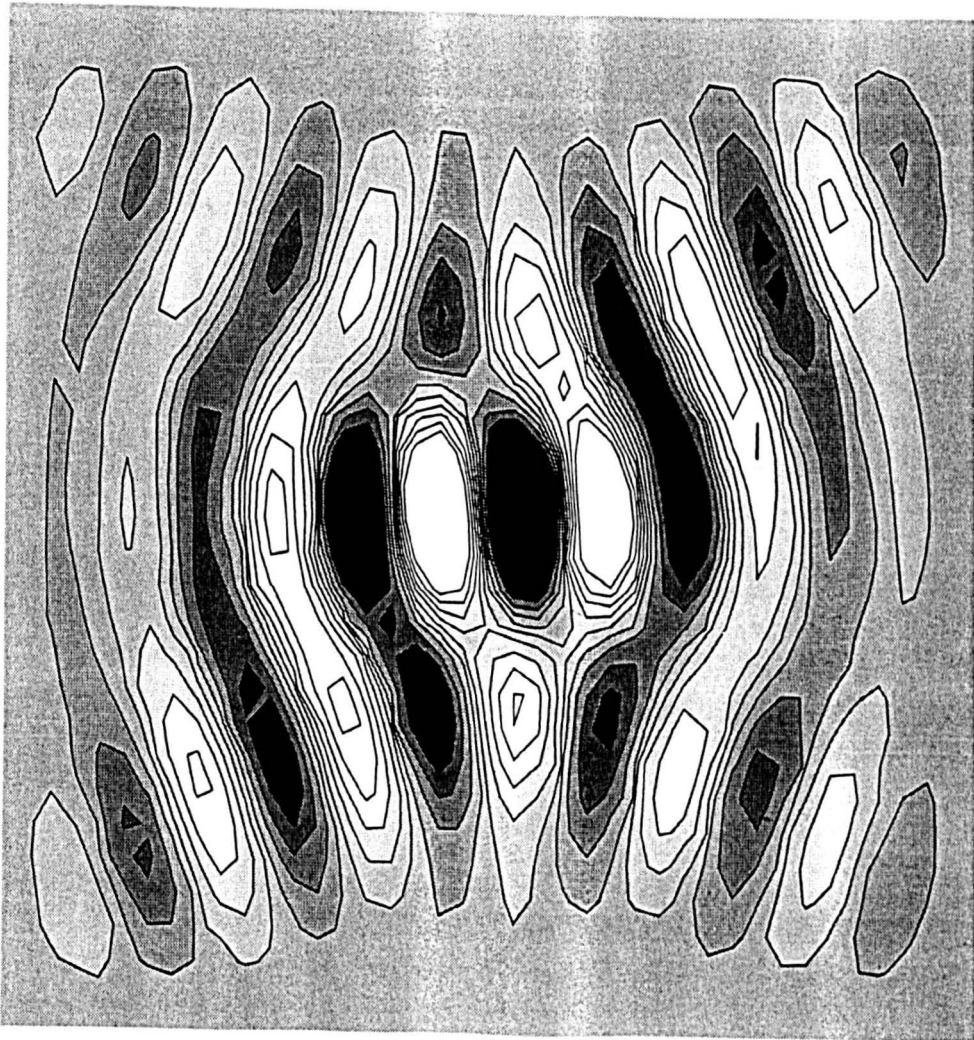


Figure 4.23: Contours of steady-state solution u for $M = 30$ obtained with an initial state $U(x, y) = R(i, j)$.

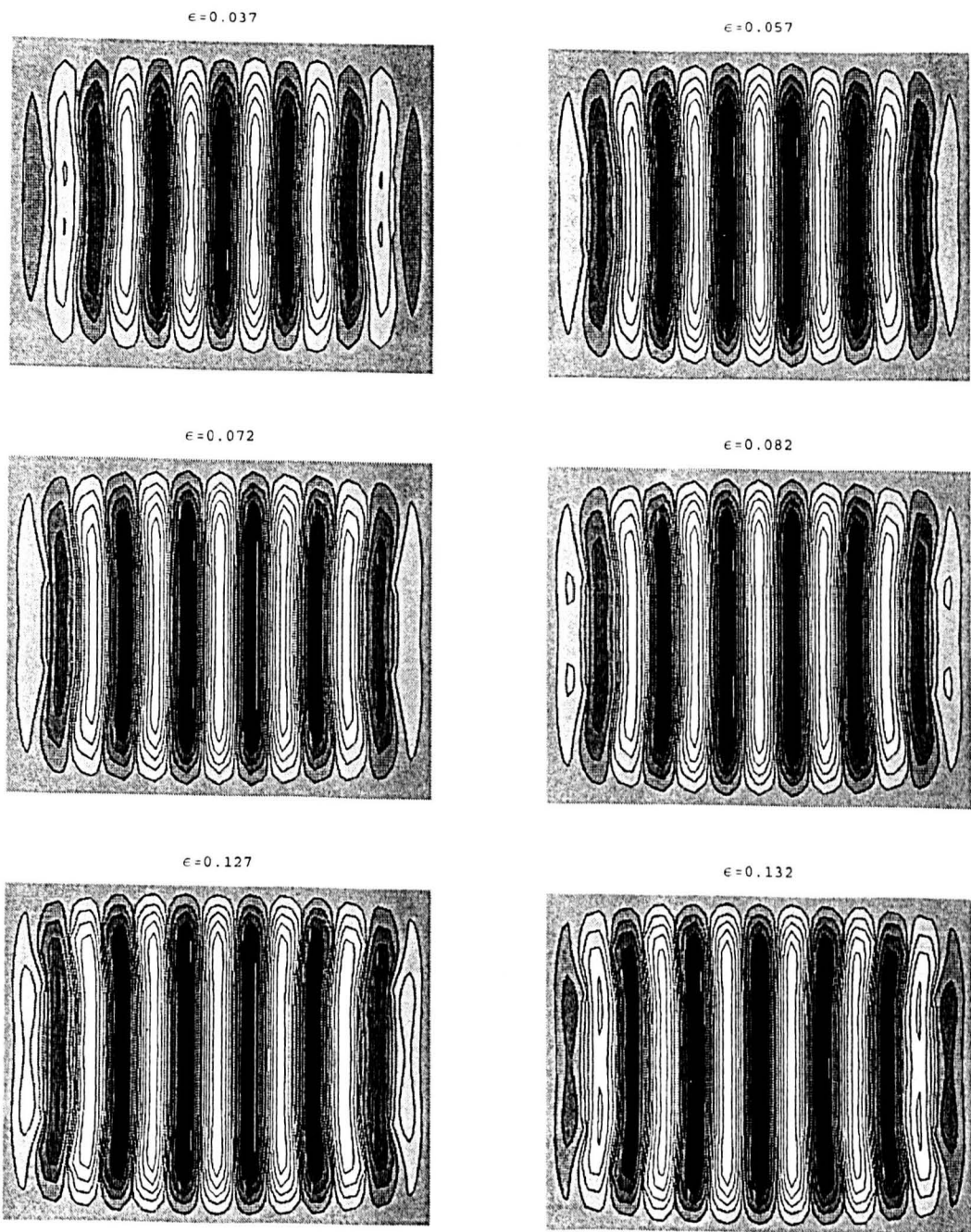


Figure 4.24: Contours of steady-state solutions u for $M = 30$ obtained with an initial state $U(x, y) = R(i, j)$.

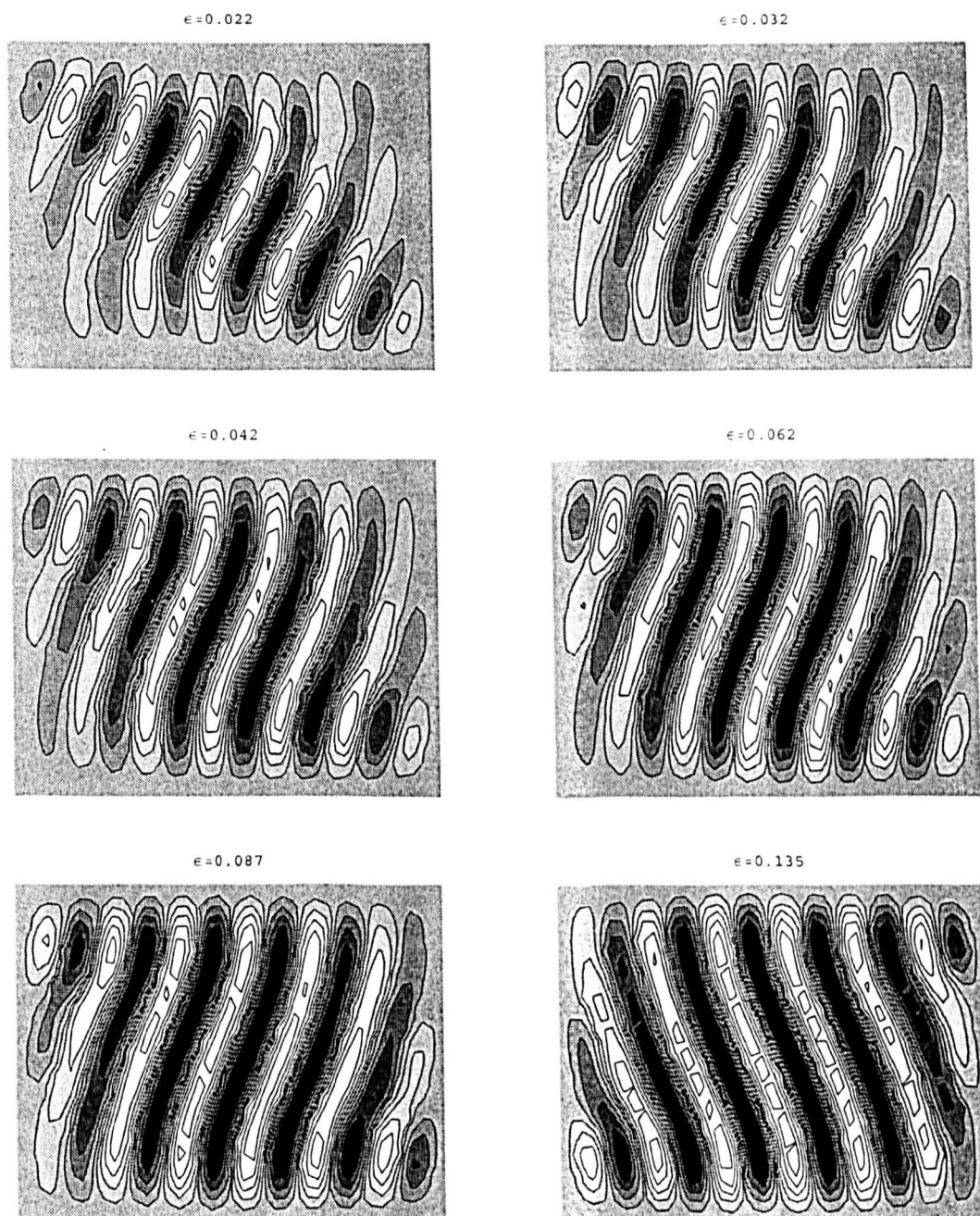


Figure 4.25: Contours of steady-state solutions u for $M = 30$ obtained with an initial state $U(x, y) = R(i, j)$.

$$16\sqrt{3}\hat{u}$$

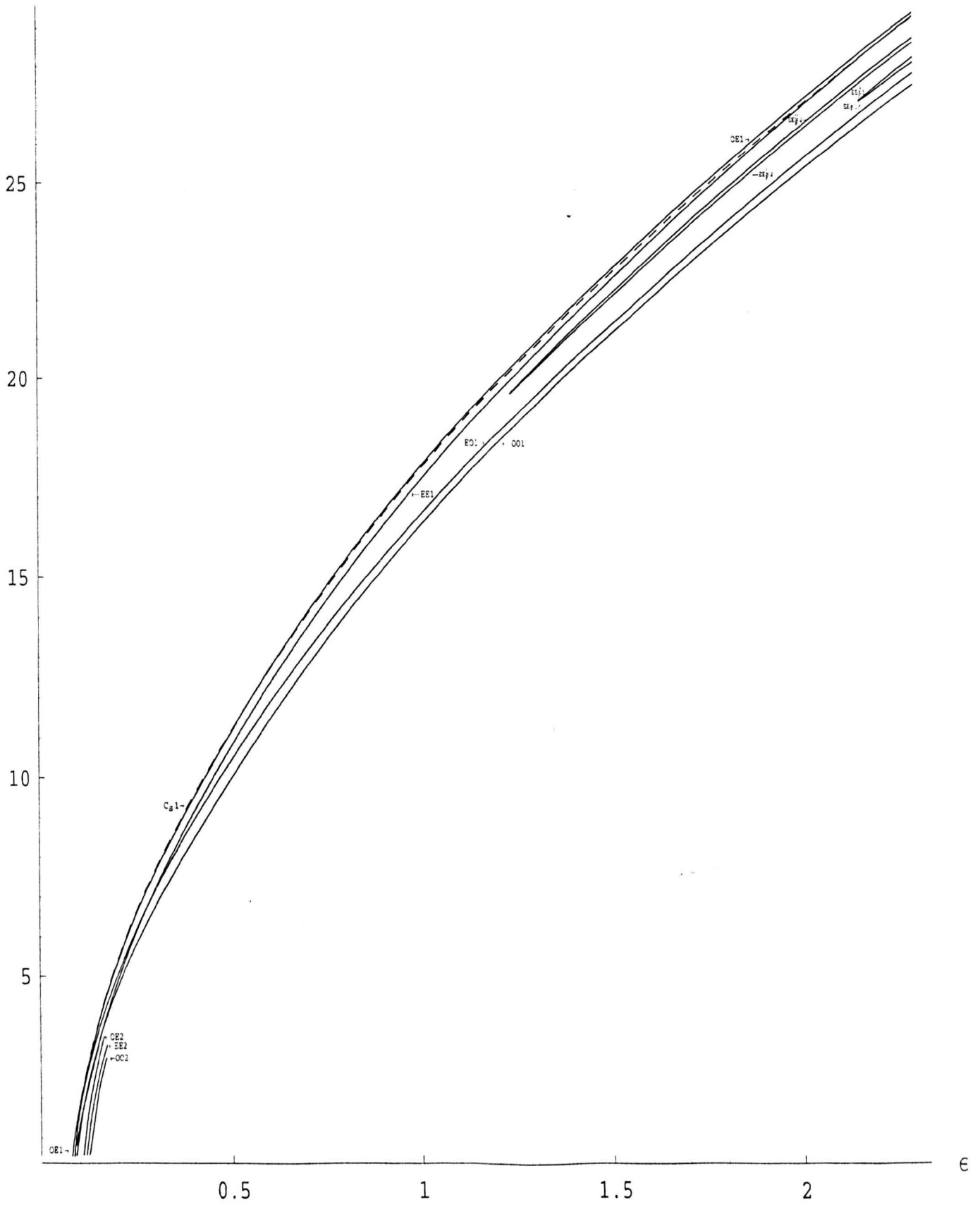


Figure 4.26: Bifurcation diagram for the case $M = 15.12$.

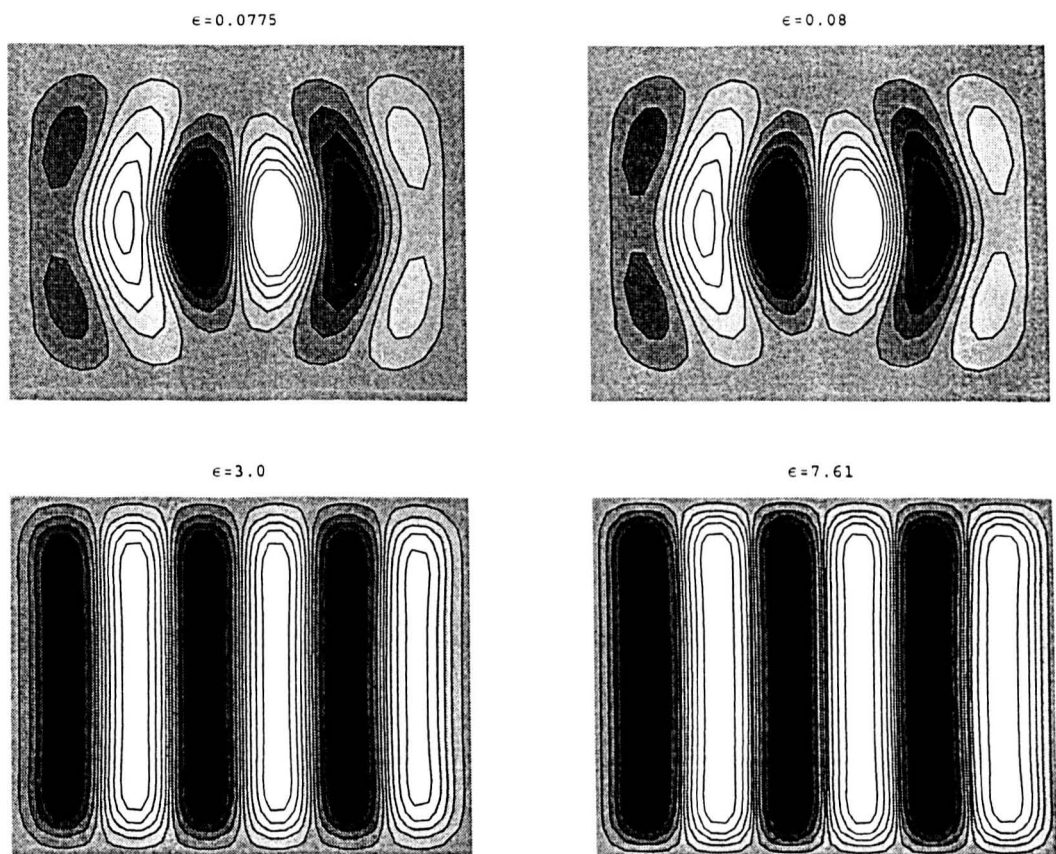


Figure 4.27: Contours of u on branch OE1 for increasing ϵ with $M = 15.12$.

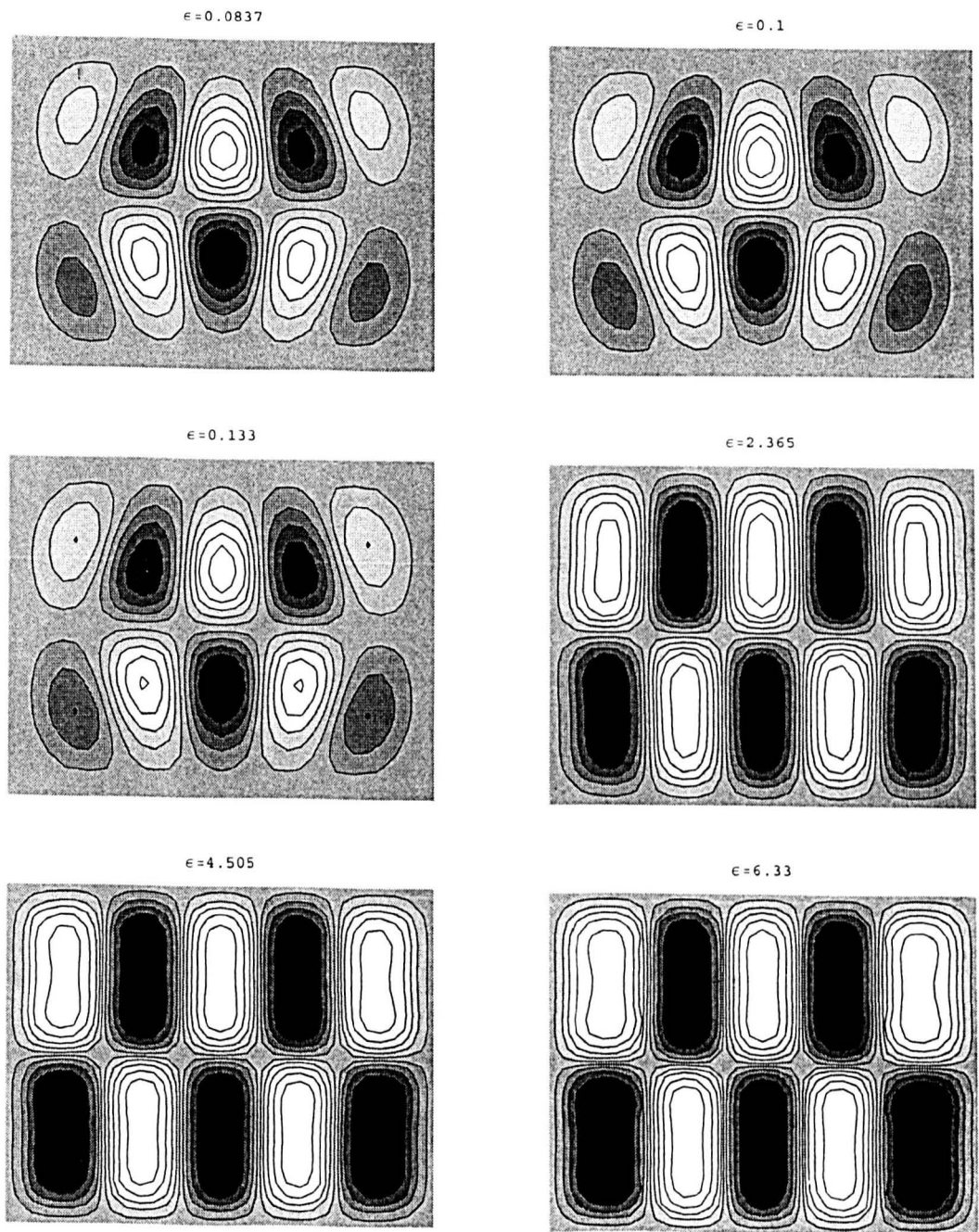


Figure 4.28: Contours of u on branch EO1 for increasing ϵ with $M = 15.12$.

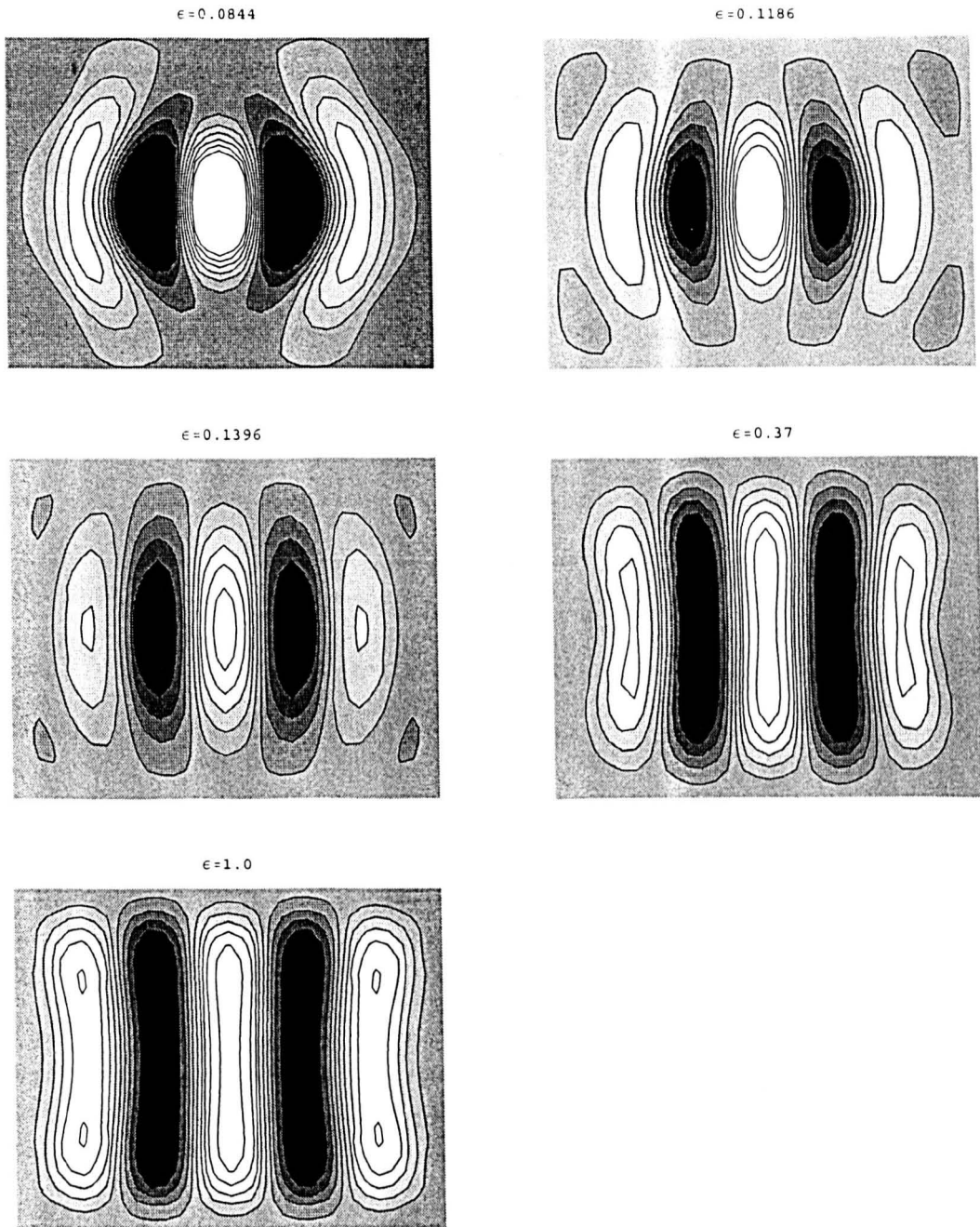


Figure 4.29: Contours of u on branch EE1 for increasing ε with $M = 15.12$.

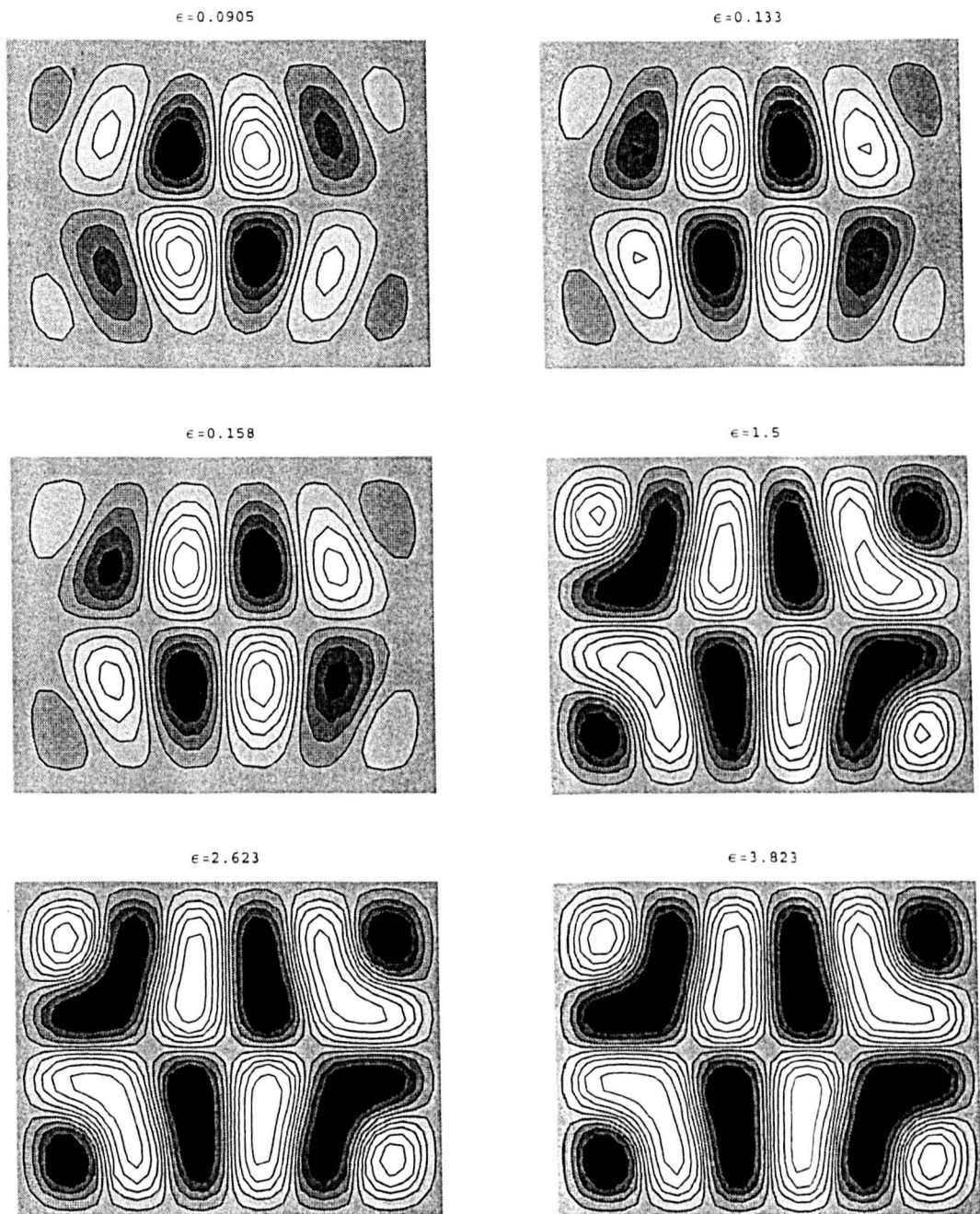


Figure 4.30: Contour of u on branch OO1 for increasing ϵ with $M = 15.12$.

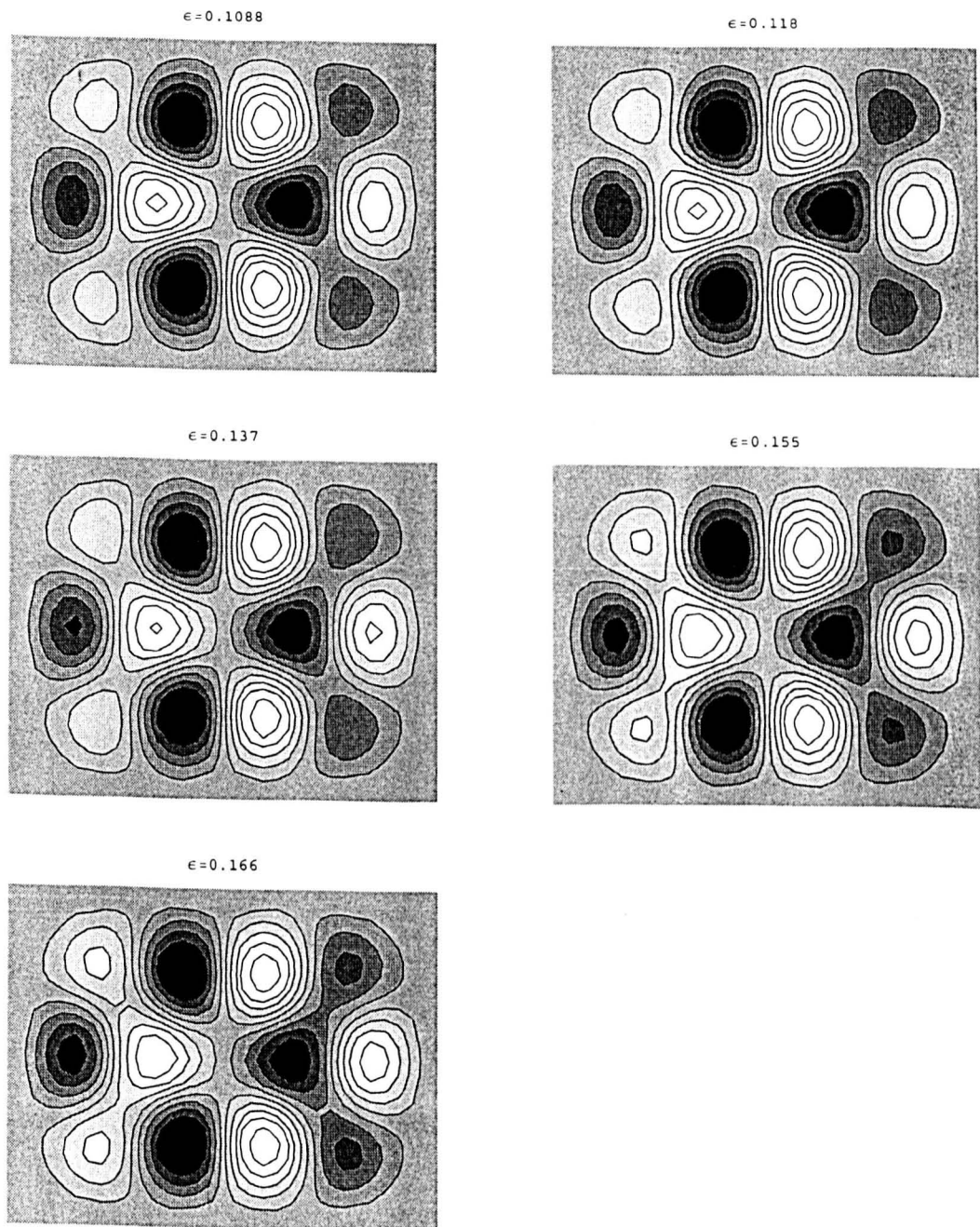


Figure 4.31: Contours of u on branch OE2 for increasing ε with $M = 15.12$.

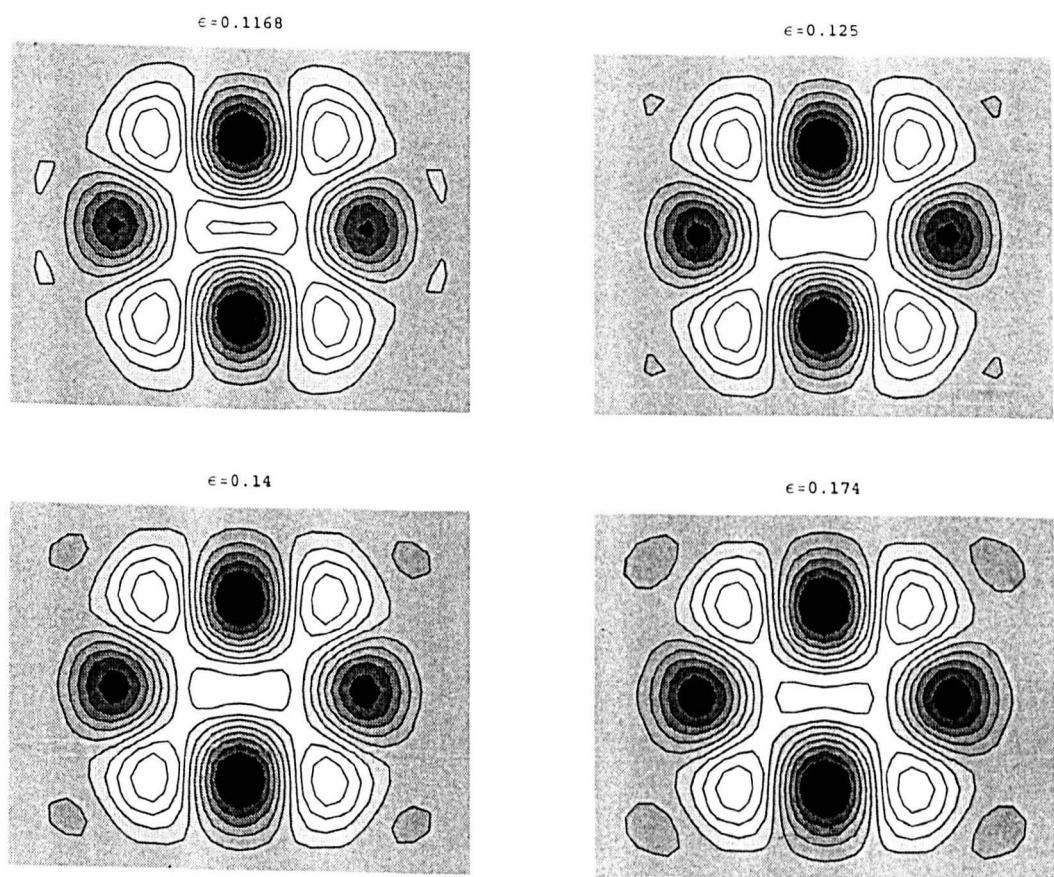


Figure 4.32: Contours of u on branch EE2 for increasing ϵ with $M = 15.12$.

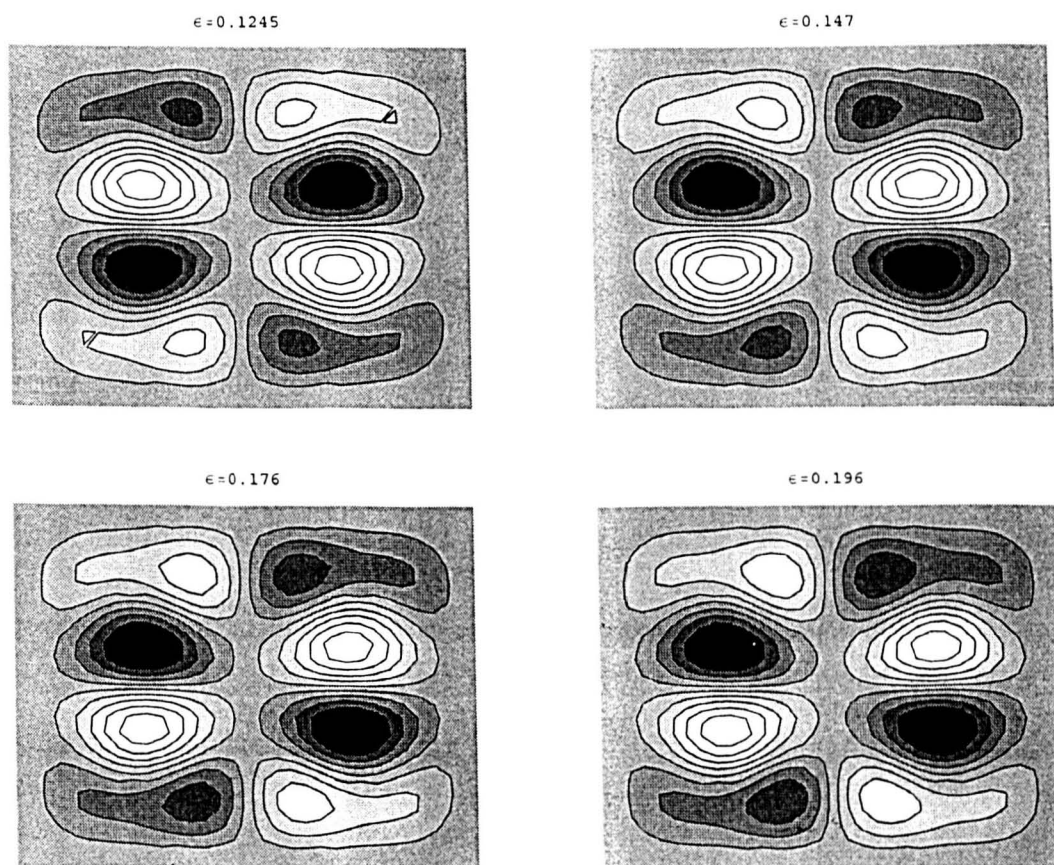


Figure 4.33: Contours of u on branch OO2 for increasing ϵ with $M = 15.12$.

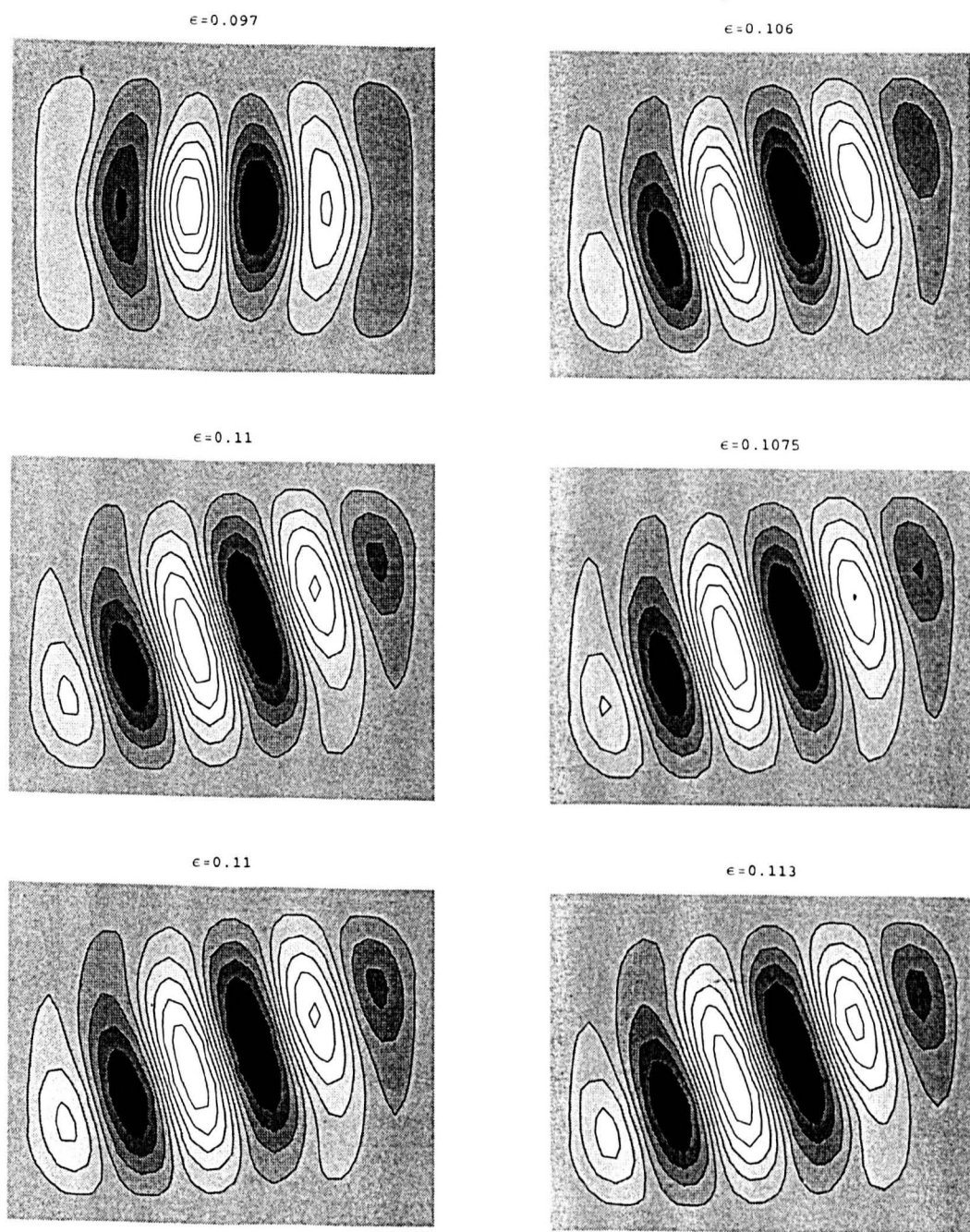


Figure 4.34: Contours of u on branch C_{S1} for increasing ϵ with $M = 15.12$.

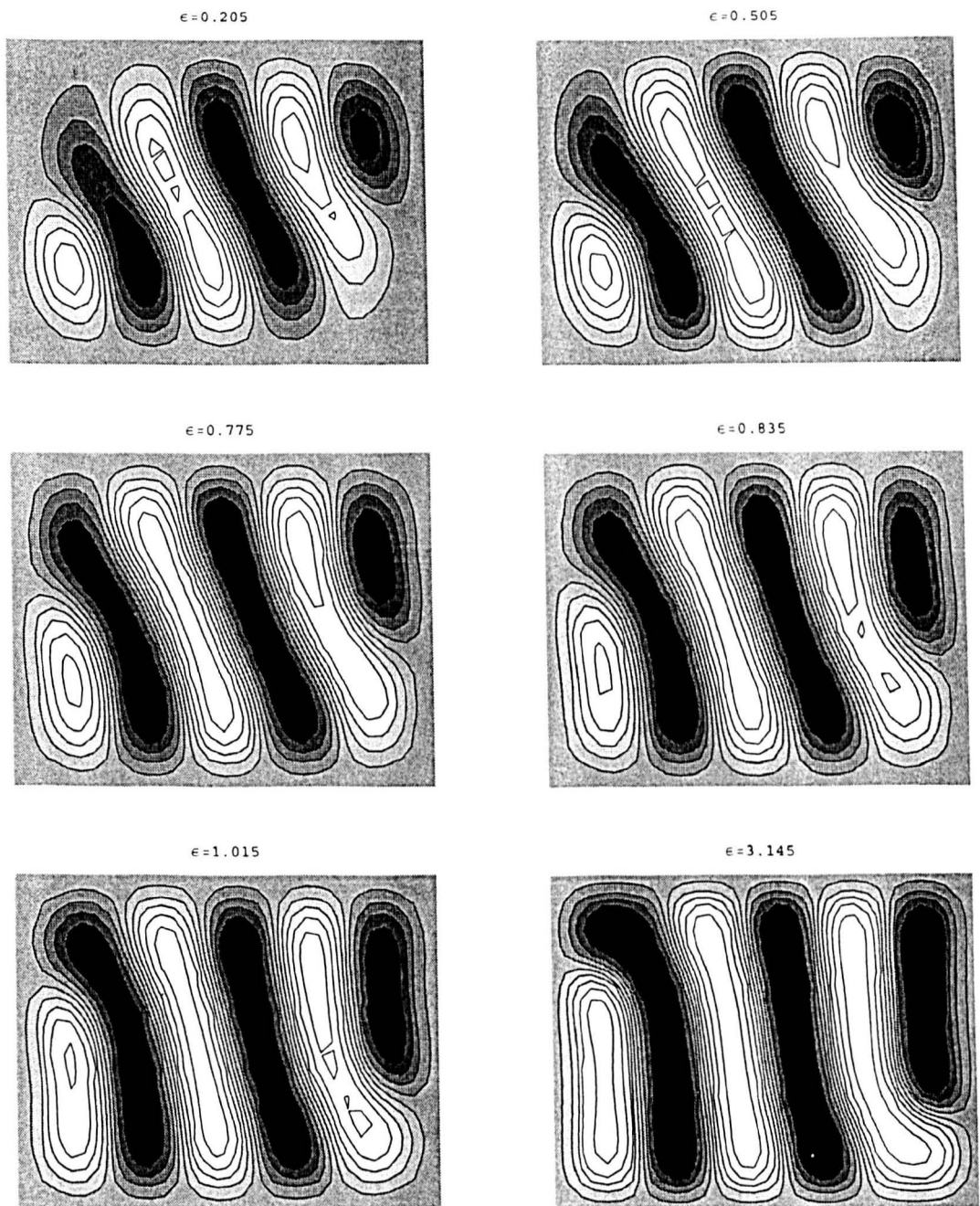


Figure 4.35: Contours of u on branch C_{S1} for increasing ϵ with $M = 15.12$.

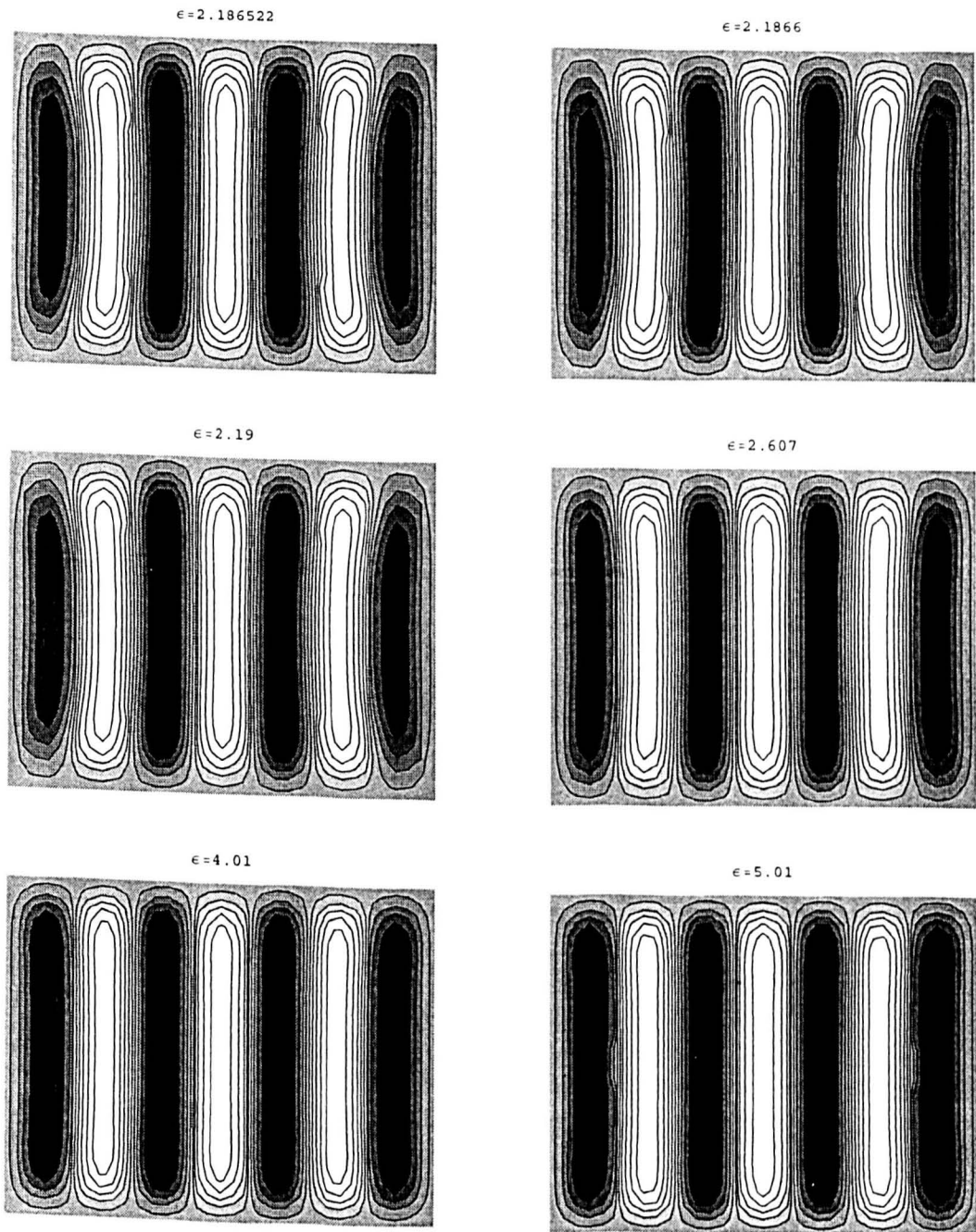


Figure 4.36: Contours of u on branch $EE_F^U 1$ for increasing ϵ with $M = 15.12$.

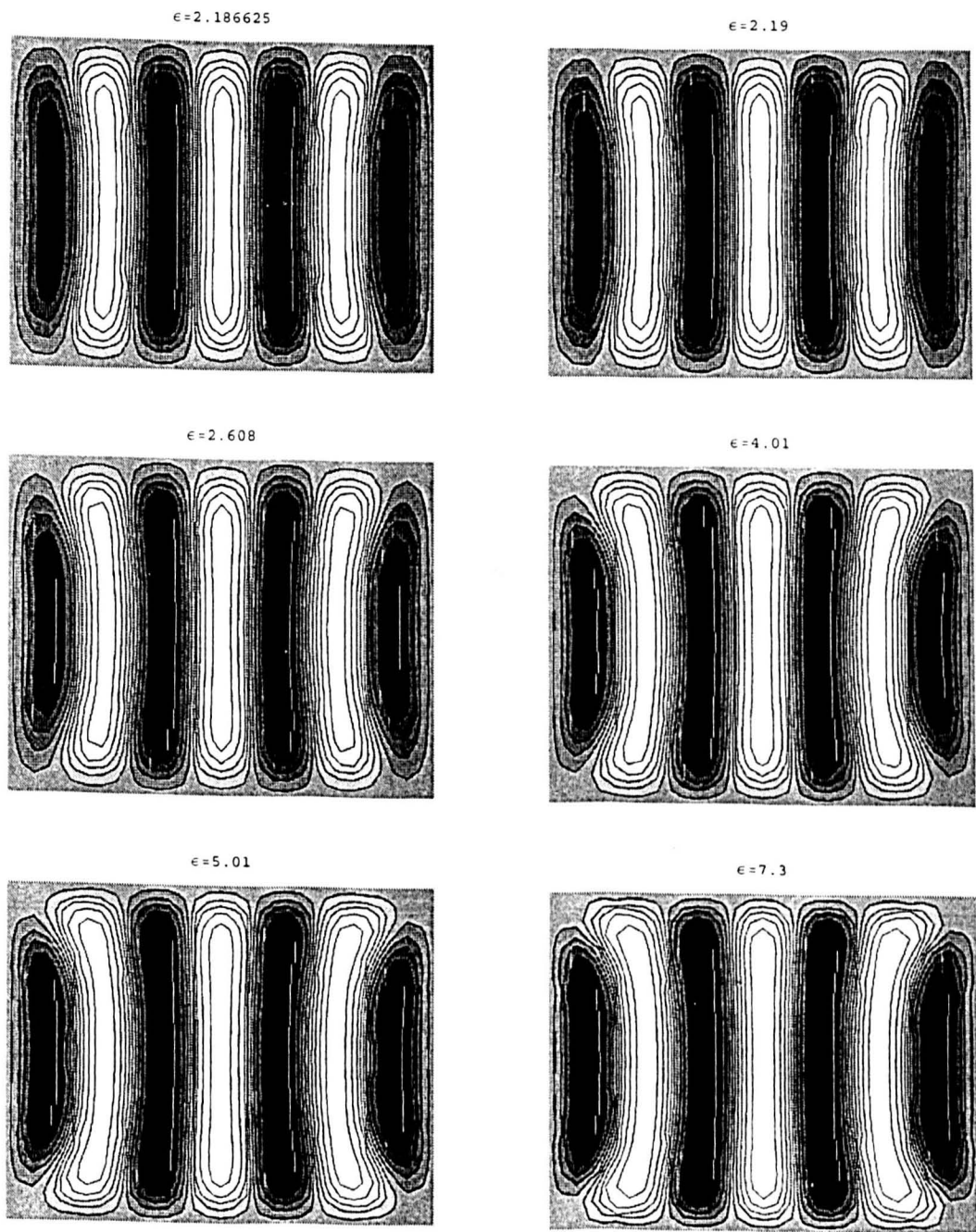


Figure 4.37: Contours of u on branch $EE_F^L 1$ for increasing ε with $M = 15.12$.

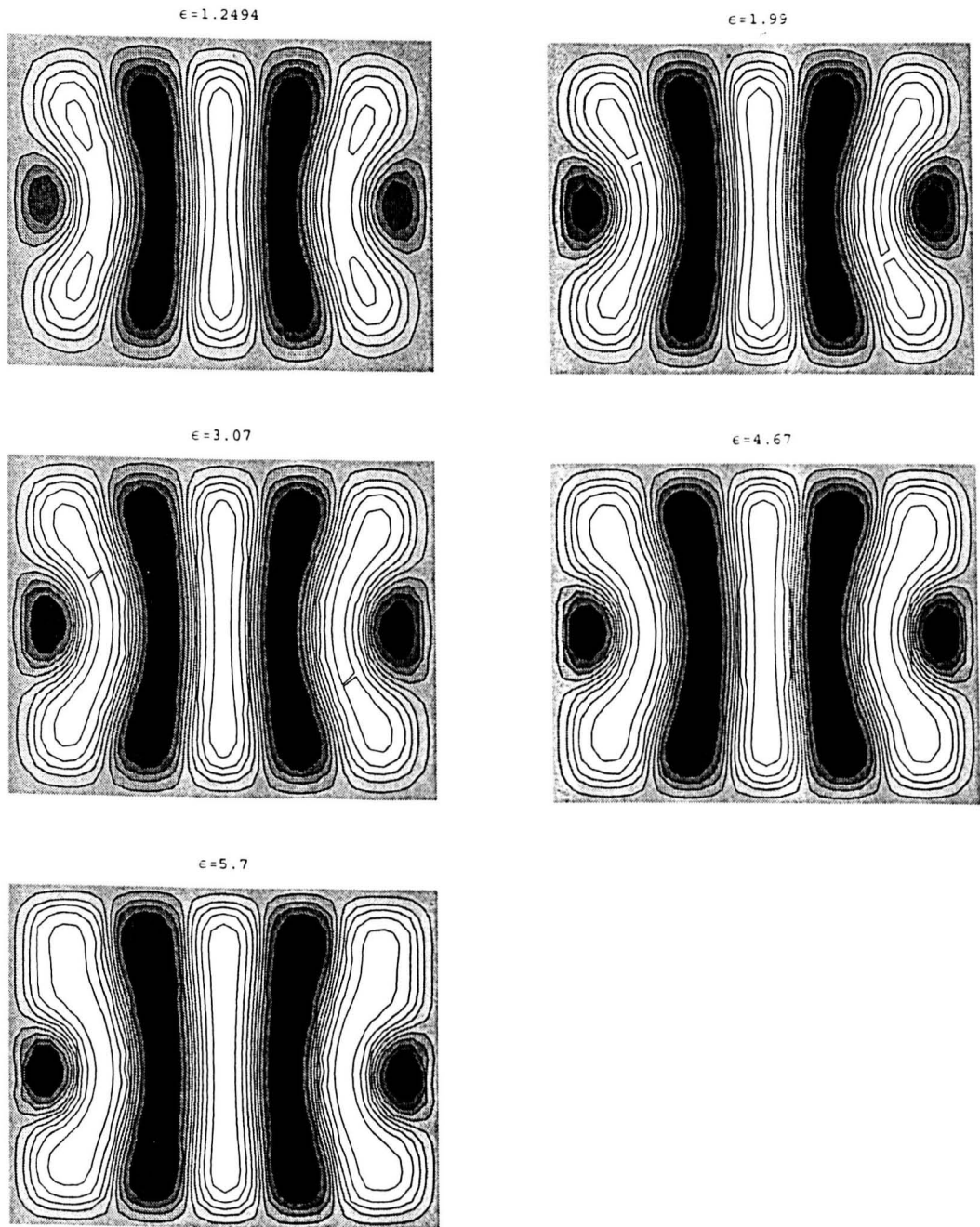


Figure 4.38: Contours of u on branch $EE_F^U 2$ for increasing ϵ with $M = 15.12$.

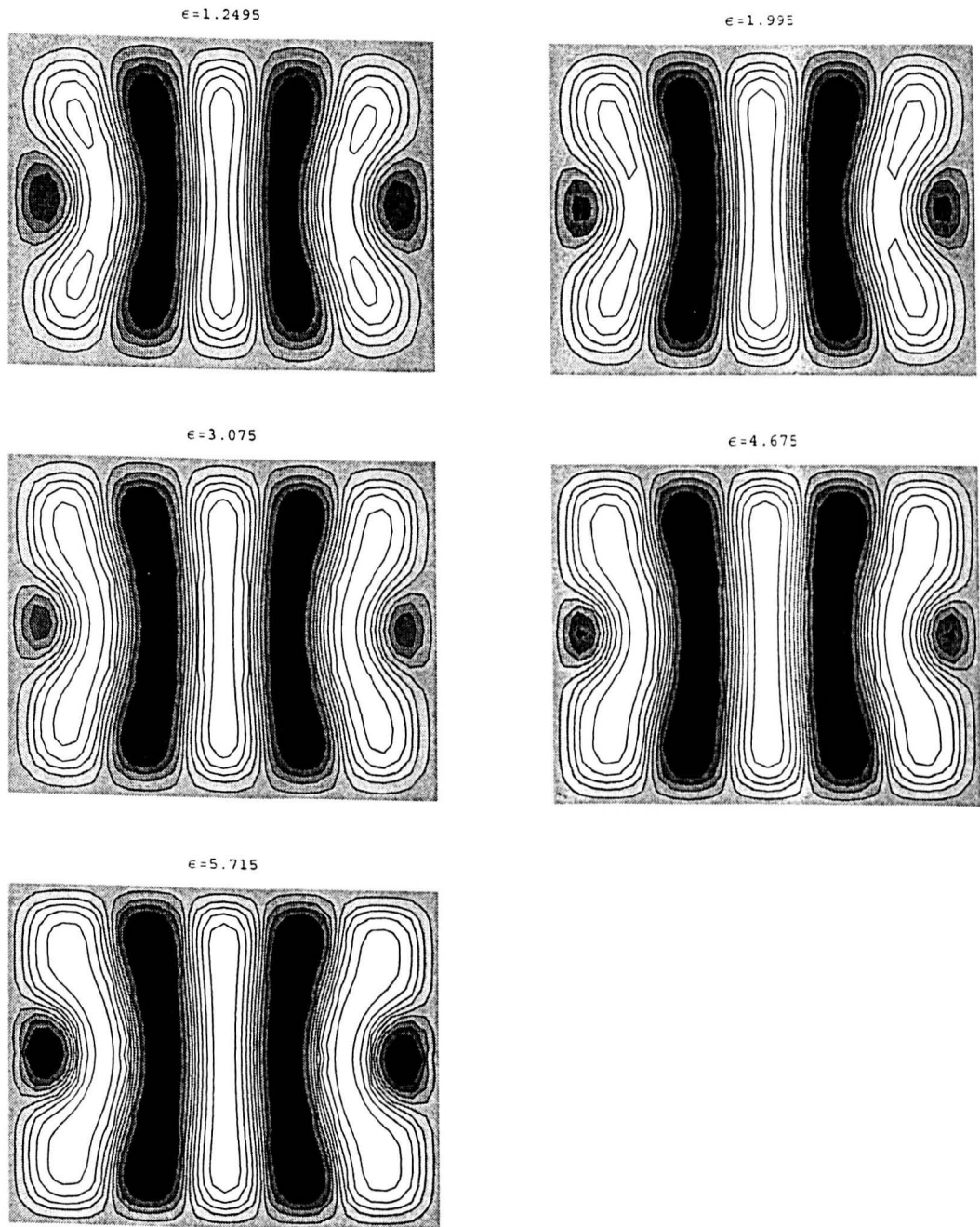


Figure 4.39: Contours of u on branch $EE_F^L 2$ for increasing ϵ with $M = 15.12$.

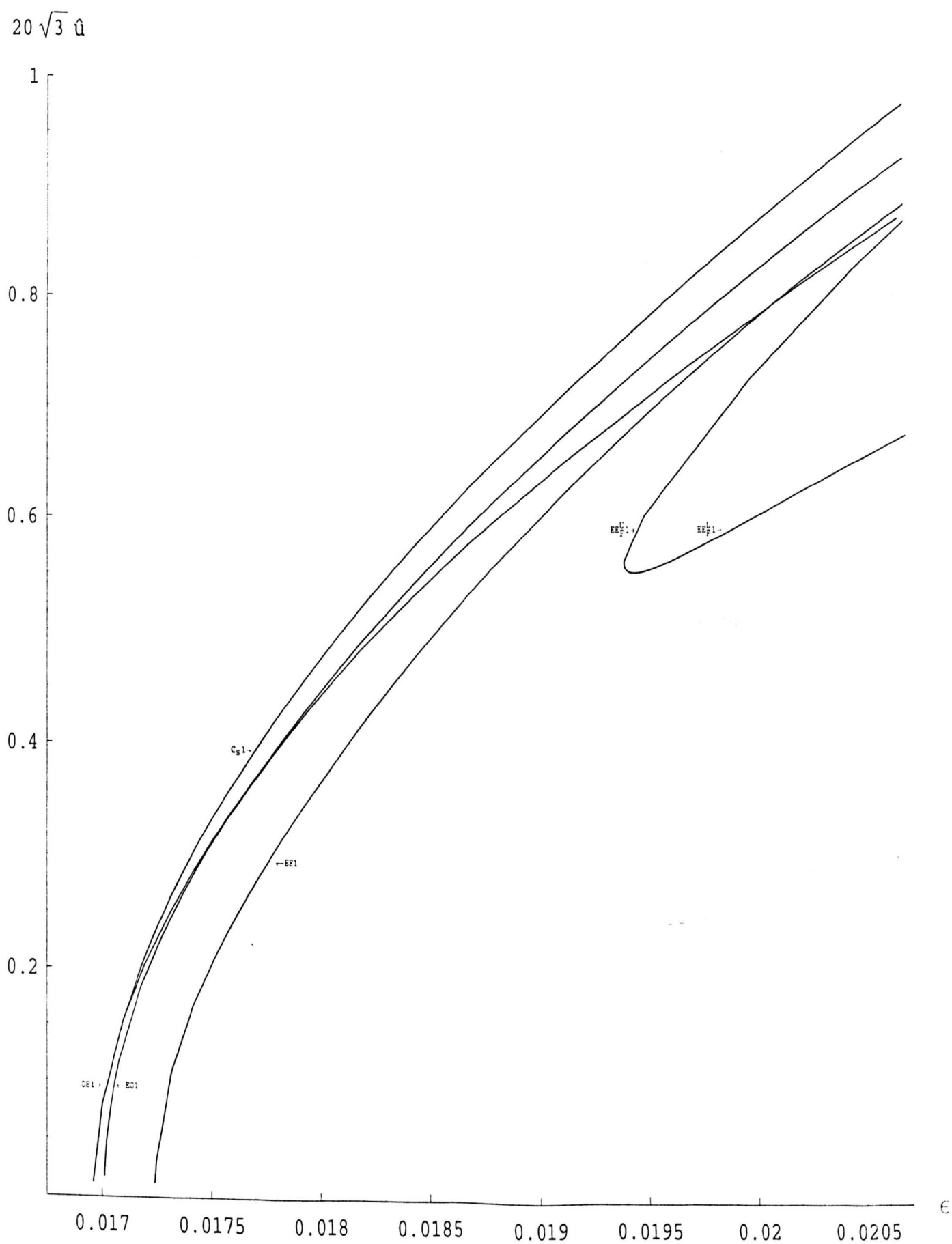


Figure 4.40: Bifurcation diagram for the case $M = 30$.

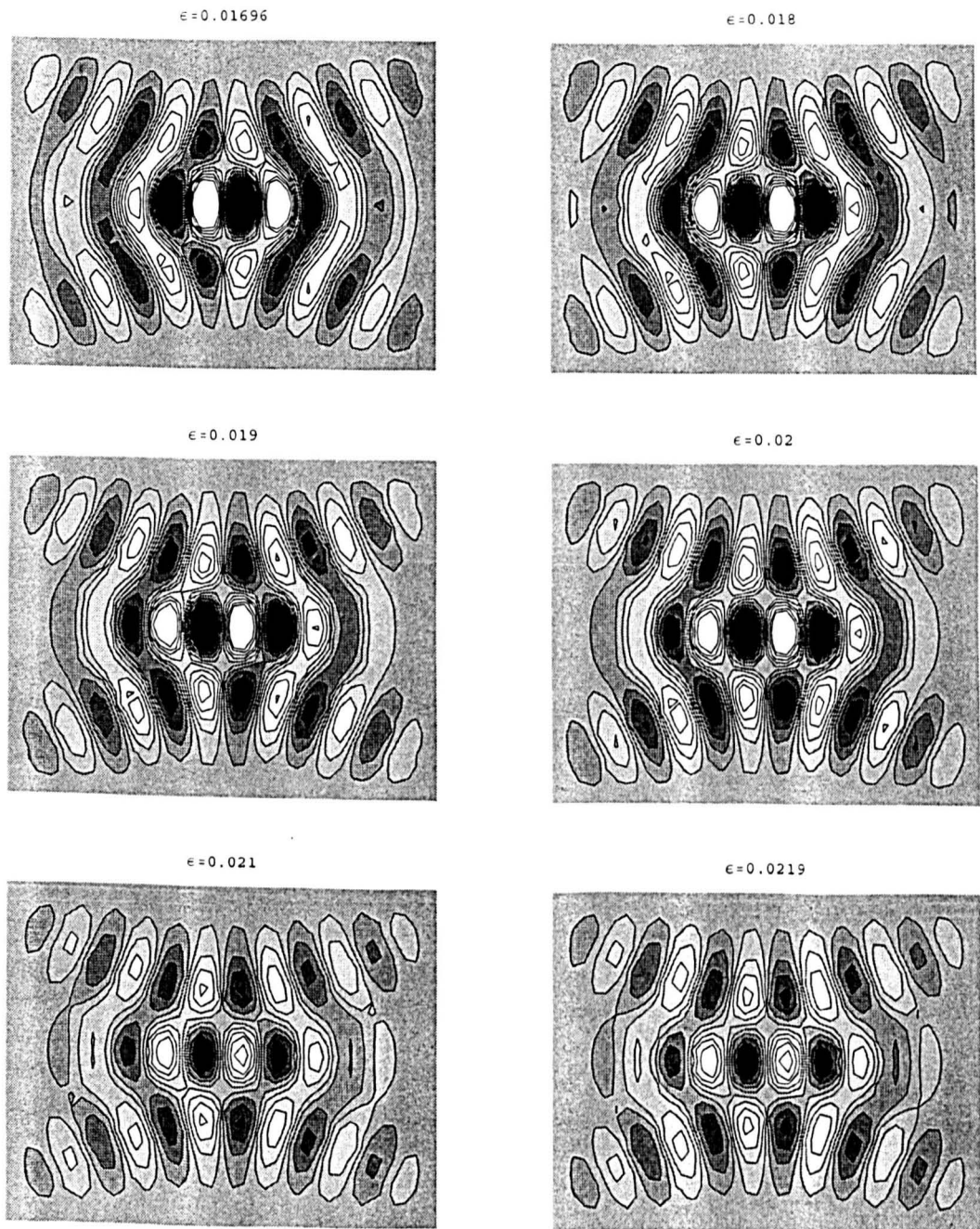


Figure 4.41: Contours of u on branch OE1 for increasing ε with $M = 30$.

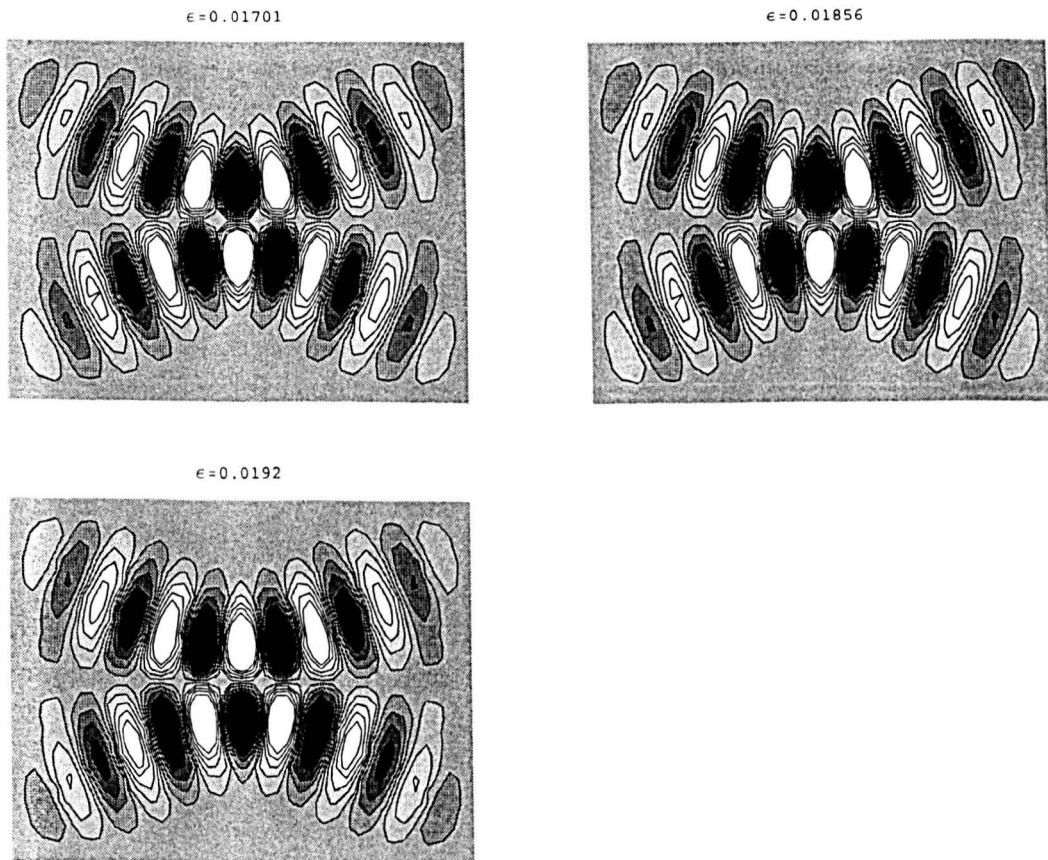


Figure 4.42: Contours of u on branch EO1 for increasing ϵ with $M = 30$.

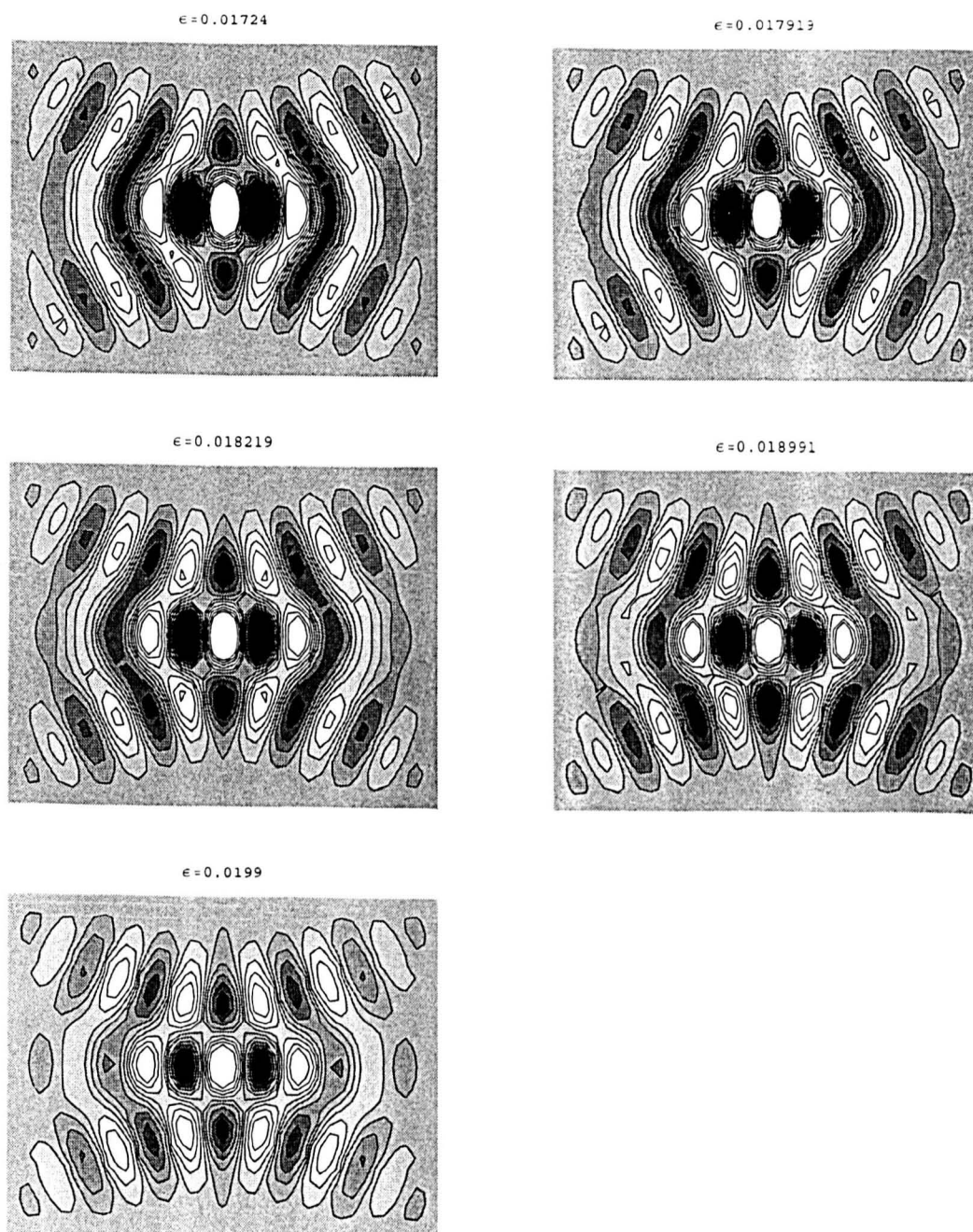


Figure 4.43: Contours of u on branch EE1 for increasing ε with $M = 30$.

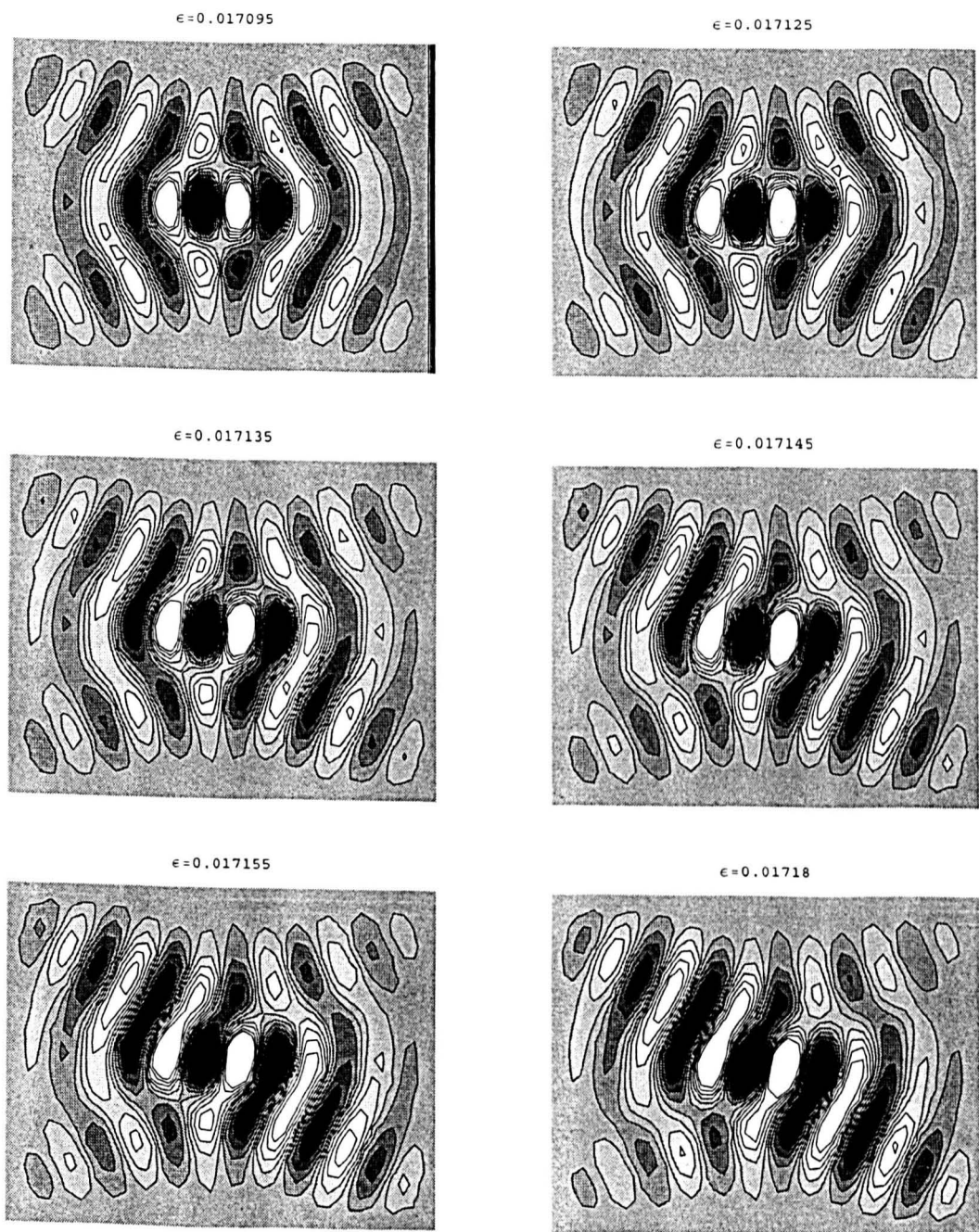


Figure 4.44: Contours of u on branch C_{S1} for increasing ϵ with $M = 30$.

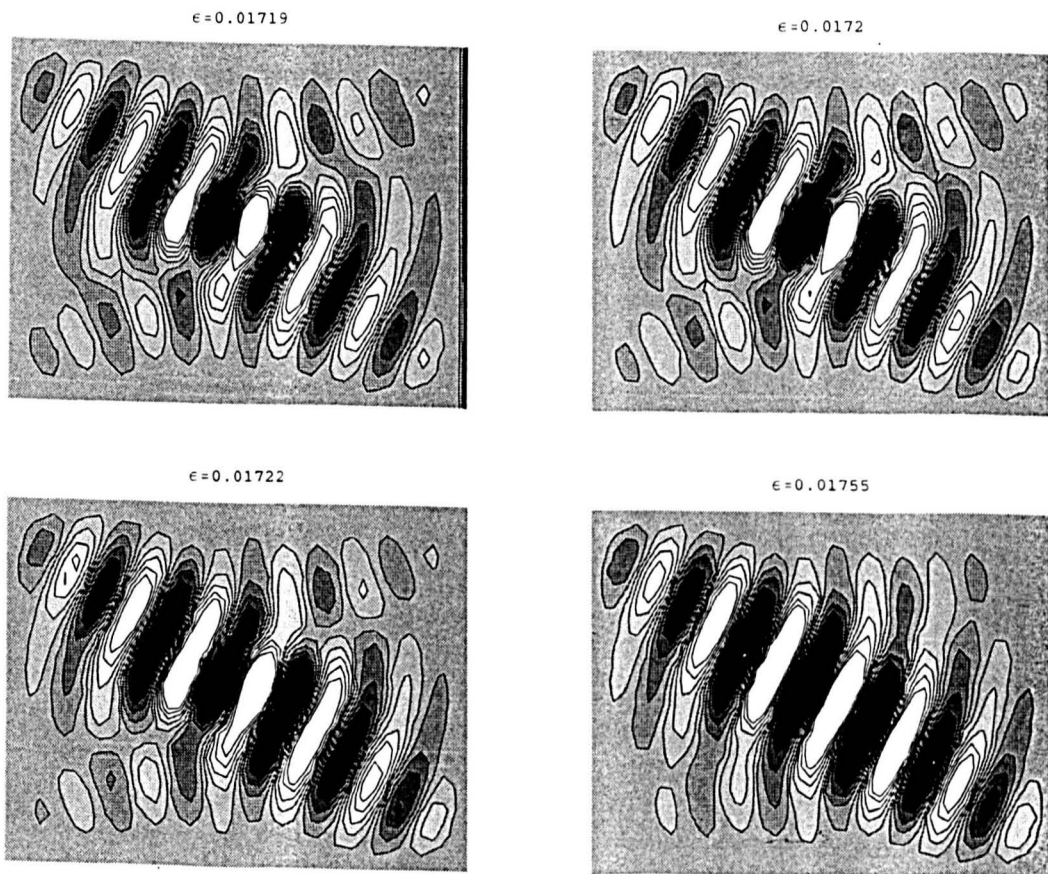


Figure 4.45: Contours of u on branch C_{S1} for increasing ϵ with $M = 30$.

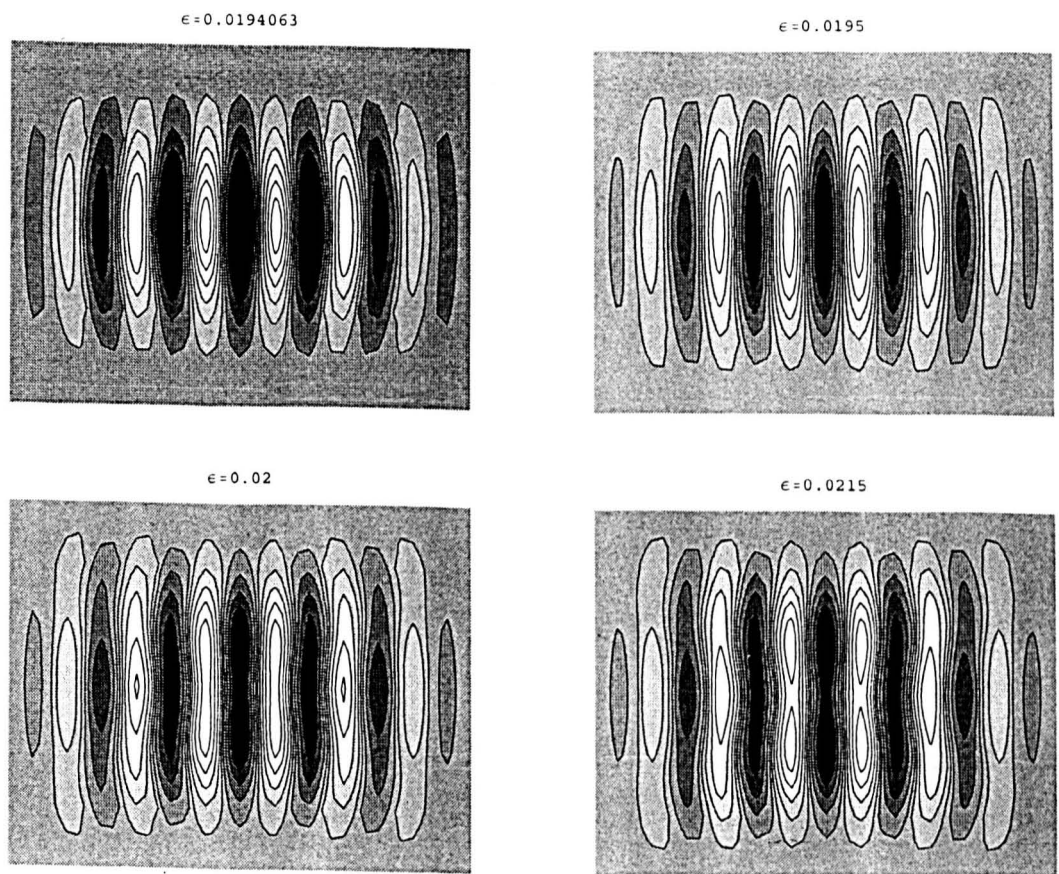


Figure 4.46: Contours of u on branch $EE_F^U 1$ for increasing ϵ with $M = 30$.

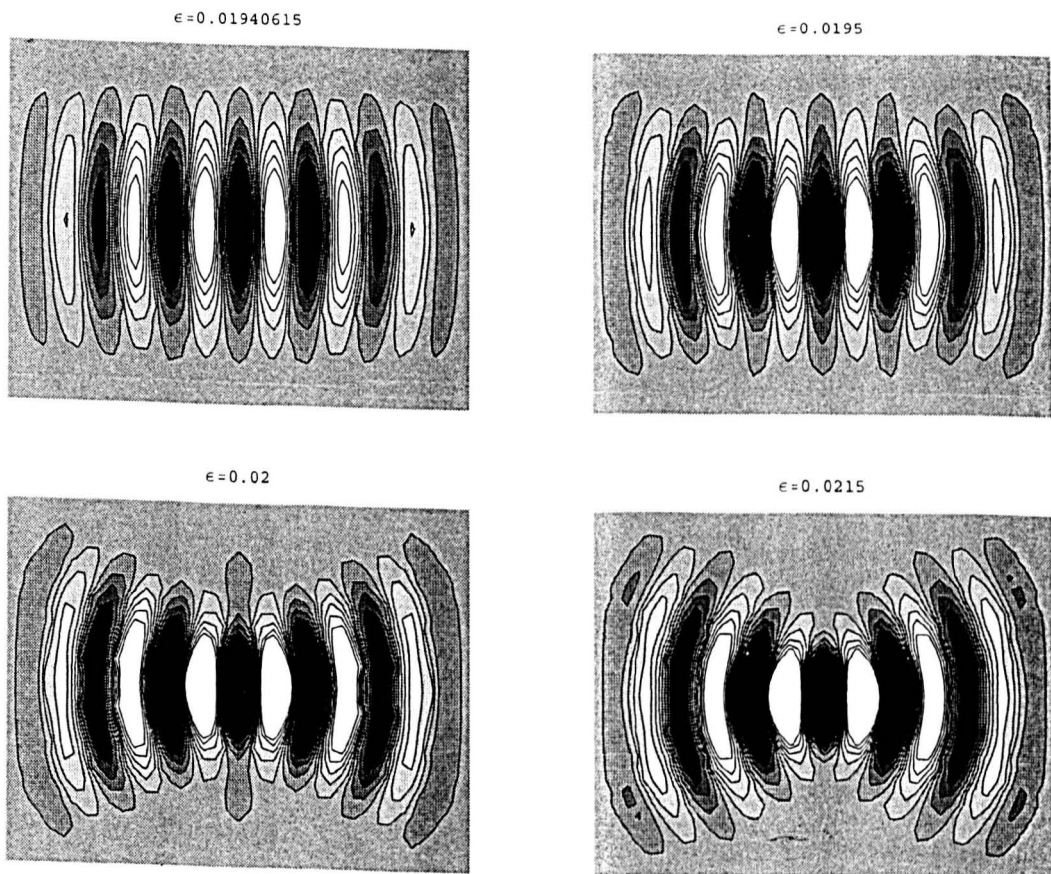


Figure 4.47: Contours of u on branch $EE_F^L 1$ for increasing ϵ with $M = 30$.

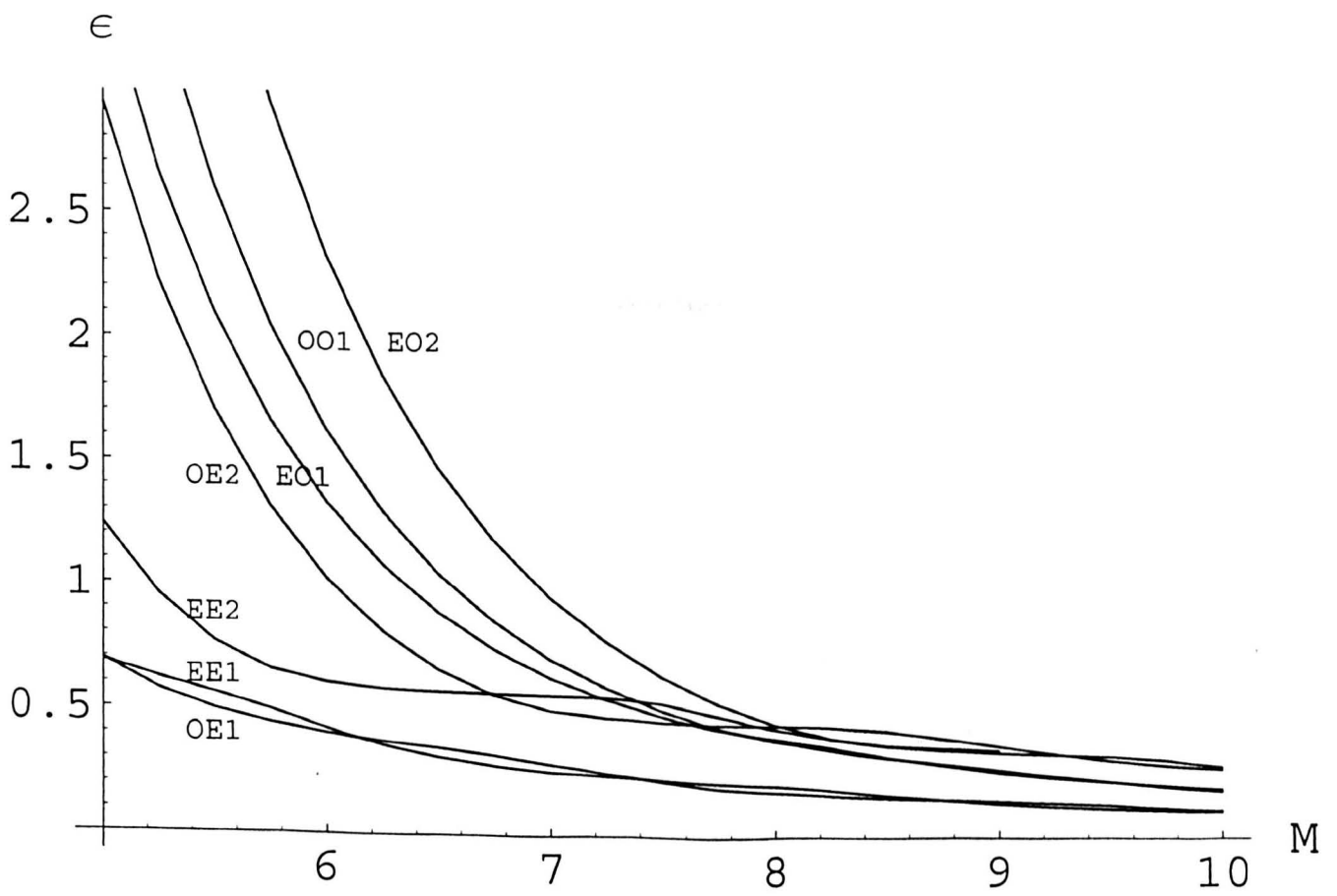


Figure 4.48: The first seven branches of the eigenvalues ϵ as functions of M for $M/L = 0.5$ obtained using a 40×20 grid.

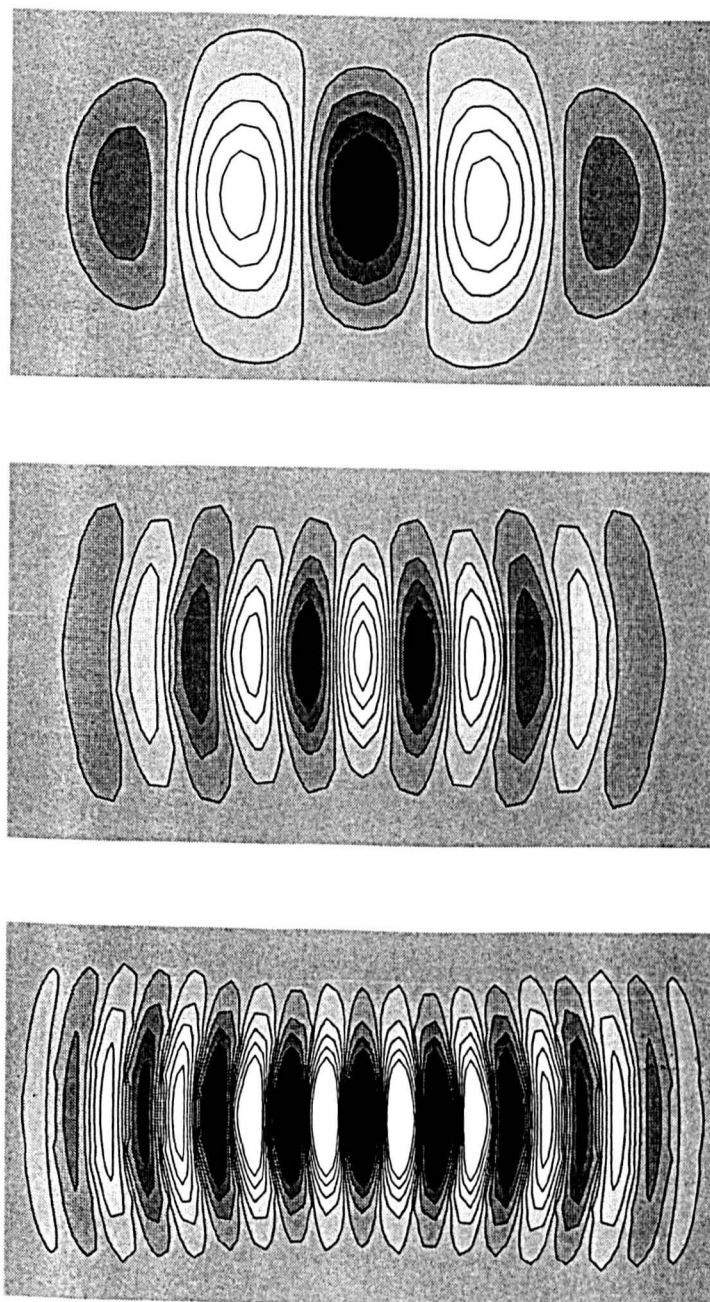


Figure 4.49: Sequence of patterns on branch EE1 for (top to bottom) $M = 10, 20, 30$.

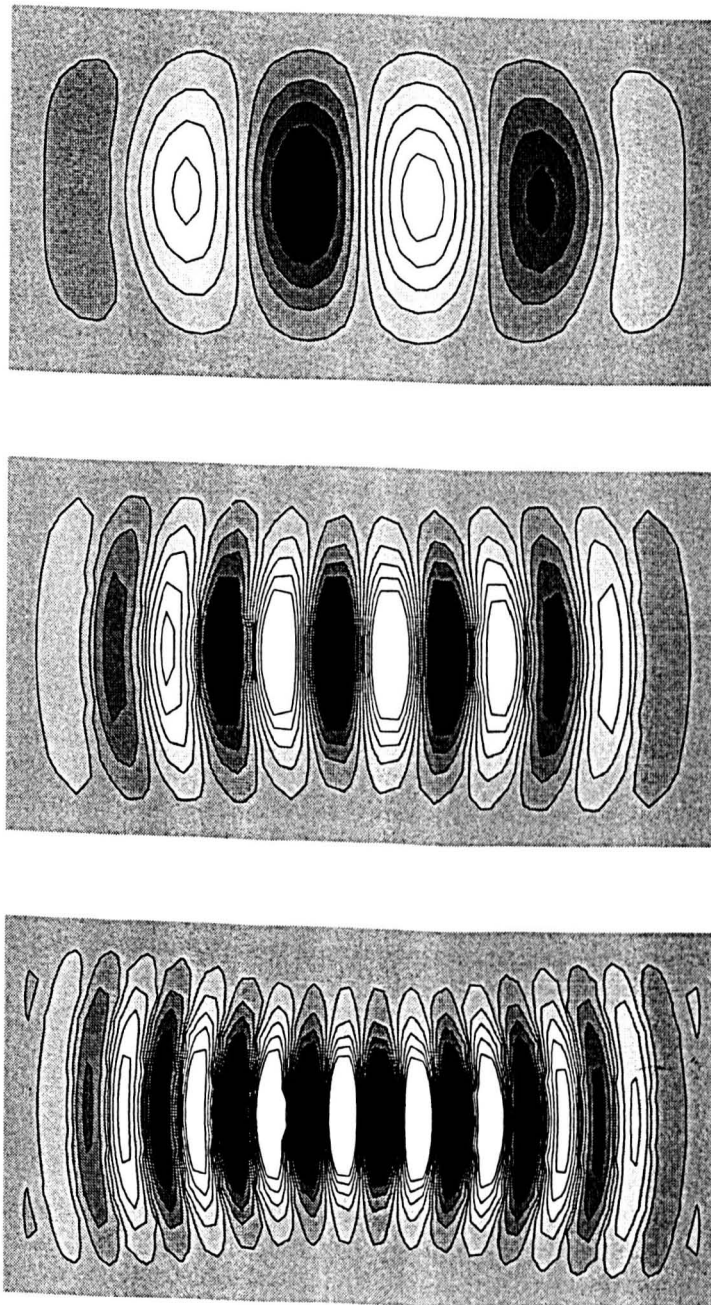


Figure 4.50: Sequence of patterns on branch OE1 for (top to bottom) $M = 10, 20, 30$.

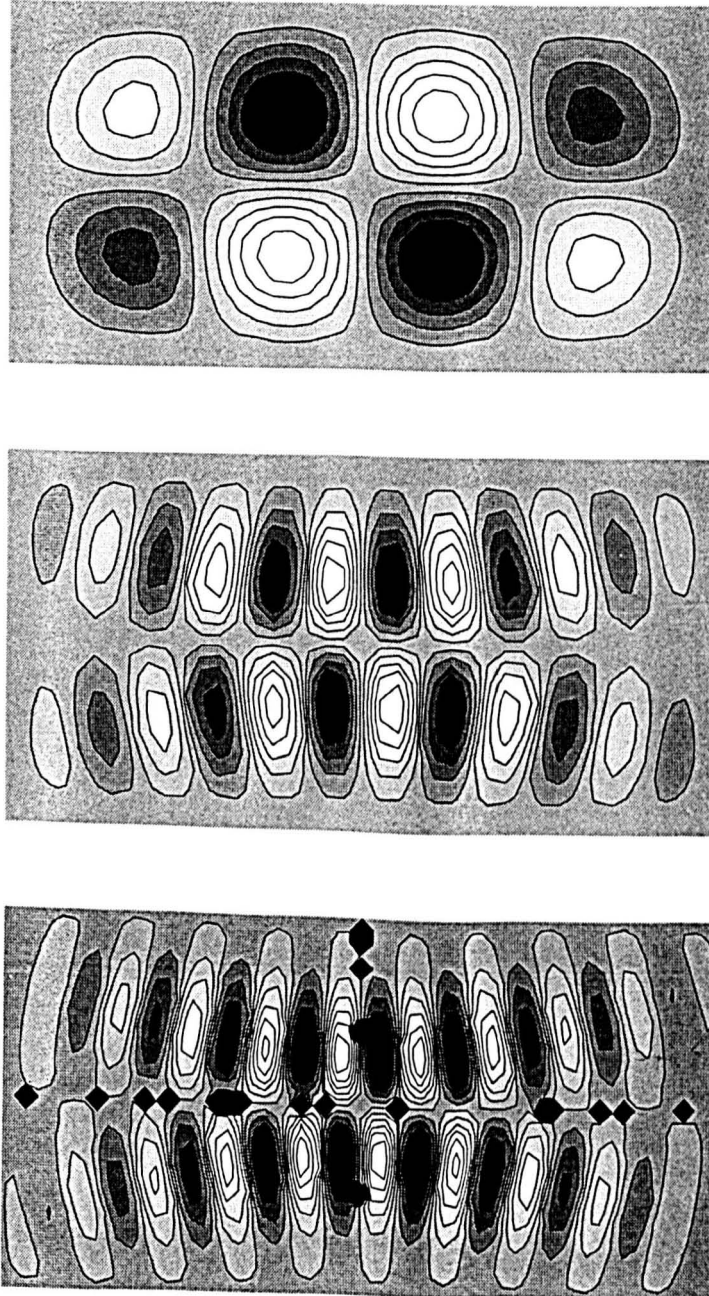


Figure 4.51: Sequence of patterns on branch OO1 for (top to bottom) $M = 10, 20, 30$.

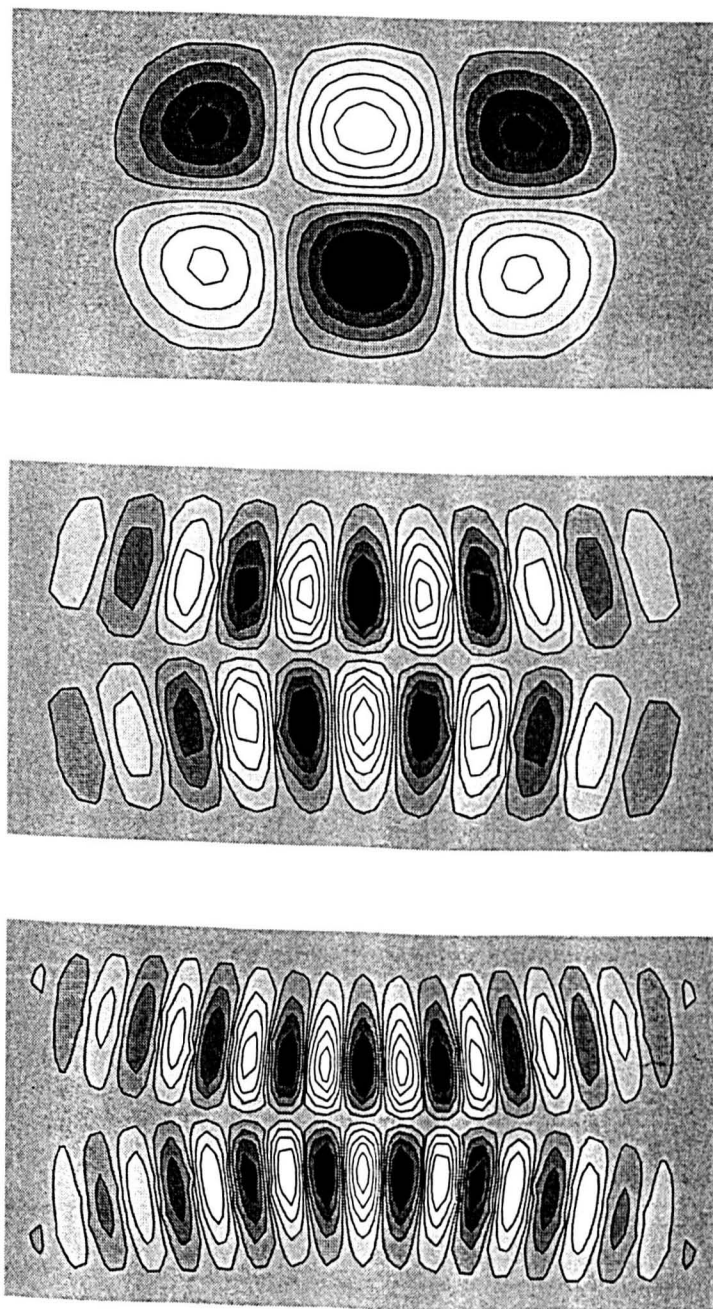


Figure 4.52: Sequence of patterns on branch EO1 for (top to bottom) $M = 10, 20, 30$.

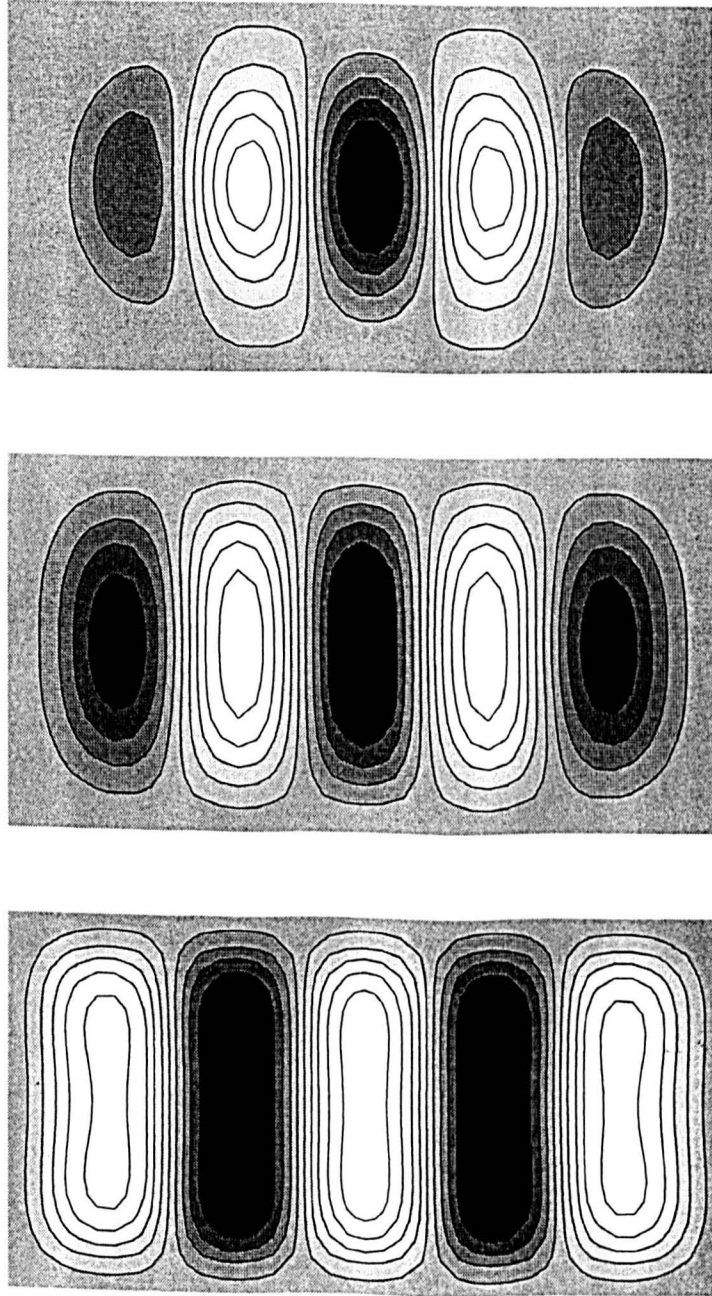


Figure 4.53: Contours of EE steady state solutions for u for $M = 10$ obtained with an initial state $U(x, y) = R(i, j)$ at (top to bottom) $\varepsilon = 0.108, 0.6, 2.8$.

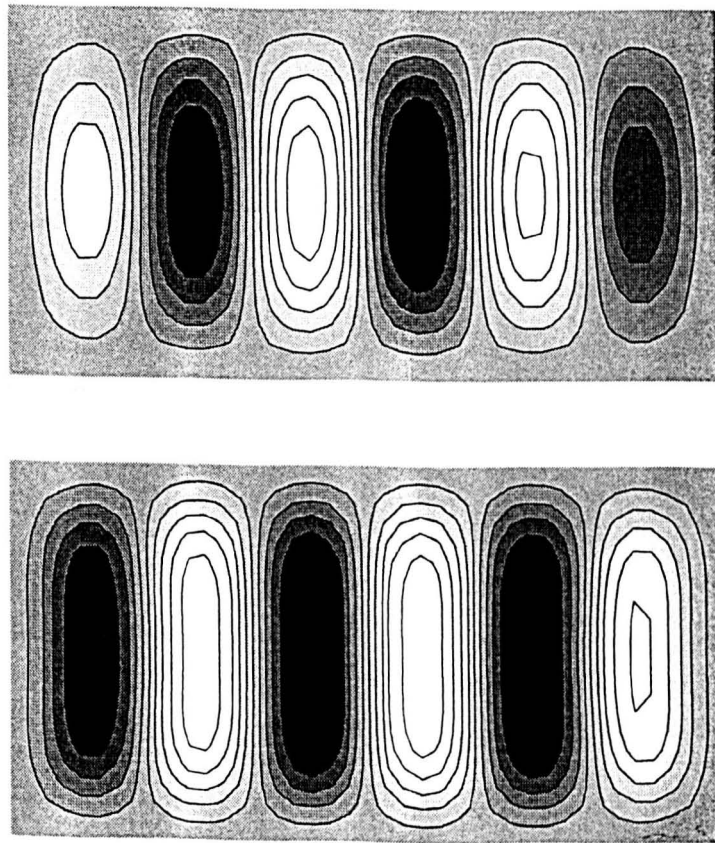


Figure 4.54: Contours of OE steady state solutions for u for $M = 10$ obtained with an initial state $U(x, y) = R(i, j)$ at $\varepsilon = 0.15, 1.6$.

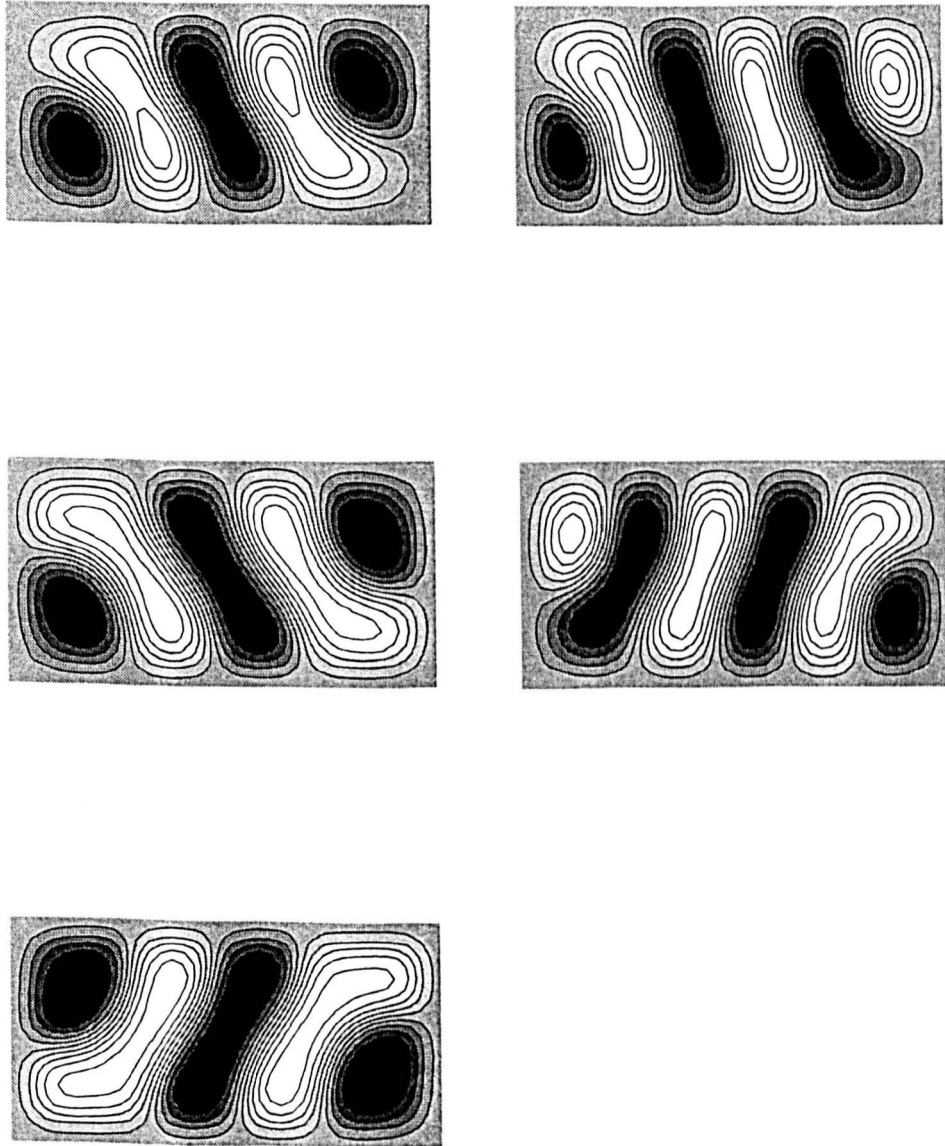


Figure 4.55: Contours of centrosymmetric steady state solutions for u for $M = 10$ obtained with an initial state $U(x, y) = R(i, j)$ at $\varepsilon = 0.8, 2.3, 3.2, 0.9, 1.4$.

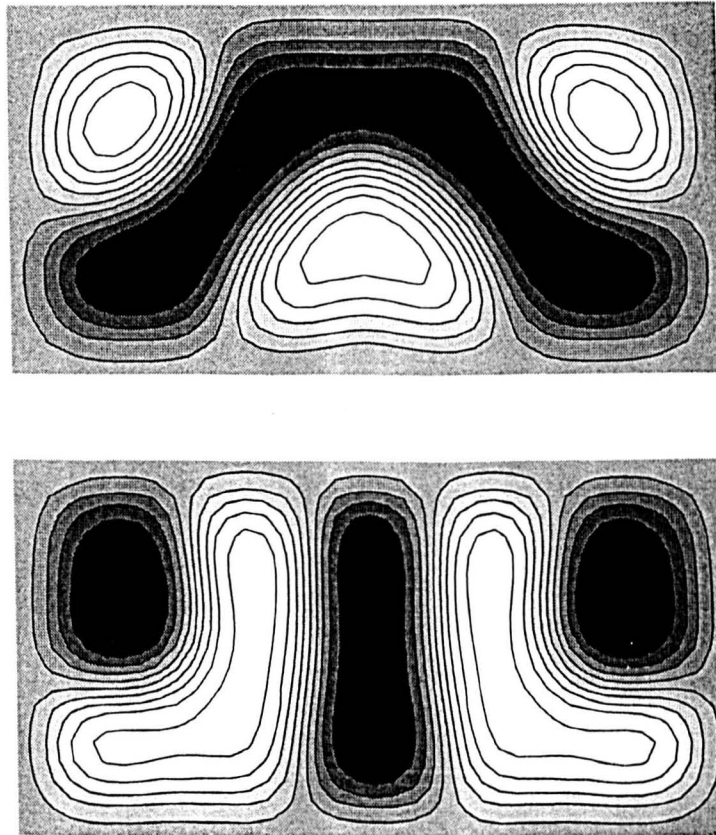


Figure 4.56: Contours of steady state solutions for u even in x for $M = 10$ obtained with an initial state $U(x, y) = R(i, j)$ at $\varepsilon = 1.8$ (top) and 3.1 (bottom).

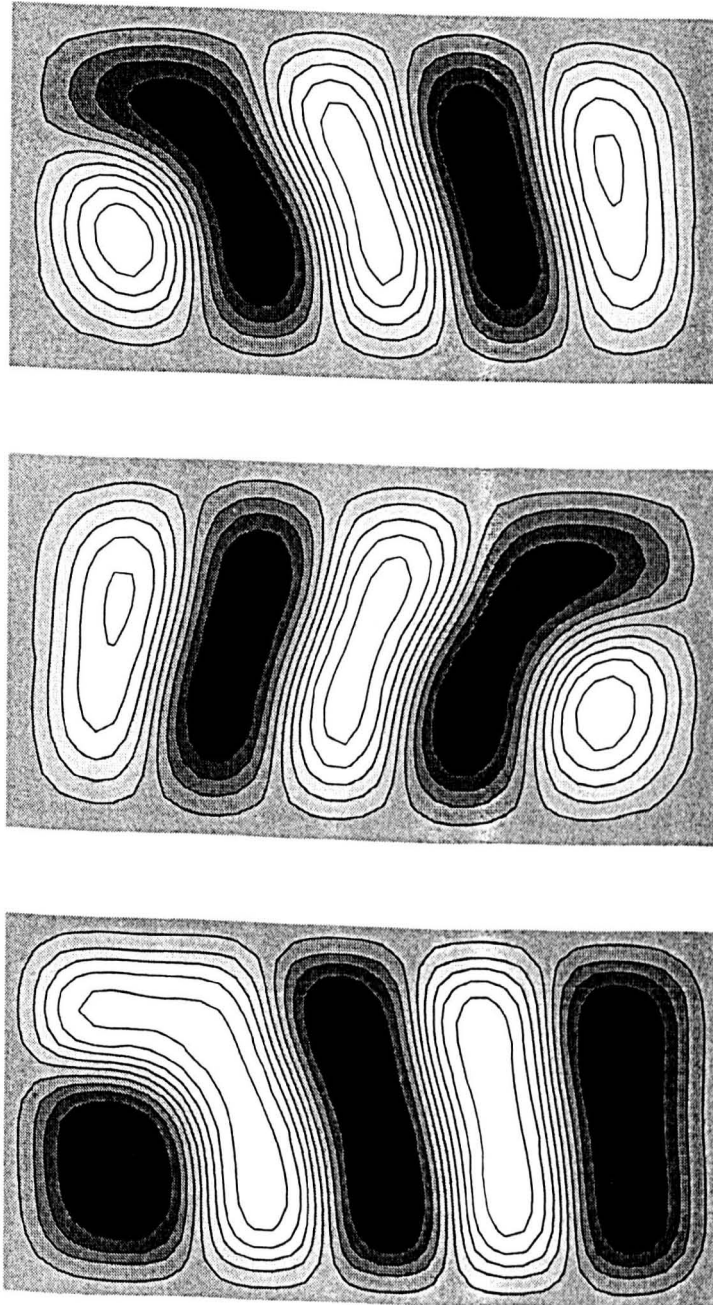


Figure 4.57: Contours of non-symmetric steady state solutions for u for $M = 10$ obtained with an initial state $U(x, y) = R(i, j)$ at (top to bottom) $\varepsilon = 1.0, 1.1, 3.4$.

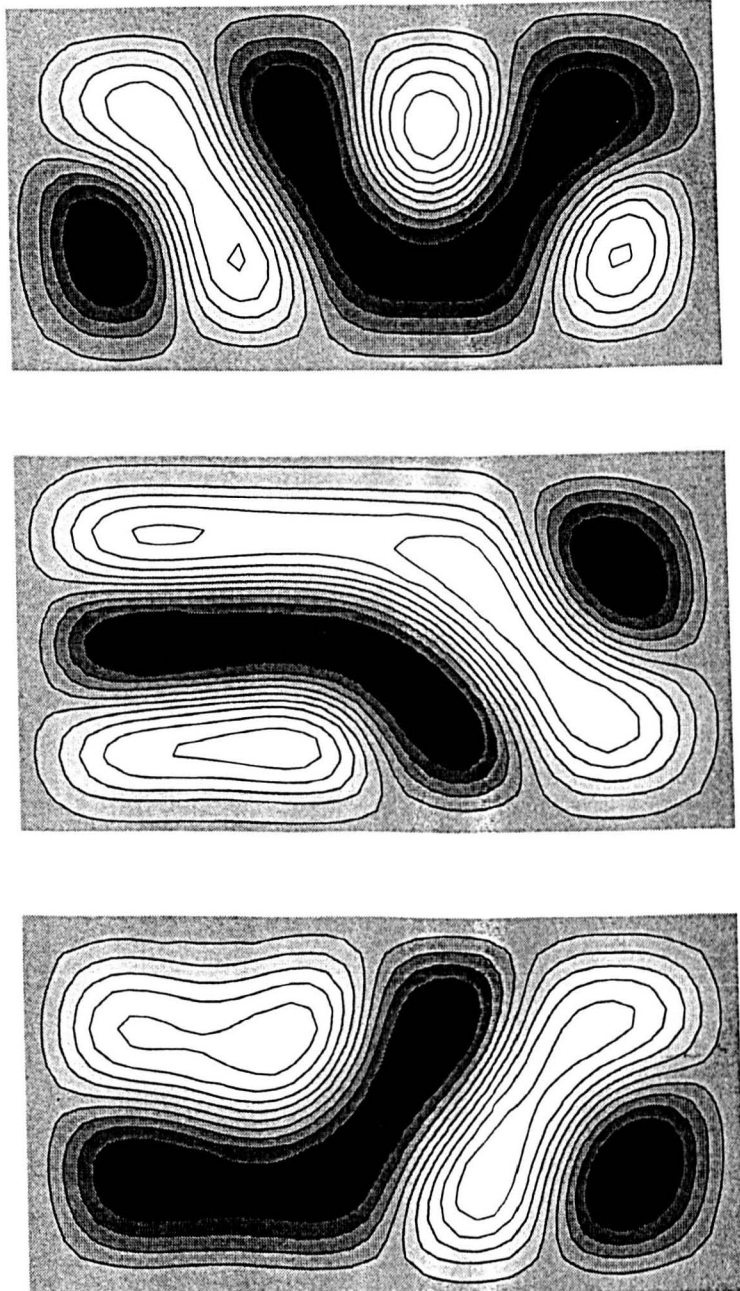


Figure 4.58: Contours non-symmetric steady state solutions for u for $M = 10$ obtained with an initial state $U(x, y) = R(i, j)$ at (top to bottom) $\varepsilon = 1.3, 1.5, 1.7$.

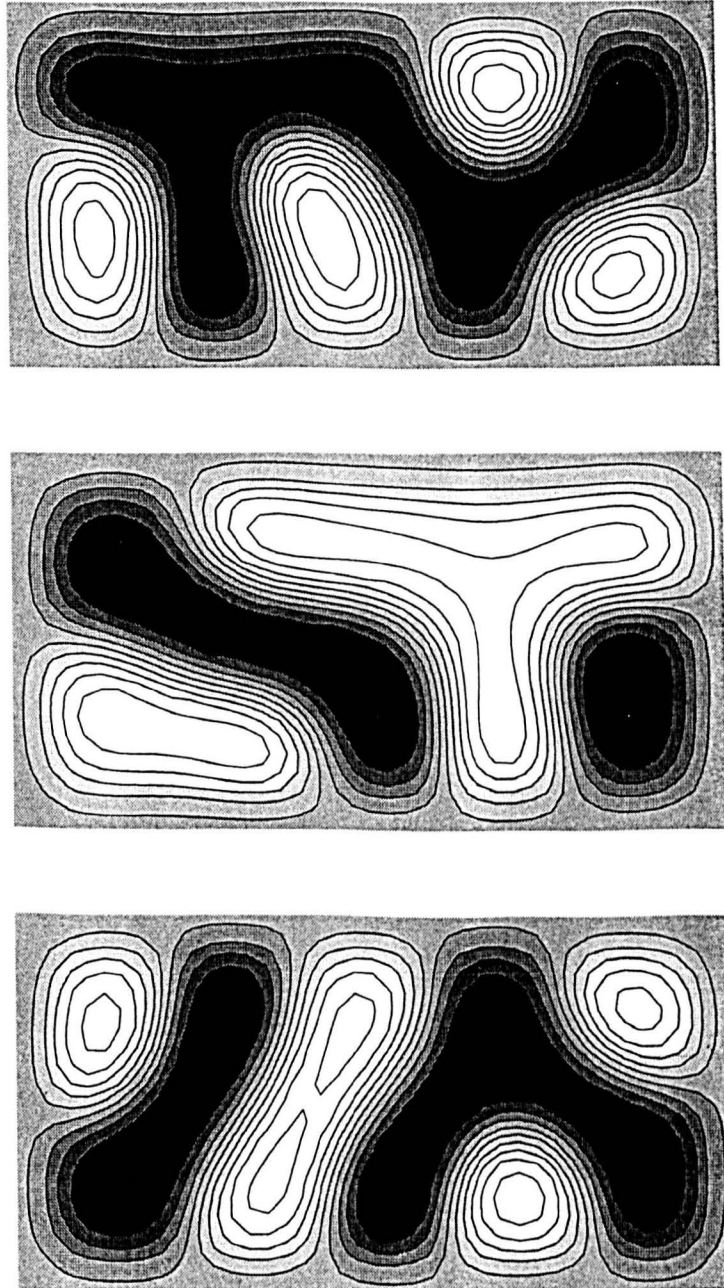


Figure 4.59: Contours of non-symmetric steady state solutions for u for $M = 10$ obtained with an initial state $U(x, y) = R(i, j)$ at (top to bottom) $\varepsilon = 2.6, 3.0, 3.3$.

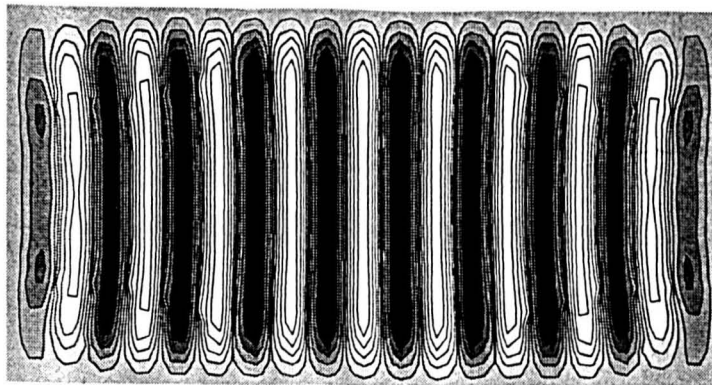
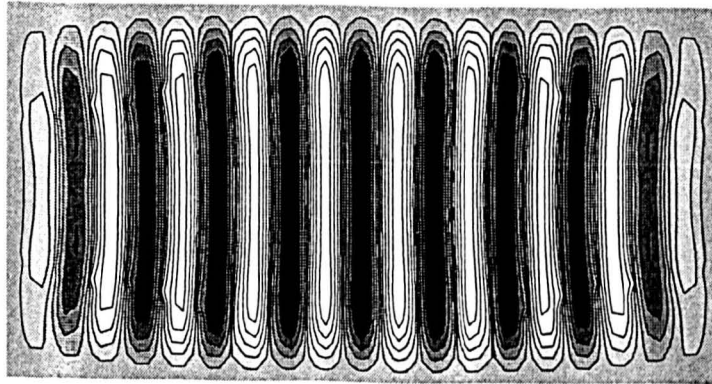
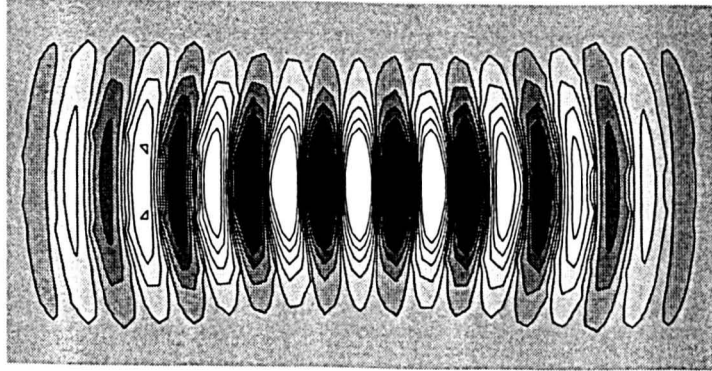


Figure 4.60: Contours of EE steady state solutions for u for $M = 30$ obtained with an initial state $U(x,y) = R(i,j)$ at (top to bottom) $\varepsilon = 0.00811, 0.1, 0.15$.

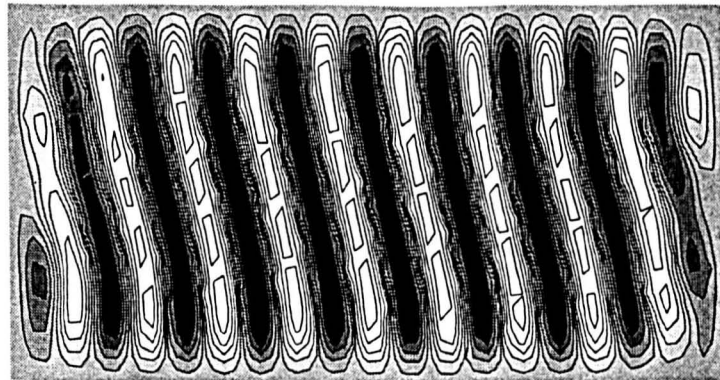
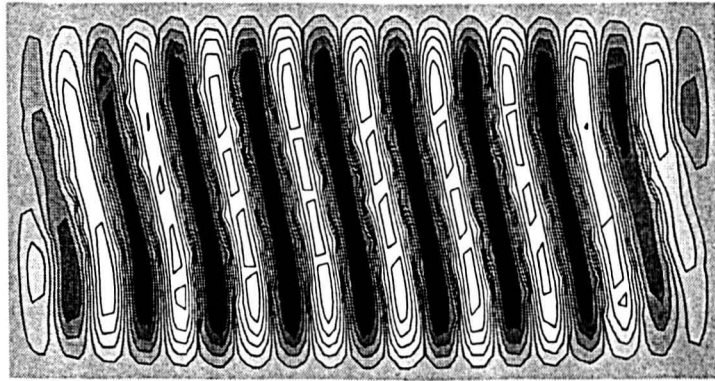
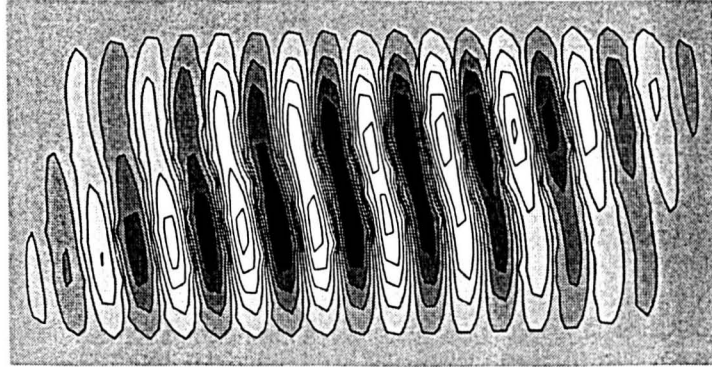


Figure 4.61: Contours of centrosymmetric steady state solutions for u for $M = 30$ obtained with an initial state $U(x, y) = R(i, j)$ at (top to bottom) $\varepsilon = 0.01211, 0.09111, 0.1811$.

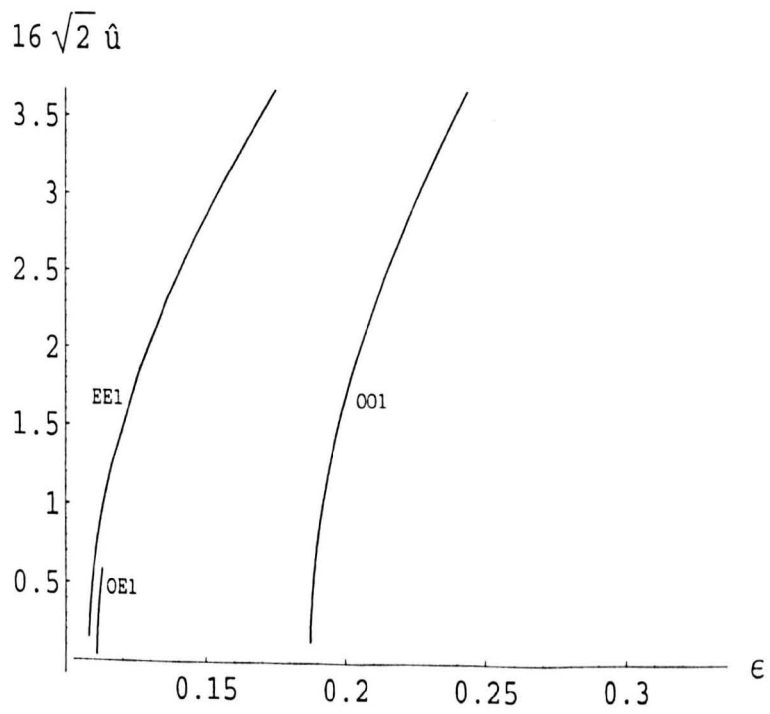


Figure 4.62: Bifurcation diagram for the case $M = 10$.

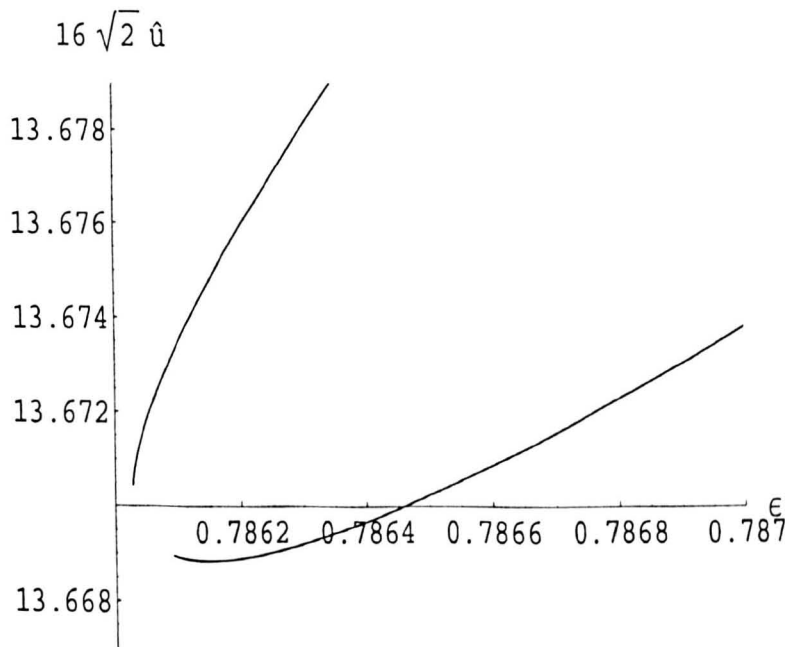


Figure 4.63: Fold bifurcation of the first centrosymmetric mode C_{F1} (the mode shown in Figure 4.55) for $M = 10$ near $\epsilon = 0.786$.

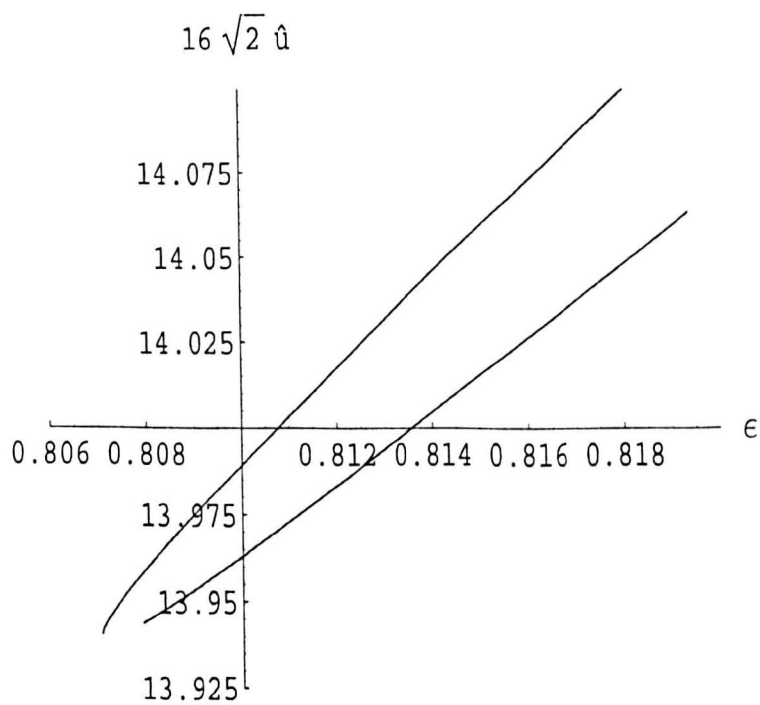


Figure 4.64: Fold bifurcation of the second centrosymmetric mode C_{F2} (the mode shown in figure 4.55) for $M = 10$ near $\epsilon = 0.807$.

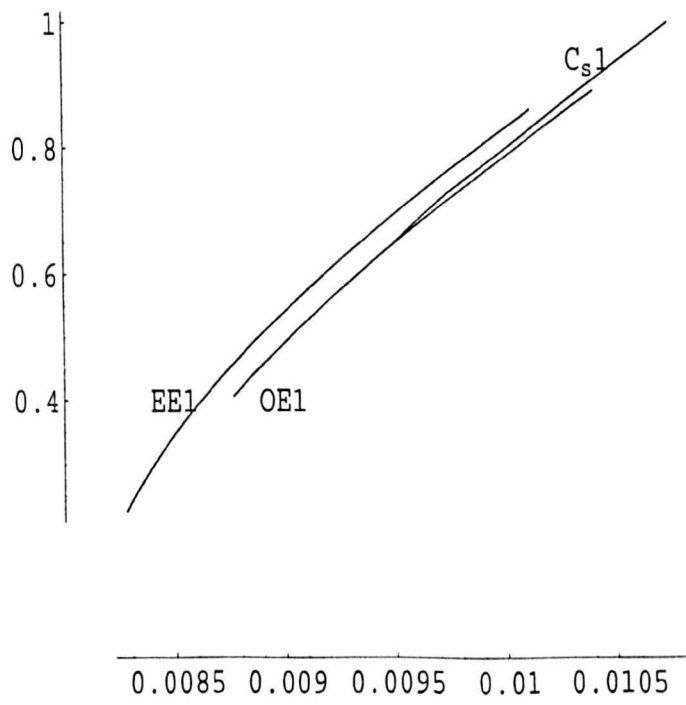


Figure 4.65: Partial bifurcation diagram for the case $M = 30$.

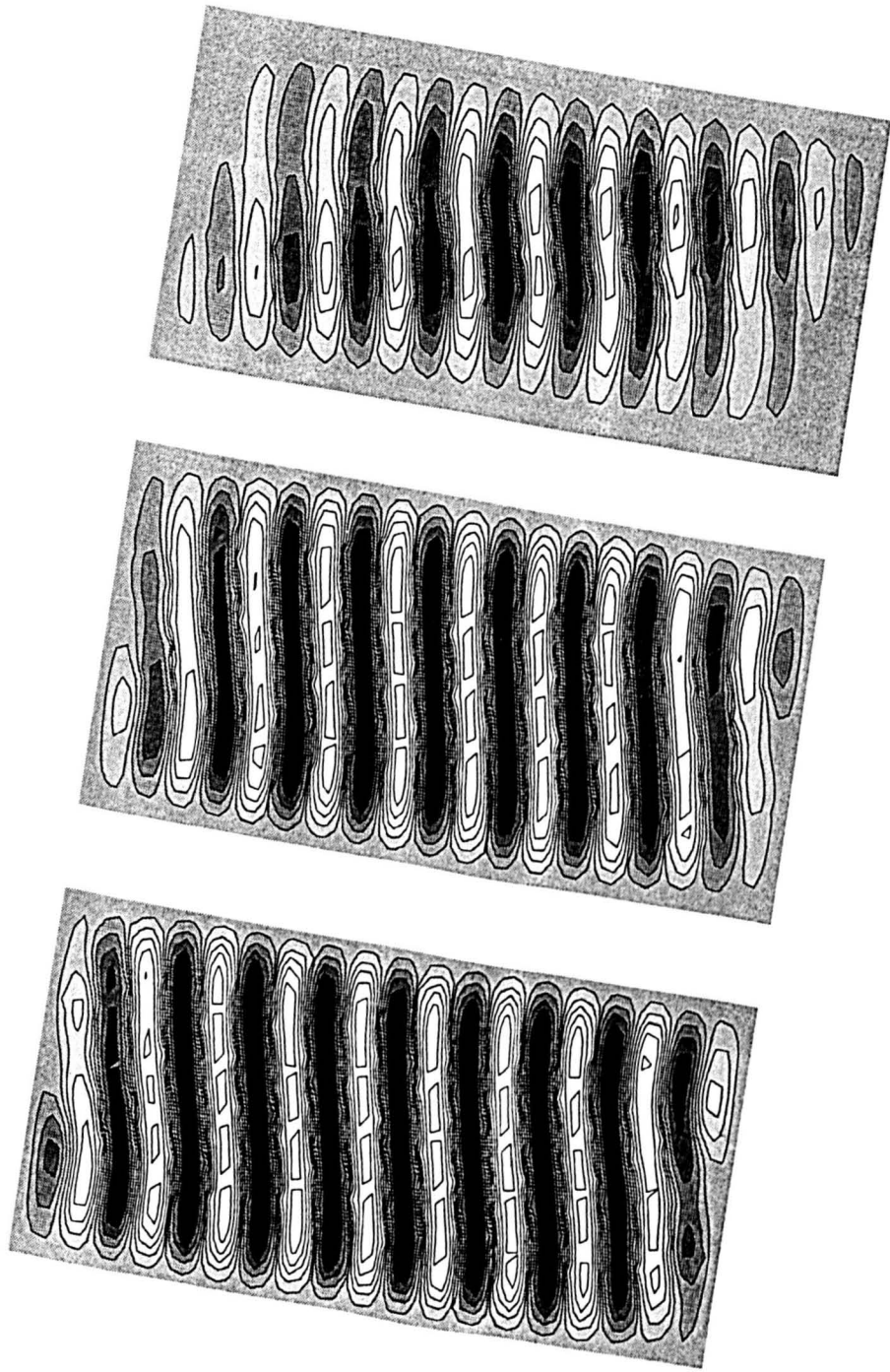


Figure 4.66: Contours of u for $M = 30$ on branch OE1 (top picture) and the centrosymmetric mode C_{s1} (bottom pictures) at $\varepsilon = 0.00948, 0.00952, 0.00976$ respectively.

Chapter 5

Pattern Formation in Large Rectangles

5.1 Introduction

This chapter adapts the theory and methodology described in Chapter 3 for the square to the case of a rectangle with sides of length L and M . We consider a solution in the regions spanning points of the boundary of maximum separation in the form of sets of rolls with axes perpendicular to the diagonals. The problem is formulated in Section 5.2 and the theory is developed in Section 5.3. Linear results are presented in Section 5.4 and nonlinear results in Section 5.5. The results are summarised in Section 5.6.

5.2 Formulation of the problem

The Swift-Hohenberg equation is

$$\frac{\partial u}{\partial t} = \varepsilon u - (1 + \nabla^2)^2 u - u^3, \quad (5.1)$$

where t is the non-dimensional time, $\nabla^2 = \frac{\partial^2}{\partial x^2} + \frac{\partial^2}{\partial y^2}$ where x and y are non-dimensional Cartesian coordinates, ε is a control parameter and $u(x, y, t)$ is a scalar field. The domain is a rectangle with sides of length L and M and the conditions

$$u = \frac{\partial u}{\partial q} = 0 \quad (5.2)$$

on the boundary, where q is used to denote the inward normal direction to the boundary.

The origin of coordinates x and y is chosen to be at the centre of the rectangle with the x -axis directed along one of the diagonals. A parameter l is introduced such that the diagonal is defined by $-l \leq x \leq l, y = 0$. Unlike the square, the diagonal does not split the corners into two equal angles. As a result we introduce the angle α where $\tan \alpha = M/L$ and $L = 2l \cos \alpha$, as shown in Figure 5.1. As in the case of the square it is expected that the onset of convection is associated with finite values of the parameter δ_1 where

$$\varepsilon = \frac{\pi^2}{l^2} + \frac{\delta_1}{l^{5/2}}. \quad (5.3)$$

5.3 Theory

The asymptotic structure of the solution as $l \rightarrow \infty$ closely follows that developed for the square in Chapter 3. The core solution in the region $-1 \leq X \leq 1, -\infty \leq Y \leq \infty$, where $x = lX$ and $y = l^{1/2}Y$, is again expanded in the form (3.6) for times $t = l^{5/2}\tau$ and an identical analysis to that of Section 3.3 leads to the same equations for the amplitude functions A_0 and A_1 :

$$4\left(\frac{\partial}{\partial X} - \frac{i}{2} \frac{\partial^2}{\partial Y^2}\right)^2 A_0 + \pi^2 A_0 = 0, \quad (5.4)$$

$$4\left(\frac{\partial}{\partial X} - \frac{i}{2} \frac{\partial^2}{\partial Y^2}\right)^2 A_1 + \pi^2 A_1 = \frac{\partial A_0}{\partial \tau} - \delta_1 A_0 + 3A_0 |A_0|^2 \quad (5.5)$$

where the leading term in the expansion of u is given by $l^{-5/4}u_0$, with

$$u_0 = A_0(X, Y, \tau)e^{ix} + A_0^*(X, Y, \tau)e^{-ix}. \quad (5.6)$$

As in the case of the square, the amplitude function A_0 satisfies

$$A_0(\pm 1, Y, \tau) = 0. \quad (5.7)$$

Corner region I near $x = -l$ is defined by $-X_- \cot \alpha \leq Y \leq X_- \tan \alpha$, $X_- \geq 0$, where $x = -l + l^{1/2}X_-$, and the solution there is given by (3.20) and (3.21) where the amplitude function A_0^- satisfies

$$\frac{\partial^2 A_0^-}{\partial X_-^2} = 0 \quad (5.8)$$

and the boundary conditions

$$A_0^- \sim X_- \frac{\partial A_0}{\partial X}(-1, Y, \tau) \quad \text{as } X_- \rightarrow \infty \quad (5.9)$$

and

$$A_0^- = 0 \quad \text{on } Y = -X_- \cot \alpha \quad \text{and } Y = X_- \tan \alpha, \quad X_- \geq 0. \quad (5.10)$$

Thus the solution for A_0^- is now given by

$$A_0^- = (X_- - Y \cot \alpha) \frac{\partial A_0}{\partial X}(-1, Y, \tau), \quad Y > 0 \quad (5.11)$$

$$A_0^- = (X_- + Y \tan \alpha) \frac{\partial A_0}{\partial X}(-1, Y, \tau), \quad Y < 0 \quad (5.12)$$

Similarly, corner region II near $x = l$ is defined by $X_+ \tan \alpha \leq Y \leq -X_+ \cot \alpha$, $X_+ \leq 0$, where $x = l + l^{1/2} X_+$, and the solution there is given by (3.22) and (3.28) where the amplitude function A_0^+ satisfies

$$\frac{\partial^2 A_0^+}{\partial X_+^2} = 0 \quad (5.13)$$

and the boundary conditions

$$A_0^+ \sim X_+ \frac{\partial A_0}{\partial X}(1, Y, \tau) \quad \text{as } X_+ \rightarrow -\infty \quad (5.14)$$

and

$$A_0^+ = 0 \quad \text{on } Y = X_+ \tan \alpha, \quad \text{and } Y = -X_+ \cot \alpha, \quad X_+ \leq 0. \quad (5.15)$$

Thus the solution for A_0^+ is now given by

$$A_0^+ = (X_+ + Y \tan \alpha) \frac{\partial A_0}{\partial X}(1, Y, \tau), \quad Y > 0, \quad (5.16)$$

$$A_0^+ = (X_+ - Y \cot \alpha) \frac{\partial A_0}{\partial X}(1, Y, \tau), \quad Y < 0. \quad (5.17)$$

Matching between the corner solutions and the core solution now implies that the core amplitude function A_1 must satisfy the boundary conditions

$$A_1(-1, Y, \tau) = \begin{cases} -Y \cot \alpha \frac{\partial A_0}{\partial X}(-1, Y, \tau), & Y > 0 \\ Y \tan \alpha \frac{\partial A_0}{\partial X}(-1, Y, \tau), & Y < 0 \end{cases} \quad (5.18)$$

$$A_1(1, Y, \tau) = \begin{cases} Y \tan \alpha \frac{\partial A_0}{\partial X}(1, Y, \tau), & Y > 0 \\ -Y \cot \alpha \frac{\partial A_0}{\partial X}(1, Y, \tau), & Y < 0. \end{cases} \quad (5.19)$$

As in the case of the square, the Fourier transform of the leading-order core amplitude function A_0 is given by

$$\bar{A}_0 = a(\omega, \tau) e^{-\frac{i\omega^2 X}{2}} \cos\left(\frac{\pi X}{2}\right) \quad (5.20)$$

and the solvability condition for the Fourier transform of the second amplitude function A_1 leads to the same result (3.37) except that the transform functions \bar{D}_\pm defined by

$$\bar{A}_1(\pm 1, \omega, \tau) = \bar{D}_\pm(\omega, \tau) \quad (5.21)$$

must now be determined from (5.18) and (5.19). This leads to the equation for the unknown function $a(\omega, \tau)$:

$$\frac{\partial a}{\partial \tau} = \delta_1 a + 2\pi(\bar{D}_+ e^{\frac{i\omega^2}{2}} + \bar{D}_- e^{-\frac{i\omega^2}{2}}) - 3I_0 \quad (5.22)$$

where

$$I_0(\omega, \tau) = \int_{-1}^1 H_0(X, \omega, \tau) e^{\frac{i\omega^2 X}{2}} \cos\left(\frac{\pi X}{2}\right) dX, \quad (5.23)$$

$$H_0(X, \omega, \tau) = \int_{-\infty}^{\infty} A_0 |A_0|^2 e^{i\omega Y} dY, \quad (5.24)$$

$$A_0(X, Y, \tau) = \frac{\cos \frac{\pi X}{2}}{2\pi} \int_{-\infty}^{\infty} a(\omega, \tau) e^{-\frac{i\omega^2 X}{2} - i\omega Y} d\omega \quad (5.25)$$

and

$$\bar{D}_+(\omega, \tau) = \int_0^{\infty} Y \tan \alpha \frac{\partial A_0}{\partial X}(1, Y, \tau) e^{i\omega Y} dY - \int_{-\infty}^0 Y \cot \alpha \frac{\partial A_0}{\partial X}(1, Y, \tau) e^{i\omega Y} dY \quad (5.26)$$

$$\bar{D}_-(\omega, \tau) = -\int_0^{\infty} Y \cot \alpha \frac{\partial A_0}{\partial X}(-1, Y, \tau) e^{i\omega Y} dY + \int_{-\infty}^0 Y \tan \alpha \frac{\partial A_0}{\partial X}(-1, Y, \tau) e^{i\omega Y} dY \quad (5.27)$$

where

$$\frac{\partial A_0}{\partial X}(\pm 1, Y, \tau) = \mp \frac{1}{4} \int_{-\infty}^{\infty} a(\omega, \tau) e^{\mp \frac{i\omega^2}{2} - i\omega Y} d\omega. \quad (5.28)$$

The system (5.22) - (5.28) is the same as that for the square except that the angle α now appears in the forms of \bar{D}_\pm in (5.26) and (5.27). When $\alpha = \pi/4$ these forms reduce to those for the square given by (3.42).

As in the case of the square, the system (5.22) - (5.28) admits solutions of the form

$$a(\omega, \tau) = r(\omega, \tau) e^{i\theta} \quad (5.29)$$

where r is real and the phase θ is constant. In this case

$$A_0 = e^{i\theta} A, \quad H_0 = e^{i\theta} H, \quad I_0 = e^{i\theta} I, \quad \bar{D}_- = e^{i\theta} D, \quad \bar{D}_+ = e^{i\theta} D^* \quad (5.30)$$

and r is the solution of the system

$$\frac{\partial r}{\partial \tau} = \delta_1 r + 2\pi \left(D e^{-\frac{i\omega^2}{2}} + D^* e^{\frac{i\omega^2}{2}} \right) - 3I \quad (5.31)$$

where

$$I(\omega, \tau) = \int_{-1}^1 H(X, \omega, \tau) e^{\frac{i\omega^2 X}{2}} \cos\left(\frac{\pi X}{2}\right) dX \quad (5.32)$$

$$H(X, \omega, \tau) = \int_{-\infty}^{\infty} A |A|^2 e^{i\omega Y} dY \quad (5.33)$$

$$A(X, Y, \tau) = \frac{\cos \frac{\pi X}{2}}{2\pi} \int_{-\infty}^{\infty} r(\omega, \tau) e^{-\frac{i\omega^2 X}{2} - i\omega Y} d\omega \quad (5.34)$$

and

$$D(\omega, \tau) = \int_{-\infty}^0 (Y \tan \alpha) F(Y, \tau) e^{i\omega Y} dY - \int_0^{\infty} (Y \cot \alpha) F(Y, \tau) e^{i\omega Y} dY \quad (5.35)$$

where

$$F(Y, \tau) = \frac{1}{4} \int_{-\infty}^{\infty} r(\omega, \tau) e^{\frac{i\omega^2}{2} - i\omega Y} d\omega. \quad (5.36)$$

Solutions are required for which

$$r \rightarrow 0 \quad \text{as} \quad \omega \rightarrow \pm\infty. \quad (5.37)$$

The value of the phase constant θ is arbitrary but, as in the case of the square, is expected to be determined at higher order in the expansion of the solution for u as $l \rightarrow \infty$.

For solutions determined by (5.29)-(5.37) it follows from (5.34) that the amplitude function A satisfies

$$A(X, Y, \tau) = A^*(-X, -Y, \tau). \quad (5.38)$$

This is equivalent to solutions that are centrosymmetric, so that, for example, if $\theta = 0$ then $u_0(x, X, Y, \tau) = u_0(-x, -X, -Y, \tau)$ and if $\theta = \frac{\pi}{2}$,

$u_0(x, X, Y, \tau) = -u_0(-x, -X, -Y, \tau)$. This just reflects the fact that the geometry of the rectangle is centrosymmetric relative to its diagonals. Odd or even symmetries in x and y , as in the case of the square, are excluded (in general) for the rectangle because its geometry is not symmetric relative to the diagonals.

A further consequence of (5.38) is that

$$H(X, \omega, \tau) = H^*(-X, \omega, \tau). \quad (5.39)$$

and from this it follows from (5.32) that I is real. Thus all of the terms in (5.31) are real and solutions can be found describing the onset of convection and its weakly nonlinear development. These are considered in the next two sections.

5.4 Linear solution

The system (5.31) - (5.36) is identical to that for the square except for the definition of $D(\omega, \tau)$ in (5.35). Thus solutions of the steady linearised version of (5.30),

$$\delta_1 r + 2\pi(De^{-\frac{i\omega^2}{2}} + D^*e^{\frac{i\omega^2}{2}}) = 0 \quad (5.40)$$

can be obtained using the same method as that described in Section 3.6.1 except that D is now defined in terms of α by (5.35).

5.4.1 Solution method

Solutions for

$$r = \sum_{n=1}^{\infty} r_n \sin n\pi\bar{\omega} \quad (5.41)$$

where

$$\bar{\omega} = \frac{1}{2}(1 + \tanh \omega), \quad 0 < \bar{\omega} < 1. \quad (5.42)$$

are no longer even or odd functions of ω and so all of the Fourier coefficients r_n are non-zero. These are determined from the system

$$\delta_1 r_m + 4\pi \sum_{n=1}^{\infty} r_n b_{mn} = 0 \quad (m = 1, 2, \dots) \quad (5.43)$$

where

$$b_{mn}=2 \int_0^1 (D_{nr} \cos \frac{\omega^2}{2} + D_{ni} \sin \frac{\omega^2}{2}) \sin m\pi\bar{\omega}d\bar{\omega} \quad (5.44)$$

and

$$D_{nr} = \int_{-\infty}^0 Y \tan \alpha (F_{nr} \cos \omega Y - F_{ni} \sin \omega Y) dY - \int_0^{\infty} Y \cot \alpha (F_{nr} \cos \omega Y - F_{ni} \sin \omega Y) dY \quad (5.45)$$

$$D_{ni} = \int_{-\infty}^0 Y \tan \alpha (F_{ni} \cos \omega Y + F_{nr} \sin \omega Y) dY - \int_0^{\infty} Y \cot \alpha (F_{ni} \cos \omega Y + F_{nr} \sin \omega Y) dY. \quad (5.46)$$

Here D_{nr} and D_{ni} are the real and imaginary parts of the Fourier coefficients D_n arising in the representation

$$D = \sum_{n=1}^{\infty} r_n D_n(\omega) \quad (5.47)$$

and F_{nr} and F_{ni} are defined, as in the case of the square, by (3.57) and (3.58). In matrix form, (5.43) is

$$(\mathbf{B} + \frac{\delta_1}{4\pi} \mathbf{I}) \mathbf{r} = 0 \quad (5.48)$$

where \mathbf{B} is the matrix with elements b_{mn} , \mathbf{I} is the identity matrix and \mathbf{r} is the column vector with elements r_m .

5.4.2 Results

The matrix eigenvalue problem (5.48) was solved using a standard Mathematica routine in the same way as outlined in Section 3.6.2. The integrals involved in the calculation of b_{mn} were evaluated using Simpson's rule, with those in ω transformed to the variable $\bar{\omega}$. The integration over Y in (5.45) and (5.46) was performed typically with a step size of $\Delta Y = 0.1$ and various outer boundaries $Y = \pm Y_{\infty}$ with Y_{∞} ranging from 10 to 80. The integrations in $\bar{\omega}$ were performed with the same number of steps as those in Y . Results were obtained for truncation levels up to $N = 10$.

Results for the first six eigenvalues δ_1 and the corresponding eigenvectors \mathbf{r} obtained for a truncation level $N = 10$ and outer boundary $Y_{\infty} = 20$ are shown in Tables 5.1 and 5.2 for $\alpha = 0.644(36.9^\circ)$ and $\alpha = \pi/6$. The first corresponds to the aspect ratio $M/L = 0.75$ studied in Chapter 4. Figure 5.2 shows the leading eigenvalue δ_1 for a range of values of α . Note that a

δ_1	15.4165	33.8769	50.19907	68.3098	93.5224	115.436
r_1	0.7925	0.1844	-0.1350	-0.0346	0.0285	-0.0037
r_2	0.1765	-0.6672	-0.2469	0.3072	0.0508	0.0711
r_3	0.4347	-0.0863	0.6130	0.1946	-0.4531	0.0648
r_4	0.1348	-0.5168	-0.0446	-0.4955	-0.1420	-0.5505
r_5	0.2782	-0.1069	0.5641	0.0661	0.5003	-0.1121
r_6	0.0969	-0.3742	0.0121	-0.5781	-0.0447	0.3873
r_7	0.1773	-0.0856	0.4097	0.0107	0.6054	-0.0439
r_8	0.0652	-0.2529	0.0210	-0.4564	-0.0031	0.5963
r_9	0.0986	-0.0524	0.2370	-0.0037	0.3903	-0.0055
r_{10}	0.0369	-0.1442	0.0136	-0.2721	0.0022	0.4093

Table 5.1: First six eigenvalues and eigenvectors for $\alpha = 0.644$.

slight dip in the curve occurs with a minimum at $\alpha \approx \pi/3$, but generally the critical value of δ_1 increases as the angle α decreases to zero because the edges of the rectangle nearest to the diagonal become more restrictive. Eigenvalues and eigenvectors for the case of the square, $\alpha = \pi/4$, are in good agreement with those obtained in Chapter 3.

The leading eigenfunction $r(\omega)$ with $\alpha = 0.644$ constructed from (5.41) and the real and imaginary parts of the corresponding amplitude function $A(X, Y)$ calculated from (5.34) are shown in Figure 5.3. The corresponding results for $\alpha = \pi/6$ are shown in Figure 5.4. Figures 5.5 and 5.6 show the solution for u_0 calculated from (5.6) in the case where l is taken as 20 and $\theta = 0$ for $\alpha = 0.644$ and $\alpha = \pi/6$ respectively.

5.4.3 Comparison with numerical results

The asymptotic results obtained here can be compared with the linearised solutions of the Swift-Hohenberg equation reported in Section 4.2. Setting $l = \frac{l}{2} \sec \alpha$ in (5.3), Figure 5.7 shows the first two eigenvalues δ_1 for $\alpha = 0.644$ listed in Table 5.1 along with the linearised solutions of the Swift-Hohenberg equation for $M/L = 0.75$ displayed in Figure 4.1. These indicate good agreement. It should be noted that in the case of the rectangle there are

δ_1	15.0994	36.8888	56.5410	76.5044	104.194	128.431
r_1	-0.7156	-0.3151	0.0810	0.0551	-0.0237	0.0063
r_2	-0.2807	0.5875	0.4182	-0.2429	-0.0873	-0.0631
r_3	-0.4338	0.1398	-0.5620	-0.3403	0.4136	-0.1141
r_4	-0.2196	0.4970	0.0660	0.4772	0.2543	0.5208
r_5	-0.2903	0.1801	-0.5347	-0.1142	-0.4931	0.2019
r_6	-0.1599	0.3737	-0.0320	0.5596	0.0802	-0.3855
r_7	-0.1898	0.1459	-0.3947	-0.0165	-0.5977	0.0792
r_8	-0.1081	0.2568	-0.0449	0.4444	0.0053	-0.5920
r_9	-0.1071	0.0898	-0.2298	0.0081	-0.3863	0.0098
r_{10}	-0.0613	0.1468	-0.0286	0.2655	-0.0041	-0.4069

Table 5.2: First six eigenvalues and eigenvectors for $\alpha = \pi/6$.

four distinct modes (EE, OO, EO and OE) that form each group of branches in the linearised solutions of Figure 4.1. These all correspond to patterns with sets of rolls along both diagonals, as observed in results for $M = 30$ in Figures 4.3, 4.5, 4.7 and 4.9. Unlike the case of the square, the modes EO and OE do not generally coincide and so there is no linearised solution consisting of rolls along only one diagonal (that is, a diagonal mode D). Thus it is expected that the asymptotic structure described in this chapter will represent a truly linear solution for general large l only when the structure occurs along both diagonals. The solution for a single diagonal will, nevertheless, correspond to a weakly nonlinear combination of the EO and OE modes that will produce a diagonal mode. In the asymptotic theory, these issues can only be resolved by taking the asymptotic expansion to higher order in l .

5.5 Nonlinear solution

5.5.1 Solution Method

Solutions of the full nonlinear version of (5.31),

$$\frac{\partial r}{\partial \tau} = \delta_1 r + 2\pi(De^{-\frac{i\omega^2}{2}} + D^*e^{\frac{i\omega^2}{2}}) - 3I \quad (5.49)$$

subject to the boundary conditions (5.37) were obtained using the same method as that described for the square in Section 3.7. This leads to the system

$$\frac{\delta r_m}{\delta \tau} = \delta_1 r_m + 4\pi \sum_{n=1}^{\infty} r_n b_{mn} - 3c_m, \quad m = 1, 2, \dots \quad (5.50)$$

to be solved for the individual modes r_m , where

$$I(\omega, \tau) = \sum_{n=1}^{\infty} c_n \sin n\pi\bar{\omega}. \quad (5.51)$$

The coefficients c_n are calculated in the same manner as that described for the square in Section 3.7 and the coefficients b_{mn} are those given by (5.44) in the linear analysis of Section 5.4. The linearised solution with a suitably chosen amplitude was used to provide an initial state at $\tau = 0$ and the solution allowed to evolve to its steady-state form at a slightly supercritical value of δ_1 . Further steady-state solutions were then computed by incrementing δ_1 and using the previous solution as the initial state.

5.5.2 Results

Figure 5.8 shows a plot of the steady-state solution for r at $\omega = 0$ as a function of δ_1 for the leading mode in the case $\alpha = 0.644$ where the bifurcation occurs at $\delta_1 = 15.417$. This was obtained using a truncation level $N = 10$ and with 20 steps in X and 100 steps in $\bar{\omega}$ and Y in the integration formulae. A time step $\Delta\tau = 0.0035$ was used and convergence to a steady-state solution was achieved typically to within an error of 0.0005 in the value of r when $\tau = 1$, although this time increased significantly in the neighbourhood of the bifurcation point. Table 5.3 shows the steady-state values of r_n for several values of δ_1 . Plots of the steady-state solution for the real and imaginary parts of A at $\delta_1 = 22.5$ are shown in Figure 5.9 and the corresponding contours of u_0 calculated from (5.6) in the case when l is taken as 20 and $\theta = 0$ in Figure 5.10. As δ_1 increases the solution increases in amplitude and spreads outwards from the diagonal; the curvature of the roll pattern decreases. Corresponding results for the case $\alpha = \pi/6$ are shown in Figures 5.11 and 5.12 and in Table 5.4.

δ_1	25	30	35
r_1	6.9926	8.7118	10.1595
r_2	1.5253	2.2729	3.1966
r_3	1.2272	1.4362	1.5732
r_4	0.5510	0.7799	1.0315
r_5	0.4199	0.4558	0.4552
r_6	0.2512	0.3404	0.4260
r_7	0.1645	0.1618	0.1398
r_8	0.1210	0.1573	0.1862
r_9	0.0586	0.0496	0.0318
r_{10}	0.0521	0.0649	0.0721

Table 5.3: Steady-state values of r_n for the leading solution branch at several values of δ_1 with $\alpha = 0.644$.

δ_1	25	30	35
r_1	6.5336	7.8601	8.7981
r_2	2.4338	3.3973	4.4477
r_3	1.5760	1.9898	2.4156
r_4	0.9516	1.2994	1.6679
r_5	0.6386	0.8031	0.9789
r_6	0.4543	0.6066	0.7610
r_7	0.2878	0.3562	0.4297
r_8	0.2255	0.2941	0.3597
r_9	0.1182	0.1428	0.1691
r_{10}	0.0990	0.1257	0.1491

Table 5.4: Steady-state values of r_n for the leading solution branch at several values of δ_1 with $\alpha = \pi/6$.

5.6 Discussion

The present chapter shows that the asymptotic theory of Chapter 3 can be extended to the case of a rectangular domain in a relatively straightforward manner. The solutions in the core region and corner regions are similar to those for the square domain except that the rectangular geometry implies that the end conditions for the amplitude functions A_1 are now asymmetric, leading to solutions for the leading order amplitude function A_0 that are centrosymmetric relative to the diagonal of the rectangle. The values of δ_1 at onset for the case $M/L = 0.75$ give critical values of ε that are in good agreement with the numerical results for the leading groups of branches as $M \rightarrow \infty$ in Figure 4.1 and the associated roll patterns are consistent with those of the numerical results of Chapter 4 at large values M . The dependence of δ_1 on $\alpha = \tan^{-1}(M/L)$ shown in Figure 5.2 is consistent with the results of Chapter 3 when $\alpha = \pi/4$ and also predicts that $\delta_1 \rightarrow \infty$ as $\alpha \rightarrow 0$. This is consistent with the fact that if $M \ll L$ the closeness of the walls at $y = 0$ and $y = M$ begins to have a significant impact on the critical value of ε which must rise above the value π^2/l^2 when M is finite and the geometry is essentially that of a narrow channel.

It is envisaged that wall regions equivalent to those of Section 3.8 for the square domain exist in order to adjust the solution to the full boundary conditions at the walls of the rectangle. Although these have not been considered in the present chapter it is expected that they will result in the main incident x -roll component ($A_0 e^{ix}$) in each corner being reflected from the boundary at an equal angle, generating a weak roll component B within each corner region where the roll axes are at angle 2α to the axes of the main roll component (i.e to the y direction in Figure 5.1). In the case of the square domain we have $\alpha = \pi/4$ and the roll axes of the reflected component B are then orthogonal to those of the main x -roll component.

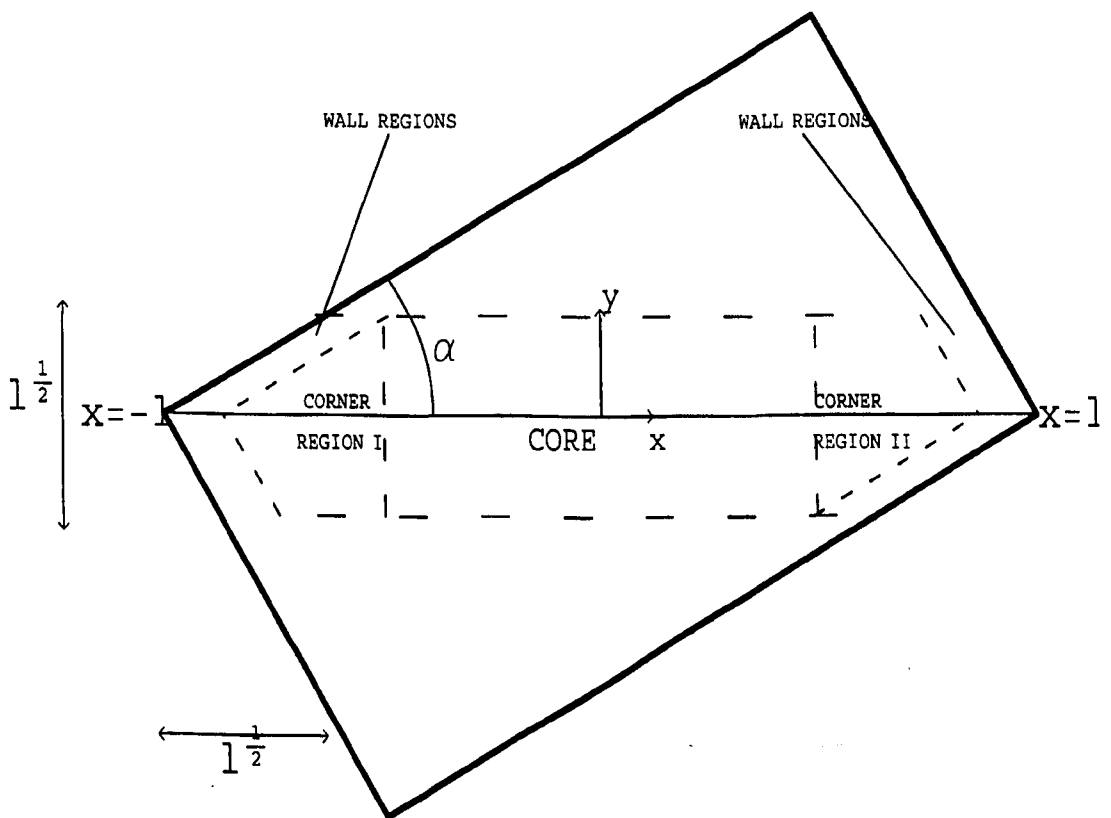


Figure 5.1: Schematic diagram of the rectangular domain, showing the diagonal from $x = -l$ to $x = l$ and the core region of width order $l^{1/2}$.

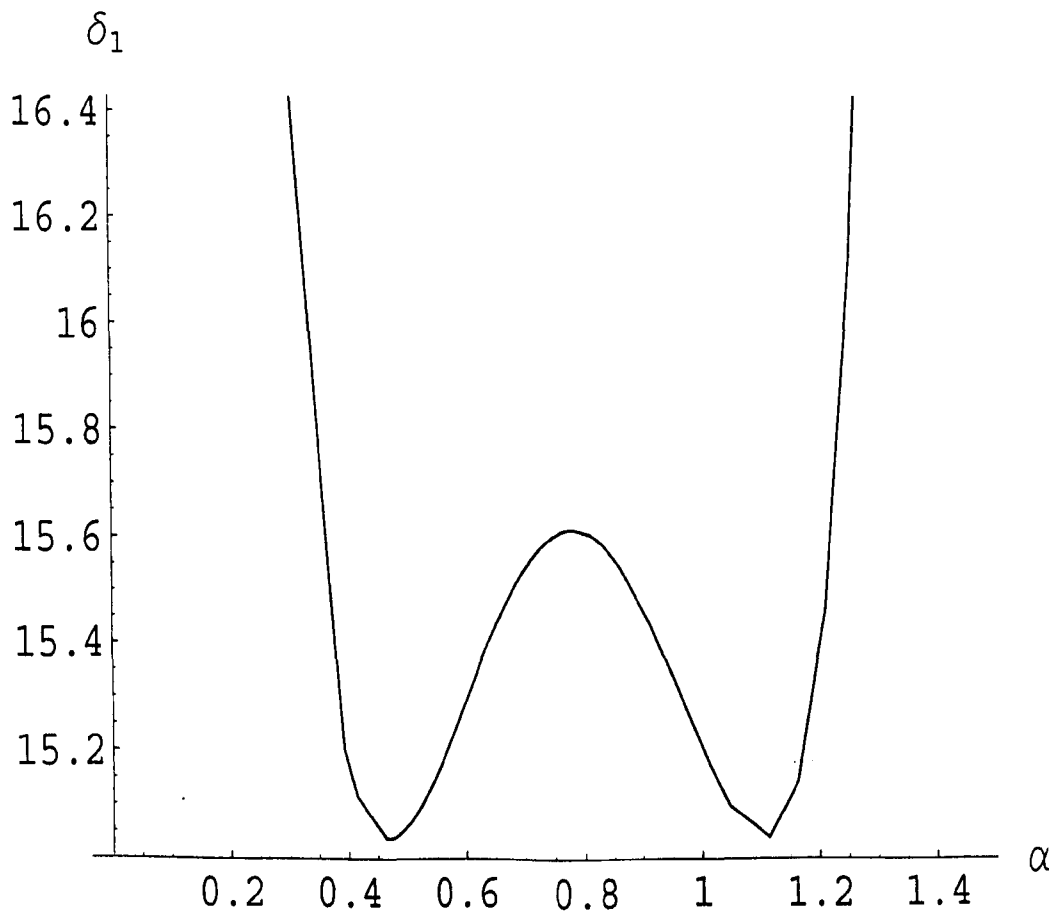


Figure 5.2: The leading eigenvalue δ_1 as a function of α

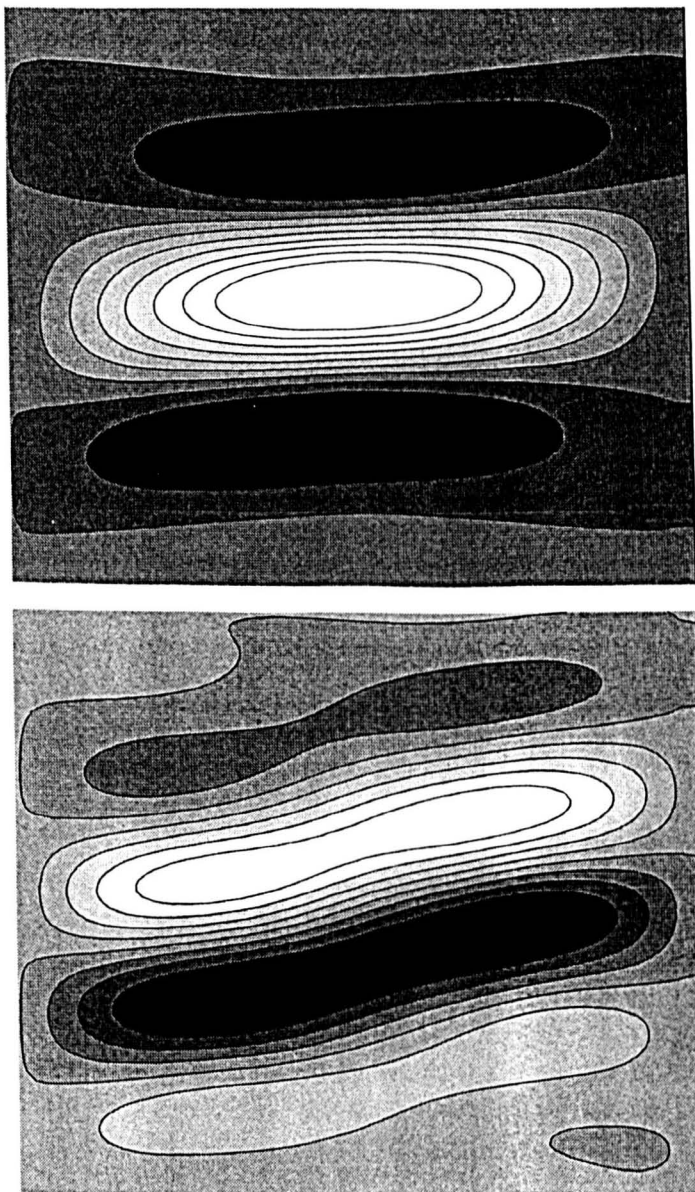


Figure 5.3: Contours of the real and imaginary parts of the amplitude function $A(X, Y)$ in the domain $-1 < X < 1$, $-5 < Y < 5$ for the leading eigenfunction with $\alpha = 0.644$

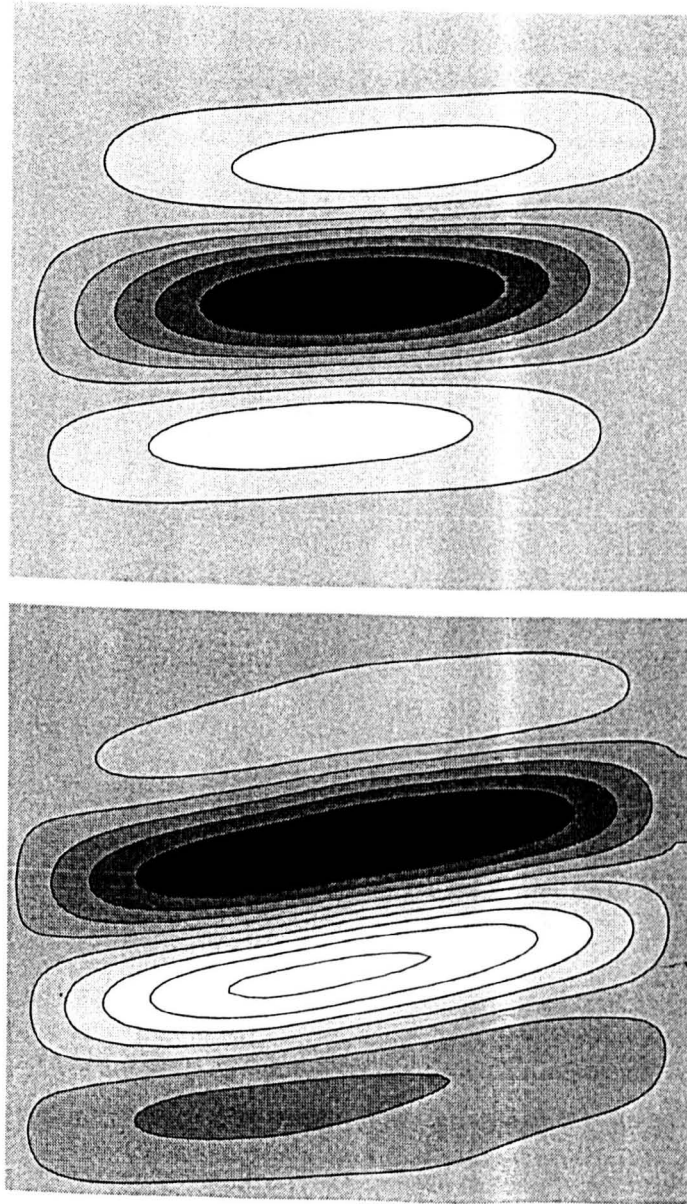


Figure 5.4: Contours of the real and imaginary parts of the amplitude function $A(X, Y)$ in the domain $-1 < X < 1$, $-5 < Y < 5$ for the leading eigenfunction with $\alpha = \pi/6$

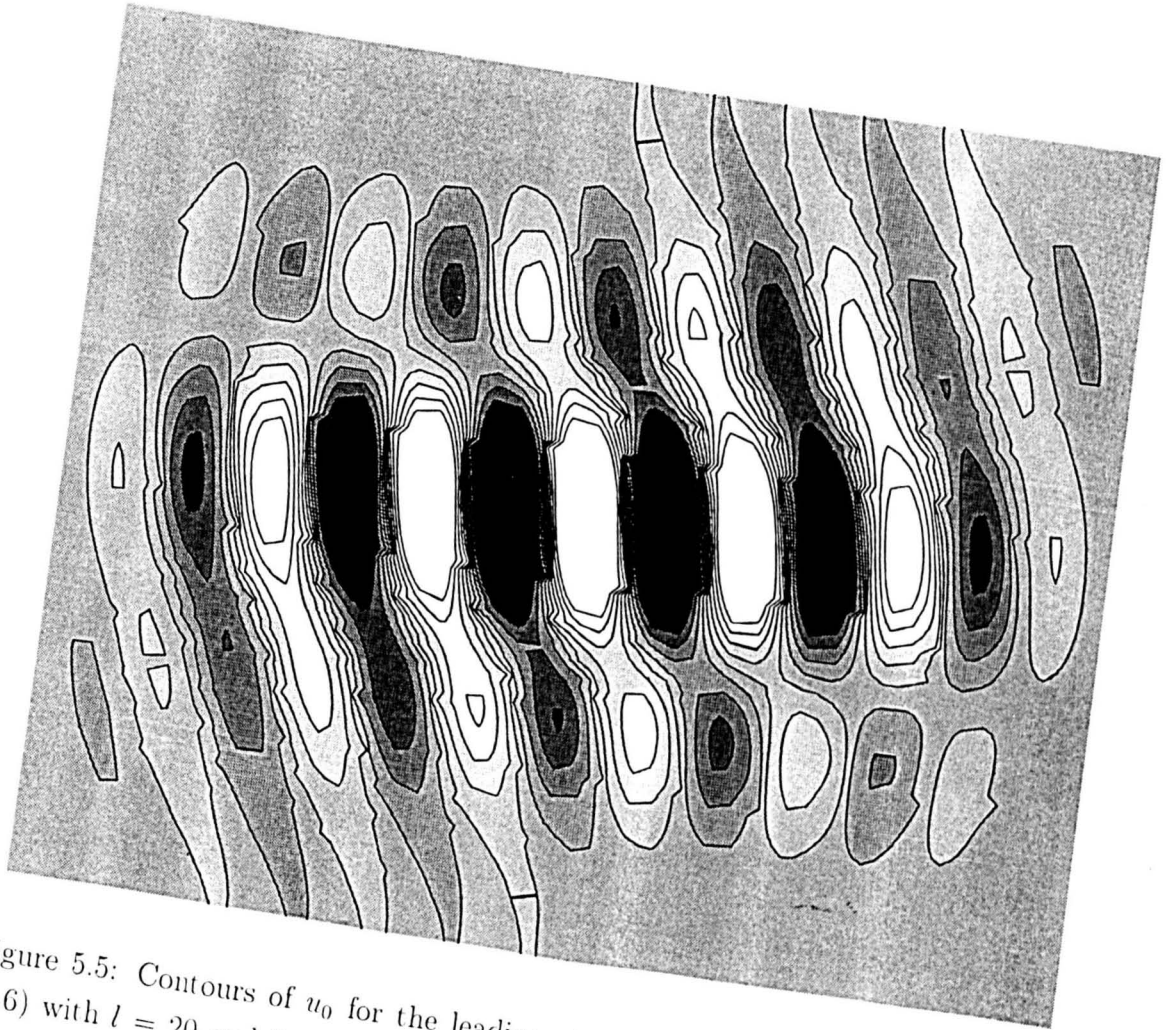


Figure 5.5: Contours of u_0 for the leading eigenfunction constructed from (5.6) with $l = 20$ and $\theta = 0$ in the domain $-1 < X < 1, -5 < Y < 5$ for $\alpha = 0.644$.

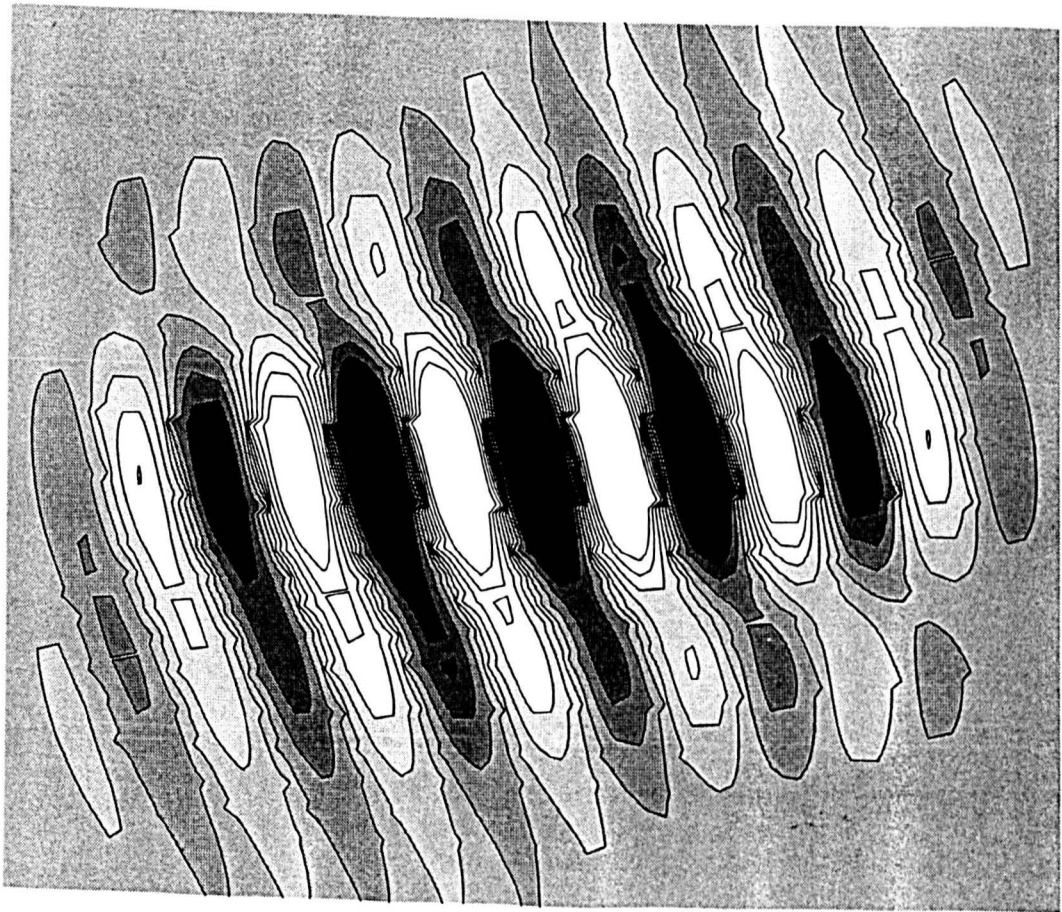


Figure 5.6: Contours of u_0 for the leading eigenfunction constructed from (5.6) with $l = 20$ and $\theta = 0$ in the domain $-1 < X < 1, -5 < Y < 5$ for $\alpha = \pi/6$.

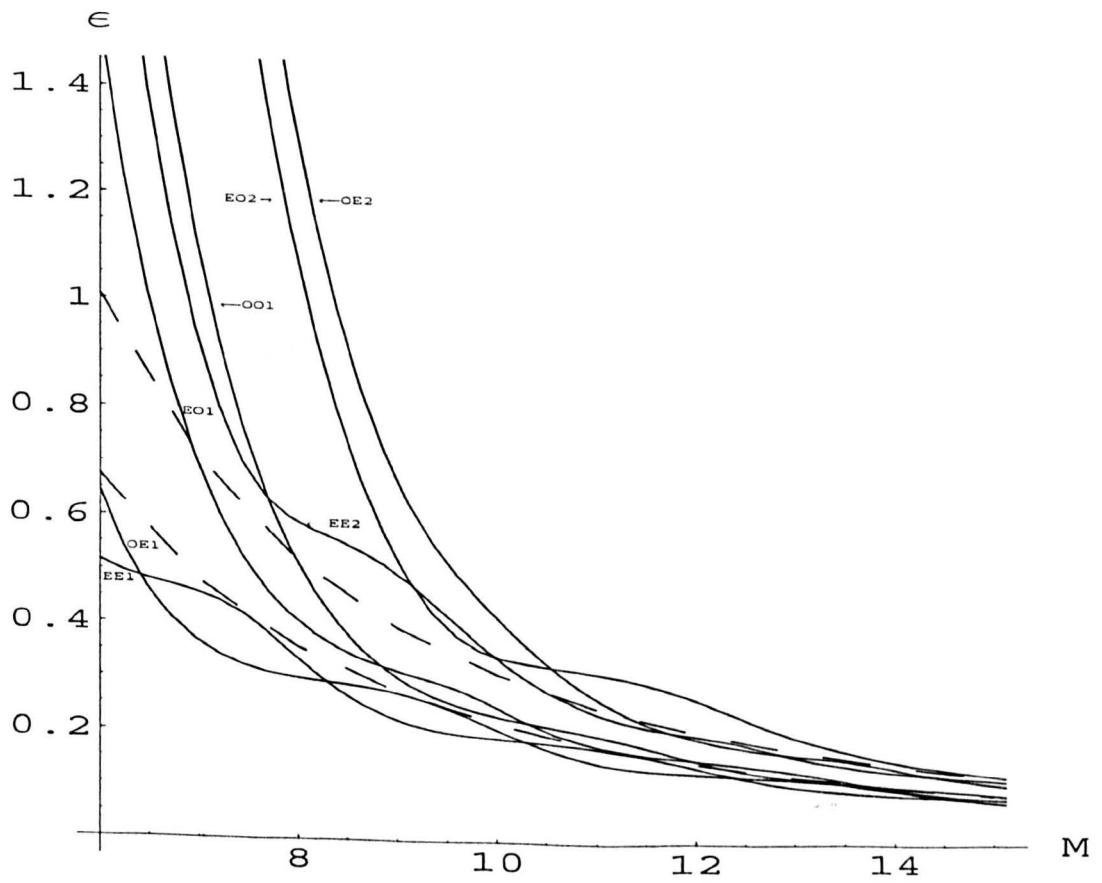


Figure 5.7: Comparison of the asymptotic theory (dashed curves) with the numerical results for the two leading eigenvalues with $M/L = 0.75$ ($\alpha = 0.644$).

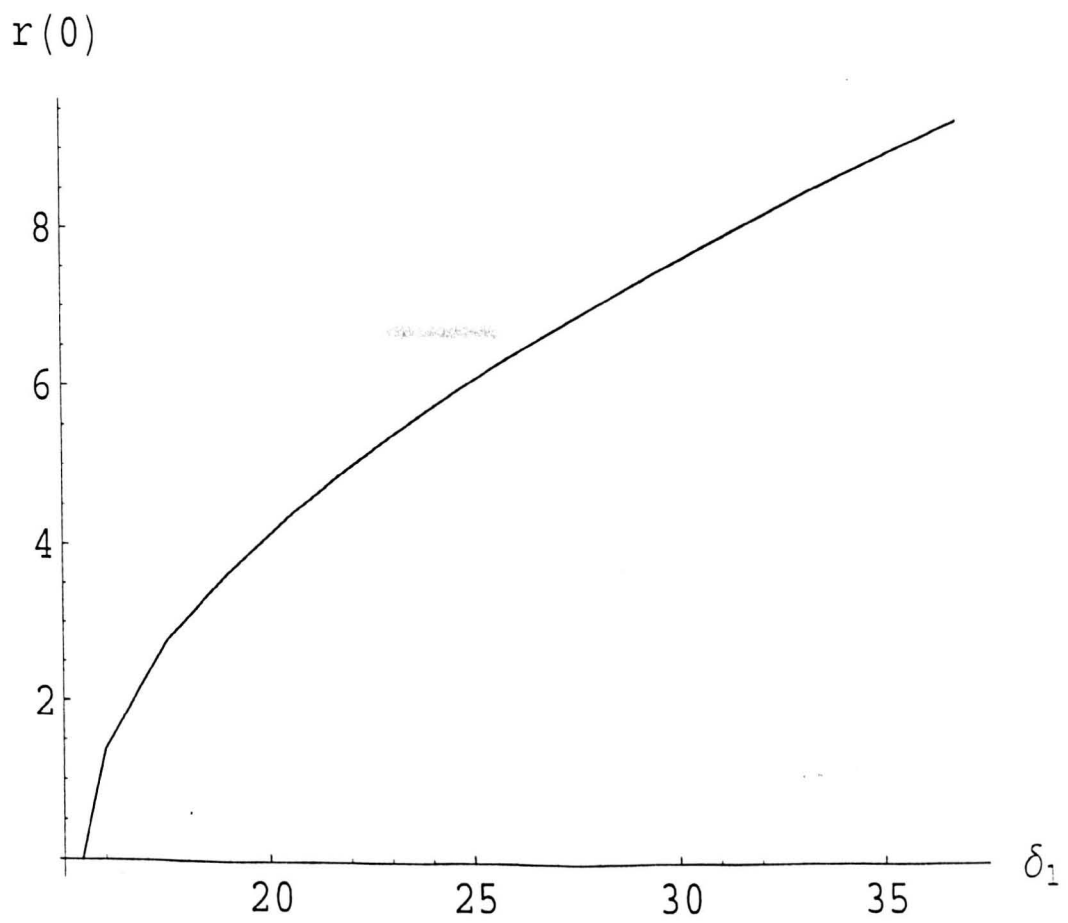


Figure 5.8: $r(0)$ versus δ_1 for the leading branch of solutions with $\alpha = 0.644$.

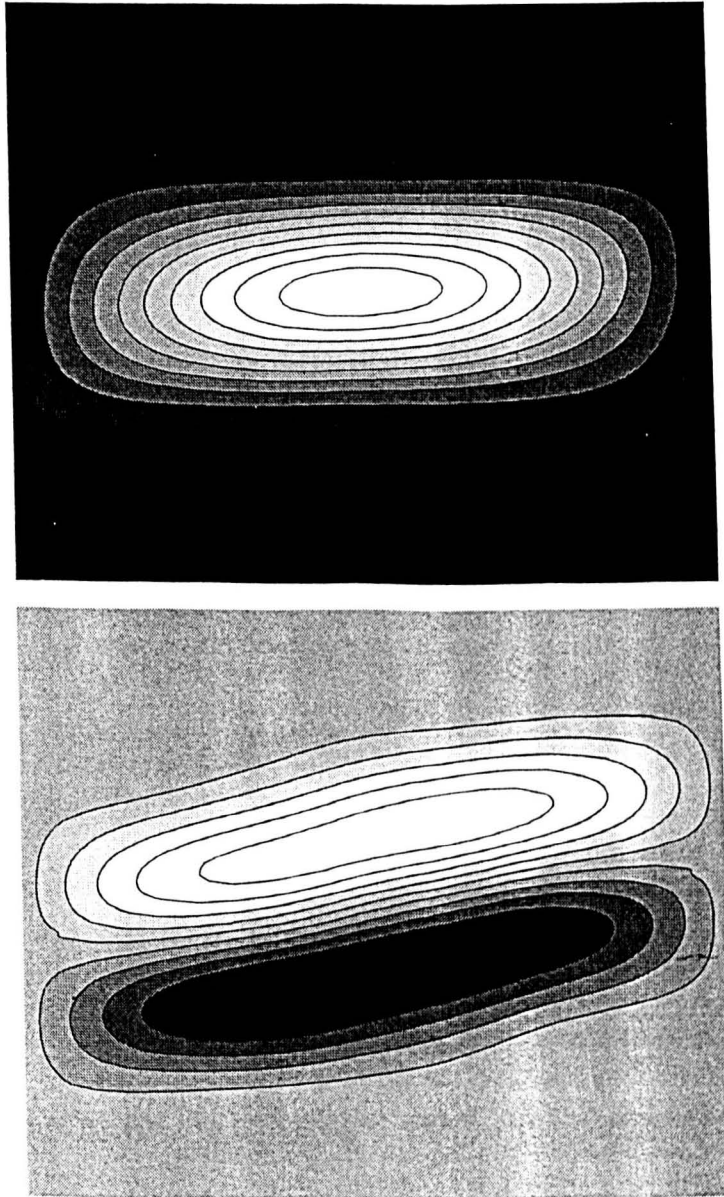


Figure 5.9: Contours of the real and imaginary parts of the amplitude function $A(X, Y)$ in the domain $-1 < X < 1$, $-5 < Y < 5$ for the leading eigenfunction with $\alpha = 0.644$ and $\delta_1 = 22.5$.

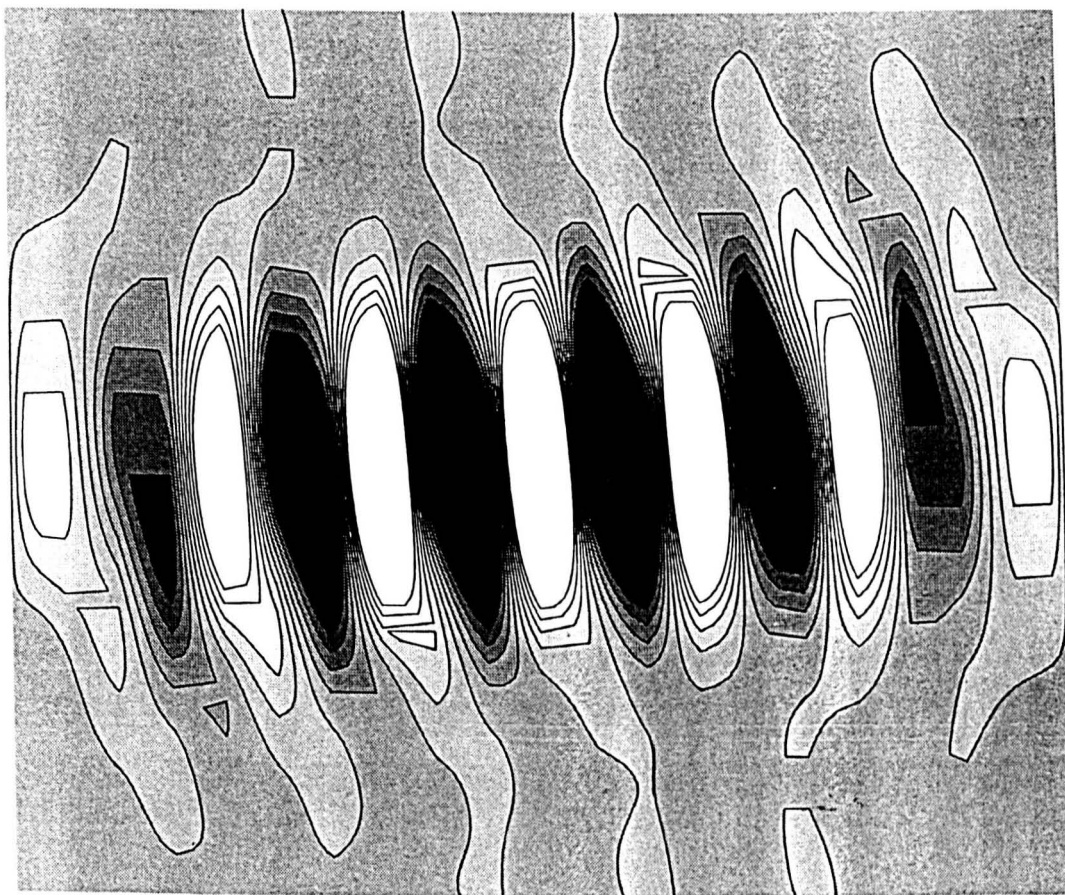


Figure 5.10: Contours of u_0 for $\delta_1 = 22.5$ on the leading solution branch constructed from (5.6) with $l = 20$ and $\theta = 0$ in the domain $-1 < X < 1$, $-5 < Y < 5$ for $\alpha = 0.644$.

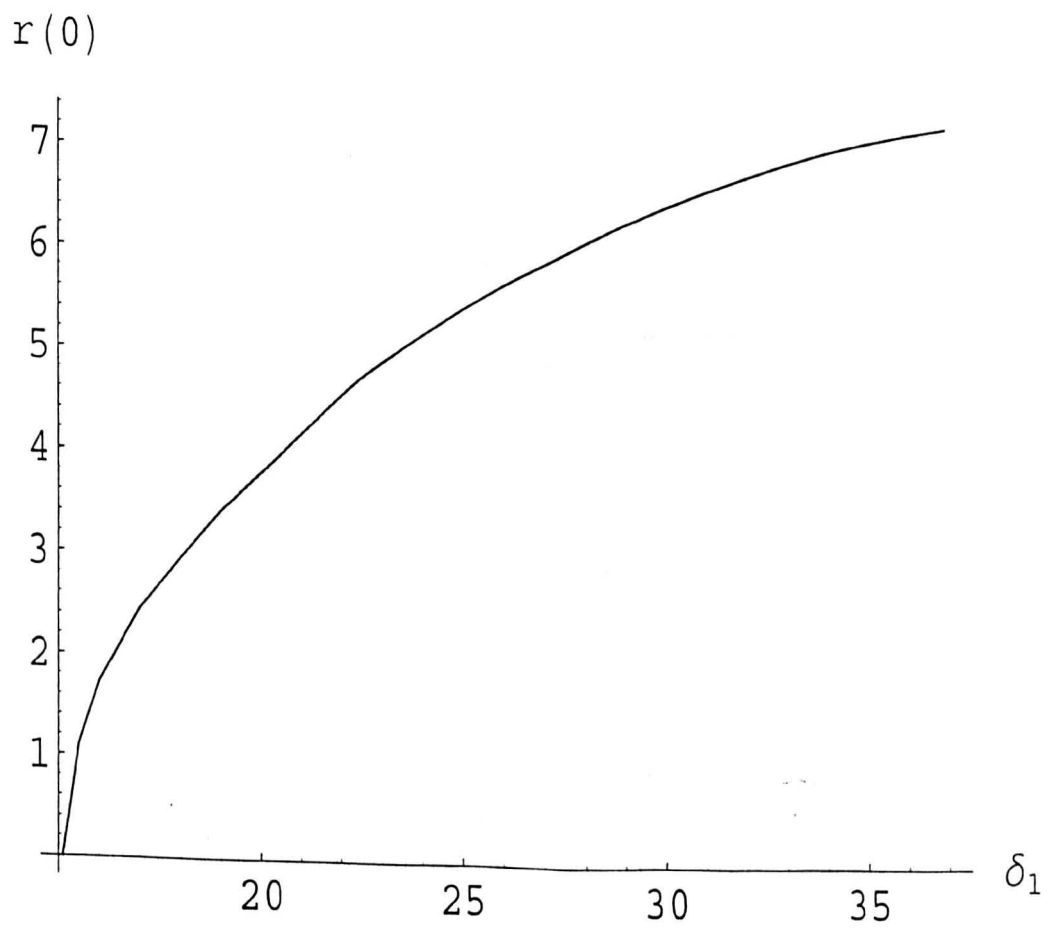


Figure 5.11: $r(0)$ versus δ_1 for the leading branch of solutions with $\alpha = \pi/6$.

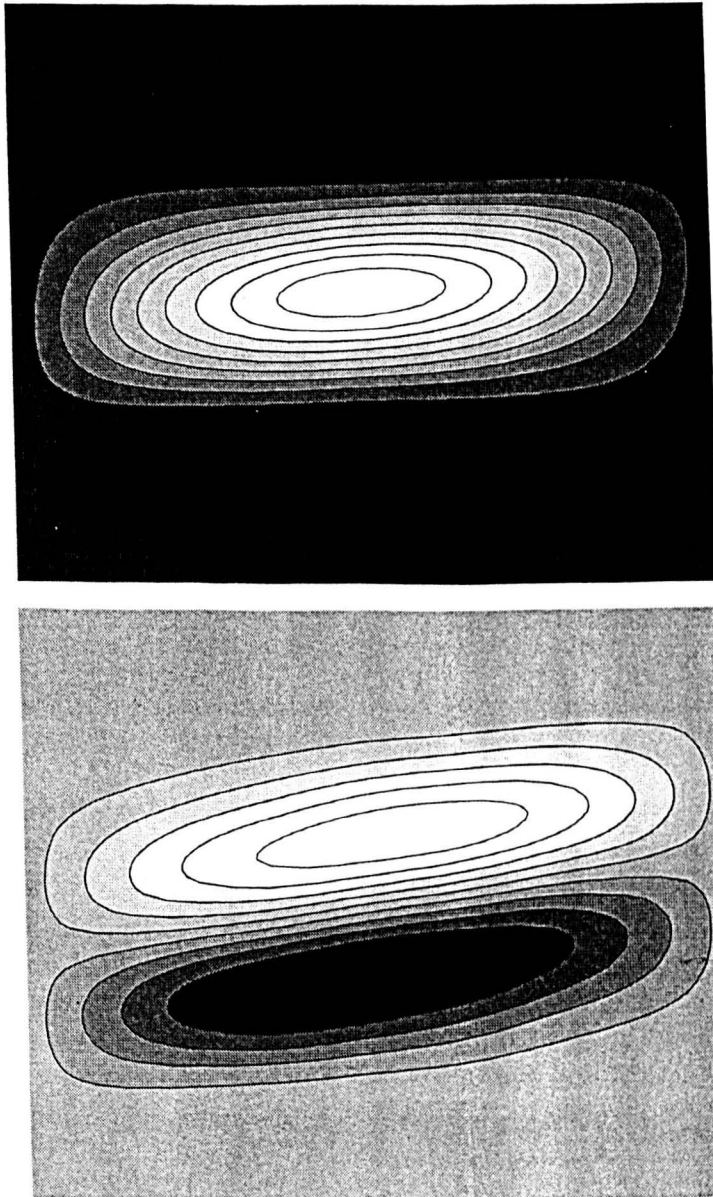


Figure 5.12: Contours of the real and imaginary parts of the amplitude function $A(X, Y)$ in the domain $-1 < X < 1$, $-5 < Y < 5$ for the leading eigenfunction with $\alpha = \pi/6$ and $\delta_1 = 22.5$.

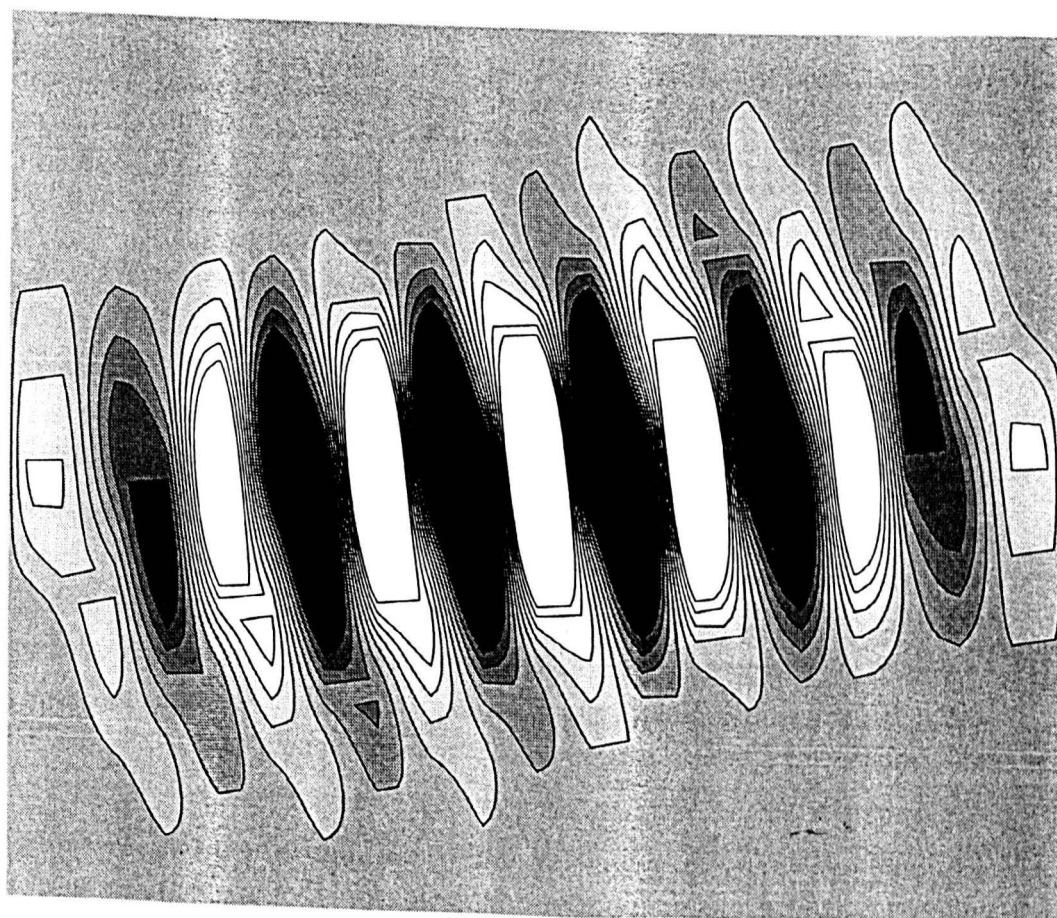


Figure 5.13: Contours of u_0 for $\delta_1 = 22.5$ on the leading solution branch constructed from (5.6) with $l = 20$ and $\theta = 0$ in the domain $-1 < X < 1$, $-5 < Y < 5$ for $\alpha = \pi/6$.

Chapter 6

Summary and conclusions

In Chapter 2, the bifurcation structure of steady-state solutions of the Swift-Hohenberg equation in square domains has been studied using a combination of weakly nonlinear analysis and computation. For periodic boundary conditions the bifurcation structure can be deduced analytically and introduction of a small rigid (non-periodic) component reveals some significant qualitative differences in the more realistic non-periodic case. For rigid boundary conditions solutions onset either as OE modes at repeated eigenvalues in which case there is also an associated diagonal mode with an even number of cells or as four fold symmetric EE or OO modes at single eigenvalues. For low values of L the single cell EE mode is the most dangerous but as L increases the leading modes of each type compete with one another so that the symmetry that occurs first depends on the precise value of L as shown in Figure 2.8. At large values of L the modes interweave forming distinct groups containing each type of symmetry.

Beyond the linear bifurcation points the complexity of nonlinear solutions becomes apparent, arising either from symmetry breaking secondary bifurcations or through new nonlinear fold bifurcations. Stable solutions occurring in this way include modes with an odd number of cells, modes with symmetry in one direction only, parallel modes and centrosymmetric modes. The ordering of these modes depends on the domain size L and even for a moderate value of L such as 5π the situation is extremely complex. The solutions shown in Figures 2.37, 2.44 and 2.60 are just a subset of the modes

that arise at moderate values of ε . For high values of L many modes fit into the domain even at low values of ε and the bifurcation structure becomes more difficult to compute.

An interesting feature of the leading rigid eigenfunction at large L is that the cells form along the diagonals of the square, either both diagonals in the case of the EE, OO or OE modes or one diagonal in the case of the D mode. For the EE and OO modes there are an odd number of cells along each diagonal whereas for the OE modes there are an even number of cells along the diagonals. For the EE, OO and OE modes the central part of the pattern is more complicated but is essentially a local superposition of the two sets of cells along each diagonal. This diagonal structure is intimately related to the non-periodic nature of the homogeneous boundary conditions and is not observed in the periodic problem. As ε increases and nonlinear effects set in patterns containing square cells or cross-rolls tend to be unstable. This is because for the Swift-Hohenberg system, like the Rayleigh-Bénard system, square cells are unstable to rolls in an infinite layer. Thus at large L if the linear onset pattern is one containing cross-rolls at the centre (EE or OO) it subsequently loses stability to a diagonal mode via a secondary bifurcation. On the other hand, if the onset pattern is OE, the corresponding diagonal mode D sets in immediately.

The intricate structure revealed here for large values of L would be difficult to compute for the Rayleigh-Bénard system because of the considerable computing power needed to simulate multiple-cell solutions in three dimensions. However it is expected that the same symmetry arguments will apply and hence that similar patterns will be observed. For moderate L , patterns similar to those of Figure 2.10 have been observed in a square planform container by Stork and Muller (1972, figure 6g). For larger L , diagonal structures have been observed in shallow square planform containers by Koschmieder (1966, figure 13) and although these bear quite a close resemblance to those of the EE1 mode in Figure 2.62 some caution is necessary in making definite comparisons. One possibility is that the container size used in the experiment corresponds to the case where the onset mode has EE symmetry and that this mode remains sufficiently stable to be observed in the experiment. However the observed motion appears to be strongly nonlinear making it

surprising that there was no evidence of a purely diagonal mode of the kind shown in Figure 2.61. The motion observed in the experiment may correspond to a secondary or fold bifurcation at higher ϵ in the Swift-Hohenberg model or it may be that experimental conditions (for example the poorly conducting glass lid used to observe the flow) were such as to favour square cell convection (see for example Hoyle 1995). Experiments focusing on the weak motion near onset are needed in order to test the main predictions of the present work for large aspect ratio systems.

In Chapter 3, the diagonal structure of solutions in square domains as $L \rightarrow \infty$ has been confirmed by a multiple scale matched asymptotic analysis, making use of the fact that the length scale of the domain is much greater than the length scale of individual rolls. The results appear to confirm both the behaviour of the eigenvalues ϵ of the linearised system and the overall structure of the weakly-nonlinear solutions in the limit as $L \rightarrow \infty$.

In Chapter 4 the numerical results for the rigid problem are extended to the case of rectangular domains. Here the main difference from the case of the square domain is that diagonal modes cannot onset as linear eigen-solutions and the repeated OE/EO/D modes of the square are replaced by distinct OE and EO modes at different eigenvalues. The results here generally confirm the prevalence of roll patterns parallel to the shorter sides of the rectangle for moderately sized planforms. However for planforms whose dimensions L, M are large in both directions local structures confined to the diagonals of the rectangle are preferred near onset. Beyond onset these solutions change into more coherent roll patterns typically by means of the structure along one diagonal strengthening relative to the other and leading to centrosymmetric curved roll patterns of the type computed numerically by Greenside and Coughran (1984, figure 10) and observed in Rayleigh-Bénard experiments (see Cross and Hohenberg 1993). Although straight roll patterns parallel to the sides of the rectangle remain possible steady-state solutions in large planforms they do not constitute the leading eigenfunctions, offering a possible explanation of why such simple patterns tend not to be observed in experiments in large planform rectangular domains.

In Chapter 5 the asymptotic analysis of Chapter 3 is extended to the case of the rectangular domain and it is confirmed that, near onset, solutions

exist consistent with a localised roll structure confined to the diagonals of the rectangle. The analysis determines the dependence of the critical eigenvalue ε on the aspect ratio of the rectangle ($M/L = \tan \alpha$) in the limit as $M \rightarrow \infty$ and $L \rightarrow \infty$ and this appears to agree well with the numerical results of Chapter 4.

An advantage of studying the Swift-Hohenberg equation is that it is sufficiently simple to allow numerical solutions to be computed for a wide range of domain sizes in a relatively straightforward manner and without the need for extensive computing power. This has allowed various key features of the system, including the role of rigid (no slip) boundaries, to be identified and compared with asymptotic solutions. Possible future avenues of research include the extension of the present work to more realistic physical systems such as the Darcy-Bénard system (governing convection in a porous medium heated from below) and the Rayleigh-Bénard system. Because of the close connection between the weakly nonlinear form of the Swift-Hohenberg equation and that of the Darcy-Bénard and Rayleigh-Bénard systems it seems possible that many features of the present study will carry over to these more realistic systems.

Other possible extensions of the present work would be to carry out a formal stability analysis of the numerous solution branches identified here and to relate the findings to values of the Lyapunov functional defined by Greenside and Coughran (1984). This was not possible within the time limitations of the present study but may help to distinguish the relative importance of the various parallel, diagonal, centrosymmetric and asymmetric modes of convection that can arise.

References

- Arter, W and Newell, A C 1988 Numerical simulation of Rayleigh-Bénard convection in shallow tanks. *Physics of Fluids* **31**, 2474-2485.
- Brown, S N and Stewartson, K 1977 On thermal convection in a large box. *Stud. Appl. Math* **57**, 187.
- Brown, S N and Stewartson, K 1978 On finite amplitude Bénard convection in a cylindrical container. *Proc. Roy. Soc. Lond* **A360**, 455-469.
- Buhler, K, Kirchartz, K R and Oertel, H 1979 Steady convection in a horizontal fluid layer. *Acta Mechanica*, **31**, 155-171.
- Catton, I 1970 Convection in a closed rectangular region: the onset of motion. *J. Heat Transfer*, **92**, 186-188.
- Chen, M M and Whitehead, J A 1968 Evolution of two-dimensional periodic Rayleigh convection cells of arbitrary wavenumber. *J. Fluid Mech.*, **31**, 1-15.
- Croquette, V 1989 Convective pattern dynamics at low Prandtl number. Part 1. *Cont. Physics*, **30**, 113-133.
- Croquette, V, Mory, M and Schosseler, F 1983 Rayleigh-Bénard convective structures in a cylindrical container. *J. Physique*, **44**, 293.
- Croquette, V and Schosseler, F 1982 Diffusive models in Rayleigh-Bénard structures. *J. Physique*, **43**, 1183-1191.
- Cross, M C 1982 Boundary conditions on the envelope function of convective rolls close to onset. *Phys. Fluids*, **25**, 936-941.
- Cross, M C and Hohenberg, P C 1993 Pattern formation outside of equilibrium. *Rev. Mod. Phys.*, **65**, 851-1112.
- Cross, M C and Newell, A C 1984 Convection patterns in large aspect ratio systems. *Physica D* , **10**, 299-328.
- Daniels, P G 1977a The effect of distant sidewalls on the transition to finite amplitude Bénard convection. *Proc. Roy. Soc. Lond.*, **A358**, 173-197.
- Daniels, P G 1977b Asymptotic sidewall effects in rotating Bénard convection. *Z. angew. Math. Phys.*, **28**, 577-584.
- Daniels, P G 1978 The effect of distant sidewalls on the transition to finite amplitude Bénard convection II. *Mathematika*, **25**, 216-235.
- Daniels, P G 1981 The effect of distant sidewalls on the stability and evolution of finite amplitude Rayleigh-Bénard convection. *Proc. Roy. Soc. Lond.*, **A378**, 539-566.

- Daniels, P G 1984 Roll pattern evolution in finite amplitude Rayleigh-Bénard convection in a two-dimensional fluid layer bounded by distant sidewalls. *J.Fluid Mech.*, **143**, 125-152.
- Daniels, P G 2000 Onset of convection in shallow cylindrical containers. *Proc.Roy.Soc.Lond.*, **A456**, 527-551.
- Daniels, P G and Lee, A T 1999 On the boundary layer structure of patterns of convection in rectangular planform containers. *J.Fluid Mech.*, **393**, 357-380.
- Daniels, P G and Weinstein, M 1992 On finite amplitude patterns of convection near a lateral boundary. *Quart.J.Mech.Appl.Math.*, **45**, 315-336.
- Daniels, P G and Weinstein, M 1996 On finite amplitude patterns of convection in a rectangular planform container. *J.Fluid Mech.*, **317**, 111-127.
- Davies-Jones, R P 1970 Thermal convection in an infinite channel with no slip sidewalls. *J.Fluid Mech.*, **44**, 695-704.
- Davis, S H 1967 Convection in a box: linear theory. *J.Fluid Mech.*, **30**, 465-478.
- Drazin, P G 1975 On the effects of sidewalls on Bénard convection. *Z.angew. Math.Phys.*, **26**, 239.
- Edwards, B F 1988 Crossed rolls at the onset of convection in a rigid box. *J.Fluid Mech.*, **191**, 583-597.
- Gollub, J P, McCarriar, A R and Steinman, J F 1982 Convective pattern evolution and secondary instabilities. *J.Fluid Mech.*, **125**, 259-281.
- Greenside, H S and Coughran, W M 1984 Nonlinear pattern formation near the onset of Rayleigh-Bénard convection. *Phys.Rev.*, **A30**, 398-428.
- Greenside, H S, Coughran, W M and Schryer, N L 1982 Nonlinear pattern formation near onset of Rayleigh-Bénard convection. *Phys.Rev.Lett.*, **49**, 726.
- Hoyle, R B, 1995 Steady squares and hexagons on a subcritical ramp. *Phys. Rev.E*, **51**, 310.
- Kirchartz, K R and Oertel H 1988 Three-dimensional thermal cellular convection in rectangular boxes. *J.Fluid Mech.*, **192**, 249-286.
- Koschmieder, E L 1966 On convection on a uniformly heated plane. *Beitr. Phys.Atmos.*, **39**, 1-11.
- Koschmieder, E L 1974 Bénard convection. *Adv.Chem.Phys.*, **26**, 177-212.

- Koschmieder, E L 1993 *Bénard Cells and Taylor Vortices*. Cambridge University Press.
- Manneville, P 1983 A numerical simulation of convection in a cylindrical geometry. *J.Phys.Lett.*, **44**, 903-916.
- Morris, S W, Bodenschatz, E, Cannell, D S and Ahlers, G 1993 Spiral defect chaos in large aspect ratio Rayleigh-Bénard convection. *Phys.Rev.Lett.*, **71**, 2026-2029.
- Newell, A C, Passot, T and Souli, M 1990 The phase diffusion and mean drift equations for convection at finite Rayleigh numbers. *J.Fluid Mech.*, **220**, 187-252.
- Newell, A C and Whitehead, J A 1969 Finite bandwidth, finite amplitude convection. *J.Fluid Mech.*, **38**, 279-303.
- Segel, L A 1969 Distant sidewalls cause slow amplitude modulation of cellular convection. *J.Fluid Mech.*, **38**, 203-224.
- Stork, K and Muller, U 1972 Convection in boxes: experiments. *J.Fluid Mech.*, **54**, 599-611.
- Swift, J and Hohenberg, P C 1977 Hydrodynamic fluctuations at the convective instability. *Phys.Rev.*, **A15**, 319-328.